DOCTORAL SCHOOL IN CIVIL, ENVIRONMENTAL AND MECHANICAL ENGINEERING

Discontinuous Galerkin methods for compressible and incompressible flows on space-time adaptive meshes

by

Francesco Fambri

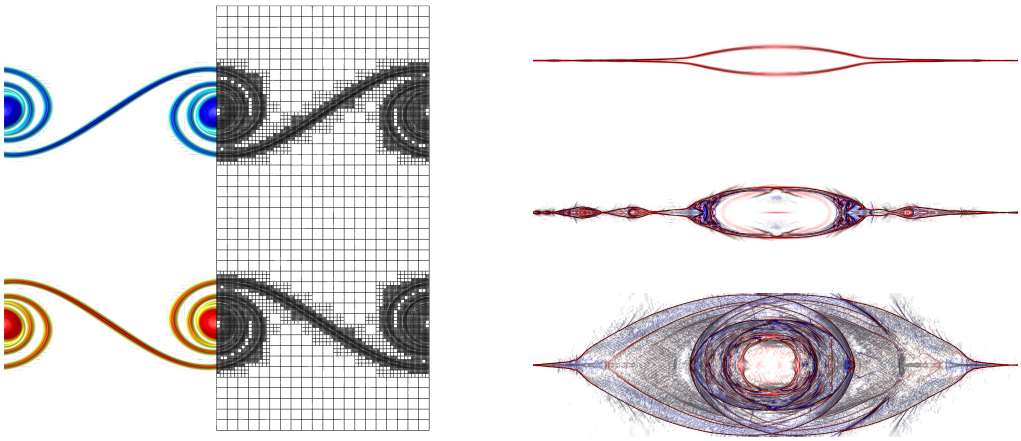

UNIVERSITY OF TRENTO

Department of Civil, Environmental and Mechanical Engineering

2016

Francesco Fambri: *Discontinuous Galerkin methods for compressible and incompressible flows on space-time adaptive meshes*, January, 2017

DOCTORAL THESIS
in Civil, Environmental and Mechanical Engineering

SCIENTIFIC AREA
Applied Mathematics - MAT/08

ACADEMIC CYCLE
2014-2016 (XXIX cycle)

SUPERVISOR
Prof.Dr.-Ing Michael Dumbser, University of Trento, Italy

University of Trento
Trento, Italy
2016

Dedicated to my family,
my wife Laura, my child Giacomo and his forthcoming sibling,

to my mother Paola,

in memory of
my father Giuliano Fambri 1930 – 2007
and my brother Nicola 1984 – 2006

ABSTRACT

In this work the numerical discretization of the partial differential governing equations for compressible and incompressible flows is dealt within the discontinuous Galerkin (DG) framework along space-time adaptive meshes. Two main research fields can be distinguished: (1) *fully explicit* DG methods on collocated grids and (2) *semi-implicit* DG methods on *edge-based staggered grids.* DG methods became increasingly popular in the last twenty years mainly because of three intriguing properties: i) non-linear L_2 stability has been proven; ii) arbitrary high order of accuracy can be achieved by simply increasing the polynomial order of the chosen basis functions, used for approximating the state-variables; iii) high scalability properties make DG methods suitable for large-scale simulations on general unstructured meshes.

It is a well known fact that a major weakness of high order DG methods lies in the difficulty of limiting discontinuous solutions, which generate spurious oscillations, namely the so-called 'Gibbs phenomenon'. Over the years, several attempts have been made to cope with this problem and different kinds of *limiters* have been proposed. Among them, a rather intriguing paradigm has been defined in the work of [71], in which the nonlinear stabilization of the scheme is sequentially and locally introduced only for troubled cells on the basis of a multidimensional optimal order detection (MOOD) criterion. In the present work the main benefits of the MOOD paradigm, i.e. the computational robustness even in the presence of strong shocks, are preserved and the numerical diffusion is considerably reduced also for the *limited* cells by resorting to a proper sub-grid. In practice the method first produces a so-called *candidate solution* by using a high order accurate *unlimited* DG scheme. Then, a set of numerical and physical detection criteria is applied to the candidate solution, namely: positivity of pressure and density, absence of floating point errors and satisfaction of a discrete maximum principle in the sense of polynomials. Then, in those cells where at least one of these criteria is violated the computed candidate solution is detected as *troubled* and is *locally* rejected. Next, the numerical solution of the *previous* time step is scattered onto cell averages on a suitable *sub-grid* in order to preserve the natural sub-cell resolution of the DG scheme. Then, a more reliable numerical solution is *recomputed a posteriori* by employing a more robust but still very accurate ADER-WENO finite volume scheme on the sub-grid averages within that troubled cell. Finally, a high order DG polynomial is reconstructed back from the evolved sub-cell averages. Moreover, handling typical multiscale problems, dynamic adaptive mesh refinement (AMR) and adaptive polynomial order methods are probably the two main ways of preserving accuracy and efficiency, and saving computational effort. The here adopted AMR-approach is the so called *'cell by cell' refinement* because of its formally very simple tree-type data structure. In the here-presented 'cell-by-cell' AMR *every single element is recursively refined*, from a coarsest refinement level $\ell_0 = 0$ to a prescribed

finest (maximum) refinement level $\ell_{max} \in \mathbb{N}_0^+$, accordingly to a *refinement-estimator function* χ that drives step by step the choice for recoarsening or refinement. The combination of the sub-cell resolution with the advantages of AMR allows for an unprecedented ability in resolving even the finest details in the dynamics of the fluid. First, the *Euler equations of compressible gas dynamics* and the *magnetohydrodynamics (MHD) equations* have been treated [281]. Then, the presented method has been readily extended to the *special relativistic ideal MHD equations* [280], but also the the case of *diffusive fluids*, i.e. fluid flows in the presence of *viscosity*, *thermal conductivity* and *magnetic resistivity* [116]. In particular, the adopted formalism is quite general, leading to a novel family of adaptive ADER-DG schemes suitable for hyperbolic systems of partial differential equations in which the numerical fluxes also *depend on the gradient of the state vector* because of the *parabolic* nature of diffusive terms. The presented results show clearly that the *shock-capturing capability* of the news schemes are significantly enhanced within the cell-by-cell *Adaptive Mesh Refinement* (AMR) implementation together with time accurate local time stepping (LTS). The resolution properties of the new scheme have been shown through a wide number of test cases performed in two and in three space dimensions, from low to high Mach numbers, from low to high Reynolds regimes.

In particular, concerning MHD equations, the divergence-free character of the magnetic field is taken into account through the so-called hyperbolic 'divergence-cleaning' approach which allows to artificially transport and spread the numerical spurious 'magnetic monopoles' out of the computational domain.

A special treatment has been followed for the *incompressible* Navier-Stokes equations. In fact, the elliptic character of the incompressible Navier-Stokes equations introduces an important difficulty in their numerical solution: whenever the smallest physical or numerical perturbation arises in the fluid flow then it will instantaneously affect the entire computational domain. Thus, a *semi-implicit* approach has been used. The main advantage of making use of a semi-implicit discretization is that the numerical stability can be obtained for large time-steps without leading to an excessive computational demand [117]. In this context, we derived two new families of *spectral* semi-implicit and spectral space-time DG methods for the solution of the two and three dimensional Navier-Stokes equations on *edge-based staggered* Cartesian grids [115], following the ideas outlined in [97] for the shallow water equations. The discrete solutions of pressure and velocity are expressed in the form of piecewise polynomials along *different* meshes. While the pressure is defined on the control volumes of the main grid, the velocity components are defined on edge-based dual control volumes, leading to a *spatially staggered* mesh. In the first family, high order of accuracy is achieved only in space, while a simple semi-implicit time discretization is derived by introducing an implicitness factor $\theta \in [0.5, 1]$ for the pressure gradient in the momentum equation. The real advantages of the *staggering* arise after substituting the discrete momentum equation into the weak form of the continuity equation. In fact, the resulting linear system for the pressure is *symmetric* and *positive definite* and either block penta-diagonal (in 2D) or block hepta-diagonal (in 3D). As a consequence, the pressure system can be solved very efficiently by means of a classical matrix-free conjugate gradi-

ent method. Moreover, a rigorous theoretical analysis of the condition number of the resulting linear systems and the design of specific preconditioners, using the theory of matrix-valued symbols and Generalized Locally Toeplitz (GLT) algebra has been successfully carried out with promising results in terms of numerical efficiency [102]. The resulting algorithm is stable, computationally very efficient, and at the same time arbitrary high order accurate in both space and time. The new numerical method has been thoroughly validated for approximation polynomials of degree up to $N = 11$, using a large set of non-trivial test problems in two and three space dimensions, for which either analytical, numerical or experimental reference solutions exist. Moreover, the here mentioned semi-implicit DG method has been successfully extended to a novel *edge-based staggered* 'cell-by-cell' adaptive meshes [114].

PREFACE

This thesis has been submitted in partial satisfaction of the requirements for the degree of Doctor of Philosophy in Civil, Environmental and Mechanical Engineering in the Doctoral school of the Department of Civil, Environmental and Mechanical Engineering (DICAM) at University of Trento, Italy.

This work has been carried out under the supervision of Prof. Dr.-Ing Michael Dumbser within the three-years Doctoral Programme in Civil, Environmental and Mechanical Engineering at DICAM Dept. of University of Trento.

The presented research has been financed mainly by the European Research Council (ERC) under the European Union's Seventh Framework Programme (FP7/2007-2013) with the research project *STiMulUs*, ERC Grant agreement no. 278267.

The author has also received funding from the European Union's Horizon 2020 Research and Innovation Programme under the project *ExaHyPE*, grant agreement number no. 671698 (call FETHPC-1-2014).

The author also acknowledges the Leibniz Rechenzentrum (LRZ) in Munich, Germany, for awarding us access to the *SuperMUC* supercomputer, as well as the support of the HLRS in Stuttgart, Germany, for awarding access to the *Hazel Hen* supercomputer.

This thesis deals with applied mathematics, as a branch of mathematical studies, or applied physics, as a branch of physical studies, but also computational science, as a branch of computer science. The main mathematical, physical and computational ingredients, are mixed together bringing this work in the context of *mathematical-engineering*. The final application is simulating physical balance laws of fluid dynamics for several different fluid theories, i.e. with or without electrical currents and magnetic fields, with or without dissipative effects of viscosity or magnetic resistivity, from the compressible to the fully incompressible limit.

Trento, January 2017

Francesco Fambri

ACKNOWLEDGEMENTS

I would like to thank Prof. Dumbser for guiding me through this research, the inspiring supervision of my PhD studies but in particular for the very friendly academic environment he inspires in his research group.

Then I would like to thank Prof. Hidalgo for the collaboration done, and many special thanks to Dr. Zanotti for the fruitful collaboration, the valuable discussions about plasma physics, relativistic hydrodynamics and for his friendship.

Many thanks also to Prof. Casulli and Prof. Toro, for introducing me to the fields of semi-implicit numerical modeling and Riemann solvers together with their enthusiastic interest in numerical analysis.

Finally, I am particularly grateful to the person who allowed me to complete these studies and at the same time enjoying the sweet company of my child Giacomo, *id est* my wife Laura and her indefatigable faith.

PUBLICATIONS

This thesis is based on the following publications:

[1] O. Zanotti, F. Fambri, M. Dumbser, and A. Hidalgo. Space-time adaptive ADER discontinuous Galerkin finite element schemes with a posteriori subcell finite volume limiting. *Computers & Fluids*, 118:204–224, (2015).

[2] O. Zanotti, F. Fambri, and M. Dumbser. Solving the relativistic magnetohydrodynamics equations with ADER discontinuous Galerkin methods, a posteriori subcell limiting and adaptive mesh refinement. *Mon. Not. R. Astron. Soc.*, 452:3010–3029, (2015).

[3] F. Fambri and M. Dumbser. Spectral semi-implicit and space-time discontinuous Galerkin methods for the incompressible Navier-Stokes equations on staggered Cartesian grids. *Applied Numerical Mathematics*, 110:41–74, (2016).

[4] F. Fambri, M. Dumbser, and O. Zanotti. Space-time adaptive ADER-DG - schemes for dissipative flows: compressible Navier-Stokes and resistive MHD equations. *Submitted to*, ISSN arXiv:1612.01410.

[5] F. Fambri and M. Dumbser. Semi-implicit discontinuous Galerkin methods for the incompressible Navier-Stokes equations on adaptive staggered Cartesian grids. *Submitted to*, ISSN arXiv:1612.09558.

[6] M. Dumbser, F. Fambri, I. Furci, M. Mazza, S. Serra- Capizzano, and M. Tavelli. Staggered discontinuous Galerkin methods for the incompressible Navier-Stokes equations: spectral analysis and computational results. *Submitted to*, ISSN arXiv:1612.04529.

CONTENTS

ACRONYMS

AMR Adaptive mesh refinement

CFL Courant-Friedrichs-Lewy

CNS Compressible Navier-Stokes

DG Discontinuous Galerkin

ENO Essentially non-oscillatory

FD Finite difference

FE Finite element

FV Finite volume

GLT Generalized locally Toeplitz

IncNS Incompressible Navier-Stokes

MHD magneto-hydro-dynamics

MOOD Multidimensional optimal order detection

PDE Partial differential equation

RK Runge-Kutta

SCL Sub-cell limiter

SI-DG Semi-implicit discontinuous Galerkin

SR-MHD Special relativistic magneto-hydro-

SR-HD Special relativistic hydro-dynamics

st-DG Space-time discontinuous Galerkin

TVD Total variation diminishing

VRMHD Viscous and resistive magneto-hydro-dynamics

VR-SR-MHD Viscous and resistive (special) relativistic magneto-hydro-dynamics

WENO Weighted essentially non-oscillatory

Part I

INTRODUCTION

The first part of the thesis is organized in two chapters with the intent to introduce the basic definitions, ideas and references for the numerical solution of PDEs (Chapter 1) and to give brief physical motivation of the treated governing equations (Chapter 2). The content of these chapters are thought to be a sort of basic handbook for those notions of numerical methods and governing equations that are used in the rest of the thesis. The introduction is based on some important references, in particular see mainly [259] but also [132, 79, 187] for the numerics, [29, 181, 118] for the main notions of continuum physics and balance laws, and [66, 180, 137, 155, 154] for the theory of fluids in magnetic fields.[1]

1 numerics: Toro [259], Leveque [187], Courant and Hilbert [79], Godunov and Ryabenkii [132]; physics: Batchelor [29], Landau et al. [181], Fasano and Marmi [118], Chen [66], Landau et al. [180], Goedbloed and Poedts [137], Javorskij and Detlaf [155], Jackson [154], Rezzolla and Zanotti [236]

1

PRELIMINARIES ON CONSERVATION LAWS AND PDE

In continuum physics, balance laws are expressed in terms of differential equations that, after stating proper boundary and initial conditions, lead to the definition of a specific physical problem. On the other hand, given a conserved physical observable Q, q being the relative density, then the conservation between the amount of Q within a control volume $T = [x_1, x_2]$ and the *flux* of Q through the boundary holds, i.e.

$$\frac{d}{dt}\int_{x_1}^{x_2} q\, dx = f(q(x_2), x_2, t) - f(q(x_1), x_1)\,. \tag{1.1}$$

Then, *assuming differentiability of* q the relative differential form holds

$$\frac{\partial}{\partial t} q = \frac{\partial}{\partial x} f(q, x, t)\,. \tag{1.2}$$

Whenever u is a discontinuous function, then the differential form holds only *in the sense of distributions*, i.e. in its weak integral form, i.e. after multiplication by a sufficiently regular test function (continuously differentiable and with compact support) φ

$$\int_{x_1}^{x_2} \varphi \frac{\partial}{\partial t} q\, dx = \int_{x_1}^{x_2} \varphi \frac{\partial}{\partial x} f(q, x, t)\; dx. \tag{1.3}$$

The integral form is important because it allows discontinuous solutions, the counterpart is that the proper initial and boundary conditions are not always sufficient for determining the uniqueness of the solution. Then a so called *entropy condition* is needed for determining the degree of admissibility for a given weak solution. In general, a system of balance laws could consider other terms in the equations, such as stiff or non-stiff *sources*, *non-conservative products*, or *parabolic* terms, which are often used to model dissipative processes.

1.1 HYPERBOLIC SYSTEMS

1.1.1 *Hyperbolic, parabolic and elliptic PDEs*

Given a physical law and the corresponding differential equation, the fundamental character of the law is independent on the chosen coordinate system. This fact, a sort of relativity principle for the nature of the governing PDEs, allows to classify second order PDEs in three families: *hyperbolic*, *elliptic* and *parabolic*. For simplicity,

let us consider a general *second order* differential operator L acting on a function $q = q(x, y)$, according to

$$L[q] = aq_{xx} + bq_{xy} + cq_{yy} + I[x, y, q, q_x, q_y], \tag{1.4}$$

a, b and c being constant real coefficients, I a general non-linear first order differential operator. It can be shown that, after a change of coordinates, the corresponding PDE $L[q] = 0$ can be written in three canonical forms depending on the so-called *discriminant* Δ of the *characteristic quadratic form* $\tilde{L} = \tilde{L}(k_x, k_y)$

$$\tilde{L}(k_x, k_y) = a\ k_x^2 + b\ k_x k_y + c\ k_y^2, \qquad \Delta = b^2 - 4ac. \tag{1.5}$$

In particular, operator L is said

i. *hyperbolic* if $\Delta > 0$,
ii. *parabolic* if $\Delta = 0$, (1.6)
iii. *elliptic* if $\Delta < 0$.

The chosen nomenclature is directly linked to the algebraic properties of the quadratic form $\tilde{L}$ at a fixed point (x,y), depicted by the geometric properties of the curve $\tilde{L} = 1$: a hyperbola, a parabola or an ellipse respectively. In particular, the corresponding PDEs written in *normal form* are

i. for *hyperbolic* PDEs : $\begin{cases} q_{\xi\xi} - q_{\eta\eta} + \tilde{I}(\xi, \eta, q, q_\xi, q_\eta) = 0 \\ \text{or} \\ q_{\xi\eta} + \tilde{I}(\xi, \eta, q, q_\xi, q_\eta) = 0 \end{cases}$

ii. for *parabolic* PDEs : $q_{\xi\xi} + \tilde{I}(\xi, \eta, q, q_\xi, q_\eta) = 0$

iii. for *elliptic* PDEs : $q_{\xi\xi} + q_{\eta\eta} + \tilde{I}(\xi, \eta, q, q_\xi, q_\eta) = 0$

Major examples are the wave equation for the hyperbolic case, the heat equation for the parabolic and the Laplace or Poisson equation for the elliptic case. Notice that conditions (1.6) implies existence of two, one or zero real solution to the characteristic equation $\tilde{L}(k_x, k_y) = 0$.

1.1.2 *Hyperbolic systems and characteristics*

Unfortunately, classifying and reducing general systems of PDEs into normal form is not straightforward. The governing PDEs approximating a real physical system rarely show a purely hyperbolic, parabolic or elliptic character. Physical dissipation is linked to parabolic terms, the divergence-free constraint to elliptic ones, but in general, the majority of the partial differential equations for dynamical systems, are directly linked to transport and wave equations at *finite velocities*, dealing with *hyperbolic systems*. Then, the more pedagogical way of introducing the main

aspects about the numerical treatment of the governing equations toward the research topic of this thesis, is to consider first a system of m conservation laws in one space dimension that can be cast into the following form

$$\mathbf{Q}_t + \mathbf{F}_x = 0, \qquad \text{or alternatively} \qquad \mathbf{Q}_t + \mathbf{A}\mathbf{Q}_x = 0. \tag{1.7}$$

Here, $\mathbf{Q} = \mathbf{Q}(\mathbf{x}, t)$ and $\mathbf{F}(\mathbf{Q}, \mathbf{x}, t)$ are respectively the vector of conserved variables and the vector of fluxes in the form

$$\mathbf{Q} = \left(\, q_1, \, q_2, \, \ldots, \, q_m \, \right), \qquad \mathbf{F} = \left(\, f_1, \, f_2, \, \ldots, \, f_m \, \right), \tag{1.8}$$

and the Jacobian of the fluxes $\mathbf{A} = \partial \mathbf{F} / \partial \mathbf{Q}$ has been introduced. This system of PDE is classified to be *hyperbolic* or *elliptic* at a given point $(\mathbf{x}, t)$ depending on the properties of the Jacobian of the fluxes $\mathbf{A} = \partial \mathbf{F} / \partial \mathbf{Q}$, in particular system (1.7) is said to be:

i. *hyperbolic* if $\mathbf{A}$ has m *linearly independent eigenvectors* $\mathbf{b}_1, \mathbf{b}_2, .., \mathbf{b}_m$ with *real eigenvalues* $\lambda_1, \lambda_2, .., \lambda_m$;

ii. *elliptic* if *none* of the eigenvalues are real.

In the simplest approximation $\mathbf{A}$ has constant coefficients and system (1.7) is said to be *linear*. For hyperbolic systems, the Jacobian matrix $\mathbf{A}$ is *diagonizable*, i.e. $\mathbf{A}$ can be written in the form $\mathbf{A} = \mathbf{B}\Lambda\mathbf{B}^{-1}$ with

$$\Lambda = \operatorname{diag}\left(\lambda_1, \, \lambda_2, \, \ldots, \, \lambda_m\right), \qquad \mathbf{B} = \left[\mathbf{b}_1, \, \mathbf{b}_2, \, \ldots, \, \mathbf{b}_m\right], \qquad \mathbf{A}\mathbf{b}_i = \lambda_i \mathbf{b}_i \tag{1.9}$$

After multiplication of system by $\mathbf{B}^{-1}$ from the left and inserting the identity $\mathbb{I} = \mathrm{B}\mathrm{B}^{-1}$, one obtains the so called *canonical*, or *normal* or *characteristic form* of system (1.7), i.e.

$$\mathbf{C}_t + \Lambda \mathbf{C}_x = 0 \tag{1.10}$$

after defining the vector of the so called *characteristic variables*

$$\mathbf{Q} = \mathbf{B}\mathbf{C}, \qquad \Longrightarrow \qquad \mathbf{Q}_t = \mathbf{B}\mathbf{C}_t, \; \mathbf{Q}_x = \mathbf{B}\mathbf{C}_x. \tag{1.11}$$

It becomes evident that for linear systems, the corresponding governing equation written in characteristic variables, yields to a set of m *independent* linear advection equations for the unknowns c_i

$$\frac{\partial c_i}{\partial t} + \lambda_i \frac{\partial c_i}{\partial t} = 0, \qquad i = 1, 2, .., m. \tag{1.12}$$

Moreover, λ_i is called *characteristic speed* and one can show that the solution for a general initial value problem for system (1.10) is

$$c_i(x, t) = c_i(x - \lambda_i t, 0), \qquad i = 1, 2, \ldots, m. \tag{1.13}$$

Notice that, for the scalar case, i.e. $m = 1$, this means that the physical state $\mathbf{C}$ is *conserved along characteristic curves*, where a *characteristic curve* (or *characteristic*) is defined by the relation $dx/dt = \lambda_i$. Then, from equation (1.11) one recovers the original *conserved variables* $\mathbf{Q}$. It is an inspiring consideration noting that the conserved variables $\mathbf{Q}$ are expressed as a linear combination of the eigenvectors of the Jacobian matrix A, i.e. from the definition of $\mathbf{B}$ and $\mathbf{C}$ (1.9) and (1.11)

$$\mathbf{Q} = \mathbf{Q}(x,t) = \sum_{i=1}^{m} c_i(x,t)\mathbf{b}_i = \sum_{i=1}^{m} c_i(x-\lambda t, 0)\mathbf{b}_i, \tag{1.14}$$

In particular, the relative linear coefficients are exactly the values of the corresponding characteristic variables c_i, that are independently advected along the characteristics. In the simplest considered case, the characteristic curves are straight lines in (x,t). In the more general case, the characteristics are curved and discontinuous solutions can be generated even with continuous initial data. The theoretical investigation of general approximate or exact solutions of a classical initial value problem for an hyperbolic system with piecewise constant initial data, i.e. $\mathbf{Q} = \mathbf{Q}_L$ for $x < 0$, $\mathbf{Q} = \mathbf{Q}_R$ for $x > 0$, is the so called *Riemann problem*. The theoretical study of characteristics and the investigation for exact or approximated Riemann solvers constitutes two of the main pillars for the development of modern numerical methods in fluid dynamics, see [259].

1.2 NUMERICAL METHODS

Nowadays, there are many numerical approaches available for solving hyperbolic systems. The main character of a given numerical strategy is given by the choice of the approximation of the solution $\mathbf{u}$, called *numerical solution* $\mathbf{u}_h$, the approximation of the physical domain Ω, in space or time, called *mesh* or *grid* Ω_h, and the definition of the reference form of the governing PDEs, e.g. differential, integral or weak form, see equations (1.1-1.3). Let us consider for simplicity one dimensional problems. The main three families of numerical methods for hyperbolic systems are: *finite-difference*, *finite-volume* and *finite-element* methods:

i. Whenever the numerical solution u_h is defined *point-wise* according to a given set of *points*, i.e.

$$\Omega_h = \{x_i \in \Omega\}_{i=1,2,..,N}, \quad u_h^{in} \approx u(x_i, t_n),$$

satisfying the differential equation (1.2), it deals with *finite-difference methods* (FD);

ii. whenever the integral equation (1.1) is considered and the numerical solution u_h is defined to be a piece-wise constant function according to a given set of non-overlapping *cells*, i.e.

$$\Omega_h = \{T_i | T_i \subset \Omega \text{ and } \cup_i T_i = \Omega\}_{i=1,2,..,N}, \quad u_h^{in} = \int_{T_i} u(x, t_n)dx,$$

it deals with *finite-volume methods* (FV); according to the finite-volume discretization, *cell-averages* u_h^{in} are evolved in time;

iii. whenever the weak equation (1.3) is considered over a set of non-overlapping *elements*, similarly to FV methods, and the numerical solution u_h is approximated by means of piece-wise polynomial functions along the space domain, it deals with *finite-element* (FE) *methods*; according to the finite-element methods, the degrees of freedom of the chosen polynomial basis are directly evolved in time

$$\Omega_h = \{T_i | T_i \subset \Omega \text{ and } \cup_i T_i = \Omega\}_{i=1,2,..,N}, \qquad u_h^{in} = \sum_j \varphi_j u^{in,j},$$

$\{\varphi_j\}$ being a polynomial basis; in particular, whenever the numerical solution is allowed to be discontinuous at element interfaces ∂T_i, then it deals with the so called discontinuous Galerkin (DG) finite-element methods; due to the use of the weak formulation (1.3), FE methods were also called *variational-difference* or *projection-difference* which probably reflect better the character of the method.

1.3 BASIC CONCEPTS OF NUMERICAL DISCRETIZATION

In the following sections, the main properties and theorems for numerical methods for hyperbolic PDE have been selected and briefly outlined.

1.3.1 *Domain of dependence, determinacy and influence*

As stated before, for linear scalar advection equations, the solution at a given point $P = (x, t)$ is solely dependent on the initial state at a single point $P_0 = (x_0, t_0)$, i.e. the intercept of the characteristic. Then, the following generalization becomes obvious: the *domain of dependence of a given point* $P = (x, t)$ is the subset $\mathbb{D}^-(P)$ of the domain of definition of the solution that is *subtended* by any characteristics passing through P. Moreover, the subtended (past) space-time area, spanning the complete dynamics of the domain of dependence of P, is called *domain of determinacy*. Vice-versa, *range of influence* $\mathbb{D}^+(P)$ of a given point $P = (x, t)$ is the sup-tended (future) space-time area by all the characteristics passing through P.

1.3.2 *Convergence and approximation*

An alternative way of defining a *discretization process* as it has been depicted in the previous section, is summarized in defining a proper space of solutions u_h as a *normed space* U_h over a mesh Ω_h, satisfying the corresponding differential, integral or weak governing equation. A normed space is a general vector space associated to a proper *scalar product*. Given a differential operator L, operating on functions u

$$L[u] = f, \tag{1.15}$$

and the corresponding discrete problem

$$L_h[u_h] = f_h, \tag{1.16}$$

one can define an equivalence correspondence between the solution u and a function $(u)_h \in U_h$, i.e. the representation or projection of u into the discrete space U_h. Then, the fundamental property of *convergence* holds if

$$\lim_{h\to 0} \frac{\|(u)_h - u_h\|_{U_h}}{h^p} \to 0 \tag{1.17}$$

for $p \geqslant 0$. In particular, referring to solution u_h, convergence is said to be *of order* p *with respect to* h.

After introducing a linear normed space F_h, corresponding to the right hand side discrete-function f_h, then the discrete system (1.16) is said to *approximate equation* (1.15) *on the solution* u if the *residual* $\delta f_h = L_h[(u)_h] - L_h[u_h]$ converges to zero with h, i.e.

$$\frac{\|\delta f_h\|_{F_h}}{h} = \frac{\|L_h[(u)_h] - L_h[u_h]\|_{F_h}}{h^k} \to 0, \tag{1.18}$$

with $k \geqslant 0$. In particular, the approximation is said to be *of order* k *with respect to* h.

1.3.3 *Stability*

A numerical scheme (1.16) is said to be *stable* if there exists $\delta > 0$, $h_\delta > 0$ such that for any mesh size $h < h_\delta$ and any residual $\delta f_h \in F_h$, with $\|\delta f_h\|_{F_h} < \delta$, then *exists one and only one solution* z_h corresponding to residual δf_h, i.e. $L_h[z_h] - L[u_h] = \delta f_h$, such that the following inequality holds

$$\|z_h - u_h\|_{U_h} \leqslant C \|\delta f_h\|_{F_h} \tag{1.19}$$

where C is a positive constant. Moreover, if the *discrete* operator approximates a *differential* operator on u and the scheme is *stable*, then convergence of order $p = k$ holds.

1.3.4 *CFL condition*

The Courant-Friedrichs-Lewy (CFL) condition is a *necessary*, not sufficient, condition for *guaranteeing convergence/stability* of a numerical scheme. The CFL condition can be stated as: in order to convergence being valid, see relation (1.17), in the limit $h \to 0$, any arbitrary neighborhood of any point belonging to the *domain of dependence* $\mathbb{D}^-(P)$ of point $P = (x, t)$ *must contain* a point of the discrete domain of dependence $\mathbb{D}_h^-(P)$ of P, for sufficiently small values of h, i.e. $\mathbb{D}^-(P) \subseteq \mathbb{D}_h^-(P)$.

1.3.5 *Monotonicity and Godunov theorem*

A numerical scheme that can be written in the form

$$u_h^{n+1}(x) = H\left(u_h^n\right), \qquad x \in T_i \tag{1.20}$$

is said to be *monotone* if

$$\frac{\partial H}{\partial u_h^n} \geqslant 0. \tag{1.21}$$

Notice that a convex (or monotone) linear combination of a set $\{q_i\}$ does not generate new maxima or minima. From one hand, monotone schemes may present the so called *clipping-effect*, i.e. the clipping of extrema. On the counterpart, whenever a non-monotone schemes is used for approximating discontinuous solution, spurious oscillations may arise.

The Godunov theorem, see [133], states that *monotone, linear schemes are at most first order accurate*. This means that for reaching higher order of accuracy, one should resort to non-monotone schemes, or non-linear schemes.

1.3.6 *From variational methods to continuous Galerkin schemes*

Following step by step [132], we consider the vector space (or linear space) $\mathbb{V}(\Omega)$ of continuous functions in a closed domain $\Omega \subset \mathbb{R}^2$ with bounded first derivatives, whose discontinuities lie along a finite set of lines, different for any function. The respective completion of $\mathbb{V}$ respect to the norm

$$\|q\|_{\mathbb{V}} = \left[\int_\Omega q^2 \, dx \, dy + \int_\Omega \left[\left(\frac{\partial q}{\partial x}\right)^2 + \left(\frac{\partial q}{\partial y}\right)^2\right] dx \, dy\right]^{\frac{1}{2}}, \qquad q \in \mathbb{V} \tag{1.22}$$

yields the definition of a Sobolev space $\mathbb{V}_2^1$. An illustrative variational formulation of a PDE with solutions q in $\mathbb{V}$ over the domain Ω is represented by the correspondence between the Dirichlet problem

$$\begin{cases} \frac{\partial^2 q}{\partial x^2} + \frac{\partial^2 q}{\partial y^2} = g(x,y), \quad (x,y) \in \Omega \\ q_{|_{\partial\Omega}} = 0 \end{cases}, \tag{1.23}$$

and *the minimum of the functional*

$$\begin{cases} \delta S[q] = 0, \\ q = S[q] = \int_\Omega \left[\left(\frac{\partial q}{\partial x}\right)^2 + \left(\frac{\partial q}{\partial y}\right)^2 + 2g\, q\right] dx \, dy \\ q_{|_{\partial\Omega}} = 0 \end{cases} \tag{1.24}$$

A numerical solution of the variational problem (1.24) consists in determining a *minimizing sequence* $\{q_n\}$ such that

$$\lim_{n \longrightarrow \infty} S[q_n] = S[q] \tag{1.25}$$

In 1908, Ritz proposed a rigorous discrete procedure, see the original version in [239], which is briefly summarized in the following steps:

1. chosen a *discrete* space $\mathbb{V}_h^N$, generated by a chosen set of linearly independent functions $\{\varphi_i\}_{i=1,..,N}$ satisfying the boundary conditions of the considered variational problem, e.g. $\varphi_{i|_{\partial\Omega}} = 0$ for (1.24);

2. the solution $q_h \in \mathbb{V}_h^N$ approximating q, solution to the variational problem (1.24) can be written as a linear combination of the basis

$$q_h = \sum_i q_h^i \varphi_i, \tag{1.26}$$

and it is solution to the *discrete variational* problem

$$\frac{\partial}{\partial q_h^i} S[q_h] = 0, \qquad i = 1, \dots, N. \tag{1.27}$$

In coherence with the rest of the thesis, q_h^i are called *degrees of freedom* for the discrete solution q_h.

3. In particular, after introducing a scalar product

$$\langle \tilde{q}, \tilde{q}' \rangle = \int_\Omega \left(\frac{\partial \tilde{q}}{\partial x} \frac{\partial \tilde{q}'}{\partial y} + \frac{\partial \tilde{q}'}{\partial x} \frac{\partial \tilde{q}}{\partial y} \right) \, dx + \int_{\partial\Omega} \sigma \tilde{q} \tilde{q}' d\Sigma \tag{1.28}$$

with σ a positive given function over $\partial\Omega$, and the corresponding norm $\|\tilde{q}\| = \langle \tilde{q}, \tilde{q} \rangle$, equation (1.27) is rewritten in the more familiar linear system

$$\sum_i \mathbb{G}^{ij}_{\langle \cdot, \cdot \rangle} q_h^j = -\int_\Omega g \varphi_j \, dx, \qquad j = 1, \dots, N; \tag{1.29}$$

where $\mathbb{G}_{\langle \cdot, \cdot \rangle} = \{\langle \varphi_i, \varphi_j \rangle\}_{i,j=1,..,N}$ is called *Gram matrix* of the basis functions $\{\varphi_i\}$ with respect to the aforementioned scalar product. In particular, $\mathbb{G}$ is symmetric, positive definite and the existence and uniqueness of the solution to (1.35) in consequently ensured.

Even more interesting, one can show that the following identity

$$\begin{aligned} S(q_h) - S(q) &= \min_{\tilde{q}_h \in \mathbb{V}_h^N} (S(\tilde{q}_h) - S(q)) && (1.30)\\ &= \min_{\tilde{q}_h \in \mathbb{V}_h^N} \langle \tilde{q}_h - q, \tilde{q}_h - q \rangle && (1.31)\\ &= \langle q_h - q, \tilde{q}_h - q \rangle \equiv \|q_h - q\|^2 && (1.32) \end{aligned}$$

is true, meaning the discrete solution $q_h \in \mathbb{V}_h^N$ is the one that minimizes the error $\epsilon_h = \|q_h - q\|$. In simple words, the *discrete solution* q_h is the *projection of* q *into the discrete space* $\mathbb{V}_h^N$ in the sense of the scalar product $\langle \cdot, \cdot \rangle$.

Later, in 1916, Galerkin applied the discrete projection strategy of Ritz to the cases in which, in principle, a corresponding variational form of the boundary-value problem is unknown. A direct substitution of the definition (1.26) of a generic discrete solution $q_h \in \mathbb{V}_h^N$ into the differential PDE, e.g. (1.23), would yield

$$\begin{cases} \frac{\partial^2 q_h}{\partial x^2} + \frac{\partial^2 q_h}{\partial y^2} - g(x,y) = \delta_h(x,y), \quad (x,y) \in \Omega \\ q_{h|_{\partial\Omega}} = 0 \end{cases} \tag{1.33}$$

with δ_h the discrete residual. A good solution q_h would give δ_h approximating zero with the characteristic mesh size h, but imposing (1.33) is a very strong condition for an estimating function q_h in the form of (1.26). Then, Galerkin defined the proper numerical condition by imposing the *projection of the residual* δ_h over the basis functions being zero, i.e.

$$(\varphi_i, L[q_h] - g) \equiv \int_\Omega \varphi_i \left(L[q_h] - g\right) \, d\boldsymbol{x} = 0, \qquad i = 1, \dots, N, \tag{1.34}$$

where $L[q]$ is the differential operator of (1.23); $(\cdot,\cdot)$ is also a scalar product, defined according to the simplest interpretation of (1.34). Then, after some computations and considering the simple boundary value problem (1.23), the following linear system for the degrees of freedom $\{q_h^i\}$ holds

$$\sum_i \mathbb{G}^{ij}_{\langle\cdot,\cdot\rangle} q_h^j = -\left(g, \varphi_j\right), \qquad j = 1, \dots, N, \tag{1.35}$$

which *matches exactly* the discrete problem obtained by means of the variational Ritz method. On important consideration is that the numerical accuracy of both Ritz and Galerkin methods depends only on the choice of the discrete space $\mathbb{V}_h^N$ and not on the basis. A natural correspondence between the variational-(Ritz) and projection-(Galerkin) methods to the known finite-difference strategy arises when considering basis functions interpolating the unity in a given set of points $\{\boldsymbol{x}_i \in \Omega\}$. Indeed, minimizing the functional $S[q_h]$ or the residual projection (φ, δ_h) would give a direct relation between the degrees of freedom of q_h with the point-wise values of the resulting discrete solution, i.e $\boldsymbol{q}_h(\boldsymbol{x}_i) \equiv q_h^i$. One of the peculiar properties of the Ritz-Galerkin method is that independently on the choice of the point set $\{\boldsymbol{x}_i\}$, the numerical formulation appears to be the same, i.e independently on the complexity of the mesh and boundaries.

2 NOTES ON COMPRESSIBLE FLUIDS AND MAGNETIC FIELDS

We recall that the Navier-Stokes equations are of general theoretical and practical interest for the description of fluid flow with a wide spectrum of applications, ranging from the field of hydraulics, oceanic and atmospheric flow modeling, mantle convection in geophysics, aerospace, mechanical and naval engineering up to the simulation of physiological fluid flows in the human cardiovascular or respiratory system. On the other hand, there are also many interesting flows of magnetized fluids (plasmas) which are typically described by the MHD equations, but in which resistivity effects of electromagnetic fields are also important, such as in solar flares, in the magnetosphere of neutron stars, in inertial or magnetic confinement fusion for civil energy production, in plasma actuators for active control of boundary layers, but also in plasma thrusters for the propulsion of satellites and small spacecraft, just to mention a few examples. In particular, the Navier-Stokes equations can be obtained by the viscous-resistive MHD (VRMHD) equation after setting the electromagnetic fields $\mathbf{E}$ and $\mathbf{B}$ equal to zero.

2.1 BALANCE LAWS FOR DISSIPATIVE FLUIDS

Mass conservation within a fluid particle at time $t = t_0$ is ensured by

$$\frac{d}{dt}_{|_{t_0}} \int_{\Omega(t)} \rho \, dV \equiv \int_{\Omega(t_0)} \frac{\partial}{\partial t} \rho \, dV - \int_{\partial\Omega(t_0)} \rho \mathbf{v} \cdot \mathbf{n} \, dS \tag{2.1}$$

yielding the corresponding differential form

$$\boxed{\frac{\partial \rho}{\partial t} - \nabla \cdot (\rho \mathbf{v}) = 0.} \tag{2.2}$$

The balance law for an arbitrary *extensive* physical quantity θ associated to a given small fluid particle Ω subject to external influences is

$$\frac{d}{dt} \int_{\Omega} (\rho\theta) = \int_{\Omega} Q \tag{2.3}$$

where Q is the *effective density of source strength* that depends on the nature of the extensive quantity θ. In general Q can can be written as the summation of two terms, the volume and surface forces acting on Ω, having

$$\int Q d\Omega = \int F \rho d\Omega + \int \sigma \cdot \hat{n} \, dS \tag{2.4}$$

where F is the volume 'force', i.e. the rate of change of θ per unit mass due to 'long range' interaction; σ is the corresponding *stress tensor* (vector in this case), the rate of change of θ per unit surface due to the surface interaction with the external fluid. By considering mass conservation and the motion of the fluid particle introducing the notion of *material derivative* D/Dt , equation 2.3 can be written in differential form as

$$\rho \frac{D}{Dt}\theta = \rho F + \nabla \cdot \sigma, \tag{2.5}$$

valid in every point $\mathbf{x}$ in the fluid. A special case of (2.5) is the *equation of motion*, with $\rho\theta$ being the momentum of the fluid. Then equation (2.5) collapses to the classical Newton law, and can be expressed as

$$\boxed{\rho \frac{D}{Dt} v_i = \rho F_i + \frac{\partial}{\partial x_j}\sigma_{ij}} \tag{2.6}$$

here v_i is the i-th component of the velocity vector, F_i is the i-th component of the resultant volume force acting in $\mathbf{x}$. Here the Einstein convention of summation over repeated indexes is assumed. Equation (2.6) is called *indefinite equation of motion* for the continuous media, because it holds for *any* continuous media. By definition, for fluids at rest tangential stresses vanish and only the isotropic part establishes the equilibrium in the fluid, i.e. σ takes the form $\sigma_{ij} = -p\delta_{ij}$ which defines the pressure $p > 0$, the minus sign states that fluids resist to compression forces. In general, the stress tensor σ has an isotropic as well as a non-isotropic component

$$\sigma_{ij} = -p\delta_{ij} + \sigma'_{ij}, \tag{2.7}$$

where σ' called the *deviatoric stress tensor* and it depends only on the fluid motion, i.e. when the local derivatives $\partial v_i/\partial x_j \neq 0$. The simplest form that allows the correct equilibrium properties for fluids at rest, uniform ($\mathbf{v}$ =const) or uniform circular motion ($\mathbf{v} = \Omega \times \mathbf{r}$), is

$$\sigma'_{ij} = \mu\left(\frac{\partial v_i}{\partial x_j} + \frac{\partial v_j}{\partial x_i} - \frac{2}{3}\delta_{ij}\frac{\partial v_k}{\partial x_k}\right) + \zeta\delta_{ij}\frac{\partial v_k}{\partial x_k} \tag{2.8}$$

Moreover the so called *symmetry of the stresses* $\sigma_{ij} \equiv \sigma_{ji}$ holds. Here, μ and ζ are the *dynamic* (or first) and *second viscosity coefficients*. Equation (2.8) follows after assuming the fluid to be *isotropic*, i.e. the physical properties of the fluid are independent on the kinematics, described by a scalar function. Mass conservation and momentum balance (2.1-2.6) constitute a system of *four* differential equations with *five* unknowns, i.e. pressure, density and velocity components only if the interaction forces depend on the kinematic fluid variables. To close the problem, at least one further equation is needed. In the following, the *energy balance equation* and *interactions* are introduced for different scenarios in fluid dynamics: the equations of viscous and resistive magneto-hydrodynamic (VRMHD), the ideal MHD (MHD), the Navier-Stokes equations (NS) and Euler equations.

2.2 GOVERNING EQUATIONS

In plasma physics, the standard procedure of deriving the MHD equations consists in the following steps: i) starting from the basic theory of motion of single charge particles in magnetic and electric fields, ii) then, a rigorous *kinetic theory is derived* by introducing the electro-magnetic interactions into the Boltzmann equations; iii) under the hypothesis of *frequent collisions* and by means of *momentum reduction* of the corresponding Boltzmann equations for the distribution function of electrons and ions, the *large-scale* equations are obtained; iv) in combination with the Maxwell equations, a corresponding *two fluid theory* is derived for the motion of ions and electrons in plasmas, i.e.

$$
\begin{aligned}
&\tfrac{\partial n_\alpha}{\partial t} + \nabla\cdot(n_\alpha \boldsymbol{v}_\alpha) = 0, && \text{mass conservation}\\
&n_\alpha m_\alpha\left(\tfrac{\partial \boldsymbol{v}_\alpha}{\partial t} + \boldsymbol{v}_\alpha\cdot\nabla\boldsymbol{v}_\alpha\right) + \nabla p_\alpha - n_\alpha q_\alpha\left(\boldsymbol{e} + \boldsymbol{v}_\alpha\times\mathbf{B}\right) = \mathbf{R}_\alpha, && \text{mom. conservation}\\
&\tfrac{\partial p_\alpha}{\partial t} + \boldsymbol{v}_\alpha\cdot\nabla p_\alpha + \gamma p_\alpha\nabla\cdot\boldsymbol{v}_\alpha = (\gamma-1)\,Q_\alpha && \text{en. conservation}\\
&\alpha = e, i
\end{aligned}
\tag{2.9}
$$

which are the *large-scale* equations for two *interpenetrating* fluids; v) after few important physical considerations about the order of magnitude of the interactions, the assumption for the fluid of *quasi charge neutrality*, the small relative motion between ions and electrons and the non-relativistic approximation, i.e.

$$
\boxed{
\begin{aligned}
|n_e - Z n_i| &\ll n_e, && \text{quasi charge-neutrality}\\
|\boldsymbol{v}_e - \boldsymbol{v}_i| &\ll v, && \text{small relative motion}\\
v &\ll c, && \text{non-relativistic regime}
\end{aligned}
}
\tag{2.10}
$$

the two fluid equations collapse to one single equations for a globally neutral and conducting fluid, written in the global physical variables

$$\rho = n_e m_e + n_i M_i, \tag{2.11}$$

$$\rho_c = -e(n_e - Z n_i) \approx 0, \tag{2.12}$$

$$v = \frac{n_e m_e \boldsymbol{v}_e + n_i m_i \boldsymbol{v}_i}{\rho}, \tag{2.13}$$

$$\mathbf{j} = -e\left(n_e \boldsymbol{v}_e - Z n_i \boldsymbol{v}_i\right). \tag{2.14}$$

In the previous equations: n_e and n_i are the electron and ion number density; e is the electron charge unit; q_α is the charge of particle α ($\alpha = e, i$: electron or ion); Z is the ionization number; m_e and M_i the electron and ion masses; ρ and ρ_c the mass and charge density for the one-fluid theory; v_e, v_i and v the electron, ion and global-fluid velocity; c the speed of light. Moreover, $\mathbf{R}_\alpha$ is the collision integral term and it is object of study in transport theory. In particular, even after neglecting (Vlasov equation), after assuming a Maxwell-Boltzmann velocity distribution or following the slightly more sophisticated formulation of the Landau collision

integral, the large-scale contribution for the single-fluid is zero, i.e. $\mathbf{R}_e = -\mathbf{R}_i$. This fact can be interpreted to be essentially result from the local momentum conservation in *like-* and *unlike*-particle collisions, in first approximation. On the other hand, for the energy balance law follows the equation for the heat dissipation term $Q_e + Q_i = \eta|\mathbf{j}|^2$.

In this work, we restrict ourselves to introducing the proper definition of *total energy*, the corresponding *energy fluxes*, the *equation of state* and the proper interaction forces into the momentum balance law (2.6).

In presence of electromagnetic (e.m.) fields the *Maxwell equations* hold

$$\begin{aligned} &\text{Ampere:} \quad \nabla \times \mathbf{B} = \mu_0 \mathbf{j}_{\text{tot}} + \epsilon_0 \mu_0 \frac{\partial \mathbf{E}}{\partial t}, \qquad &&\text{Gauss (B):} \quad \nabla \cdot \mathbf{B} = 0 \\ &\text{Faraday:} \quad \nabla \times \mathbf{E} = -\frac{\partial \mathbf{B}}{\partial t} &&\text{Gauss (E):} \quad \nabla \cdot \mathbf{E} = \frac{\rho_{\text{tot}}}{\epsilon_0}, \end{aligned} \tag{2.15}$$

which are used in the following dimensional analysis because it helps in estimating the order of magnitude of the interactions. In Gaussian units (which are more convenient), the Maxwell equations read

$$\begin{aligned} &\text{Ampere:} \quad \nabla \times \mathbf{B} = \frac{1}{c}\left(4\pi \mathbf{j}_{\text{tot}} + \frac{\partial \mathbf{E}}{\partial t}\right), \qquad &&\text{Gauss (B):} \quad \nabla \cdot \mathbf{B} = 0 \\ &\text{Faraday:} \quad \nabla \times \mathbf{E} = -\frac{1}{c}\frac{\partial \mathbf{B}}{\partial t} &&\text{Gauss (E):} \quad \nabla \cdot \mathbf{E} = 4\pi \rho_{\text{tot}}. \end{aligned} \tag{2.16}$$

$\mathbf{E}$ and $\mathbf{B}$ are correspondingly the electric and magnetic fields, $\mathbf{j}$ the current density, ρ the charge density, ϵ_0 and μ_0 are correspondingly the vacuum permittivity and permeability constant, where c is the speed of light.

2.2.1 *Scales and approximations*

Under a coordinate transformation between inertial reference frames with relative velocity $\boldsymbol{v}$, the e.m. fields change according to

$$\mathbf{E}' = \Gamma\left(\mathbf{E} + \frac{\boldsymbol{v} \times \mathbf{B}}{c}\right) - \frac{\Gamma^2}{\Gamma + 1}\left(\frac{\boldsymbol{v} \cdot \mathbf{E}}{c}\right)\frac{\boldsymbol{v}}{c}, \tag{2.17}$$

$$\mathbf{B}' = \Gamma\left(\mathbf{B} - \frac{\boldsymbol{v} \times \mathbf{E}}{c}\right) - \frac{\Gamma^2}{\Gamma + 1}\left(\frac{\boldsymbol{v} \cdot \mathbf{B}}{c}\right)\frac{\boldsymbol{v}}{c}, \tag{2.18}$$

$\Gamma = (1 - v^2/c^2)^{-1/2}$ being the Lorentz factor. In the non-relativistic limit $\Gamma \approx 1$ and $v/c \approx 0$, and then from (2.18)

$$\mathbf{E}' \approx \left(\mathbf{E} + \frac{\boldsymbol{v} \times \mathbf{B}}{c}\right), \qquad \mathbf{B}' \approx \left(\mathbf{B} - \frac{\boldsymbol{v} \times \mathbf{E}}{c}\right), \tag{2.19}$$

The most important considerations arise in evaluating the relative order of magnitude of $\mathbf{E}$ and $\mathbf{B}$ in the *non-relativistic* and *low-frequency* limit. After doing some

dimensional analysis of the Faraday's law in (2.16), i.e. second row and first column, and the transformation law of B in (2.19)

$$|\nabla \times \mathbf{E}| = \left|\frac{1}{c}\frac{\partial \mathbf{B}}{\partial t}\right| \quad \longrightarrow \quad \left|\frac{E}{L}\right| \approx \left|\frac{1}{c}\frac{B}{T}\right| \quad \Rightarrow \quad |E| \approx \frac{V}{c}|B|, \tag{2.20}$$

$$\left|\frac{\mathbf{B}' - \mathbf{B}}{B}\right| = \left|\frac{\boldsymbol{v} \times E}{cB}\right| \quad \longrightarrow \quad \left|\frac{\mathbf{B}' - \mathbf{B}}{B}\right| \approx \frac{V}{c}\left|\frac{E}{B}\right| \quad \Rightarrow \quad \left|\frac{\mathbf{B}' - \mathbf{B}}{B}\right| \approx \frac{V^2}{c^2}, \tag{2.21}$$

$$\frac{\frac{1}{c}\left|\frac{\partial \mathbf{E}}{\partial t}\right|}{|\nabla \times \mathbf{B}|} \approx \frac{\frac{1}{c}|E/T|}{\mathbf{B}/L} \approx \frac{V}{c}\frac{|E|}{|B|} \quad \Rightarrow \quad \frac{\frac{1}{c}\left|\frac{\partial \mathbf{E}}{\partial t}\right|}{|\nabla \times \mathbf{B}|} \approx \frac{V^2}{c^2}, \tag{2.22}$$

with $V = L/T$, L and T being correspondingly the spatial and temporal scales. Then, considering the non-relativistic/low-frequency limit $V/c \ll 1$, one obtains

$$\boxed{\frac{|E|}{|B|} \ll 1, \qquad \left|\frac{\mathbf{B}' - \mathbf{B}}{B}\right| \ll 1, \qquad \frac{\frac{1}{c}\left|\frac{\partial \mathbf{E}}{\partial t}\right|}{|\nabla \times \mathbf{B}|} \ll 1} \tag{2.23}$$

stating (i) the dominance of magnetic interaction with respect to the electric counterpart, (ii) the univocal definition of magnetic fields independently on the chosen inertial reference system and (iii) the Maxwell's displacement current being negligible in the approximated field theory.

2.2.2 *Mass, momentum and energy*

Equation (2.2) gives the balance law for the conservation of mass. In presence of an external magnetic field $\mathbf{B}$, a current density $\mathbf{j}$ is subjected to the Lorentz force according to $\mathbf{F}_L = \mathbf{j} \times \mathbf{B}$, which is exactly the interaction force source that is introduced in the momentum balance law (2.6) for a quasi-neutral conducting fluid. Indeed, thanks to the quasi-charge neutrality approximation, Coulomb forces $\mathbf{F}_C = \rho\mathbf{E}$ are negligible. The resulting balance equation is then

$$\boxed{\rho\frac{D}{Dt}\boldsymbol{v} - \frac{\mathbf{j} \times \mathbf{B}}{c} - \nabla \cdot \boldsymbol{\sigma} = 0.} \tag{2.24}$$

The energy equation arise or from the single-fluid approximation of (2.9) or from a proper manipulation of the mass and momentum conservation laws (2.2) and (2.24), and the proper fundamental thermodynamic relations. The demonstration could become too long for the context of this thesis. Then, the final result is reported in the following with the fundamental intuitive motivations.

The first principle of thermodynamics for a dynamic system states:

$$d\left(U + \frac{Mv^2}{2}\right) = \delta Q + \delta A', \quad \text{or} \quad d\left(H + \frac{Mv^2}{2}\right) = \delta Q + \delta A' + d(pV) \tag{2.25}$$

where U and H are the fundamental variable of thermodynamics called *internal energy* and *enthalpy* of the dynamic system, respectively; M is the mass; v the velocity of the system kinematics; δQ the *heat absorbed by the system* from the external

environment; $\delta A'$ the amount of *work done by external forces* (the sign is positive); p the pressure and V the volume of the thermodynamic system. Notice that the aforementioned balance law for a general extensive quantity θ (2.5) shows the same contribution: with $\rho\theta = \rho E$, the *total energy* of the system, then its differential is a perfect balance between external/internal work, internal dissipation and heat transfer. The corresponding differential equation can be written, similarly to the third equation in (2.9), as

$$\boxed{\frac{\partial}{\partial t}(\rho E) + \nabla \cdot \left\{ \mathbf{v} \cdot \left[(\rho E + p)\mathbf{I} - \boldsymbol{\sigma}' - \boldsymbol{\beta} \right] - \kappa \nabla T - \frac{\eta c^2}{(4\pi)^2} \mathbf{B} \cdot \left(\nabla \mathbf{B} - \nabla \mathbf{B}^T \right) \right\} = 0,} \tag{2.26}$$

where the total energy density ρE,

$$\rho E = \rho \epsilon + \frac{1}{2}\rho \mathbf{v}^2 + \frac{1}{8\pi}\mathbf{B}^2 \tag{2.27}$$

which contains the internal energy density ρe, the kinetic energy density, $\frac{1}{2}\rho \mathbf{v}^2$ and $\mathbf{B}^2/8\pi$ is related to the fluid pressure p by the ideal gas equation of state (EOS)

$$\boxed{p = \rho \epsilon \, (\gamma - 1)\,;} \tag{2.28}$$

γ is the ratio of specific heats; the shear stress $\boldsymbol{\sigma}$ has been written in its isotropic (pressure) and non-isotropic (viscous) components, see equation (2.7), as

$$\boldsymbol{\sigma} = -p\mathbf{I} + \boldsymbol{\sigma}' = -p\mathbf{I} + \mu \left(\nabla \mathbf{v} + \nabla \mathbf{v}^T - \frac{2}{3} \nabla \cdot \mathbf{v} \right). \tag{2.29}$$

A very similar form is assumed by the so called *Maxwell stress tensor* that contains the stress due to the electro-magnetic forces

$$\boldsymbol{\beta} = \frac{1}{4\pi} \left(-\frac{1}{2}\mathbf{B}^2 \, \mathbf{I} + \mathbf{B} \otimes \mathbf{B} \right), \tag{2.30}$$

where the *negative* and *isotropic* component $-\mathbf{B}^2 \, \mathbf{I}/8\pi$ is called *magnetic pressure* for obvious reasons, and which is the same term appearing in (2.27), the remaining terms are the so called *magnetic tension*. The non resistive component of the flux tensor for the energy balance law can be regarded to be the e.m. energy density transported through the *Pointing vector* $\mathbf{S} = c\mathbf{E} \times \mathbf{B}/4\pi$, momentum and energy carrier for e.m. fields. Notice the Maxwell stress tensor is independent on any viscous-resistive effect due to internal physical friction or dissipation. Then the last two terms in the energy flux represent the real viscous-resistive terms in the energy equations, that are the heat flux vector $\mathbf{q}_\kappa$, proportional to the heat conduction coefficient κ, i.e.

$$\mathbf{q}_\kappa = -\kappa \nabla T \tag{2.31}$$

and the electric current dissipation term $\mathbf{q}_\eta$, proportional to the electric resistivity η of the medium, i.e.

$$\mathbf{q}_\eta = -\frac{\eta c^2}{(4\pi)^2}\mathbf{B}\cdot\left(\nabla\mathbf{B} - \nabla\mathbf{B}^T\right) \tag{2.32}$$

which arise from the evaluation of the collision integral of the third of the two-fluid equations (2.9), yielding to the *Ohmic dissipation term* $Q = \eta|j|^2$.

2.2.3 *The B equation and the generalized Ohm's law*

Until here, we have written six equations (mass, momentum, energy and equation of state) with eight unknowns. Indeed, a field equation is needed for the magnetic vector $\mathbf{B}$ and a proper equation of the current density $\mathbf{j}$ should be defined. The *pre-Maxwell Ampere's law*, i.e. neglecting the Maxwell's displacement current, see equation (2.23), gives a direct relation between the current density $\mathbf{j}$ and $\mathbf{B}$ in the simplified form

$$\boxed{\nabla\times\mathbf{B} = \frac{4\pi}{c}\mathbf{j}} \tag{2.33}$$

Moreover, *Faraday's law* in (2.16) shows the time derivative of B and it seems to be a good candidate for a governing equation of the field. Nevertheless, it introduces the dependency on the electric counterpart $\mathbf{E}$ and it calls for a new equation. Also in this case, kinetic and transport theory is used. Combining the *two fluid* equations, after some manipulation and (i) considering the *low-frequency motion*, i.e. when inertial (cyclotron frequency) effects are unimportant, (ii) the *limit of mass ratio* $m/M \to 0$, one obtains the so called *generalized Ohm's law*

$$\mathbf{E} + \frac{\boldsymbol{v}\times\mathbf{B}}{c} = \eta\mathbf{j} + \frac{1}{en}\left(\mathbf{j}\times\mathbf{B} - \nabla p_e\right) \tag{2.34}$$

where term $\mathbf{j}\times\mathbf{B}$ is called the *Hall current* and, if considered, the so called *Hall MHD* can be derived. In many cases, the two last terms at the right of the equations can be neglected, reducing to

$$\boxed{\mathbf{E} + \frac{\boldsymbol{v}\times\mathbf{B}}{c} = \eta\,\mathbf{j}} \qquad \text{or} \qquad \mathbf{j} = \sigma_\eta\left(\mathbf{E} + \frac{\boldsymbol{v}\times\mathbf{B}}{c}\right) \tag{2.35}$$

η and $\sigma_\eta = \eta^{-1}$ are the electric resistivity and conductivity, respectively. Then, combining *Faraday's with Ohm's* laws one obtains the governing equation for the magnetic field in

$$\boxed{\frac{1}{c}\frac{\partial\mathbf{B}}{\partial t} + \nabla\times\left(\eta\,\mathbf{j} - \frac{\boldsymbol{v}\times\mathbf{B}}{c}\right) = 0,} \tag{2.36}$$

closing the equation system for the viscous and resistive equations of magneto-hydrodynamics (VRMHD).

2.2.4 *The VRMHD equations*

By direct substituting the *approximated Ampere's law* (2.33) into the momentum and magnetic field equations (2.6) and (2.36), follow

$$\rho\left(\frac{\partial}{\partial t}+\boldsymbol{v}\cdot\nabla\right)\boldsymbol{v}-\frac{1}{4\pi}\left(\nabla\times\mathbf{B}\right)\times\mathbf{B}-\nabla\cdot\boldsymbol{\sigma}=0 \tag{2.37}$$

$$\frac{\partial\mathbf{B}}{\partial t}+\nabla\times\left(\frac{\eta c^2}{4\pi}\nabla\times\mathbf{B}-\boldsymbol{v}\times\mathbf{B}\right)=0, \tag{2.38}$$

which can be manipulated together with the mass and energy conservation laws (2.1) and (2.26) to constitute the complete set of *viscous/resistive MHD equations* (VRMHD), *in Gaussian units* and written in *conservative form*

$$\frac{\partial}{\partial t}\begin{pmatrix}\rho\\ \rho\mathbf{v}\\ \rho E\\ \mathbf{B}\end{pmatrix}+\nabla\cdot\begin{pmatrix}\rho\mathbf{v}\\ \rho\mathbf{v}\otimes\mathbf{v}+p\mathbf{I}-\boldsymbol{\sigma}-\boldsymbol{\beta}\\ \mathbf{v}\cdot\left((\rho E+p)\mathbf{I}-\boldsymbol{\sigma}-\boldsymbol{\beta}\right)-\kappa\nabla T-\frac{\eta c^2}{(4\pi)^2}\mathbf{B}\cdot\left(\nabla\mathbf{B}-\nabla\mathbf{B}^T\right)\\ \mathbf{B}\otimes\mathbf{v}-\mathbf{v}\otimes\mathbf{B}-\frac{\eta c^2}{4\pi}\nabla\left(\nabla\mathbf{B}-\nabla\mathbf{B}^T\right)\end{pmatrix}=0, \tag{2.39}$$

completed by the equation of state for ideal gases and the physical constraint for the initial condition of $\mathbf{b}$, i.e.

$$p=\rho\epsilon\left(\gamma-1\right); \tag{2.40}$$

$$\nabla\cdot B=0 \tag{2.41}$$

Notice that, once the divergence-free condition for $\mathbf{B}$ is ensured at the initial time, then it holds in time thanks to the Faraday's law in (2.16), i.e. after operating the divergence

$$\nabla\cdot\left[\nabla\times\mathbf{E}+\frac{1}{c}\frac{\partial\mathbf{B}}{\partial t}\right]=0 \qquad \Rightarrow \qquad \frac{\partial}{\partial t}\left(\nabla\cdot\mathbf{B}\right)=0 \tag{2.42}$$

because the divergence of the curl of any vector field is exactly zero.

2.2.5 *Computational magnetohydrodynamics and div*$(B)=0$

Even if the equations ensure exactly the conservation of the divergence-free condition in the medium, from the computational point of view this is not true because the discretization error of $\nabla\cdot\mathbf{B}$ can be non-zero in general, and may increase in time.

In this case, errors in the divergence free condition of the magnetic field give rise to the same modifications of magnetic streamlines that the *magnetic monopoles* would have introduced. A magnetic monopole plays the same role of a single charge particle for the electric field, i.e. it is a magnetic source from which the

respective magnetic streamlines depart: sinks or sources of magnetic field. The resulting *'modified'* field $\tilde{\mathbf{B}} = \mathbf{B} + \delta\mathbf{B}$ will enter in the governing equations (2.39) through different contributions: the Lorentz force in the momentum equation (2.24); the pre-Maxwell Ampere's law (2.33), the Ohm's law (2.35). In principle, also Faraday's law will suffer of these spurious changes, but or indirectly, i.e. by means of the electric field (coupled with Ohm's law, coupled with Ampere's...), or by means of the initial condition. Just to mention one simple example, a small perturbation $|\delta\mathbf{B}|/|\mathbf{B}| \ll 1$ corresponds to a variation of the Lorentz force $\delta\mathbf{F}$ that will be nevertheless orthogonal to $\mathbf{j}$, i.e. $\mathbf{j} \perp \delta\mathbf{F}$, which is physically correct, but due to orthogonal distortions $\delta\mathbf{B} \perp \mathbf{B}$, the resulting trajectory is *wrongly accelerated in the orthogonal direction to the magnetic field* $\mathbf{B}$. In the simplest case of a charge particle moving in space with velocity parallel to the initial magnetic field ($\mathbf{j} /\!/ \mathbf{B}$), then an orthogonal $\delta\mathbf{B} \perp \mathbf{B}$ would change the equilibrium depending on the distribution of the numerical monopoles; surely, for long times and/or for non-perturbative regimes, the final position will be significantly different from the correct one and the corresponding plasma transport following an unphysical behavior. In general, unphysical effects may arise, such as the plasma transport in the *orthogonal* direction to the magnetic field $\mathbf{B}$, spurious forces in the *parallel direction*, and wrong contribution to the momentum and energy balance laws, see the work by Brackbill and Barnes [45, 44], and Balsara and Spicer [17]. Then specific procedures must be adopted to prevent significant deviations from $\nabla \cdot \mathbf{B} = 0$ due to accumulation of the numerical errors.

Over the years, several approaches have been adopted to solve this problem (see the review by Tóth [264] but also [82]). The divergence-free condition is an *elliptical constraint*, similarly to the incompressibility condition for incompressible fluids, and, from the computational point of view, it introduces an *instantaneous* linkage between all the streamlines of the magnetic field: the magnetic streamlines *must* be closed lines. From the physical point of view, this is simply a constraint on the magnetic field, similarly to a wall boundary for a moving particle in kinematics: the physical system is not allowed to go through a determined boundary in the phase space. From the computational point of view, whenever a magnetic streamline deviates from being closed, then, *simultaneously* the rest should rearrange to re-establish the constraint. Godunov [135] was surprised in noticing that he was unable to write the current version of the MHD equations (2.39) in the form of a *symmetric hyperbolic system*. This fact introduces non-trivial problems in the definition of the eigenvalues of the system, and the corresponding analysis of characteristics. In [135], it has been shown that a corresponding entropy condition can be derived only if condition $\nabla \cdot \mathbf{B} = 0$ is added within a linear combination of the equations. Then, Godunov formulated the so called *symmetric MHD equations* after introducing the auxiliary variable $D = \nabla \cdot \mathbf{B}$ and the corresponding balance law in such a way that D is demonstrated to be *constant along particle trajectories*. In this way, the elliptic behavior of (2.41) is circumvented by means of a hyperbolic and thermodynamically-compatible re-formulation of the original equations, so that a proper discretization via numerical methods for hyperbolic PDEs is possible. Inspired by Godunov's idea, Powell and collaborators [224, 225]

extended the MHD equations to the so called $\nabla \cdot \mathbf{B}$-waves by adding new source terms proportional to $\nabla \cdot \mathbf{B}$. A very interesting approach have been introduced by Assous et al. [10] in the context of the Maxwell equations that are reformulated in the form of a *constrained wave equation system*, coupled to the divergence-free condition by means of a Lagrange multiplier approach. In principle, an operator-splitting approach can be used for solving first the purely hyperbolic component of the equation system, and then forcing the Poisson equation for the scalar potential to be valid only after solving, in a projection-type strategy, see appendix A of [40], allowing the divergence errors te be reduced up to computational round-off accuracy. Munz and collaborators [214, 215] extended Assous's approach to the so called *generalized Lagrange multiplier* formulation (GLM) of Maxwell's equations, letting free choice for the Lagrange constraint to be hyperbolic, elliptic, parabolic or mixed. After choosing an elliptic equation for the Lagrange constraint a projection method is obtained, after choosing a parabolic constraint the parabolic approach of Marder can be derived, in which the numerical errors are *diffused away*, see [200]. In the hyperbolic case divergence errors are transported out from the computational domain. It should be emphasized that in the GLM formulation, proper artificial modifications to the original equations are introduced for controlling the behavior of spurious divergences. In particular, it has been demonstrated that, even if divergences errors arise, they are *bounded* in time. For numerical methods that enforce the divergence condition rigorously also at the discrete level in the context of the MHD equations, see the work of Balsara et al. [17, 20, 15, 21, 22]. In the following, we have chosen the *hyperbolic formulation of the generalized Lagrangian multiplier* (GLM) *divergence cleaning method extended to the case of the MHD equations* by Dedner et al., see [82].

2.2.6 *The augmented VRMHD system*

After defining an additional auxiliary variable ψ, then a coupling term and a linear scalar PDE are introduced into the MHD system (2.39) in order to allow the resulting *augmented* system to transport and dissipate any possible divergence error (or numerical magnetic monopole) out of the numerical domain, with an established cleaning velocity c_h. In this way, the augmented MHD system can be written in conservative form by defining the state vector $\mathbf{u}$ and the flux tensor $\mathbf{F}$ as (in Gauss units)

$$\boxed{\frac{\partial}{\partial t}\begin{pmatrix} \rho \\ \rho\mathbf{v} \\ \rho E \\ \mathbf{B} \\ \psi \end{pmatrix} + \nabla \cdot \begin{pmatrix} \rho\mathbf{v} \\ \rho\mathbf{v}\otimes\mathbf{v} + p\mathbf{I} - \boldsymbol{\sigma} - \boldsymbol{\beta} \\ \mathbf{v}\cdot((\rho E + p)\mathbf{I} - \boldsymbol{\sigma} - \boldsymbol{\beta}) - \kappa\nabla T - \frac{\eta}{4\pi}\mathbf{B}\cdot\left(\nabla\mathbf{B} - \nabla\mathbf{B}^{T}\right) \\ \mathbf{B}\otimes\mathbf{v} - \mathbf{v}\otimes\mathbf{B} - \eta\left(\nabla\mathbf{B} - \nabla\mathbf{B}^{T}\right) + \psi\mathbf{I} \\ c_h^2\mathbf{B} \end{pmatrix} = \mathbf{S},} \tag{2.43}$$

with equation of state of ideal gases $p = \rho\epsilon(\gamma - 1)$, *initial* constraint $\nabla \cdot B = 0$, total energy density ρE given by

$$\rho E = \rho\epsilon + \frac{1}{2}\rho\mathbf{v}^2 + \frac{1}{8\pi}\mathbf{B}^2 \tag{2.44}$$

where the magnetic resistivity η has been re-defined grouping together the physical constants $\eta c^2/4\pi$. $\mathbf{S}$ contains only the source term for the auxiliary variable ψ, i.e.

$$\mathbf{S} = \begin{pmatrix} 0, & 0, & 0, & 0, & -\omega_d\psi \end{pmatrix}^T \tag{2.45}$$

The damping coefficient ω_d drives the solution towards $\nabla \cdot B = 0$ over a timescale $1/\omega_d$. In our calculations we have typically used $\omega_d \in [1; 10]$. Moreover, notice the VRMHD system consists in a PDE system of *nine coupled nonlinear equations*. This PDE system includes, as special cases, most of the equations we have solved numerically in this thesis. A very short section will be devoted to a synthetic description of the formulation of ideal MHD in *special-relativity*.

2.2.7 *The augmented ideal MHD system*

By setting the physical dissipation processes, i.e. viscous ν, resistive η and heat conductivity κ constant to zero, one obtains the respective *augmented ideal MHD equations*

$$\boxed{\frac{\partial}{\partial t}\begin{pmatrix} \rho \\ \rho\mathbf{v} \\ \rho E \\ \mathbf{B} \\ \psi \end{pmatrix} + \nabla \cdot \begin{pmatrix} \rho\mathbf{v} \\ \rho\mathbf{v}\otimes\mathbf{v} + p\mathbf{I} - \boldsymbol{\sigma} - \boldsymbol{\beta} \\ \mathbf{v}\cdot((\rho E + p)\mathbf{I} - \boldsymbol{\sigma} - \boldsymbol{\beta}) \\ \mathbf{B}\otimes\mathbf{v} - \mathbf{v}\otimes\mathbf{B} + \psi\mathbf{I} \\ c_h^2\mathbf{B} \end{pmatrix} = \begin{pmatrix} 0 \\ 0 \\ 0 \\ 0 \\ -\omega_d\psi \end{pmatrix}.} \tag{2.46}$$

with equation of state of ideal gases $p = \rho\epsilon(\gamma - 1)$, *initial* constraint $\nabla \cdot B = 0$, total energy density ρE given by

$$\rho E = \rho\epsilon + \frac{1}{2}\rho\mathbf{v}^2 + \frac{1}{8\pi}\mathbf{B}^2 \tag{2.47}$$

This equation system describes the non-relativistic motion of neutral conducting plasmas in equilibrium state, characterized by an *infinite conductivity* σ_η.

2.2.8 *Navier-Stokes equations*

By setting the magnetic field to zero, the *four* balance laws for the magnetic field and the auxiliary variable ψ of the VRMHD system collapse to zero, yielding the compressible *Navier-Stokes equations*

$$\boxed{\frac{\partial}{\partial t}\begin{pmatrix}\rho\\ \rho\mathbf{v}\\ \rho E\end{pmatrix}+\nabla\cdot\begin{pmatrix}\rho\mathbf{v}\\ \rho\mathbf{v}\otimes\mathbf{v}+p\mathbf{I}-\boldsymbol{\sigma}\\ \mathbf{v}\cdot((\rho E+p)\mathbf{I}-\boldsymbol{\sigma})-\kappa\nabla T\end{pmatrix}=0.} \tag{2.48}$$

with equation of state of ideal gases $p=\rho\epsilon\,(\gamma-1)$ and total energy density ρE given by

$$\rho E=\rho\epsilon+\frac{1}{2}\rho\mathbf{v}^2 \tag{2.49}$$

This equation represents the fundamental governing PDE for compressible dynamics of viscous fluids.

2.2.9 *Euler equations*

By setting the viscous dissipation to zero in (2.49), the *Euler equations* are obtained, i.e.

$$\boxed{\frac{\partial}{\partial t}\begin{pmatrix}\rho\\ \rho\mathbf{v}\\ \rho E\end{pmatrix}+\nabla\cdot\begin{pmatrix}\rho\mathbf{v}\\ \rho\mathbf{v}\otimes\mathbf{v}+p\mathbf{I}\\ \mathbf{v}\cdot((\rho E+p)\mathbf{I})\end{pmatrix}=0.} \tag{2.50}$$

with equation of state of ideal gases $p=\rho\epsilon\,(\gamma-1)$ and total energy density ρE given by

$$\rho E=\rho\epsilon+\frac{1}{2}\rho\mathbf{v}^2 \tag{2.51}$$

This equation represents the fundamental governing PDE for compressible dynamics of *inviscid* fluids.

2.2.10 *Incompressible Navier-Stokes equations*

For constant density flows (ρ =const.) the continuity equation reduces to $\nabla\cdot\boldsymbol{v}=0$, i.e. the *incompressibility condition*, the energy conservation drops out and the PDE system (2.48) yields the *incompressible Navier-Stokes equations*

$$\boxed{\begin{aligned}\nabla\cdot\boldsymbol{v}&=0\\ \tfrac{\partial}{\partial t}(\mathbf{v})+\nabla\cdot(\mathbf{v}\otimes\mathbf{v}+p\mathbf{I}-\boldsymbol{\sigma})&=0,\end{aligned}} \tag{2.52}$$

where the viscous stress tensor of equation (2.8) collapses to $\boldsymbol{\sigma} = \nu\nabla\boldsymbol{v}$ and $\nu = \mu/\rho$ is the *kinematic viscosity*. It should be mentioned that the incompressible governing equations can be obtained rigorously from the compressible Navier-Stokes equations in the limit of *very low Mach numbers*, see [170].

2.2.11 *Special relativistic ideal MHD*

The degree of complexity related to magnetohydrodynamics can vary notably. Within the Solar system, the non-relativistic approximation of ideal or viscous-resistive magnetohydrodynamics is almost sufficient for describing the motion of the majority plasma scenario. In principle, deeper transport phenomena could be considered by considering a multi-fluid modelization, that is the case of inhomogeneous plasmas. In those cases in which gravitational forces are negligible if compared to electro-magnetic interactions, but the kinematics is distributed at velocity comparable to the speed of light, then the *special-relativistic* MHD equations can be used for simulating the plasma hydrodynamics. Examples are high energy astrophysical phenomena like extragalactic jets [34], gamma-ray bursts [176] and magnetospheres of neutron stars [203], and all those physical systems, leaving aside the problem of the origin of relativistic jets, which clearly involves the role of the accretion disc and of the corresponding central compact object, general relativistic effects can be fairly neglected. As it has been depicted in the previous sections, the single fluid approximation still persists in the special relativistic MHD. Here, we restrict ourselves in giving the fundamental equations, having in mind that they are written in the relativistic formalism. It means that, if in the previous section Maxwell equations have been approximated within the the symmetry of the *Galilean transformation group*. In this case, at the contrary, the hydrodynamics have been extended to the symmetry of the *Lorentz transformation group*.

We consider a flat space-time in pseudo-Cartesian coordinates, namely the *metric* $g_{\mu\nu} = \mathrm{diag}(-1,1,1,1)$, where Greek letters run from 0 to 3 and Latin letters $i,j,k,\ldots$ run from 1 to 3. The speed of light is set to $c = 1$ and we make use of the Lorentz-Heaviside notation for the electromagnetic quantities, such that all $\sqrt{4\pi}$ factors disappear. Finally, we use Einstein summation convention over repeated indices. The energy-momentum tensor of a single-component plasma with infinite conductivity is given by [4]

$$T^{\mu\nu} = (\rho h + b^2)u^\mu u^\nu + (p + b^2/2)g^{\mu\nu} - b^\mu b^\nu\,, \tag{2.53}$$

where u^μ is the four velocity of the fluid, b^μ is the four vector magnetic field, $b^2 = b_\mu b^\mu$, while h, ρ and p are the specific enthalpy, the rest mass density and the thermal pressure, each of them measured in the co-moving frame of the fluid. The metric of the space-time is the Minkowski one, namely $g^{\mu\nu} = g_{\mu\nu} = \mathrm{diag}(-1,1,1,1)$. We recall the in ideal MHD the electric field in the co-moving frame of the fluid vanishes. If we instead select a static laboratory observer defined by the four-velocity vector $n^\mu = (-1,0,0,0)$, then the electric field E^μ and B^μ

measured in such a frame are related to the electromagnetic tensor $F^{\mu\nu}$, and to its dual $F^{*\mu\nu}$, by

$$F^{\mu\nu} = n^{\mu}E^{\nu} - E^{\mu}n^{\nu} + \epsilon^{\mu\nu\lambda\kappa}B_{\lambda}n_{\kappa} \tag{2.54}$$

$$F^{*\mu\nu} = n^{\mu}B^{\nu} - B^{\mu}n^{\nu} - \epsilon^{\mu\nu\lambda\kappa}E_{\lambda}n_{\kappa}\,, \tag{2.55}$$

where $\epsilon^{\mu\nu\lambda\kappa}$ is the completely antisymmetric space-time Levi-Civita tensor, with the convention that $\epsilon^{0123} = 1$. Note that the four vectors of the electric and of the magnetic field are purely spatial, i.e. $E^0 = B^0 = 0$, $E^i = E_i$, $B^i = B_i$. Moreover, the fluid four velocity u^{μ} and the standard three velocity in the laboratory frame are related as $v^i = u^i/\Gamma$, where $\Gamma = (1 - v^2)^{-1/2}$ is the Lorentz factor of the fluid. We stress that the electric field does not need to be evolved in time through the Maxwell equations, since within the ideal MHD assumption it can always be computed a posteriori as $\vec{E} = -\vec{v} \times \vec{B}$. Moreover, the ideal gas equation of state $p = \rho\epsilon(\gamma - 1)$ holds. The equations of ideal SR-MHD, which in covariant form are

$$\nabla_{\alpha}(\rho u^{\alpha}) = 0, \tag{2.56}$$

$$\nabla_{\alpha}T^{\alpha\beta} = 0, \tag{2.57}$$

$$\nabla_{\alpha}F^{*\alpha\beta} = 0\,, \tag{2.58}$$

for numerical purposes are better expressed in conservative form as[1] [173, 14]

$$\frac{\partial}{\partial t}\begin{pmatrix} D \\ S_j \\ U \\ B^j \end{pmatrix} + \partial_i \cdot \begin{pmatrix} v^i D \\ W^i_j \\ S^i \\ \epsilon^{jik}E^k \end{pmatrix} = 0. \tag{2.59}$$

The conserved variables (D, S_j, U, B^j) are related to the rest-mass density ρ, to the thermal pressure p, to the fluid velocity v_i and to the magnetic field B^i by

$$D = \rho\Gamma, \tag{2.60}$$

$$S_i = \rho h\Gamma^2 v_i + \epsilon_{ijk}E_jB_k, \tag{2.61}$$

$$U = \rho h\Gamma^2 - p + \frac{1}{2}(E^2 + B^2)\,, \tag{2.62}$$

where ϵ_{ijk} is the spatial Levi-Civita tensor and δ_{ij} is the Kronecker symbol. The spatial tensor W^i_j in (2.59), representing the momentum flux density, is

$$W_{ij} \equiv \rho h\Gamma^2 v_i v_j - E_iE_j - B_iB_j + \left[p + \frac{1}{2}(E^2 + B^2)\right]\delta_{ij}\,, \tag{2.63}$$

1 Although formally written in conservative form, the evolution of the magnetic field is based on Stokes' theorem rather than on Gauss' theorem. See Londrillo and Del Zanna [192] for a careful discussion about these aspects.

where δ_{ij} is the Kronecker delta. Eqs. (2.58) above include the divergence free condition $\vec{\nabla} \cdot \vec{B} = 0$. Also for the SR-MHD PDE system we have adopted the aforementioned *divergence-cleaning approach*, yielding the *augmented* SR-MHD equations

$$\boxed{\frac{\partial}{\partial t}\begin{pmatrix} D \\ S_j \\ U \\ B^j \\ \psi \end{pmatrix} + \partial_i \cdot \begin{pmatrix} v^i D \\ W^i_j \\ S^i \\ \epsilon^{jik} E^k + \psi \delta^{ij} \\ B^i \end{pmatrix} = \begin{pmatrix} 0 \\ 0 \\ 0 \\ 0 \\ -\omega_d \psi \end{pmatrix}.} \tag{2.64}$$

More details about this approach can be found in Komissarov [174], Palenzuela et al. [219], Dionysopoulou et al. [85].

An important remark about this set of equations, is that in the relativistic framework *the conversion from the conserved variables* (D, S_i, U, B_i) *to the primitive* variables (p, ρ, v_i, B_i), which are needed for the computation of the fluxes, *is not analytic*, and a numerical root-finding approach is therefore needed. In our numerical code we adopted the third method reported in Sect. 3.2 of [84]. A full account about alternative methods to invert the system (2.60)-(2.62) was given in [217]. Additional information about the mathematical properties of the SR-MHD equations can be found in Balsara and Spicer [17], Komissarov [173], Antón et al. [5], Del Zanna et al. [84], Antón et al. [6]. The latter, in particular, contains a detailed discussion about the renormalization of the eigenvectors of the associated Jacobian.

Part II

DG METHODS FOR COMPRESSIBLE FLUIDS

The second part of the thesis is organized in two chapters, presenting the published research contributions of the author concerning ADER-DG methods for compressible gas dynamics, dealing with the Euler equations and ideal MHD, see [281], compressible Navier-Stokes and viscous and resistive MHD, see [116], but also special relativistic ideal MHD, see [280]. In particular, chapter 3 is devoted to the theoretical description of our ADER-DG finite-element supplemented by a SCL finite-volume method. Chapter 4 collects all the numerical tests with the aim of demonstrating the capabilities of the presented method, in terms of high-resolution properties, high-order convergence, robustness and stability.

3

ADER-DG METHODS WITH SUB-CELL LIMITERS AND AMR

3.1 ADER-DG METHODS FOR COMPRESSIBLE GAS DYNAMICS

3.1.1 *ADER-DG methods for MHD, Navier Stokes and Euler equations*

The partial differential equations considered in this chapter, namely the compressible Navier-Stokes (CNS), the viscous and resistive magnetohydrodynamics (VRMHD) equations, the ideal MHD, Euler and the special relativistic MHD equations can be written in a general form that resembles the standard form of a hyperbolic conservation law, except for the fact that diffusivity enters the PDE by means of an extra dependence of the flux tensor on the gradient of the solution, i.e.

$$\begin{aligned} &\frac{\partial \mathbf{u}}{\partial t} + \nabla \cdot \mathbf{F}(\mathbf{u}, \nabla \mathbf{u}) = 0, \\ &\mathbf{u} = \mathbf{u}(\mathbf{x}, t), \quad \mathbf{x} \in \Omega \subset \mathbb{R}^d, \quad t \in \mathbb{R}_0^+, \end{aligned} \tag{3.1}$$

with $\mathbf{u} = \mathbf{u}(\mathbf{x}, t)$ being the vector of conserved variables, $\mathbf{F} = \mathbf{F}(\mathbf{u}, \nabla \mathbf{u}) = (\mathbf{f}, \mathbf{g}, \mathbf{h})$ being the nonlinear flux tensor depending in general on the state $\mathbf{u}$ and on its *gradient* $\nabla \mathbf{u}$.

The numerical solution of hyperbolic problems has attracted a lot of attention over the years, as they arise in many physical and technological applications. Many of them are in the field of computational fluid dynamics, such as compressible gas dynamics, multiphase flows, air flow around aircraft or cars, astrophysical flows, free surface flows, environmental and geophysical flows like avalanches, dam break problems and water flow in channels, rivers and oceans, to mention but a few. Among the numerical methods specifically developed to solve hyperbolic problems, there are finite volume (FV) methods and discontinuous Galerkin (DG) methods. While until a few years ago FV methods were comparatively more popular, the situation is now rapidly changing and DG schemes, first introduced by Reed and Hill in [235] to solve a first order neutron transport equation, are now widely applied in several different fields, in particular those related to fluid dynamics. In a series of well-known papers [73, 72, 76, 77, 74], Cockburn and Shu provided a rigorous formal framework of these methods, contributing significantly to their widespread use. DG methods are very robust and, among high order numerical methods, they show high flexibility and adaptivity strategies in handling complex geometries [234]. Moreover, Jiang and Shu proved in [156] that DG methods verify an entropy condition which confers them nonlinear L_2 stability. Despite this interesting property, for hyperbolic problems explicit DG methods have a strong stability limitation, since usually the CFL restriction for these schemes is very severe and the time step in d space dimensions is constrained as $\Delta t \leqslant h/[d(2N+1)|\lambda_{max}|]$, where d is the number of space dimensions, h is a

characteristic mesh size, λ_{max} is the maximum signal velocity and N is the degree of the basis polynomial.

In DG schemes a high order time integration is typically performed by means of TVD Runge-Kutta schemes [139], leading to the family of so-called RKDG schemes. These methods are certainly efficient, but they have a maximum reachable order of accuracy in time, which is four. However, due to the high complexity of the fourth order TVD Runge-Kutta scheme, only up to third order TVD Runge-Kutta methods are used in practice. In the presence of stiff source terms, usually the so-called IMEX Runge-Kutta schemes are employed, see [220]. To overcome these limitations, in our approach we follow the so-called ADER strategy, which was first introduced by Toro and Titarev in the finite volume context [263, 256, 260, 258, 261], and it is a very attractive tool allowing to achieve arbitrary order of accuracy in *space and time* in one single step by incorporating the approximate solution of a Generalized Riemann Problem (GRP) at the element interfaces. There are essentially two different families of approximate GRP solvers: those who first interact the spatial derivatives and subsequently compute a temporal expansion at the interface [35, 122, 42, 263, 256, 260, 258, 261, 99], and those who first evolve the data locally *in the small* inside each element and then interact the evolved data at the element interfaces via a classical Riemann solver, see e.g. [142, 193, 125, 106, 101, 105]. For a more detailed discussion on the approximate solution of the GRP, see [52, 211, 138]. Nevertheless, the original ADER approach has two main drawbacks: first, it makes use of the rather cumbersome and problem-dependent Cauchy-Kowalewski procedure and, second, it fails in the presence of stiff source terms. A subsequent version of the ADER approach that solves both these difficulties was developed in [106], where the Cauchy-Kowalewski procedure was replaced with a local space-time DG predictor approach based on a weak formulation of the problem in space-time. This formulation is usually referred to as the *local space-time discontinuous Galerkin* (LSTDG) *predictor* and it has been successfully adopted in a variety of mathematical and physical problems [101, 145, 95, 107, 108, 24]. We remark that, although this LSTDG approach is locally implicit, the full formulation remains explicit and, therefore, the above mentioned CFL restriction still holds. The ADER time stepping method has been also applied successfully to the discontinuous Galerkin finite element framework, see e.g. [99, 229, 104].

The combination of DG schemes with AMR has been considered in a significant number of papers, although in this context the concept of adaptive mesh refinement is commonly absorbed into that of *hp-adaptivity*. Two well-known early series of papers on hp-adaptive DG schemes are due to Baumann and Oden [30, 31] and Houston, Süli and Schwab, see [150, 149, 148]. Furthermore, in [185] a DG scheme was proposed with anisotropic AMR for the compressible Navier-Stokes equations, while in [198, 276] the Euler equations have been solved on adaptive unstructured meshes. In the context of atmospheric simulations, on the other hand, [175] implemented a numerical scheme which includes implicit-explicit RKDG, artificial viscosity and adaptive mesh refinement on two dimensional non-conforming elements. Other relevant results have been obtained in [126], [197]. Our goal is to improve with respect to these approaches by proposing a space-time adaptive

ADER-DG scheme with time-accurate local time stepping that can be arbitrarily high order accurate both in space and time, that avoids Runge-Kutta sub-steps as well as artificial viscosity of any kind, and that incorporates a proper *a posteriori* sub-cell limiter within the full advantages of AMR.

3.1.2 *ADER-DG methods for special relativistic MHD*

The numerical solution of the special relativistic magnetohydrodynamics equations has been particularly fostered by the introduction of Godunov methods based on Riemann solvers, which had already been successfully applied to relativistic hydrodynamics. This was the approach followed in the pioneering works by [173] and [14], who implemented for the first time second order Total Variation Diminishing (TVD) schemes with a specific interest towards astrophysical applications. Since then, relativistic magnetohydrodynamics has developed along different directions with impressive results. From one side several approximate Riemann solvers have been introduced [204, 147, 206, 167]. From another side, relativistic magnetohydrodynamics has been extended to the general relativistic regime [94, 32, 5, 84, 130], and it is currently used to study a variety of high energy physical processes. An additional direction of research has been represented by the inclusion of dissipative effects, namely non-ideal resistive magnetohydrodynamics, with encouraging results [174, 219, 101, 283, 250, 49]. Moreover, high order numerical schemes have also been pursued [83, 3], while simulations of multi-fluids in SR-MHD are emerging as a new frontier [282, 25]. Finally, Adaptive Mesh Refinement (AMR) within SR-MHD codes has been also considered [18, 216, 113, 207, 163, 279] and it is an active field of research. In most of the approaches mentioned so far the evolution in time is performed through the method of lines, resulting in multistep Runge-Kutta schemes, either explicit or implicit. A valuable alternative is again provided by ADER schemes, which were introduced by Titarev and Toro [258], Toro and Titarev [260] and became popular after the modern reformulation by [106, 105, 23]. ADER schemes have been already applied to the equations of relativistic MHD, both in the ideal case [105, 279] and in the resistive case [101]. Another common choice that is typically adopted in the majority of modern SR-MHD codes is that of using finite difference or finite volume conservative schemes. Although rather successful, these schemes require larger and larger stencils when the order of accuracy is increased, a fact that can give rise to substantial overhead when they are parallelized. Discontinuous Galerkin (DG) schemes [72, 76, 77, 74], on the contrary, do not need any spatial reconstruction and they allow for an arbitrary order of accuracy. DG schemes are still relatively unknown in high energy astrophysics, and only a few investigations have been performed so far in the relativistic regime [286, 230, 278]. We apply this idea for the first time to solve the SR-MHD equations in combination with space-time adaptive mesh refinement and time-accurate local time stepping, extending a similar work proposed for classical fluid dynamics in [281].

3.2 DISCRETE EQUATIONS

In this section the ADER-DG scheme with *a posteriori* sub-cell limiter (SCL) on AMR grids is presented in its fundamental facets.

The spatial domain Ω is discretized with a total number of N_E Cartesian and non-overlapping elements T_i

$$\Omega = \bigcup_{i=1,\dots N_E} T_i, \qquad \bigcup_{i\neq j;\ i,j=1,\dots N_E} T_i^\circ \cap T_j^\circ = \varnothing \tag{3.2}$$

[1] over which we provide the weak formulation of the governing equations (3.1), namely

$$\int_{T_i\times\tau_{n+1}} \phi_k \left(\frac{\partial \mathbf{u}}{\partial t} + \nabla\cdot\mathbf{F}(\mathbf{u},\nabla\mathbf{u}) \right) d\mathbf{x}dt = 0. \qquad i = 1,2,\dots N_E, \quad n \in \mathbb{N}_0^+ . \tag{3.3}$$

Here $\tau_{n+1} = [t^n, t^{n+1}]$ is the current time interval, while $\phi_k \in \mathcal{U}_h^N$ is a generic piece-wise polynomial test-function belonging to the vector space $\mathcal{U}_h^N$ of piecewise polynomials defined over Ω and of maximum degree $N \geqslant 0$, whose discontinuities lie along the element interfaces ∂T_i, $i = 1,2,\dots N_E$. As basis and test functions ϕ_k we use the set of Lagrange interpolation polynomials of maximum degree N over T_i passing through the Gauss-Legendre quadrature points of the element T_i. After integration by parts of the divergence term, equation (3.3) becomes

$$\begin{aligned} \int_{T_i\times\tau_{n+1}} \phi_k \frac{\partial \mathbf{u}}{\partial t}\, d\mathbf{x}dt + \int_{\partial T_i\times\tau_{n+1}} \phi_k \mathbf{F}(\mathbf{u},\nabla\mathbf{u})\cdot\mathbf{n}\, dSdt + \\ - \int_{T_i\times\tau_{n+1}} \nabla\phi_k\cdot\mathbf{F}(\mathbf{u},\nabla\mathbf{u})\, d\mathbf{x}dt = 0, \end{aligned} \tag{3.4}$$

Notice the total dimension of the chosen space of solutions is $dim(\mathcal{U}_h^N) = N_E \cdot N_{dof}$, having $N_{dof} = (N+1)^d$ degrees of freedom (d.o.f) for each spatial element T_i. After integrating in time the first term and restricting the space of the solutions to the set of piecewise polynomials $\mathbf{u}_h(\mathbf{x},t) \in \mathcal{U}_h^N$, i.e.

$$\mathbf{u}_h(\mathbf{x},t) = \phi_k(\mathbf{x})\ \hat{\mathbf{u}}_k(t) \tag{3.5}$$

the following higher order accurate ADER-DG scheme is obtained for the expansion coefficients $\hat{\mathbf{u}}_k^n = \hat{\mathbf{u}}_k(t^n)$:

$$\begin{aligned} \left(\int_{T_i} \phi_k\phi_l\, d\mathbf{x} \right) \left(\hat{\mathbf{u}}_l^{n+1} - \hat{\mathbf{u}}_l^n \right) - \int_{T_i\times\tau_{n+1}} \nabla\phi_k\cdot\mathbf{F}(\mathbf{q}_h,\nabla\mathbf{q}_h)\, d\mathbf{x}dt, + \\ + \int_{\partial T_i\times\tau_{n+1}} \phi_k \mathcal{G}\left(\mathbf{q}_h^-,\nabla\mathbf{q}_h^-;\mathbf{q}_h^+,\nabla\mathbf{q}_h^+\right)\cdot\mathbf{n}\, dS\, dt = 0 \end{aligned} \tag{3.6}$$

1 In (3.2) $\circ$ denotes the *interior* operator, i.e. only the boundary surfaces of the elements overlap, not the volumes.

where a so-called local space-time predictor solution $\mathbf{q}_h(\mathbf{x},t)$ has been introduced and the jumps at the element boundaries are resolved by the (approximate) solution of a Riemann problem at the element interfaces. In (3.6) above, the Riemann solver (numerical flux function) is denoted by the symbol $\mathcal{G}\left(\mathbf{q}_h^-, \nabla\mathbf{q}_h^-; \mathbf{q}_h^+, \nabla\mathbf{q}_h^+\right)$, depending on a left pair of state $\mathbf{q}_h^-$ and gradient $\nabla\mathbf{q}_h^-$ taken from within the element T_i, and a right pair of state $\mathbf{q}_h^+$ and gradient $\nabla\mathbf{q}_h^+$ computed from the adjacent neighbor element, respectively. It has to be noted that even for parabolic equations, an appropriate numerical flux function can be obtained by the solution of a generalized Riemann problem, see the work of Gassner et al. [124], which has also been adopted in [95, 96, 145]. For the numerical simulations presented in this part of the thesis, $\mathcal{G}$ has been chosen to be, whenever not explicitly written, a classical and very simple Rusanov-type (local Lax-Friedrichs - LLF) Riemann solver [241], which has been suitably adapted to account for both hyperbolic and *parabolic* terms, see [95, 145]:

$$\mathcal{G}\left(\mathbf{q}_h^-, \nabla\mathbf{q}_h^-; \mathbf{q}_h^+, \nabla\mathbf{q}_h^+\right)\cdot\mathbf{n} = \frac{1}{2}\left(\mathbf{F}(\mathbf{q}_h^+, \nabla\mathbf{q}_h^+) + \mathbf{F}(\mathbf{q}_h^-, \nabla\mathbf{q}_h^-)\right) + - \frac{1}{2} s_{max}\left(\mathbf{q}_h^+ - \mathbf{q}_h^-\right), \tag{3.7}$$

with

$$s_{max} = \max\left(|\lambda_c(\mathbf{q}_h^-)|, |\lambda_c(\mathbf{q}_h^+)|\right) + 2\eta\max\left(|\lambda_v(\mathbf{q}_h^-)|, |\lambda_v(\mathbf{q}_h^+)|\right), \tag{3.8}$$

and

$$\eta = \frac{N+1}{h}, \tag{3.9}$$

where N is the polynomial approximation degree and h is a characteristic length scale of the elements. The λ_c denote the eigenvalues of the convective (hyperbolic) part of the PDE, i.e. the eigenvalues of the matrix $(\partial\mathbf{F}/\partial\mathbf{u})\cdot\mathbf{n}$, while the λ_v are the eigenvalues of the parabolic part of the PDE, i.e. those of the matrix $(\partial\mathbf{F}/\partial(\nabla\mathbf{u}\cdot\mathbf{n}))\cdot\mathbf{n}$. Assuming the space-time predictor $\mathbf{q}_h$ is a polynomial known up to order $(N+1)$ in space and time, see the next paragraphs for the details, then the integrals in (3.6) can be computed *exactly* and the scheme (3.6) yields an *explicit* and *fully-discrete* one-step formula for the computation of the unknowns at the new time level $\hat{\mathbf{u}}_l^{n+1}$. For smooth-solutions, the scheme (3.6) is of order $(N+1)$, see [95], in principle for *any* integer $N \in \mathbb{N}_0^+$. On the other hand, a severe time step restriction is the curse of all known explicit DG discretizations, i.e. a CFL-type time step restriction of the type

$$\Delta t < CFL\frac{h_{min}}{d\,(2N+1)}\left[\lambda_c^{max} + \lambda_v^{max}\frac{2(2N+1)}{h_{min}}\right]^{-1}, \tag{3.10}$$

with the minimum mesh size h_{min} and $CFL < 1$. Condition (3.10) provides a dependence of the maximum admissible numerical time step Δt on the degree N of the polynomial basis, the number of space-dimensions d, the minimum mesh

size given by the insphere diameter h_{min}, the maximum *hyperbolic* signal velocity λ_c^{max} and the *parabolic* penalty λ_v^{max} (see [193, 125, 124, 96]).

Equation (3.6) is the elementary equation for the time-evolution of the presented ADER-DG-P_N method. In the following paragraphs the aforementioned local space-time predictor $\mathbf{q}_h(\mathbf{x}, t)$ and the ADER-WENO sub-cell limiter, coupled within the space-time AMR framework, are briefly discussed. More details are available in the work of [107, 108, 279, 109, 281, 280]. Concerning alternative sub-cell limiter approaches of the DG method, the reader is referred to [248, 51, 151, 119, 202].

3.2.1 *The element local space-time DG predictor*

A direct computation of the integral of the non-linear fluxes in equation (3.4) is subordinate to the knowledge of the physical variables $\mathbf{u}_h$ for any time $t \in T_{n+1}$ along the entire computational domain Ω or, in other words, to a *fully coupled implicit* solution of the non-linear equation (3.4) in the coefficients $\widehat{\mathbf{u}}(t)$ that can become computationally very demanding. Notice that equation system (3.6) is already formally conservative, hence it is possible to use a *non-conservative* predictor solution $\mathbf{q}_h$, which can be computed *locally* inside each element, without considering any coupling to neighbor elements. In this manner, the resulting computational costs are drastically reduced with respect to the original fully coupled system (3.4). A natural solution to this problem has been presented for the first time in the work of [106] in the context of finite volume schemes.

In this paper we use a *nodal* space-time basis of degree N, given by the set of Lagrange interpolation polynomials θ_k of maximum degree N over $\Omega_i \times T_{n+1}$, passing through the *space-time* Gauss-Legendre quadrature points. Since a nodal basis is used, we also expand the nonlinear flux tensor as well as the gradient of the solution in the same basis, see [95]. Hence, we have

$$\mathbf{q}_h(\mathbf{x}, t) = \theta_k(\mathbf{x}, t)\hat{\mathbf{q}}_k, \tag{3.11}$$

$$\nabla \mathbf{q}_h(\mathbf{x}, t) = \nabla\theta_k(\mathbf{x}, t)\hat{\mathbf{q}}_k := \theta_k(\mathbf{x}, t)\hat{\mathbf{q}}'_k, \tag{3.12}$$

$$\mathbf{F}_h(\mathbf{x}, t) = \theta_k(\mathbf{x}, t)\hat{\mathbf{F}}_k, \quad \text{with} \quad \hat{\mathbf{F}}_k = \mathbf{F}(\hat{\mathbf{q}}_k, \hat{\mathbf{q}}'_k). \tag{3.13}$$

Then, equation (3.3) reduces to the following element-local system of nonlinear equations for the local space-time predictor polynomials $\mathbf{q}_h(\mathbf{x}, t)$:

$$\int_{\Omega_i \times T_{n+1}} \theta_k \frac{\partial \mathbf{q}_h}{\partial t} \, d\mathbf{x}\, dt + \int_{\Omega_i \times T_{n+1}} \theta_k \nabla \cdot \mathbf{F}(\mathbf{q}_h, \nabla \mathbf{q}_h) \, d\mathbf{x}dt = 0. \tag{3.14}$$

After integrating the first integral by parts in time, and using the *causality principle* (the current solution depends only on the past, i.e. we use some sort of *upwinding in time*) then the following element-local system is obtained:

$$\int_{\Omega_i} \theta_k(\mathbf{x}, t^{n+1}) \mathbf{q}_h(\mathbf{x}, t^{n+1}) \, d\mathbf{x} - \int_{\Omega_i} \theta_k(\mathbf{x}, t^n) \mathbf{u}_h(\mathbf{x}, t^n) \, d\mathbf{x} + \tag{3.15}$$

$$- \int_{\Omega_i \times T_{n+1}} \frac{\partial \theta_k}{\partial t} \mathbf{q}_h(\mathbf{x}, t) \, d\mathbf{x} \, dt + \int_{\Omega_i \times T_{n+1}} \theta_k \nabla \cdot \mathbf{F}(\mathbf{q}_h, \nabla \mathbf{q}_h) \, d\mathbf{x} dt = 0, \tag{3.16}$$

which can be solved for the unknown space-time degrees of freedom $\hat{\mathbf{q}}_k$ defined in (3.13). Equation (3.16) is solved for each element Ω_i via a simple iterative method for every $i = 1, 2, \ldots, N_E$ that has been successfully tested with and without stiff or non-stiff source terms in the work of [105, 101]. All the multi-dimensional integrals appearing in the relations above can be computed *exactly*, since the solution $\mathbf{q}_h(\mathbf{x}, t)$ as well as the fluxes and the gradients are approximated by polynomials of degree N in space and time.

3.3 AMR AND SUB-CELL LIMITING

In 1984, Berger and collaborators presented the adaptive mesh refinement (AMR) approach for finite difference and finite volume schemes for hyperbolic equations, see [37, 36]. Their version of AMR was written in the form of *nested, logically rectangular and refined meshes*, or *patches* and the employed numerical schemes were at most second order accurate. The first higher order patch-based AMR method was provided by Baeza and Mulet in [12], using up to fifth order accurate WENO schemes. The so-called *cell-by-cell* AMR approach, which has been adopted in this work, has first been introduced by Khokhlov in [164] and was later also extended to high-order ADER-WENO finite volume schemes in [107, 108] for general conservative and non-conservative hyperbolic systems of PDE. Other interesting applications to the shallow water systems have been done by [93], to mention a few. Then other AMR strategies have been also introduced, e.g. the *quadtree/octree* AMR, see [1] and [265]. Compact-WENO (CWENO) schemes have been also successfully applied on AMR meshes, i.e. by [152, 153]. Because of their great flexibility and since they directly allow the use of non-conforming meshes, DG methods have already been extensively implemented on adaptive meshes, commonly known as *hp-adaptive* DG methods, see in particular [30, 31, 148, 149, 148]. DG methods with AMR have been successfully extended also to the *unstructured* and the anisotropic mesh case, see respectively [198, 276] for the Euler equations and [185] for the compressible Navier-Stokes equations. Concerning implicit time discretizations, Kopera and Giraldo [175] presented an interesting implicit-explicit (IMEX) DG method on AMR meshes for the compressible Euler equations with application to atmospheric flow simulations. For further references see also [126, 197].

DG schemes are very efficient in smooth regions, but in the presence of sharp gradients and/or shock waves, they cannot escape from the Gibbs phenomenon

and, as a consequence, they give rise to undesirable oscillations in the solution, since they are linear in the sense of Godunov. In fact, according to Godunov's theorem [133] there are no *linear* and monotone schemes of order higher than the first. In the finite volume framework Godunov's theorem is circumvented by carrying out a *nonlinear* reconstruction within each cell. Here, TVD slope limiters [262] and ENO/WENO reconstructions [142, 157, 16, 257] are among the most popular. In the discontinuous Galerkin approach, on the other hand, even if in principle no spatial reconstruction is needed, in practice it is necessary to introduce some sort of *limiters* to avoid oscillations in the presence of discontinuities. Among the most relevant limiters proposed so far we mention the use of artificial viscosity [237, 221, 65, 121, 91, 120], of spectral filtering [230], of (H)WENO limiting procedures [227, 228, 159, 19, 160, 161, 146], and of slope and moment limiting [72, 191, 234, 50, 275, 88]. In [109] it has been recently proposed a totally different and alternative solution to this longstanding problem, which relies on a new *a posteriori* sub-cell finite volume limiting approach. In practice, the solution is first computed by means of an *unlimited* DG scheme, and subsequently the computational domain is examined by using some very simple but effective *a posteriori* detection criteria, namely the positivity of the solution and a relaxed discrete maximum principle in the sense of polynomials. Once the *troubled cells* have been identified, a sub-grid of size $(2N+1)^d$ is created within these cells and a more robust ADER-WENO finite volume approach is used to recompute the solution on the sub-grid. A peculiar aspect of this new paradigm is that the size of the sub-grid is chosen as to make sure that the maximum admissible time step of the finite volume scheme on the sub-cells matches the time step of the DG scheme on the main grid. The idea of introducing an *a posteriori* approach to the problem of limiting has been recently established by Clain, Diot and Loubère in the finite volume context, by means of the so-called Multi-dimensional Optimal Order Detection (MOOD) method [71, 86, 87, 194]. The MOOD paradigm may in fact be considered as the progenitor of our *a posteriori* limiting procedure for DG schemes [109].

3.3.1 *A sub-cell finite-volume limiter*

The high order ADER-DG scheme given by (3.6) is an *unlimited* scheme and thus oscillatory in the sense of Godunov. It therefore still requires a special treatment for discontinuities. Once the local space-time predictor $\mathbf{q}_h(\mathbf{x},t)$ has been obtained from the iterative solution of equation (3.16), as mentioned above, then the *candidate solution* $\mathbf{u}_h^*(\mathbf{x},t^{n+1})$ can be directly computed according to equation (3.6) in one single step. Since the candidate solution $\mathbf{u}_h^*$ may still contain spurious oscillations in the vicinity of steep gradients, under-resolved flow features, shock waves or other flow discontinuities, nothing can be said about the reliability and about the general physical admissibility of the candidate solution. Consequently, a set of physical and numerical admissibility criteria needs to be prescribed and tested. A reference point for building shock-capturing finite-volume schemes is represented

by the *discrete maximum principle* (DMP) which is tested on the candidate solution accordingly to its *relaxed version* in the sense of polynomials, i.e. in the form

$$\min_{y\in\mathcal{V}_i}(\mathbf{u}_h(\mathbf{y},t^n)) - \delta \leqslant \mathbf{u}_h^*(\mathbf{x},t^{n+1}) \leqslant \max_{\mathbf{y}\in\mathcal{V}_i}(\mathbf{u}_h(y,t^n)) + \delta, \qquad \forall \mathbf{x}\in T_i\,, \tag{3.17}$$

where $\mathcal{V}_i$ is the set containing the element T_i and the respective Voronoi neighbor elements (neighbors which share a common node with T_i); δ is chosen to be a *solution-dependent* tolerance given by

$$\delta = \max\left(\delta_0, \epsilon\cdot\left(\max_{y\in\mathcal{V}_i}(\mathbf{u}_h(y,t^n)) - \min_{y\in\mathcal{V}_i}(\mathbf{u}_h(\mathbf{y},t^n))\right)\right), \tag{3.18}$$

with $\delta_0 = 10^{-4}$ and $\epsilon = 10^{-3}$, similarly to [109, 281, 280]. The tolerance is added since it is very difficult to compute the global extrema of $\mathbf{u}_h(\mathbf{x},t^n)$ in T_i. Therefore, we compute an approximation of the extrema by making use of the sub-grid representation of the solution, as detailed below. Moreover, it is of fundamental importance to check $\mathbf{u}_h^*$ also for a set of *physical* admissibility criteria, e.g. the positivity of pressure and density variables in the case of compressible fluid flows. We furthermore check the solution for the presence of floating point errors (NaN). Once the numerical and physical admissibility criteria have been tested and whenever a local candidate solution $\mathbf{u}_h^*(\mathbf{x}\in T_i, t^{n+1})$ is detected to be *'troubled'*, then $\mathbf{u}_h^*(\mathbf{x}\in T_i, t^{n+1})$ is directly rejected and the limiter-status of T_i is set to $\tilde{\beta}_i = 1$, meaning the limiter is activated. Then, the older ADER-DG solution $\mathbf{u}_h(\mathbf{x}\in T_i, t^n)$ is projected along a suitable *sub-grid of* N_s *spatial sub-cells per space-dimension* within T_i, resulting in a *piecewise-constant* representation of the discrete solution $\boldsymbol{w}_h(\mathbf{x}\in T_i, t^n) = \mathcal{P}[\mathbf{u}_h(\mathbf{x}\in T_i, t^n)]$, $\mathcal{P}$ being a suitable projector operator (see [109, 281, 280]). Then, a new discrete solution is obtained for the sub-grid averages by using a more robust ADER-WENO finite volume scheme [107], generating a new set of piecewise-constant cell averages $\boldsymbol{w}_h(\mathbf{x}\in T_i, t^{n+1})$. The new sub-cell averages are then directly gathered back to a high order DG polynomial $\mathbf{u}_h(\mathbf{x}\in T_i, t^{n+1}) = \mathcal{R}[\boldsymbol{w}_h(\mathbf{x}\in T_i, t^{n+1})]$, where $\mathcal{R}$ is a suitable high order accurate *reconstruction* operator satisfying $\mathcal{R}\circ\mathcal{P} = 1$ (see [109, 281, 280]). The high order ADER-WENO method has been shown to be an excellent candidate for the sub-cell finite volume limiting stage because of its well established capabilities in handling discontinuities, together with high-order convergence properties under the time-step constraint

$$\Delta t < \mathrm{CFL}\frac{h_{\min}}{dN_s}\left[\lambda_c^{\max} + \lambda_\nu^{\max}\frac{2N_s}{h_{\min}}\right]^{-1}. \tag{3.19}$$

The WENO scheme furthermore does not clip local extrema, in contrast to standard second order TVD schemes. Notice that the local number of sub-cells N_s per space-dimension should be chosen $N_s \geqslant N+1$ in order to preserve the information contained in the available degrees of freedom of the high order polynomial data representation used in the DG scheme. In our simulations, N_s has been chosen to be $N_s = 2N+1$, thus matching the maximum time-step allowed by the ADER-WENO finite volume scheme (3.19) with the one for the ADER-DG method (3.10) .

3.3.2 *A 'cell by cell' AMR*

There are mainly two strategies for defining an automatically refined grid, namely the so called *patched* and the *cell by cell* AMR method. In this work the second strategy is chosen, leading to a tree data structure by defining up to ℓ_{max} refinement levels Ω_h^ℓ, $\ell = 1, 2, \dots, \ell_{max}$, the coarser grid Ω_h^0 given, covering the entire spatial domain Ω, i.e.

$$\Omega \equiv \bigcup_{T_i \in \Omega_h^\ell} T_i, \quad \forall \ell = 0, 1, \dots, \ell_{max}. \tag{3.20}$$

An integer number $\mathfrak{r}$ for the spatial refinement ratio, or *refinement factor*, between adjacent refinement levels drives the refinement scales. Figure 1 gives an illustrative sketch of the resulting adaptive mesh. In order to refine the grid only whenever and wherever necessary, a *refinement-estimator function* χ can be chosen to be a function of the space-derivatives of a given indicator function $\Phi(\mathbf{x}, t)$, e.g. in the form of

$$\chi(\Phi) = \sqrt{\frac{\sum_{k,l} \left(\partial^2 \Phi / \partial x_k \partial x_l \right)^2}{\sum_{k,l} \left[\left(|\partial \Phi / \partial x_k|_{i+1} + |\partial \Phi / \partial x_k|_i \right) \Big/ \Delta x_l + \epsilon \left| \frac{\partial^2}{\partial x_k \partial x_l} \right| |\Phi| \right]^2}}, \tag{3.21}$$

which considers up to the second space derivatives. The indicator function Φ can be any physical quantity of interest, e.g. the pressure, the vorticity, the kinetic energy or any other function of the flow quantities. χ will be evaluated periodically in time, according to the time-scales of the physical problem. Then, the space-elements T_i will be *refined* or *recoarsened* whenever the prescribed upper and lower threshold values χ_{ref} and χ_{rec}, respectively, are exceeded. The resulting *active* mesh Ω_h is the set of space-elements belonging to the refinement levels Ω_h^ℓ, $\ell = 1, 2, \dots, \ell_{max}$, such that Ω is spanned and the non-overlapping property is satisfied, i.e.[2]

$$\Omega_h = \left\{ T_i \;\middle|\; T_i \in \bigcup_{\ell=1}^{\ell_{max}} \Omega_h^\ell, \;\text{ and }\; \Omega = \bigcup_i T_i, \right.$$
$$\left. \text{and } \; \varnothing = \bigcup_{T_i \neq T_j} \left(T_i^\circ \cap T_j^\circ \right), \;\text{ with }\; i, j = 1, 2, \dots, N_{elem} \right\}. \tag{3.22}$$

For practical purposes, it becomes useful to define the '*status* β' of the complete set of spatial elements. The *active elements* T_i (i.e. $\beta = 0$) are those *non-overlapping* spatial elements that constitute the current numerical mesh, i.e. satisfying (3.1), where the discrete solution is chosen for being updated following the presented ADER-DG+SCL method. The *virtual children* belonging to a relative refinement level $\ell(T_i^{Vc})$ are those spatial elements which *are (spatially) contained within at least*

2 $\circ$ denotes the *interior* operator, i.e. with $T^\circ = T \setminus \partial T$.

one active element in its -adjacent coarser- *tree-structure* $\ell = \ell(T_i^{Vc}) - 1$. The numerical solution is updated in time by means of a standard L_2 projection for the ADER-DG from the *mother* cell at the $(\ell(T_i^{Vc}) - 1)$-th level. Finally, the *virtual parent cells* T_i^{Vm} ($\sigma = -1$) belonging to a relative refinement level $\ell(T_i^{Vm})$ are those spatial elements which *(spatially) contains at least one active element in its adjacent* -finer- *tree-structure* $\ell = \ell(T_i^{Vm}) + 1$. In this case, the numerical solution is updated in time by averaging the solution from the *children*-elements (i.e. $\ell = \ell(T_i^{Vm}) + 1$). Within this new computational grid, N_{tot} is the total number of elements that should be distinguished from the total number of *active* elements N_E which appears in our numerical equations. These properties are summarized in the following definition for β

$$\forall T_i \in \bigcup_{\ell} \Omega_h^{\ell}$$

$$\beta_i = \begin{cases} -1, & \text{for the so called } \textit{virtual parent cells} \text{ (Vm), i.e.} \quad \exists T_j \in \Omega_h \big| T_j \supset T_i \\ 0, & \text{for } \textit{active elements}, \text{ i.e.} \quad T_i \in \Omega_h \\ 1, & \text{for the so called } \textit{virtual children} \text{ (Vc), i.e.} \quad \exists T_j \in \Omega_h \big| T_j \subset T_i \end{cases} .$$

These three β-status are necessary during the mesh-adaptation stage whenever an active cell is refined or recoarsened, and then, inactivated. Indeed, whenever this is the case, a proper transformation is needed for mapping the numerical solution (limited or unlimited, finer or coarser) from one refinement level to the adjacent one. A simple sketch of the transformation-mapping between the discrete solution spaces of the DG polynomials and the WENO sub-cell averages, between two adjacent refinement levels ℓ and $\ell + 1$ is shown in Figure 3.

Moreover, virtual cells allow us to perform polynomial WENO reconstructions along the same refinement level, independently on the effective refinement level of two adjacent active elements (see Figure 2). For more details see [281, 280], for information about the parallel message passing interface (MPI) implementation of the presented AMR framework see [108, 107]. It should be noticed that whenever an automatic adaptation of the grid is used, the scheme can in principle handle simultaneously small and large spatial scales. However, due to the CFL condition, also a characteristic time scale is implied by the local mesh spacing.

In order to make things simpler, in this work, two *neighbor and active* elements T_i and T_j are allowed to belong only to the same or to an adjacent refinement level, i.e. if $T_i \in \Omega_h^{\ell}$ then $T_j \in \Omega_h^{\ell-1 \leqslant \tilde{\ell} \leqslant \ell+1}$, or in a simpler notation $|\ell(T_j) - \ell(T_i)| \leqslant 1$, where $\ell(T)$ is the refinement level of a general space-element T.

3.3.3 *Incorporation of the sub-cell limiter into the AMR framework*

What we discussed in section 3.3.1, namely the *a posteriori* sub-cell limiter which is activated in the troubled zones of the ADER-DG scheme, must be properly nested within the AMR framework. In order to understand how the interaction works, let us first list the basic rules that we have followed

- The virtual children cells inherit the limiter status of their active mother cell.

- If at least one active child is flagged as troubled, then the (virtual) mother is also flagged as troubled.
- Cells which have been flagged as troubled cannot be recoarsened.

Because of the presence of the limiter, the two typical AMR operations represented by *projection* and *averaging* must be also extended to the alternative data representation $\mathbf{v}_h(\mathbf{x}, t^n)$. Let us denote the sub-grid of a generic cell $\mathcal{C}_n$ at level ℓ as $\mathcal{S}_n^\ell$ and the data representation $\mathbf{v}_h(\mathbf{x}, t^n)$ at level ℓ simply as $\mathbf{v}_h(\mathcal{S}_n^\ell)$. Let us further denote a generic virtual child cell as $\mathcal{C}_v$ and the virtual mother or parent cell as $\mathcal{C}_p$. Then, in general, we need to be able to perform the two operations

$$\mathbf{v}_h(\mathcal{S}_n^\ell) \rightarrow \mathbf{v}_h(\mathcal{S}_v^{\ell+1}) : \quad \text{DG limiter - AMR projection}, \tag{3.23}$$

$$\mathbf{v}_h(\mathcal{S}_n^\ell) \rightarrow \mathbf{v}_h(\mathcal{S}_p^{\ell-1}) : \quad \text{DG limiter - AMR averaging}, \tag{3.24}$$

which we describe below.

DG limiter - AMR projection

This operation becomes necessary when an active cell with limiter status $\tilde{\beta} = 1$, namely a troubled cell, has virtual children cells. In such circumstances, we need to project the alternative data representation $\mathbf{v}_h(\mathbf{x}, t^n)$ from the sub-cells of a given level of refinement ℓ to the sub-cells of the next level $\ell + 1$. We recall that a pure DG scheme with AMR, but without limiters, would not require any virtual cell (status $\beta = \pm 1$), because pure DG schemes do not perform any reconstruction. We also recall that in our implementation virtual children cells are created to allow any cell marked for refinement to perform a spatial reconstruction, and more precisely when the stencil corresponding to the specific reconstruction procedure chosen (TVD, WENO, etc.) covers adjacent cells belonging to different levels of refinement. However, our DG scheme is not pure, because it works in combination with the limiter, and the limiter involves a WENO reconstruction on the sub-grid. Hence, our ADER-DG-AMR scheme still implies the introduction of virtual cells, which must be created when the WENO reconstruction on the sub-grid of level $\ell + 1$ uses a stencil that covers a portion of the grid belonging to level ℓ. In such circumstances, it is necessary to perform the operation expressed by (3.23) above. A simplified situation is reported in figure 2, sketching a two-dimensional configuration in which AMR and the sub-cell limiter of the DG scheme are interlinked. In that figure two AMR refinement levels are involved. The cell $\mathcal{C}_n$ at level ℓ and the cell $\mathcal{C}_m$ at level $\ell + 1$ have limiter status $\tilde{\beta} = 1$, and for this reason they are colored in red. In order to allow $\mathcal{C}_m$ to perform the WENO reconstruction on its sub-grid, cell $\mathcal{C}_n$ must project $\mathbf{v}_h$ from the sub-grid of level ℓ to the sub-grid of level $\ell + 1$ in the virtual cell $\mathcal{C}_v$. Hence, the sub-cell averages on the finer level $\ell + 1$ are computed from the condition that

$$\int_{S_{v,j}} \mathbf{v}_h(\mathcal{S}_v^{\ell+1}) \, d\mathbf{x} = \int_{S_{i,j}} \mathcal{W}\left(\mathbf{v}_h(\mathcal{S}_n^\ell)\right) d\mathbf{x}, \qquad \forall S_{v,j} \in \mathcal{S}_v^{\ell+1}, \tag{3.25}$$

where $\mathcal{W}$ denotes the WENO reconstruction operator applied on the cell averages of the sub-grid on level ℓ. We use a WENO reconstruction to pass sub-grid data from the coarse level to the finer one, since this projection operation is carried out in troubled cells where typically discontinuities are present. Therefore, we need a nonlinear, essentially non-oscillatory reconstruction that is at the same time high order accurate and which is also able to deal with shocks and other discontinuities.

DG limiter - AMR averaging

Conversely, we also need to perform the averaging of $\mathbf{v}_h(\mathbf{x}, t^n)$ from the sub-cells of a given level ℓ to the sub-cells of the previous level $\ell - 1$. Then the averaging operator acting on the degrees of freedom of the sub-grid WENO polynomial can be written in a compact form as

$$\int_{S_{p,j}} \mathbf{v}_h(\mathcal{S}_p^{\ell-1}) d\mathbf{x} = \int_{S_{p,j}} \mathbf{v}_h(\mathcal{S}_n^{\ell}) d\mathbf{x}, \qquad \forall S_{p,j} \in \mathcal{S}_p^{\ell-1}, \tag{3.26}$$

From an operational point of view, this transformation is most conveniently performed in a dimension-by-dimension fashion. No reconstruction is needed here, since the averaging over known cell averages is trivial.

3.3.3.1 *MPI parallelization and ghost-cells*

Full details about the implementation and the parallelization of the AMR framework through the standard Message Passing Interface (MPI) can be found in [107, 108]. The code has been parallelized through the standard message passing interface (MPI). A proper strategy is necessary to let *two spatially adjacent CPU*, i.e. one element of one CPU is a neighbor of an element belonging to the other, communicate the sufficient information both for the refinement/recoarsening-process and for the interface-flux integration. This has been accomplished by adding to the standard set of elements of every specific CPU a layer of MPI-ghost cells at the MPI-boundaries, defined to be a copy of the real neighbor elements belonging to the MPI-adjacent CPUs.

3.3.4 *Local time-stepping*

The whole scheme described so far can be implemented over adaptively refined meshes (AMR), together with time-accurate local time-stepping (LTS). Indeed, if the CFL restriction (3.10) and (3.19) would apply to a global time-step, any medium-size numerical simulation with more than one refinement levels would become unfeasible. By definition, see section 1.3.4, the local-time-step Δt for any given integration of (3.6) should be sufficiently small, so that the resulting discrete domain of dependence $\mathbb{D}_h^-(P)$ of the numerical scheme of any given point $P = (\mathbf{x}, t^n + \Delta t)$ lies within the real domain of dependence $\mathbb{D}^-(P)$. In other words, the numerical information can not travel faster than physical waves. This condition is applied in the approximation of the *Godunov states* at discontinuous interfaces

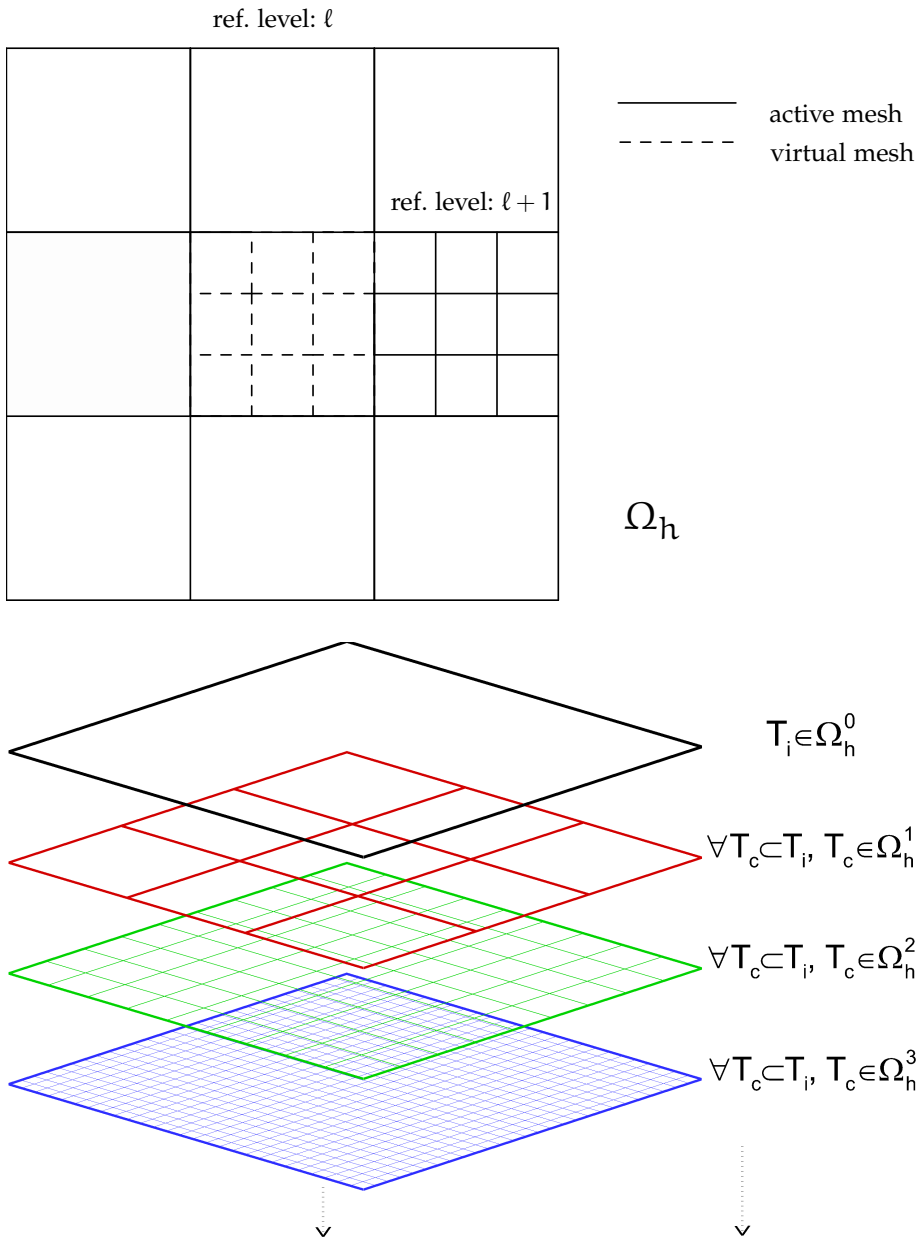

Figure 1: At the top, a simple sketch of the AMR grid Ω_h with one single refinement level is shown. At the bottom, the *tree-structure* of the refinement levels $\ell = 0,1, \ldots, \ell_{max}$ for a single element at the coarsest level $T_i \in \Omega_h^0$ is shown. (See colored version on-line)

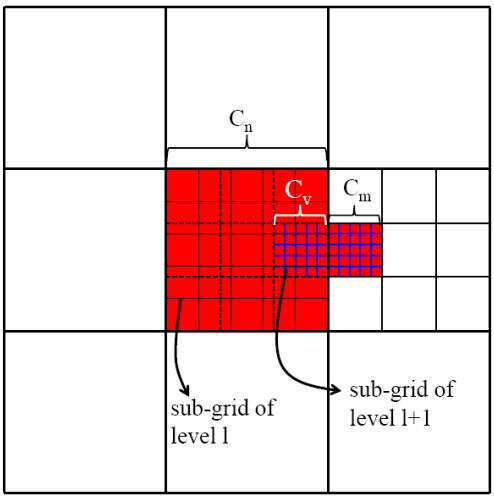

Figure 2: At the left, a simple sketch of the combination of AMR and DG sub-cell reconstruction. The limited elements ($\tilde{\beta} = 1$) are highlighted in red, i.e. cell $\mathcal{C}_n$ at the ref. level ℓ and cell $\mathcal{C}_m$ at $\ell + 1$. Then, the cell $\mathcal{C}_n$ must project $\mathbf{v}_h$ from the original sub-grid of the ℓ-th ref. level to the sub-grid of level $\ell + 1$, within the virtual cell $\mathcal{C}_v$.

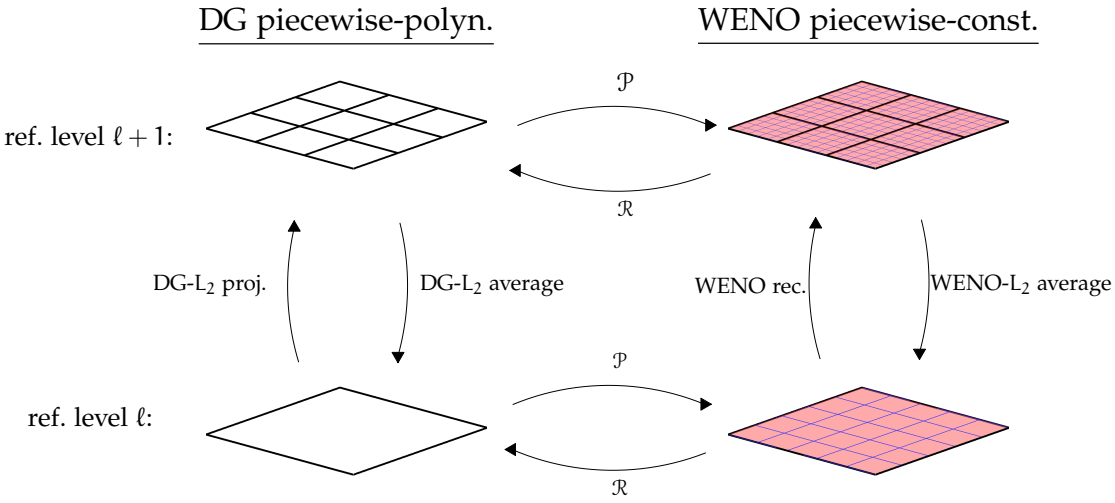

Figure 3: Mapping of the numerical solution between the DG piecewise polynomial and the WENO piecewise constant spaces, between two different AMR-levels ℓ and $\ell + 1$.

in equation (3.6). In particular, given a time line $\Sigma = (x, t \in [t^n + \Delta t])$ belonging to a space-time interface $\partial T \times \tau_{n+1}$ between a left and a right space-elements T_L and T_R, the *fastest approximated* characteristics passing through any point of Σ, from the left or from the right, is allowed to cross only the right space-element T_R or the left T_L at $t = t^n$. This means that finer elements allow smaller time-steps with respect to coarser elements. In order to take advantage from the maximum local-time-step Δt^ℓ allowed by the CFL condition, depending on the refinement level, in a first cycle only the solution for the finer elements are integrated with $\Delta t^{\ell_{max}}$ as many times as necessary until matching the time-step of the coarser elements $\Delta t^{\ell-1}$, then in the recursive phases, the solution at the lower refinement levels is recursively integrated in time. In should be noticed that the adopted *predictor* solution suits perfectly with local-time-stepping, since a space-time piecewise-polynomial q_h is always available at the left and right of the space-time interfaces $\partial T \times \tau_{n+1}$.

Full details on the high order local time stepping (LTS) procedure are available in [107].

4

NUMERICAL VALIDATION AND RESULTS

4.1 CONVERGENCE TESTS

4.1.1 *Isentropic vortex (Euler)*

In order to asses the convergence properties of the ADER-DG-AMR scheme we have considered the solution of the two-dimensional isentropic vortex, which admits an analytic solution [247]. The test consists of the advection of a vortex with initial conditions given by a perturbation superposed to a uniform mean flow as

$$(\rho, u, v, w, p) = (1 + \delta\rho, 1 + \delta v_x, 1 + \delta v_y, 0, 1 + \delta p)\,, \tag{4.1}$$

with

$$\begin{pmatrix} \delta\rho \\ \delta v_x \\ \delta v_y \\ \delta p \end{pmatrix} = \begin{pmatrix} (1+\delta T)^{1/(\gamma-1)} - 1 \\ -(y-5)\epsilon/2\pi \exp\left[0.5(1-r^2)\right] \\ (x-5)\epsilon/2\pi \exp\left[0.5(1-r^2)\right] \\ (1+\delta T)^{\gamma/(\gamma-1)} - 1 \end{pmatrix}. \tag{4.2}$$

The perturbation in the temperature is

$$\delta T = -\frac{\epsilon^2(\gamma-1)}{8\gamma\pi^2}\, \exp\left(1-r^2\right), \tag{4.3}$$

where $r^2 = (x-5)^2 + (y-5)^2$, while the vortex strength is $\epsilon = 5$ and the adiabatic index is $\gamma = 1.4$. It is easy to check that, under these conditions, the entropy per unit mass $s = p/\rho^\gamma$ is constant everywhere. The numerical domain is the square $\Omega = [0, 10] \times [0, 10]$, and periodic boundary conditions are used along the four edges. In this way, after setting the final time of the simulation to $t_{final} = 10$, the vortex recovers the initial position. We have solved this problem using the Rusanov flux with reconstruction in characteristic variables. Due to the smoothness of the solution, we expect that the sub-cell limiter is never activated, which is indeed the case. We have performed a convergence study by varying N from 2 to 8, with $\ell_{max} = 1$ and a refinement factor $r = 3$, except for the case $N = 8$, for which we have used $r = 2$. A regular refinement over the moving vortex is better obtained by applying a refinement criterion based on the cell average of the mass density, rather than by applying the standard procedure based on equation (3.21). In practice, and just for this test, a cell is marked for refinement if the cell average of the variable ρ is smaller than the threshold $\bar{\rho} = 0.75$. Table 1 summarizes the results of this analysis by reporting the L^1, L^2 and L^∞ norms of the error, computed with respect to the available analytic solution at time $t = t_{final}$. The second column of

the table reports the number of cells, along each direction, of the initial grid at the level zero. When $N \geqslant 6$, very coarse initial meshes have been adopted, since for larger values of N_x the round-off errors affect negatively the outcome of the test. With this caveat in mind, the computed orders of convergence are in very good agreement with the nominal ones up to $N = 8$, thus confirming the high order of accuracy of the proposed ADER-DG scheme even in combination with AMR and time-accurate local time stepping.

4.1.2 *Alfen wave (SR-MHD)*

We have tested the convergence of our new numerical scheme by considering the propagation of a circularly polarized Alfven wave, for which an analytic solution is known [172, 84]. Choosing x as the direction of propagation, and η as the amplitude of the wave, the magnetic field is given by

$$B_x = B_0 \tag{4.4}$$
$$B_y = \eta B_0 \cos[k(x - v_A t)] \tag{4.5}$$
$$B_z = \eta B_0 \sin[k(x - v_A t)]\,, \tag{4.6}$$

where B_0 is the uniform magnetic field along x, k is the wave number, while v_A is the Alfven speed at which the wave propagates (see [84] for its analytic form). The vector tips of the transverse velocity field describe circles in the yz plane normal to $\vec{B}_0$, according to

$$v_y = -v_A B_y/B_0, \quad v_z = -v_A B_z/B_0\,. \tag{4.7}$$

We have used $\rho = p = B_0 = \eta = 1$, and since the wave is incompressible, the background values of ρ and p are not affected. The test has been performed in two spatial dimensions, using periodic boundary conditions, over the computational domain $\Omega = [0; 2\pi] \times [0; 2\pi]$. We compare the numerical solution with the analytic one after one period $T = L/v_A = 2\pi/v_A$. The results of this analysis are reported in Tab. 2, which report the L_1, L_2 and L_∞ norms of the error of B^y. The Rusanov flux has been adopted, with $\ell_{max} = 2$ and a Courant factor $CFL = 0.8$. We emphasize that, due to the smoothness of the solution, the sub-cell limiter is never activated. As it is apparent from the table, the nominal order of convergence is essentially confirmed.

4.2 1D RIEMANN PROBLEMS

4.2.1 *Sod and Lax problems (Euler)*

Having verified the convergence properties of the ADER-DG-AMR scheme, we have considered two classical Riemann problems, proposed by Sod and Lax, with initial conditions given, respectively, by

$$(\rho, u, p)_{Sod} = \begin{cases} (1.0, 0.0, 1.0) & \text{if} \quad x \in [0; 0.5]\,, \\ (0.125, 0.0, 0.1) & \text{if} \quad x \in [0.5; 1.0]\,, \end{cases} \tag{4.8}$$

Isentropic vortex problem – ADER-DG-P_N + WENO3 SCL

	N_x	L^1 error	L^2 error	L^∞ error	L^1 order	L^2 order	L^∞ order	Theor.
DG-P_2	15	5.5416E-2	1.1075E-2	1.2671E-2	—	—	—	3
	30	5.7101E-3	1.0984E-3	1.7374E-3	3.28	3.33	2.87	
	60	8.8511E-4	1.8805E-4	3.4727E-4	2.69	2.55	2.32	
	90	3.0025E-4	6.6257E-5	1.3176E-4	2.67	2.57	2.39	
DG-P_3	15	6.4357E-3	1.0325E-3	1.0026E-3	—	—	—	4
	30	2.9981E-4	4.4304E-5	4.2822E-5	4.42	4.54	4.55	
	60	1.1141E-5	1.6679E-6	2.2108E-6	4.75	4.73	4.27	
	90	1.6787E-6	2.9117E-7	5.0366E-7	4.67	4.30	3.65	
DG-P_4	10	5.0587E-3	8.2103E-4	1.0921E-3	—	—	—	5
	15	6.3888E-4	1.0137E-4	1.2972E-4	5.10	5.16	5.25	
	20	1.5369E-4	2.3219E-5	3.5064E-5	4.95	5.12	4.55	
	25	5.1581E-5	7.8567E-6	1.2824E-5	4.89	4.86	4.51	
DG-P_5	15	1.1135E-4	1.6708E-5	2.5184E-5	—	—	—	6
	20	1.8700E-5	2.7597E-6	3.4678E-6	6.20	6.26	6.89	
	25	3.9941E-6	6.0874E-7	9.4323E-7	6.92	6.77	5.83	
	30	1.4623E-6	2.1969E-7	3.0234E-7	5.51	5.59	6.24	
DG-P_6	5	1.5485E-2	2.5835E-3	2.6686E-3	—	—	—	7
	10	1.8390E-4	2.9877E-5	4.1129E-5	6.40	6.43	6.02	
	15	9.8578E-6	1.6642E-6	2.9090E-6	7.22	7.12	6.53	
	20	1.2041E-6	2.0205E-7	3.6192E-7	7.31	7.33	7.24	
DG-P_7	5	6.2402E-3	1.0963E-3	1.4947E-3	—	—	—	8
	9	6.0168E-5	1.0210E-5	1.2830E-5	7.90	7.96	8.09	
	11	1.5676E-5	2.4524E-6	4.0665E-6	6.70	7.11	5.73	
	13	4.8297E-6	7.7831E-7	1.0593E-6	7.05	6.87	8.05	
DG-P_8	7	1.3473E-4	2.1259E-5	2.3665E-5	—	—	—	9
	9	1.8066E-5	2.8661E-6	3.6534E-6	7.99	7.97	7.43	
	11	2.7718E-6	4.2166E-7	5.2952E-7	9.34	9.55	9.62	
	13	6.2220E-7	1.0475E-7	1.4401E-7	8.94	8.34	7.79	

Table 1: L^1, L^2 and L^∞ errors and convergence rates for the 2D isentropic vortex problem for the ADER-DG-P_N scheme with sub-cell limiter and adaptive mesh refinement. One level of refinement has been used with a refinement factor $r = 3$, except for the case $N = 8$, for which we have used $r = 2$.

Circularly polarized Alfven Wave problem – ADER-DG-P_N + WENO3 SCL

	N_x	L_1 error	L_2 error	L_∞ error	L_1 order	L_2 order	L_∞ order	Theor.
DG-P_2	30	2.9861E-3	7.2314E-4	4.2388E-4	—	—	—	3
	60	2.9229E-4	8.0346E-5	7.0230E-5	3.35	3.17	2.59	
	90	8.8069E-5	2.5059E-5	2.3319E-5	2.95	2.87	2.72	
	120	3.6687E-5	1.0900E-5	1.0948E-5	3.04	2.89	2.63	
DG-P_3	15	1.2671E-4	2.5939E-5	1.1433E-5	—	—	—	4
	20	3.1455E-5	6.5949E-6	2.9456E-6	4.48	4.76	4.71	
	25	1.1743E-5	2.5410E-6	1.4527E-6	4.41	4.27	3.17	
	30	5.7046E-6	1.2767E-6	7.5875E-7	3.96	3.77	3.56	
DG-P_4	10	6.6600E-5	1.4648E-5	7.5420E-6	—	—	—	5
	15	7.8640E-6	1.9384E-6	1.2828E-6	5.26	4.98	4.36	
	20	1.8748E-6	4.9562E-7	3.6520E-7	4.98	4.74	4.36	
	25	6.1631E-7	1.6408E-7	1.3283E-7	4.98	4.95	4.53	

Table 2: L_1, L_2 and L_∞ errors and convergence rates for the 2D circularly polarized Alfven wave problem for the ADER-DG-P_N scheme with sub-cell limiter and adaptive mesh refinement. Two levels of refinement have been used with a refinement factor $r = 3$. The errors have been computed for the variable B^y.

and

$$(\rho, v, p)_{Lax} = \begin{cases} (0.445, 0.698, 3.528) & \text{if} \quad x \in [0; 0.5]\,, \\ (0.5, 0.0, 0.571) & \text{if} \quad x \in [0.5; 1.0]\,. \end{cases} \tag{4.9}$$

The computational domain is actually two-dimensional, but the second direction y acts as a passive one. Moreover, the adiabatic index of the gas is $\gamma = 1.4$, and the final time of the simulation is $t_{final} = 0.2$ for Sod's problem, while it is $t_{final} = 0.14$ for Lax's. Both tests have been solved using the ADER-DG-P_9 scheme, supplemented with our *a posteriori* ADER-WENO3 finite volume sub-cell limiter. The initial grid is composed of $N_x \times N_y = 20 \times 5$ cells, which are then adaptively refined using $r = 3$ and $\ell_{max} = 2$. The results of our calculations, for which we have used the Osher flux [100], are reported in figures 4–5. Figure 4, in particular, shows the three-dimensional view of the solution by plotting the corresponding polynomials, highlighted in blue (for the unlimited cells) and in red (for the limited cells) according to our standard convention. We recall that the blue polynomials really represent the DG polynomials within each cell, while in the red cells we visualize the data as a piecewise linear interpolation of the sub-cell averages, produced by the sub-cell limiter. As in figure 4 of [109], in both the tests the contact discontinuity is resolved within one single cell, which, due to our AMR algorithm, in the present case is always at the maximum level of refinement. We further note that the contact wave is unlimited (blue). This is due to the fact that after a certain time our ADER-DG scheme recognizes this linear degenerate wave as a *smooth feature*, after the initial smoothing of the contact discontinuity by the sub-cell limiter

Problem		ρ	$(v_x$	v_y	$v_z)$	p	$(B_x$	B_y	$B_z)$	t_{final}	γ
RP1	$x > 0$	0.125	0.0	0.0	0.0	0.1	0.5	-1.0	0.0	0.4	2.0
(Test 1 in [14])	$x \leqslant 0$	1.0	0.0	0.0	0.0	1.0	0.5	1.0	0.0		
RP2	$x > 0$	1.0	-0.45	-0.2	0.2	1.0	2.0	-0.7	0.5	0.55	5/3
(Test 5 in [14])	$x \leqslant 0$	1.08	0.4	0.3	0.2	0.95	2.0	0.3	0.3		

Table 3: Initial conditions for the one–dimensional Riemann problems.

and the Riemann solver. The right propagating shock, on the contrary, is always limited (red), as expected, and it is very sharply resolved. In figure 5 we have instead reported the comparison of the exact solution of the Riemann problem [262] with the numerical solution for a few representative variables, extracted from the polynomial data representation of the DG scheme -or the sub-cell limiter- along a 1D line of 200 equidistant sample points. The agreement between numerical and exact solution is excellent. Finally, for this test we have also performed a profiling analysis to quantify the relative computational costs of the sub-cell limiter. In a representative simulation using the ADER-DG-P_2 scheme, with approximately 15% of the cells that are limited, the overhead with respect to the unlimited DG scheme amounts to a factor ≈ 1.5 in terms of CPU time.

4.2.2 *Shock tube problems in SR-MHD (SR-MHD)*

Once the convergence properties have been verified, we consider a few relevant shock-tube problems to test the new ADER-DG-AMR method. Specifically, we concentrate on two classical Riemann problems for SR-MHD, already proposed by [270] and classified as 'Test 1' and 'Test 5' in table 1 of [14]. The corresponding initial conditions, referred to as RP1 and RP2 in the following, are given in table 3, which reports also the final times and the adiabatic indices.[1]

The two chosen Riemann problems are solved along two coarse grids of 40×5 and 25×5 elements, respectively. Then, the initial grid is adaptively refined in space and time according to $r = 3$ and $\ell_{max} = 2$. The computational domain is two-dimensional, but the second direction y acts as a passive one. Both tests have been solved using the ADER-DG-P_3 scheme, but they differ in the sub-cell limiter, which is the second order TVD finite volume scheme for RP1, while it is the third order ADER-WENO finite volume scheme for RP2. The HLL solver has been used for both RP1 and RP2 with a Courant factor CFL $= 0.5$. The damping factor for the divergence-cleaning procedure is set to $\kappa = 10$.

Figure 6 shows the three-dimensional plot of the solution for the rest mass density and the corresponding AMR grid, by plotting the real DG polynomials (highlighted in blue) for every single unlimited cell and the piecewise linear interpolation of the ADER-WENO limiter along the sub-cell averages (highlighted

1 The adiabatic index γ of RP1 in unphysical, as it violates Taub's inequality based on kinetic theory [251, 205] but it is fixed equal to 2 anyway to ease comparison with [270] and [14].

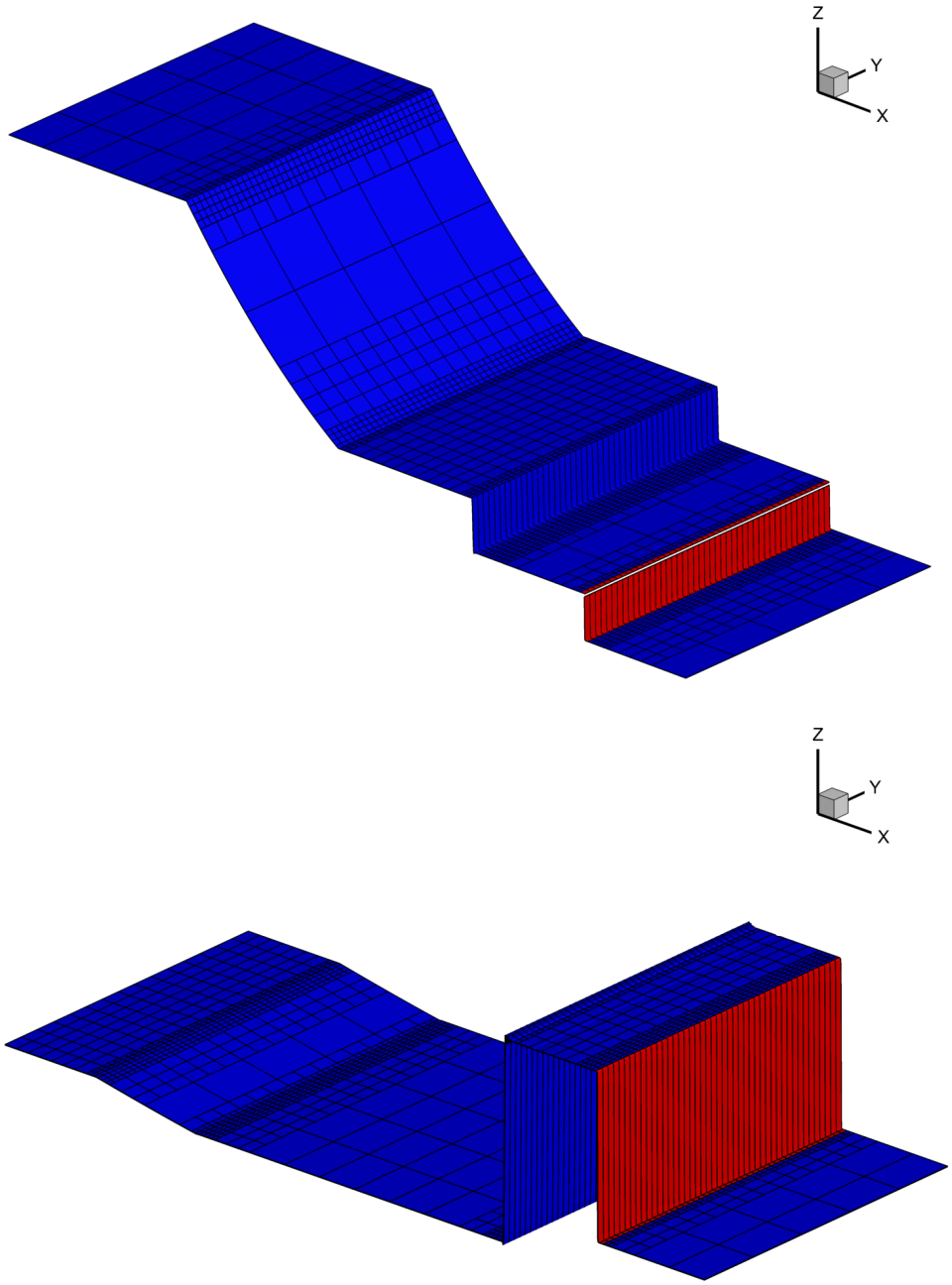

Figure 4: 3D view of the density variable and of the corresponding AMR grid. Top panel: Sod problem at $t_{final} = 0.2$. Bottom panel: Lax problem at $t_{final} = 0.14$. The limited cells, using the sub-cell ADER-WENO3 finite volume scheme, are highlighted in red, while unlimited DG-P_9 cells are highlighted in blue.

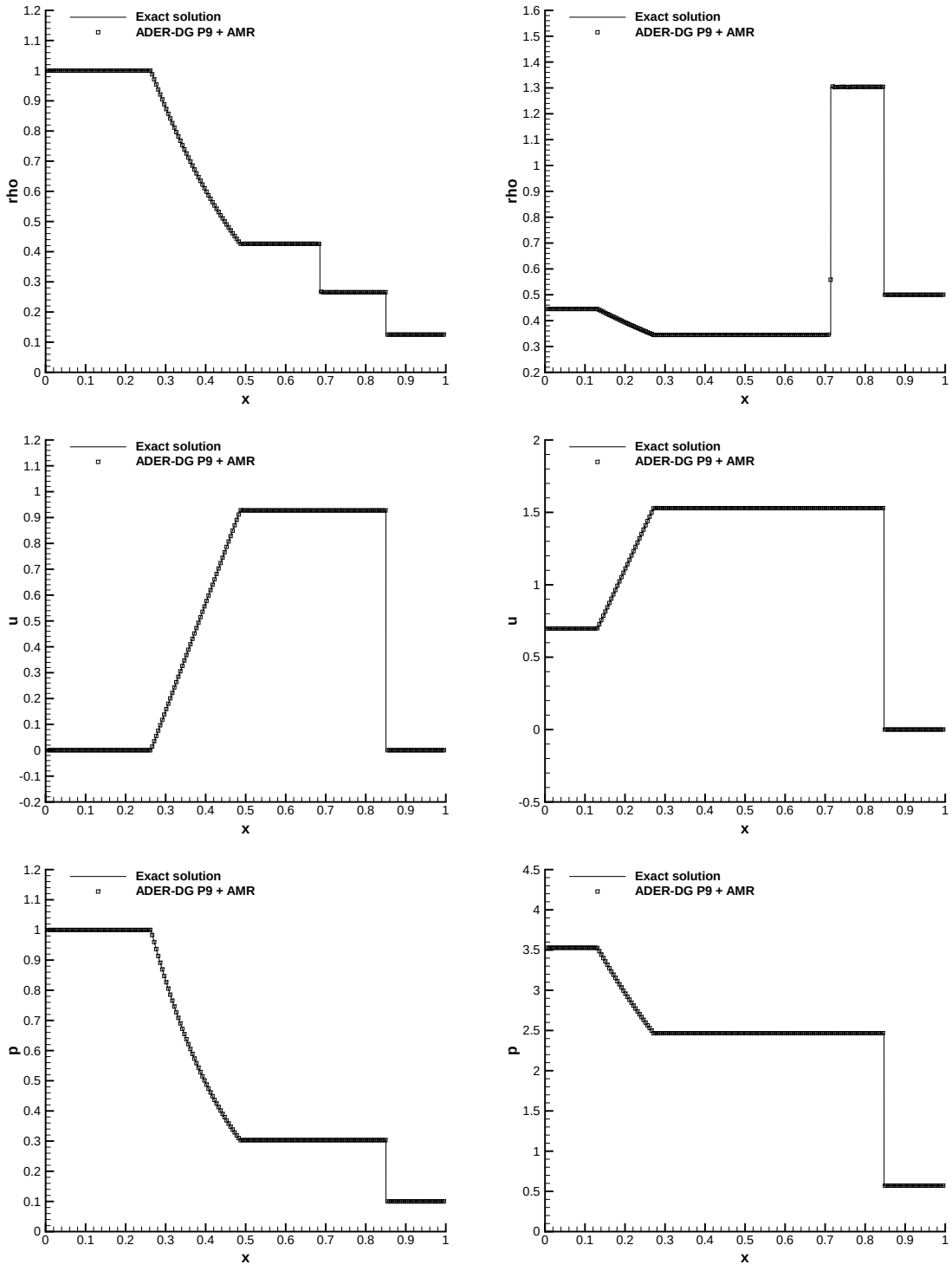

Figure 5: Sod shock tube problem (left panels) at $t_{final} = 0.2$ and Lax problem (right panels) at $t_{final} = 0.14$.

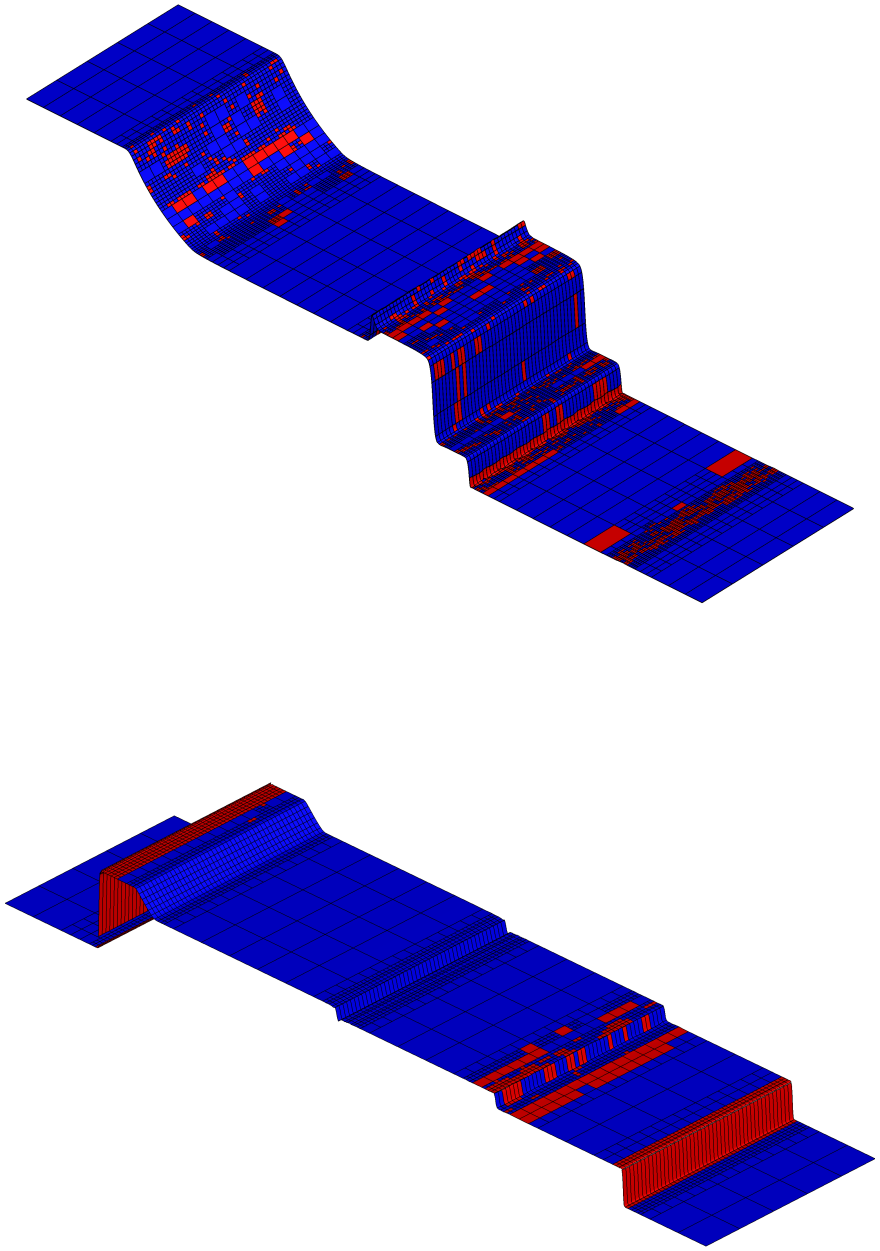

Figure 6: 3D view of the density variable and the corresponding AMR grid. Top panel: RP1 at $t_{final} = 0.4$ (coarsest grid of 40×5 elements). Bottom panel: RP2 at $t_{final} = 0.55$ (coarsest grid of 25×5 elements). The limited cells, using the sub-cell ADER-WENO3 finite volume scheme, are highlighted in red, while unlimited DG-P_3 cells are highlighted in blue.

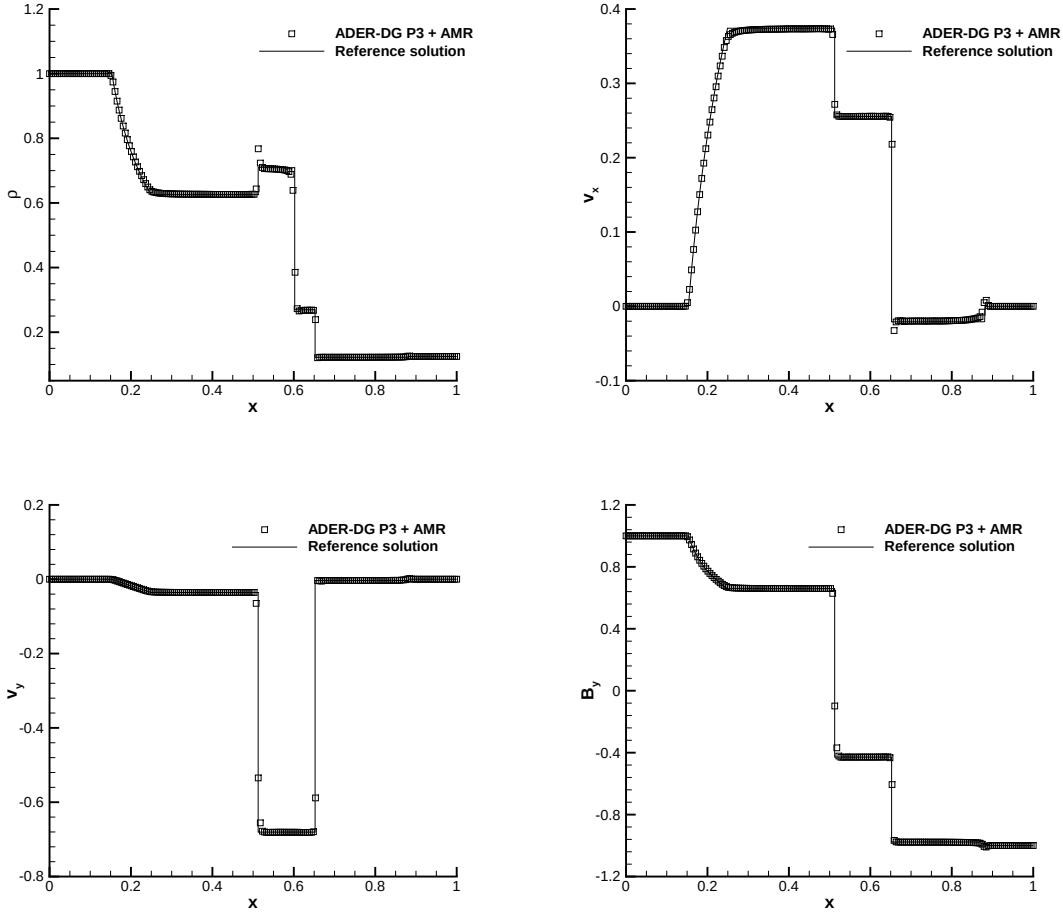

Figure 7: RP1: physical variables interpolated along a 1D cut on 200 equidistant points at $t_{final} = 0.4$, starting from a coarsest grid of 40×5 elements by using the ADER-DG-P_3 scheme supplemented with the *a posteriori* ADER-TVD sub-cell limiter.

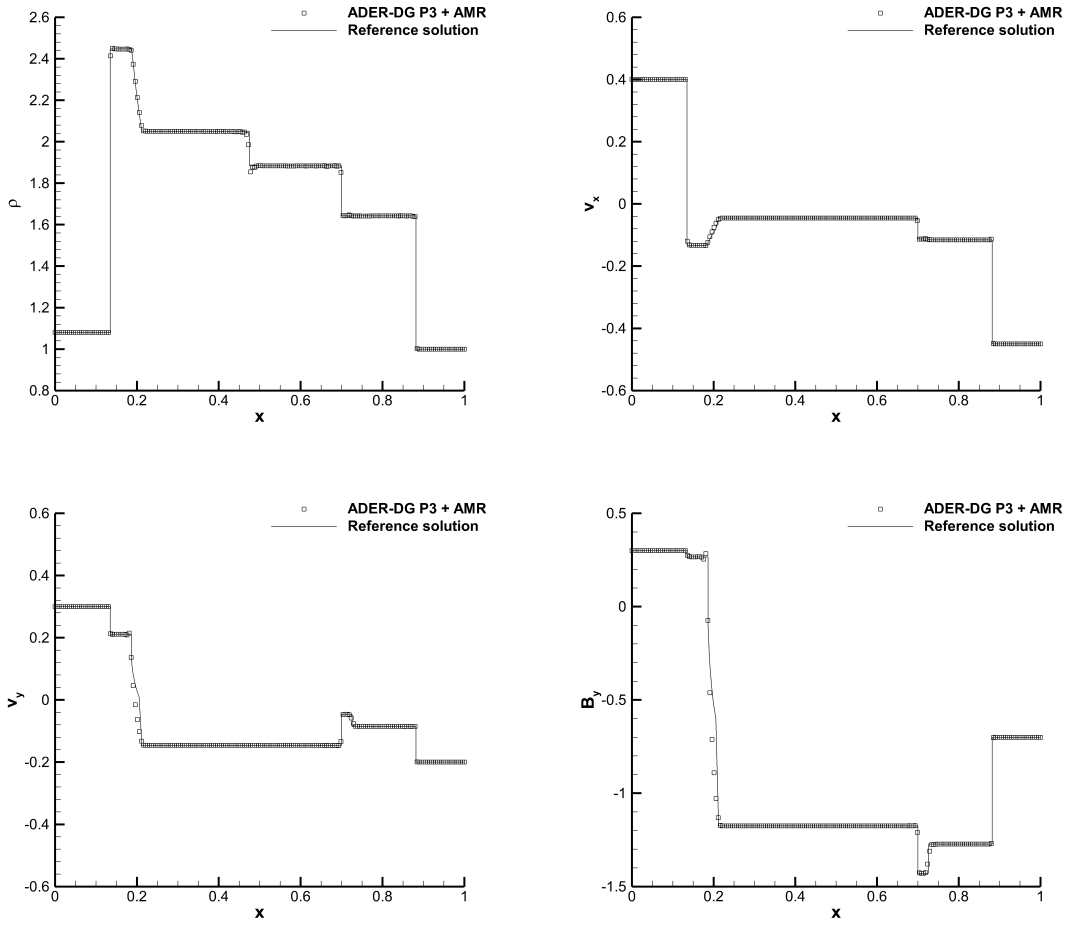

Figure 8: RP2: physical variables interpolated along a 1D cut on 200 equidistant points at $t_{final} = 0.55$, starting from a coarsest grid of 25×5 elements by using the ADER-DG-P_3 scheme supplemented with the *a posteriori* ADER-WENO3 sub-cell limiter.

in red) for the limited cells. A reference solution for these Riemann problems is computed with the exact Riemann solver proposed by [129]. Figures 7 and 8 show the comparison with the reference solution by plotting the rest mass density, the $x-$ and the $y-$ velocity components and the $y-$ component of the magnetic field, interpolated over a one-dimensional cut composed of 200 equidistant points at the final state. A remarkable agreement between the numerical and the reference solution is obtained. All the waves are well captured, five for RP1 and seven for RP2. More specifically, RP1 has a left-going and a right-going fast rarefaction wave, a left-going compound wave, a central contact discontinuity, and a right-going slow shock. RP2 has instead a left-going and a right-going fast shock, a left-going and a right going Alfén wave, a left-going rarefaction wave, a central contact discontinuity and a right-going slow shock. Due to the combined action of the sub-cell-limiter and of AMR, all discontinuities are resolved within just one cell or two cells at most. We note that, while the compound wave is absent by construction in the exact solution, its width in the numerical solution is rather small and its amplitude is also comparatively smaller with respect to that obtained with other numerical schemes, indicating that this might really be a numerical artifact. However, see also the discussion in [206].

The small asymmetries visible in figure 6 for RP1 along the passive y direction are attributable to the joint interaction between: (1) the lack of reconstruction in characteristic variables, which could typically help in these cases; (2) some residual *post-shock* oscillations, that in [13] were suppressed by means of artificial viscosity. In spite of these small defects, these results show the capabilities of the new scheme, which does not resort to any artificial viscosity, in resolving the strongly non-linear waves of SR-MHD equations, for which an unlimited DG schemes would catastrophically fail.

4.3 TWO-DIMENSIONAL TESTS

4.3.1 *Double Mach reflection problem (Euler)*

A complex test problem in two space dimensions which contains a variety of waves such as strong shock waves, contact waves and shear waves, we have considered the so called *double Mach reflection problem*, which was first proposed in [273]. The initial conditions are given by a right-moving shock wave with a Mach number $M = 10$, which intersects the $x-$ axis at $x = 1/6$ with an inclination angle of $\alpha = 60°$. In order to provide the physical states ahead and behind the shock, it is necessary to solve the Rankine–Hugoniot conditions, which provide

$$(\rho, u, v, p)(\mathbf{x}, t = 0) = \begin{cases} \frac{1}{\gamma}(8.0, 8.25\gamma, 0.0, 116.5), & \text{if} \quad x' < 0.1, \\ (1.0, 0.0, 0.0, \frac{1}{\gamma}), & \text{if} \quad x' \geqslant 0.1, \end{cases} \tag{4.10}$$

where $x' = (x - 1/6)\cos\alpha - y\sin\alpha$ is the coordinate in the rotated frame, while $\gamma = 1.4$. The boundary conditions on the left side and on the right side are just given by inflow and outflow, while on the bottom we have used reflecting boundary conditions. On the other hand, the boundary conditions on the top require

some more attention, since we need to impose the exact solution of an isolated moving oblique shock wave with the same shock Mach number $M_s = 10$. The computational domain is given by $\Omega = [0; 3.0] \times [0; 1]$, which is covered by an initial uniform grid composed of 75×25 cells. For our simulations, the Rusanov flux has been used and AMR is activated with $\ell_{max} = 2$ and $r = 3$. The results of our calculations at time $t = 0.2$ are reported in figures 9-11, for which we have used three different schemes: ADER-DG-P_N with $N = 2, 5, 8$. In all these figures we have zoomed into the interaction zone with $1.8 \leqslant x \leqslant 2.8$ in order to highlight the differences among the orders of accuracy. Moreover, the bottom right panel in each of these figures refers to a configuration with a finer initial grid, composed of 150×50 cells. Figure 9, in particular, shows the contour lines of the density. Figure 10 shows the AMR grid and the troubled cells, highlighted in red, which required the activation of the limiter. Finally, figure 11 reports the Schlieren images of the density. There are a number of comments that can be made about these results. First, and mostly obvious, all DG schemes can detect the shock waves very well. On the other hand, by increasing the order of accuracy, the vortex-type flow structures manifest a larger and richer rolling-up, especially in the transition from ADER-DG-P_2 to ADER-DG-P_5. Second, the largest number of troubled cells, including false-positive troubled cells, is present for the lowest order scheme, i.e. the ADER-DG-P_2, and it is concentrated along the shocks, while leaving the vortex-type flow structures unaffected. This is reassuring, since it indicates that higher order DG schemes have *better sub-cell resolution* capabilities. Last but not least we would like to note that the vortices generated by the rolling of the shear waves create *sound waves*, which travel through the computational domain. Although these simulations do not contain physical viscosity, and as such the vortex generation and rolling is only controlled by numerical viscosity, we can deduce from our numerical results that the novel scheme is able to resolve shock waves properly, as well as shear waves, vortex structures and sound waves.

4.3.2 *Forward facing step (Euler)*

The forward facing step problem is a classical test, often referred to as the *Mach 3 wind tunnel test*, which was proposed for the first time in [273]. We take as computational domain $\Omega = [0; 3] \times [0; 1] \backslash [0.6; 3] \times [0; 0.2]$. The initial conditions are given by a uniform flow moving to the right with Mach number $M = 3$, $\rho = 1$, $p = 1/\gamma$, $u = 3$, $v = 0$, and adiabatic index $\gamma = 1.4$. The final time of simulation is $t = 4.0$. Regarding the boundary conditions, we have used reflecting boundaries at the lower and upper parts of the numerical domain, while inflow boundary conditions are imposed at the entrance and outflow boundary conditions at the exit. Figure 12 represents the numerical solution obtained using the ADER-DG-P_5 scheme with *a posteriori* ADER-WENO3 sub-cell limiter. The panel on the top is a 2D view of the AMR grid showing, as usual, in red the limited cells and in blue the unlimited ones. The bottom panel, on the other hand, is a contour plot with 41 equidistant density contour levels in the interval $[0.1; 4.5]$. The mesh at the coarsest level has 150×50 cells, which is subsequently refined using AMR

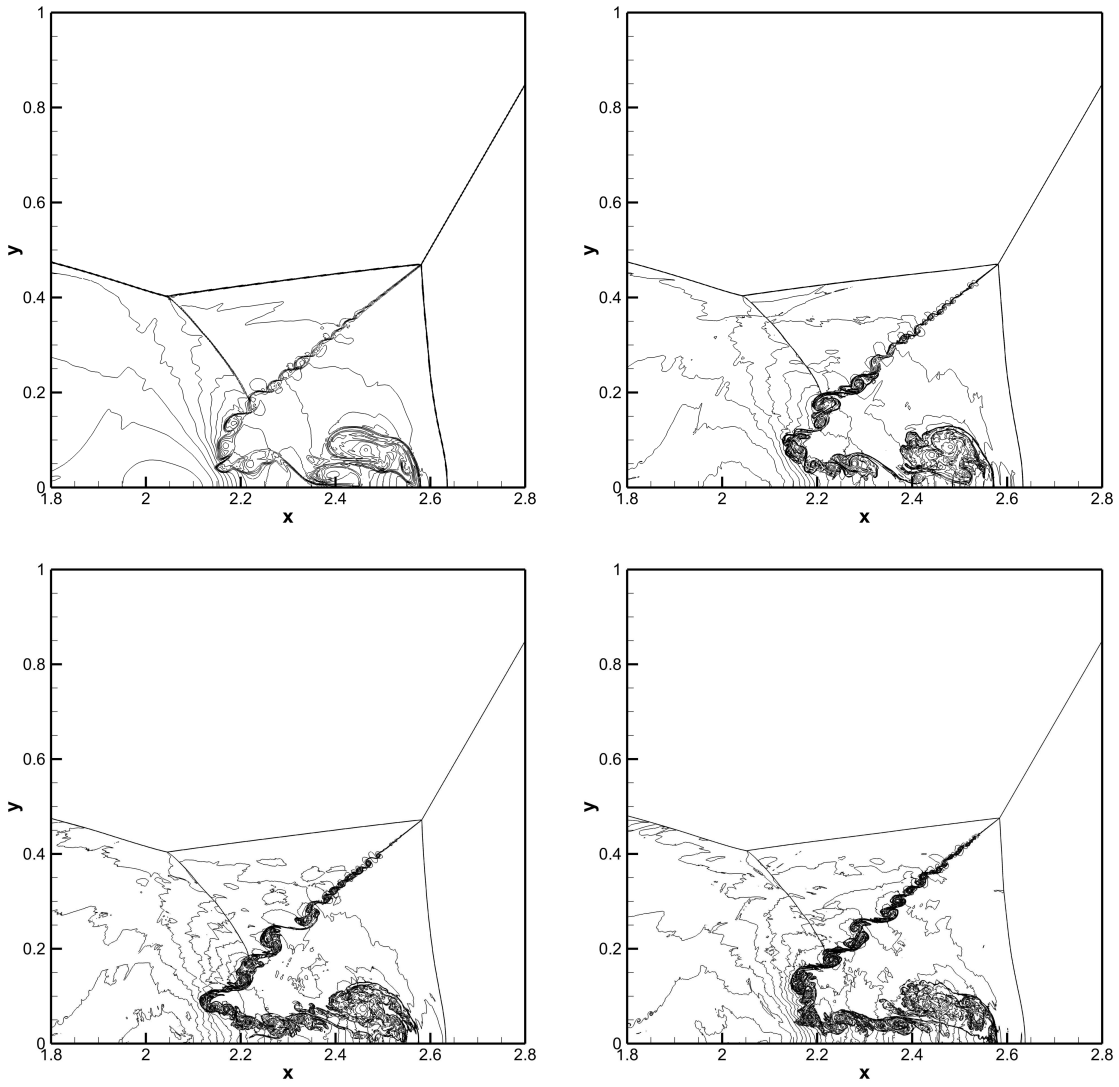

Figure 9: Zooms of the interaction zone for the double Mach reflection problem at t = 0.2. Equidistant contour lines of the density variable are shown. Top left: AMR-ADER-DG-P_2 with initial 75×25 grid. Top right: AMR-ADER-DG-P_5 with initial 75×25 grid. Bottom left: AMR-ADER-DG-P_8 with initial 75×25 grid. Bottom right: AMR-ADER-DG-P_5 with initial 150×50 grid.

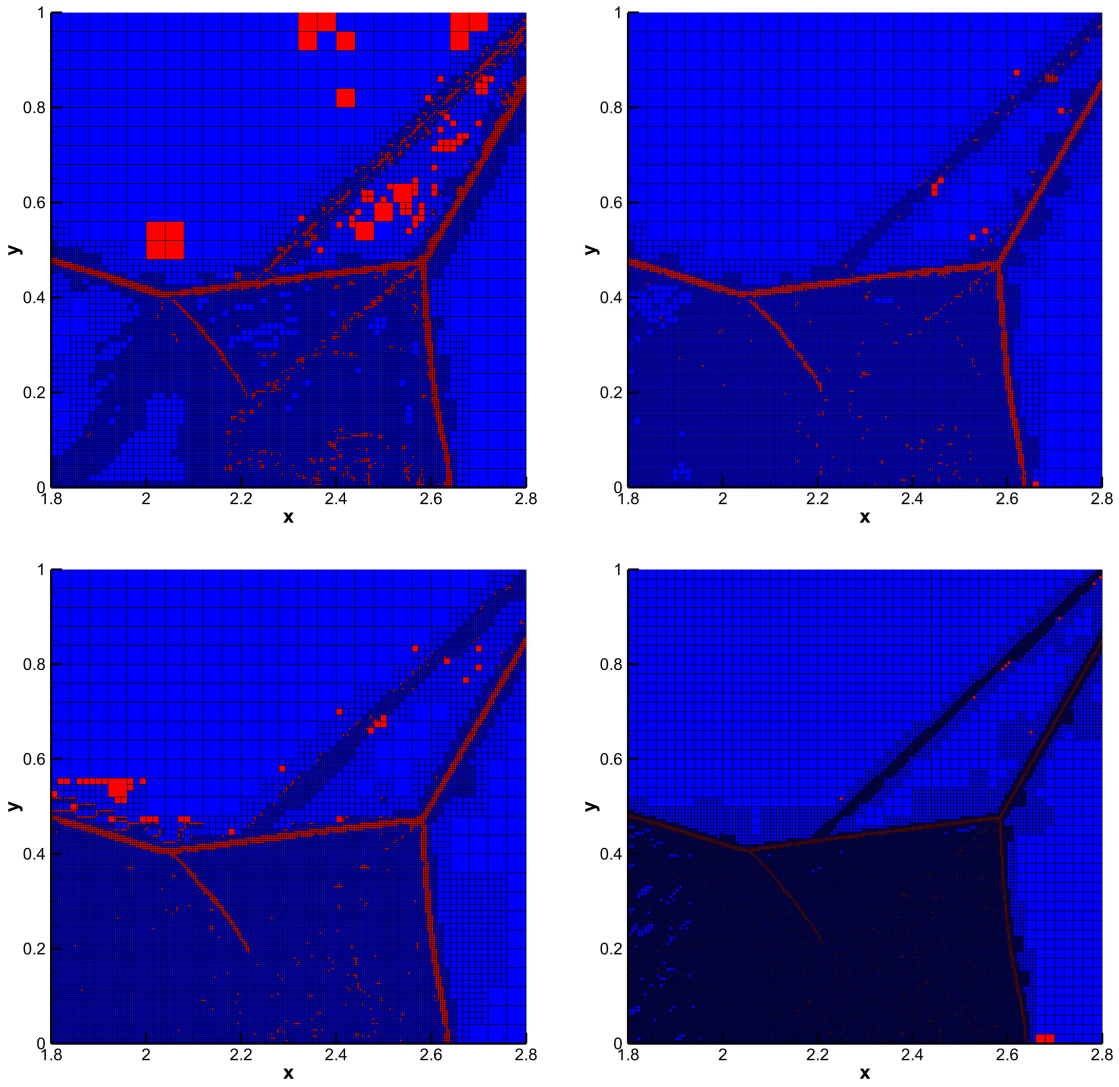

Figure 10: Zooms of the interaction zone for the double Mach reflection problem at $t = 0.2$. The AMR grid and the limited cells (highlighted in red) are shown. Top left: ADER-DG-P_2 with initial 75×25 grid. Top right: ADER-DG-P_5 with initial 75×25 grid. Bottom left: ADER-DG-P_8 with initial 75×25 grid. Bottom right: ADER-DG-P_5 with initial 150×50 grid.

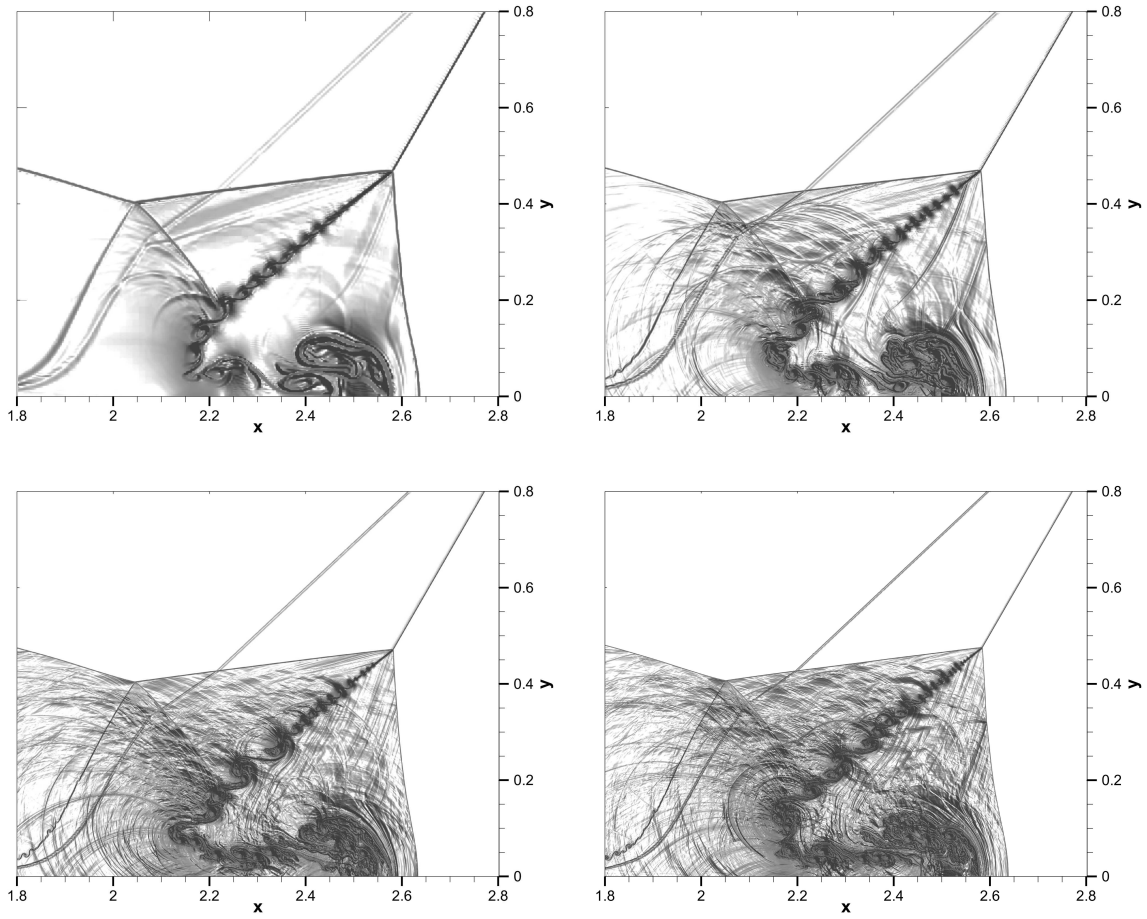

Figure 11: Schlieren image of the density variable for the double Mach reflection problem at $t = 0.2$. Top left: ADER-DG-P_2 with initial 75×25 grid. Top right: ADER-DG-P_5 with initial 75×25 grid. Bottom left: ADER-DG-P_8 with initial 75×25 grid. Bottom right: ADER-DG-P_5 with initial 150×50 grid.

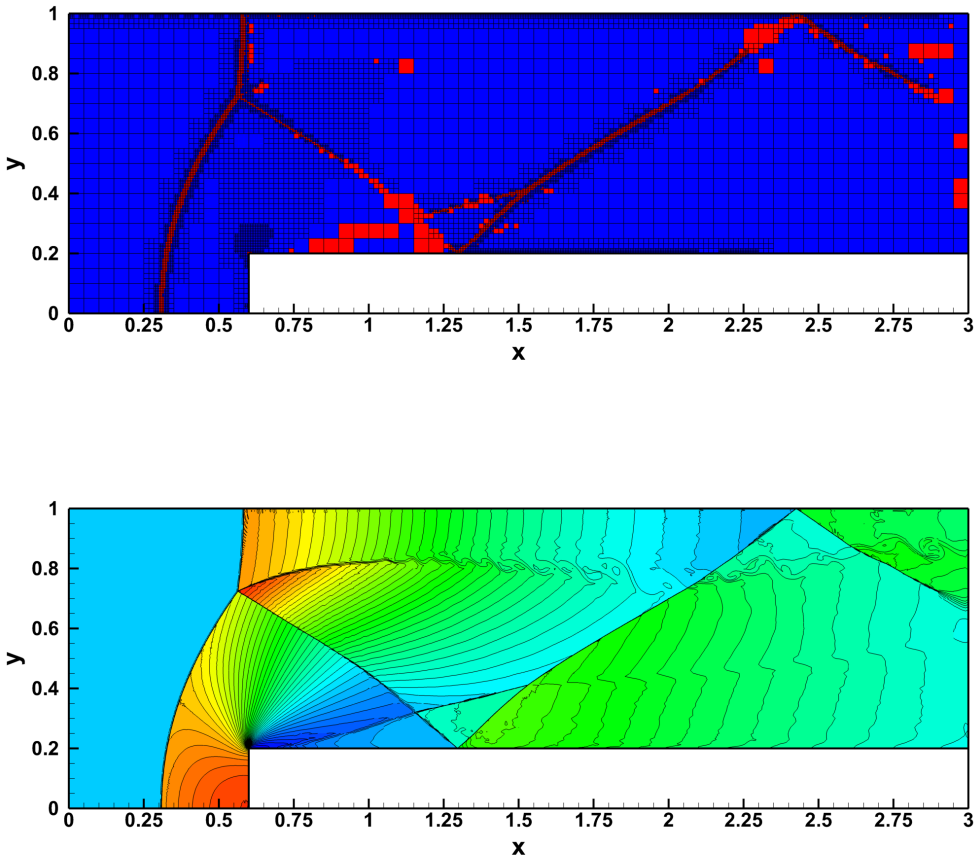

Figure 12: Forward facing step problem using ADER-DG-P_5 with *a posteriori* ADER-WENO3 sub-cell limiter. Top: 2D view of the AMR grid together with limited cells (red) and unlimited cells (blue). Bottom: 41 equidistant density contour levels in the interval $[0.1; 4.5]$.

parameters $\ell_{max} = 2$ and $r = 4$, corresponding to a uniform grid composed of 2400×800 cells. It can be appreciated that there is a very good resolution of the physical instability and also it can be observed that both AMR and sub-cell limiter act where they are needed.

4.3.3 *2D Riemann problems (Euler)*

The two dimensional Riemann problems first proposed in [178] have become a classic benchmark for any numerical scheme solving the Euler equations. The

		ρ	u	v	p	ρ	u	v	p	t_{final}
		$x \leqslant 0$				$x > 0$				
RP1	$y > 0$	0.5323	1.206	0.0	0.3	1.5	0.0	0.0	1.5	0.25
(Case 3 in KT)	$y \leqslant 0$	0.138	1.206	1.206	0.029	0.5323	0.0	1.206	0.3	
RP2	$y > 0$	0.5065	0.8939	0.0	0.35	1.1	0.0	0.0	1.1	0.25
(Case 4 in KT)	$y \leqslant 0$	1.1	0.8939	0.8939	1.1	0.5065	0.0	0.8939	0.35	
RP3	$y > 0$	2.0	0.75	0.5	1.0	1.0	0.75	-0.5	1.0	0.30
(Case 6 in KT)	$y \leqslant 0$	1.0	-0.75	0.5	1.0	3.0	-0.75	-0.5	1.0	
RP4	$y > 0$	1.0	0.7276	0.0	1.0	0.5313	0.0	0.0	0.4	0.25
(Case 12 in KT)	$y \leqslant 0$	0.8	0.0	0.0	1.0	1.0	0.0	0.7276	1.0	

Table 4: Initial conditions for the two–dimensional Riemann problems. The "Case No. in KT" refers to the classification of [178].

initial conditions are represented by constant states in each of the four quadrants of the computational domain $\Omega = [-0.5; 0.5] \times [-0.5; 0.5]$, namely

$$\mathbf{u}(x, y, 0) = \begin{cases} \mathbf{u}_1 & \text{if} \quad x > 0 \wedge y > 0, \\ \mathbf{u}_2 & \text{if} \quad x \leqslant 0 \wedge y > 0, \\ \mathbf{u}_3 & \text{if} \quad x \leqslant 0 \wedge y \leqslant 0, \\ \mathbf{u}_4 & \text{if} \quad x > 0 \wedge y \leqslant 0\,. \end{cases} \tag{4.11}$$

The data of the four configurations that we have considered are reported in table 4. We emphasize that the adiabatic index is $\gamma = 1.4$ in all cases. The simulations have been performed over a level zero grid of 50×50 elements, adopting $\ell_{max} = 2$ and $r = 3$. On the other hand, the numerical scheme is the ADER-DG-P_5, with the Rusanov Riemann solver and reconstruction in characteristic variables. Figures 13-14 show the result of the simulations at the final time t_{final} for each model. The left panels report the isolines of the density, while the right panels show, as usual, the AMR mesh and the cells updated through the sub-cell limiter, which have been highlighted in red. Due to the unprecedented high order of accuracy adopted, which reduces drastically the numerical dissipation of the numerical scheme, several small-scale features appear in the solution, typically attributed to the Kelvin–Helmholtz instability but not visible in the original versions shown by [178]. A similar effect was already noticed by [109] for the test **RP3**, even in the absence of AMR. However, when adaptive mesh refinement is activated, the effects of the Kelvin–Helmholtz instability emerge clearly also in model **RP2** (along the diagonal of the cocoon structure), and in model **RP4** (along the boundary of the bottom-left quadrant). Moreover, we emphasize that the use of AMR makes the sub-cell limiter operate only along strong discontinuities, which are resolved within very few cells at the maximum level of refinement.

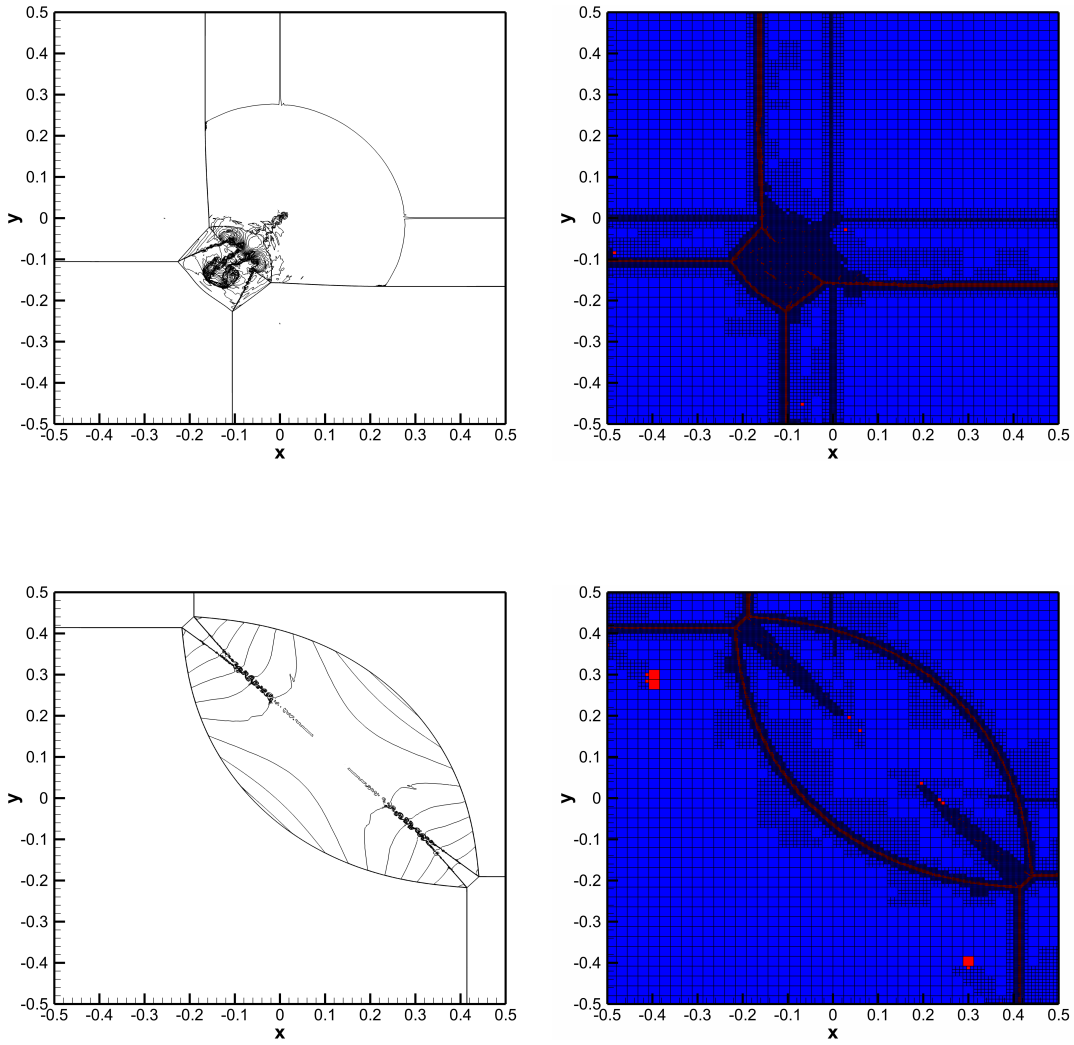

Figure 13: Two-dimensional Riemann problems solved with the AMR-ADER-DG-P_5 method with sub-cell limiter on an initial uniform grid with 50×50 cells. Two levels of refinement have been adopted, with refinement factor $\mathfrak{r} = 3$. Left panels: isolines of the density. Right panels: AMR grid (black), limited cells (red) and unlimited cells (blue). RP1 and RP2, from the top to the bottom.

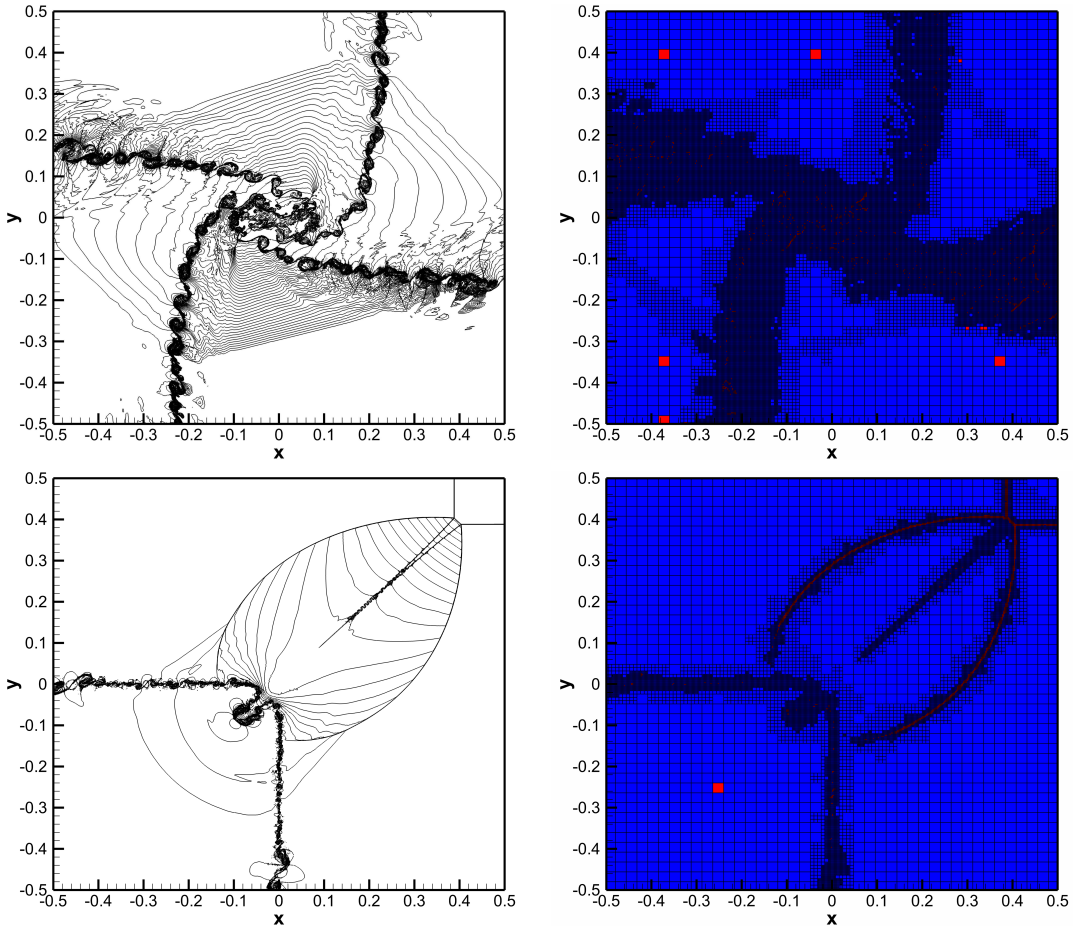

Figure 14: Two-dimensional Riemann problems solved with the AMR-ADER-DG-P_5 method with sub-cell limiter on an initial uniform grid with 50×50 cells. Two levels of refinement have been adopted, with refinement factor $r = 3$. Left panels: isolines of the density. Right panels: AMR grid (black), limited cells (red) and unlimited cells (blue). RP3 and RP4, from the top to the bottom.

4.3.4 *Cylindrical explosion problem (Euler)*

In multiple space dimensions, a conceptually simple but interesting extension of the one-dimensional Riemann problem is represented by the cylindrical and by the spherical explosion problem, both of them described with great detail in [258] and [262]. These two tests are indeed relevant, since they involve the propagation of a shock wave that is not aligned with the coordinates, and they can therefore be used to check the ability of the numerical scheme in preserving the physical symmetries of the problem. The basics of the problem is depicted here next to the two dimensional results. The three-dimensional results are given in next section. As initial conditions, we assume the flow variables to be constant for $r \leqslant R$ and for $r \geqslant R$, namely

$$(\rho, \mathbf{v}, p) = \begin{cases} (1, 0, 0, 0, 1) & \text{for} \quad r \leqslant R, \\ (0.125, 0, 0, 0, 0.1) & \text{for} \quad r > R, \end{cases} \tag{4.12}$$

where $r = \sqrt{\mathbf{x}^2}$ is the radial coordinate, $\mathbf{x}$ is the vector of spatial coordinates, while $R = 0.5$ denotes the radius of the initial discontinuity. The computational domain is $\Omega = [-1; 1]^d$, whereas the adiabatic index of the ideal-gas equation of state has been set to $\gamma = 1.4$. As suggested by [262], a reference solution can be computed after solving an equivalent one dimensional problem in the radial direction r, in which the additional geometric terms arising from the choice of curvilinear coordinates can be moved to the right hand side of the governing PDEs as source terms.

We have solved the two-dimensional, cylindrical, explosion problem with the ADER-DG-P_9 scheme in combination with our usual *a posteriori* sub-cell WENO finite volume limiter, the Osher-type flux of [100] and the reconstruction in characteristic variables. On the level zero grid, the mesh consists of 50×50 elements, which are then refined using a refinement factor of $r = 3$ and $\ell_{max} = 2$. This leads to an equivalent resolution on a uniform fine grid of $450 \times 450 = 202,500$ elements. Considering that each P9 element uses 10 degrees of freedom per space dimension, this corresponds to a total resolution of $20,250,000$ spatial degrees of freedom on a uniform fine grid. Figure 15 shows a 3D plot of the density distribution obtained for the cylindrical explosion case, as well as the AMR grid configuration at the final time $t = 0.20$. Moreover, a 2D view of the AMR grid together with 1D cuts through the numerical solution on 150 equidistant sample points along the x-axis are depicted in figure 16. For comparison, figure 16 also contains the 1D reference solution as well as the numerical solution obtained with the ADER-DG-P_9 scheme on the uniform fine grid. First of all, we observe that the numerical results coincide perfectly well with the reference solution. Second, one can note that the uniform fine grid solution as well as the result obtained with AMR are essentially identical.

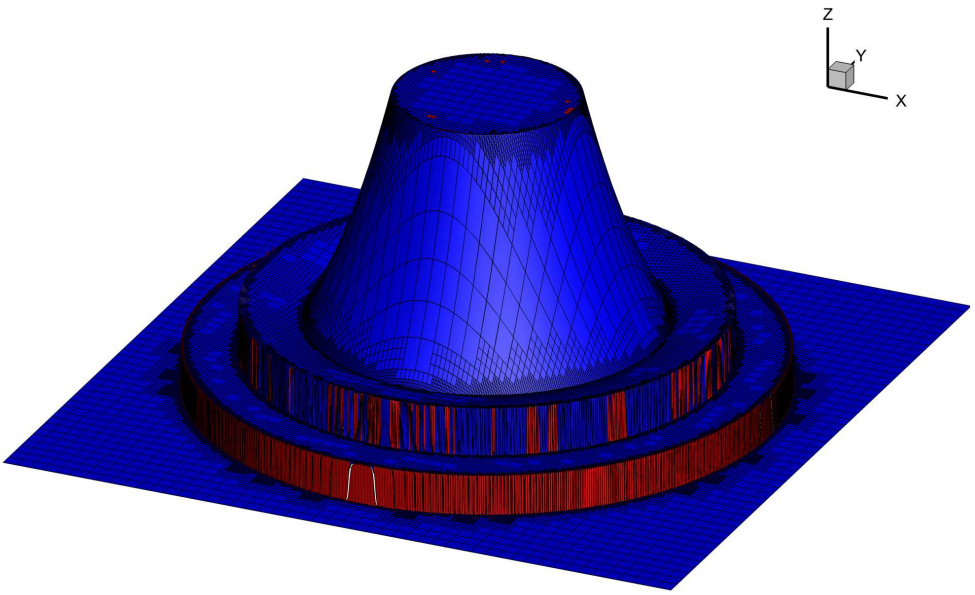

Figure 15: Three-dimensional view of the density variable and the AMR grid for the two dimensional explosion problem at $t_{final} = 0.20$. Limited cells (red) updated with the sub-cell ADER-WENO3 finite volume scheme and unlimited cells (blue) with the ADER-DG-P_9 scheme. The level zero AMR grid uses 50×50 elements.

4.3.5 *Lid-driven cavity flow at low Mach number – M=0.1 (CNS)*

The so-called lid-driven cavity flow became a standard benchmark problem for testing numerical methods for the incompressible Navier-Stokes equations, see [127]. In this two dimensional test a *nearly* incompressible flow is considered. In a *closed* square cavity the fluid-flow is driven by the moving upper-wall with tangential velocity $u = 1$. No-slip boundary conditions are applied at the remaining three walls. The spatial domain $\Omega = [-1, 1] \times [-1, 1]$ has been discretized into 10×10 space-elements for the coarsest mesh at level zero; the AMR-framework has been activated accordingly to a refine factor $r = 3$ and $\ell_{max} = 2$, the associated maximally refined mesh-level, and the magnitude of the velocity as estimator-function for the mesh adaptation. We compare the numerical solution obtained with our ADER-DG-P_3 supplemented with the *a posteriori* WENO3 SCL for the compressible Navier-Stokes equations in the low-Mach regime ($M = 0.1$) with the reference solution of [127] in figure 17. A very good agreement between computed and reference solution has been obtained, despite the compressibility of the simulated fluid-flow and the non-trivial singularities at the upper corners. Notice that the limiter has been needed only next to the flow singularities at the upper corners where, in fact, the solution is a double valued function, i.e. $u = 0$ at the side walls and $u = 1$ at the moving upper lid.

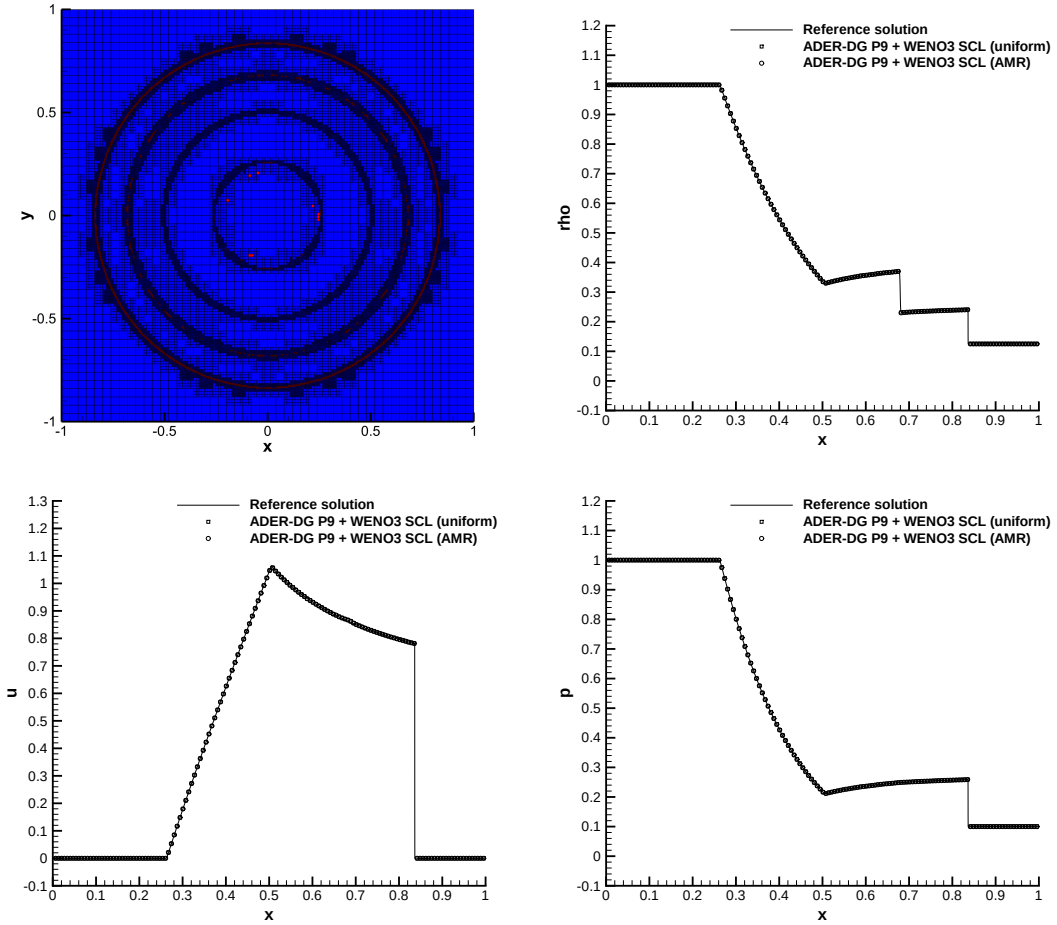

Figure 16: Two-dimensional explosion problem. 2D view of the AMR grid together with limited and unlimited cells (top left). One dimensional cuts of the numerical solution for density ρ (top right), velocity u (bottom left) and fluid pressure p (bottom right) on 150 equidistant sample points along the positive $x-$axis obtained at $t_{\text{final}} = 0.20$ with the space-time adaptive ADER-DG-P_9 scheme, supplemented with *a posteriori* ADER-WENO3 sub-cell limiter. For comparison, the solution computed on a uniform fine mesh corresponding to the finest AMR grid level and the 1D reference solution are also reported.

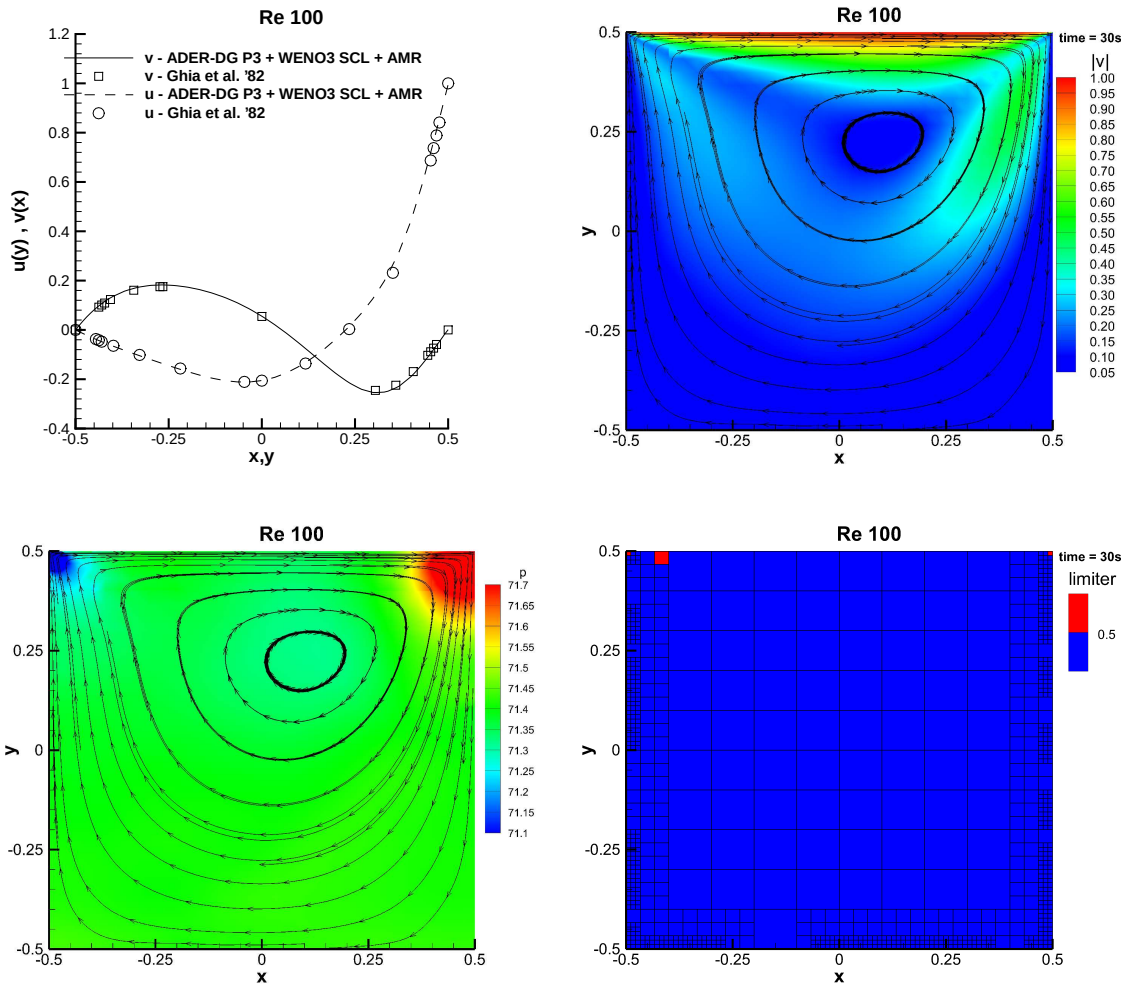

Figure 17: The numerical solution obtained for the two dimensional lid-driven cavity problem compared with the numerical results of [127] at different Reynolds $Re = 100$, obtained with our ADER-DG-P_3 method using 10x10 elements at the coarsest level, up to $\ell_{max} = 2$ maximum number of refinement levels with a refine factor $r = 3$. In the first two rows, from left to right, from the top to the bottom the data-comparison, the magnitude of the velocity field with streamlines, the pressure and the limiter status have been plotted.

4.3.6 *Compressible 2D mixing layer (CNS)*

In this test, originally proposed in [78] and then extended to three space dimensions in the work of [11] and then reproposed also in [125, 95, 111], the high order of accuracy of our ADER-DG scheme and the judiciousness of the implementation of the SCL are tested. A well known unsteady physical instability is generated along a compressible two dimensional mixing layer, between the parallel motion of two streams. The upper stream flows at velocity $u_\infty = 0.5$, the lower one at $u_{-\infty} = 0.25$ corresponding to a velocity ratio $\lambda = u_\infty/u_{-\infty} = 2$; pressure and density are initialized as $\rho = \rho_0 = 1$ and $p = p_0 = 1/\gamma$ with a ratio of specific heats $\gamma = 1.4$. The singularity at $y = 0$ has been smoothed by means of a very simple hyperbolic tangent function

$$u = \frac{1}{8}\left(\tanh(2y) + 3\right). \tag{4.13}$$

The lengths are made dimensionless with respect to the vorticity thickness at the inflow, given by

$$\delta_{\omega_z}(x_0) = \frac{u_\infty - u_{-\infty}}{\max(\frac{\partial u}{\partial y}|_{x_0})} := 1, \tag{4.14}$$

which allows to define the corresponding Reynolds number

$$Re = \frac{\rho_0 u_\infty \delta_{\omega_z}(x_0)}{\mu}. \tag{4.15}$$

From a rigorous linear stability analysis of the inviscid Rayleigh equations, a proper oscillatory forcing term can be introduced at the inflow in order to facilitate the instability to arise. More details about the resolution of the inviscid Rayleigh but also the viscous Orr-Sommerfeld equations are available in the work of [78] and [11]. Here, the following very simple perturbation has been introduced at the left boundary

$$\delta(y,t) = A(y)\left[\cos(\omega_0 t) + \cos(\omega_1 t + \phi_1) + \cos(\omega_2 t + \phi_2) + \cos(\omega_3 t + \phi_3)\right] \tag{4.16}$$

where: $\omega_0 = -2\pi f_0 = -0.3147876$ is the fundamental angular frequency ($f_0 \approx 0.0501$); $\omega_1 = \omega_0/2$, $\omega_2 = \omega_0/4$ and $\omega_3 = \omega_0/8$ are the corresponding first three subharmonics; $\phi_1 = -0.028$, $\phi_2 = 0.141$ and $\phi_3 = 0.391$ are the chosen phase-shift of the subharmonic with respect to the fundamental perturbation that allow to minimize the distance of the vortex pairing, according to [78]; $A(y)$ is an amplitude factor ($A << 1$) that can be chosen in the form of a Gaussian distribution centered in the origin of the physical instability, i.e.

$$A(y) = \tilde{A} e^{-y^2/4}, \qquad \tilde{A} = -10^{-3}. \tag{4.17}$$

The spatial domain is $\Omega = [-50, 50] \times [0, 400]$, discretized by only 20×40 elements at the coarsest grid level, with a refinement factor $r = 3$ and up to $\ell_{max} = 2$

maximum number of refinement levels. An ADER-DG-P_5 scheme is employed, supplemented by a third order ADER-WENO finite volume sub-cell limiter. Figure 18 shows the numerical results for the density variable and the AMR grid by choosing a dynamic viscosity of $\mu_1 = 10^{-3}$, corresponding to a Reynolds number of $Re_1 = 500$.The obtained results are directly comparable with the results available in the papers of [78, 11, 125, 95, 111] with a good agreement. Figure 18 shows the obtained results for the density and vorticity variables, and the AMR grid colored by the limiter-status (limited cells are highlighted in red, unlimited cells are plotted in blue). The first vortex pairing occurs at around $x_{p'} \sim 190$. We notice that the SCL has never been activated during the simulation and this is because the physics of the fluid flow has been well-resolved and no spurious oscillations are generated. This is a very important result and we would like to stress at this point that the presented sub-cell limiting procedure does *not* dissipate the real physical instabilities, but only the numerical ones, preserving the original resolution of high order unlimited DG scheme for smooth flows. Finally, figure 19 shows the comparison of the time series of the horizontal velocity evaluated at $y = 0$ at different axial positions. These plots give a better idea on the time-scales of the development of the instability; they seem to be well compatible with literature results (see [78, 95]).

4.3.7 *Shock-vortex interaction (CNS)*

An interesting two dimensional problem for testing the AMR framework dealing with shocks and smooth waves together is the so called *shock-vortex interaction* test. In this problem a smooth vortex hits a stationary normal shock wave, representing an optimal scenario for testing high order shock capturing schemes. The spatial domain is $\Omega = [0, 2] \times [0, 1]$ with periodic boundary conditions in the vertical direction, analytical boundary conditions at the left boundary and a classical outflow boundary condition at the right. The vortex is centered at $(x_V, y_V) = (0.25, 0.5)$ and its strength is characterized by a Mach number of $M_V = v_m/c_0 = 0.7$, $c_0 = \sqrt{\gamma p_0/\rho_0}$ being the adiabatic sound speed upstream the shock, with $p_0 = 1$ and $\rho_0 = 1$. The angular velocity ω_V is distributed according to

$$\omega_V = \begin{cases} \omega_m \frac{r}{a} & \text{for} \quad r \leqslant a\,, \\ \omega_m \frac{a}{a^2-b^2}\left(r - \frac{b^2}{r}\right) & \text{for} \quad a \leqslant r \leqslant b\,, \\ 0 & \text{otherwise}\,, \end{cases} \tag{4.18}$$

where $r^2 = (x - x_V)^2 + (y - y_V)^2$. Pressure and density are evaluated according to the equations

$$p = p_0 \left(\frac{T}{T_0}\right)^{\frac{\gamma}{\gamma-1}}, \qquad \rho = \rho_0 \left(\frac{T}{T_0}\right)^{\frac{1}{\gamma-1}}. \tag{4.19}$$

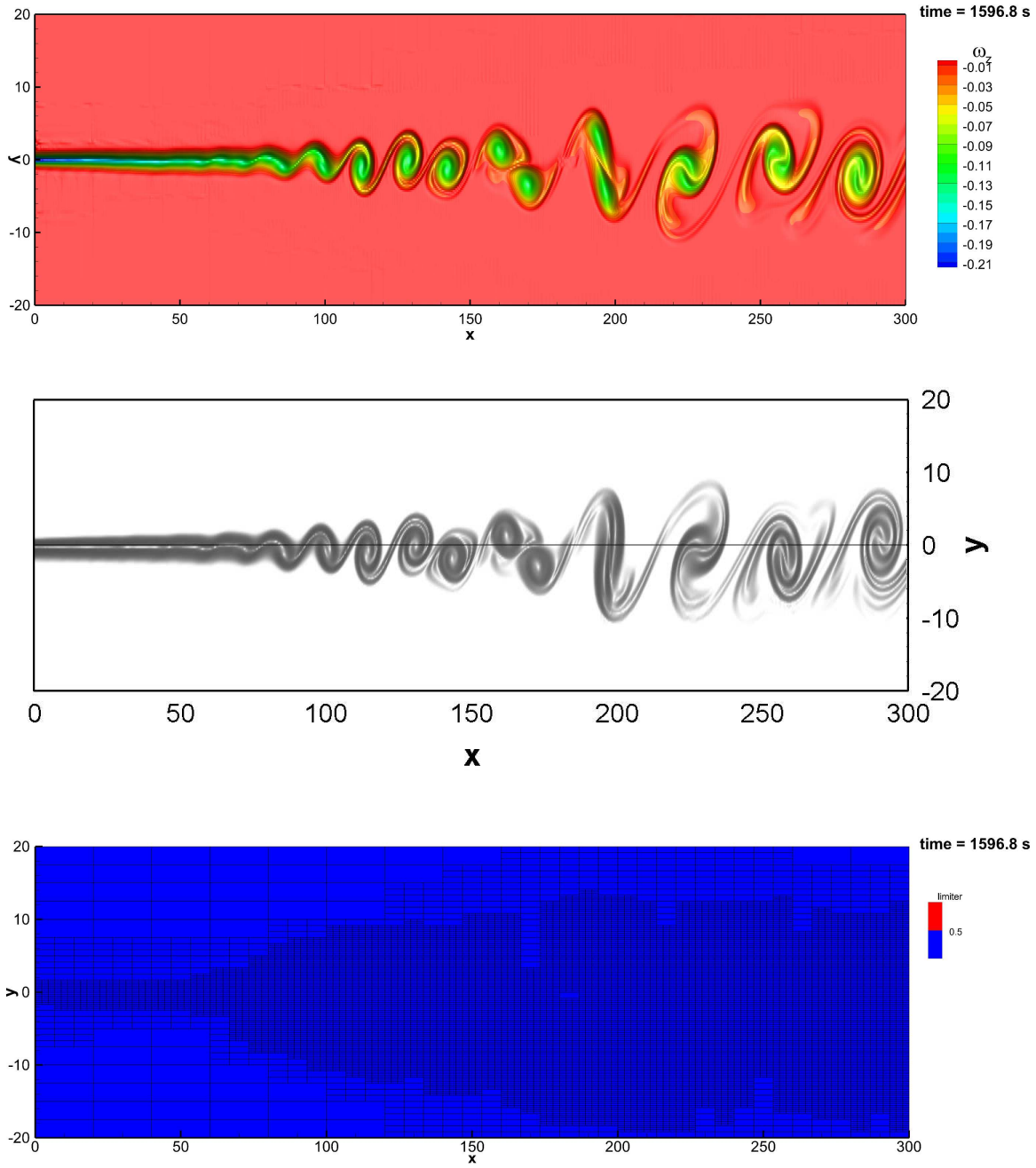

Figure 18: Vorticity field (top row) and AMR grid (bottom row) ω_z obtained with the ADER-DG-P_5 scheme supplemented with the *a posteriori* ADER-WENO SCL for the compressible mixing layer test for $\mu = 10^{-3}$ at $t = 68\,T_f = 1596.8$s with $T_f = 1/f_0$, where f_0 is the fundamental frequency of the mixing layer. Up to $\ell_{max} = 2$ maximum number of refinement levels with a refine factor $r = 3$ are used. The limiter is never active. A reference solution [95] for the vorticity field obtained with a high order P_3P_5 scheme using a locally refined unstructured triangular grid is provided for comparison (middle row).

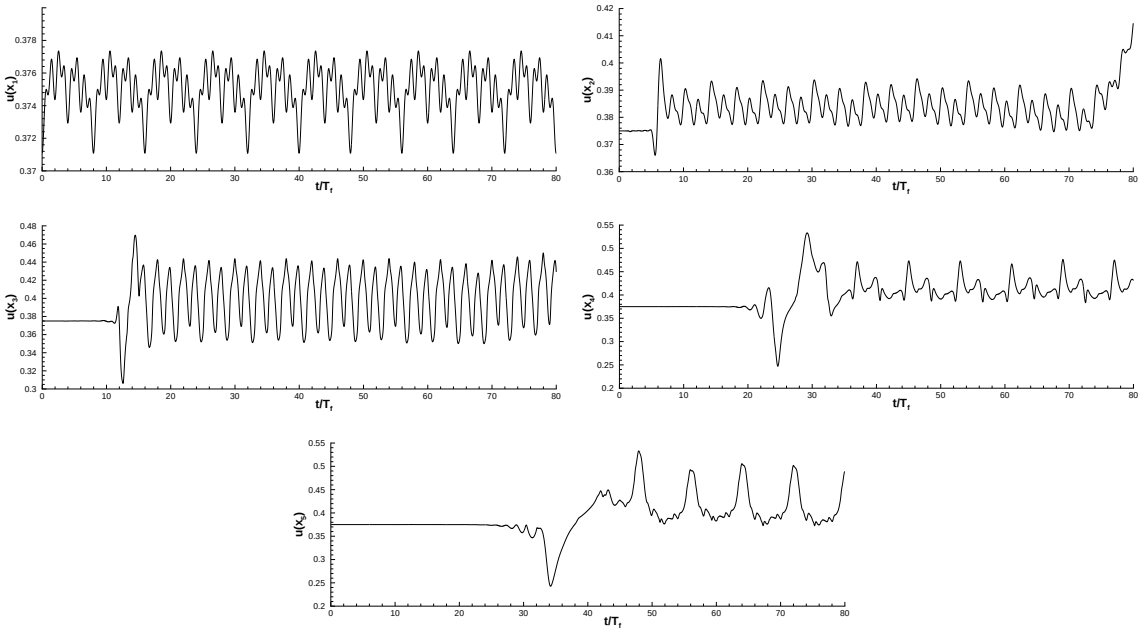

Figure 19: History of the horizontal velocity component evaluated at $y = 0$, along five different axial positions $x_1 = 0$, $x_2 = 45$, $x_3 = 100$, $x_4 = 200$ and $x_5 = 285$ (from left to right, from the top to the bottom) for the compressible mixing layer test at $\mu = 10^{-3}$.

after solving the ordinary differential equation for the temperature

$$\frac{dT}{dr} = \frac{\gamma - 1}{R\gamma} \frac{\omega_V^2(r)}{r} . \tag{4.20}$$

The unperturbed upstream variables are chosen in compliance with the equation of state of ideal gases $p_0 = R\rho_0 T_0$ where the the gas constant is $R = 1$. The remaining parameters are chosen to be $\gamma = 1.4$, $a = 0.0075$ and $b = 0.175$ and the Prandtl number of $Pr = 0.7$. Finally, the stationary shock with Mach number $M_S = 1.5$ is placed at $x = 0.5$ and the downstream variables are computed according to the classical Rankine-Hugoniot conditions [181]. The current test has been solved with the P_5 version of our ADER-DG method, supplemented only by a second order accurate shock capturing TVD finite volume scheme on the sub-grid, based on reconstruction in primitive variables. Figure 20 shows the computed results for the density variable and the AMR grid colored by the limiter status for $\mu = 10^{-8}$ (limited cells are highlighted in red, unlimited cells are plotted in blue). The obtained results are in agreement with the results available in literature [109, 103, 233]. Moreover, figure 21 shows the computed results obtained by choosing a viscosity of $\mu = 10^{-3}$. The effect of higher physical viscosity is evident, since the final solution is much smoother because of the presence of viscous effects and heat conduction. We observe that the SCL is never activated (although the entire MOOD framework is switched on in this test problem!), since for sufficiently resolved viscous flows, the use of a limiter becomes unnecessary.

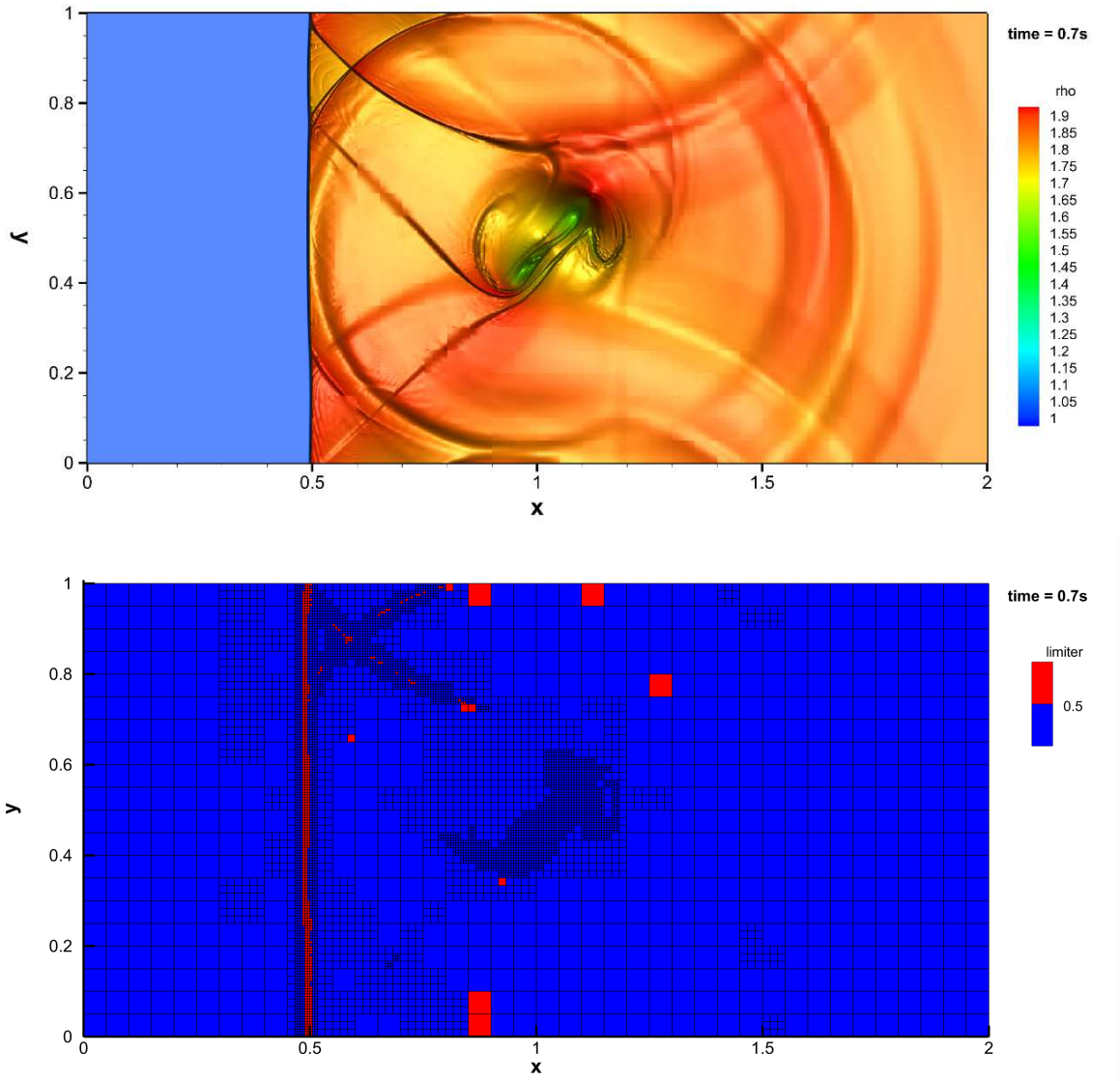

Figure 20: Density (top) and AMR grid colored by the limiter status (bottom) obtained with our ADER-DG-P_5 supplemented with the *a posteriori* TVD SCL in *primitive variables* for the shock-vortex interaction test at $t = 0.7$s. Up to $\ell_{max} = 2$ maximum number of refinement levels with a refine factor $r = 3$ are used. The kinematic viscosity is $\nu = 10^{-8}$.

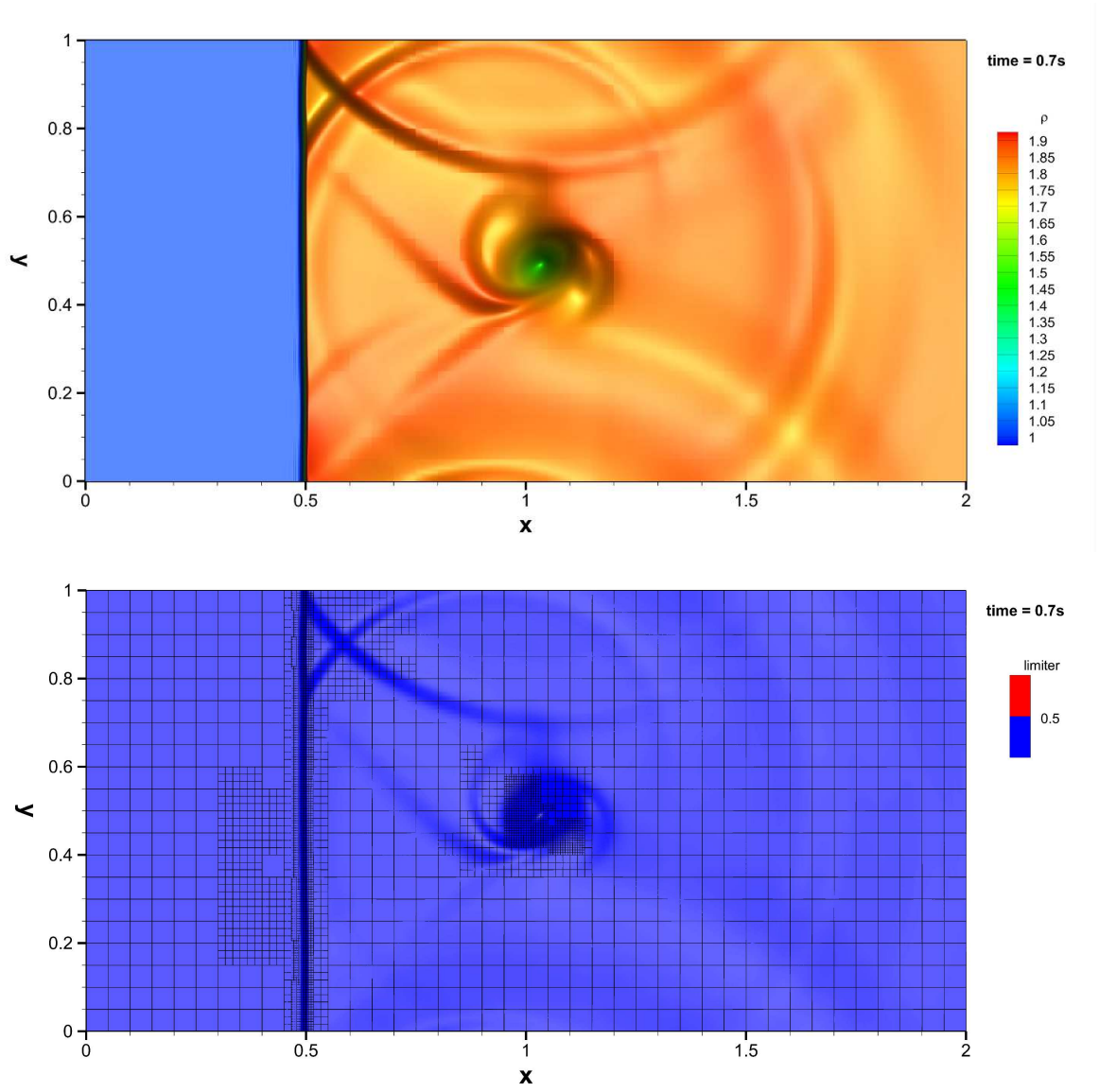

Figure 21: Density (top), and limiter status (bottom) obtained with our ADER-DG-P_5 supplemented with the *a posteriori* SCL for the shock-vortex interaction test at $t = 0.7s$. Up to $\ell_{max} = 2$ maximum number of refinement levels with a refine factor $r = 3$ are used. The kinematic viscosity is $\nu = 10^{-3}$.

4.3.8 *Viscous double Mach reflection problem (CNS)*

Originally proposed by Woodward and Colella in [272] for the inviscid case, see also section 4.3.1, here we solve a *viscous* version of the two dimensional double Mach reflection problem at very high Mach number ($M_S = 10$). In this test, a planar shock wave hits a rigid wall at an angle of incidence of $\alpha_S = 60°$. The shock wave reflection, the viscous wall boundary layer, but also the physical instabilities inside the front of incidence for high Reynolds numbers, make this scenario very intriguing for testing the ability of a high-order numerical scheme to capture all the flow physics, from the smaller and the larger vortex structures to the strong shock waves that appear at $M = 10$, (see [272, 95, 109, 281]). The 60°-inclined wavefront of the viscous shock-wave is initialized by imposing $x = 0$ as the initial point of incidence at the wall, and prescribing the classical Rankine-Hugoniot conditions of the compressible Euler equations at the shock interface with respect to the chosen downstream variables, having

$$(\rho_0, u_0', v_0', p_0) = \begin{cases} (8, 8.25\gamma, 0, 116.5)\,\frac{1}{\gamma} & \text{for } x' \text{ upstream} \\ (\gamma, 0, 0, 1)\,\frac{1}{\gamma} & \text{for } x' \text{ downstream} \end{cases}. \tag{4.21}$$

where the primed variables and coordinates u', v' and x' are evaluated with respect to the rotated coordinate system, x' being the streamwise direction. The Prandtl number is $Pr = 3/4$. The spatial domain is chosen to be $\Omega = [0,4] \times [0,1]$ with no-slip boundary condition at the bottom, outflow boundary condition at the right, and the aforementioned analytical solution of the moving incident shock-wave in the remaining left and top boundaries. For this test the ADER-DG-P_5 scheme has been used, together with a third order ADER-WENO finite volume scheme as sub-cell limiter (SCL). The coarsest mesh, the one of the $0-th$ refinement level, is made up of 80×20 elements upgraded by up to $\ell_{max} = 2$ maximum number of refinement levels with a refine factor $r = 3$. Then, the corresponding characteristic lengths h_ℓ of the three refinement levels are $h_0 = 1/20$, $h_1 = 1/60$ and $h_2 = 1/180$ and the *effective characteristic lengths* $\tilde{h}_\ell$ that take account of the d.o.f of the polynomial basis ($\tilde{h}_\ell = h_\ell/(N+1)$) are $\tilde{h}_0 = 1/120$, $\tilde{h}_1 = 1/360$ and $\tilde{h}_2 = 1/1080$. Figure 22 shows the numerical results for the density contour lines at time $t = 0.05$ and 0.2 for differed dynamic viscosity coefficients, i.e. $\mu_1 = 10^{-3}$ leading to the shock-Reynolds number $Re_1 = \rho_0 M_S/\mu_1 = 10^4$, $\mu_2 = 10^{-4}$ leading to $Re_2 = 10^5$ and the almost inviscid limit case $\mu_3 = 10^{-8}$. It is important to note that when the inviscid compressible Euler equations are solved, the present problem will develop smaller and smaller spatial scales in an unbounded manner, since there is no physical viscosity in the Euler equations that prevents the generation of small scale vortex structures. In the presence of physical viscosity, however, there exists a smallest spatial scale at which vortex structures dissipate energy into internal energy and below which no smaller spatial scales can exist.

The classical *'crow's feed'*-shaped (i.e. the right $3+1$ shock-wave-interfaces that are *incident* with respect to a central node) front-wave is well reproduced. It holds some interest noticing the differences of the distance between the central node and the location of the first vortex appearance along the central slip line, which

is affected by a Kelvin-Helmholtz instability at higher Reynolds numbers. Then, the same numerical simulation has been repeated by applying reflective (inviscid) slip-wall boundary conditions at the bottom, instead of the classical no-slip wall-boundary conditions. Figure 23 shows the numerical solution for the density contour lines obtained at time $t = 0.2$. Notice that the no-slip boundary conditions at the bottom wall lead to a completely different flow pattern compared to the usual slip wall boundaries used for the simulation of inviscid flows: the development of the well known 'mushroom'-type shape of the the purely reflective slip-wall case is prevented because of the thin boundary layer at the wall, leading to $\partial u/\partial y \neq 0$ at $y = 0$. The complete AMR grids colored by the limiter status are depicted in figure 24 for the considered Reynolds number regimes and boundary conditions. One can notice that the AMR method worked properly, following the main shock waves and resolving also the vortexes generated by the Kelvin-Helmholtz instability along the slip line. Moreover, also the SCL ADER-WENO3 is essentially activated only when and where it is necessary, i.e. only next to the stronger shocks (see red cells in figure 24 allowing the ADER-DG P_5-polynomials to represent the numerical solution in the smoother zones and throughout the non-linear instabilities. Notice that only a minor number of *'false-positive'* limited cells have been detected for this test-problem.

It should be emphasized that there are not many reference results published in the literature concerning the *viscous* double Mach reflection problem. In the case of high Reynolds numbers and inviscid slip wall boundary conditions, our obtained results seem to be in good agreement with the results present in the literature [272, 95, 109, 281, 111].

4.3.9 *MHD rotor problem (MHD)*

In the following, we consider two nontrivial well-known problems of classical ideal MHD, by adopting the ADER-DG-P_5 scheme, supplemented with our *a posteriori* WENO3 sub-cell limiter, with the Rusanov Riemann solver.

Our first test is the MHD rotor problem sketched in [17]. The computational domain is $\Omega = [-0.6, 0.6] \times [-0.6, 0.6]$, with an initial mesh on the coarsest level composed of 50×50 elements. The AMR framework is activated with $r = 4$ and $\ell_{max} = 2$. In this problem a high density fluid is rotating rapidly with angular velocity ω, embedded in a low density fluid at rest. More specifically, the initial conditions are given by

$$\rho = \begin{cases} 10 & \text{for } 0 \leqslant r \leqslant 0.1; \\ 1 & \text{otherwise;} \end{cases}, \qquad \omega = \begin{cases} 10 & \text{for } 0 \leqslant r \leqslant 0.1; \\ 0 & \text{otherwise;} \end{cases}, \tag{4.22}$$

$$\mathbf{B} = \begin{pmatrix} 2.5, & 0, & 0, \end{pmatrix}^T, \qquad p = 1. \tag{4.23}$$

Torsional Alfvén waves are generated by the spinning rotor and launched into the ambient medium. As a consequence, the angular momentum of the rotor is diminishing. In order to validate the accuracy of the method, the AMR computation

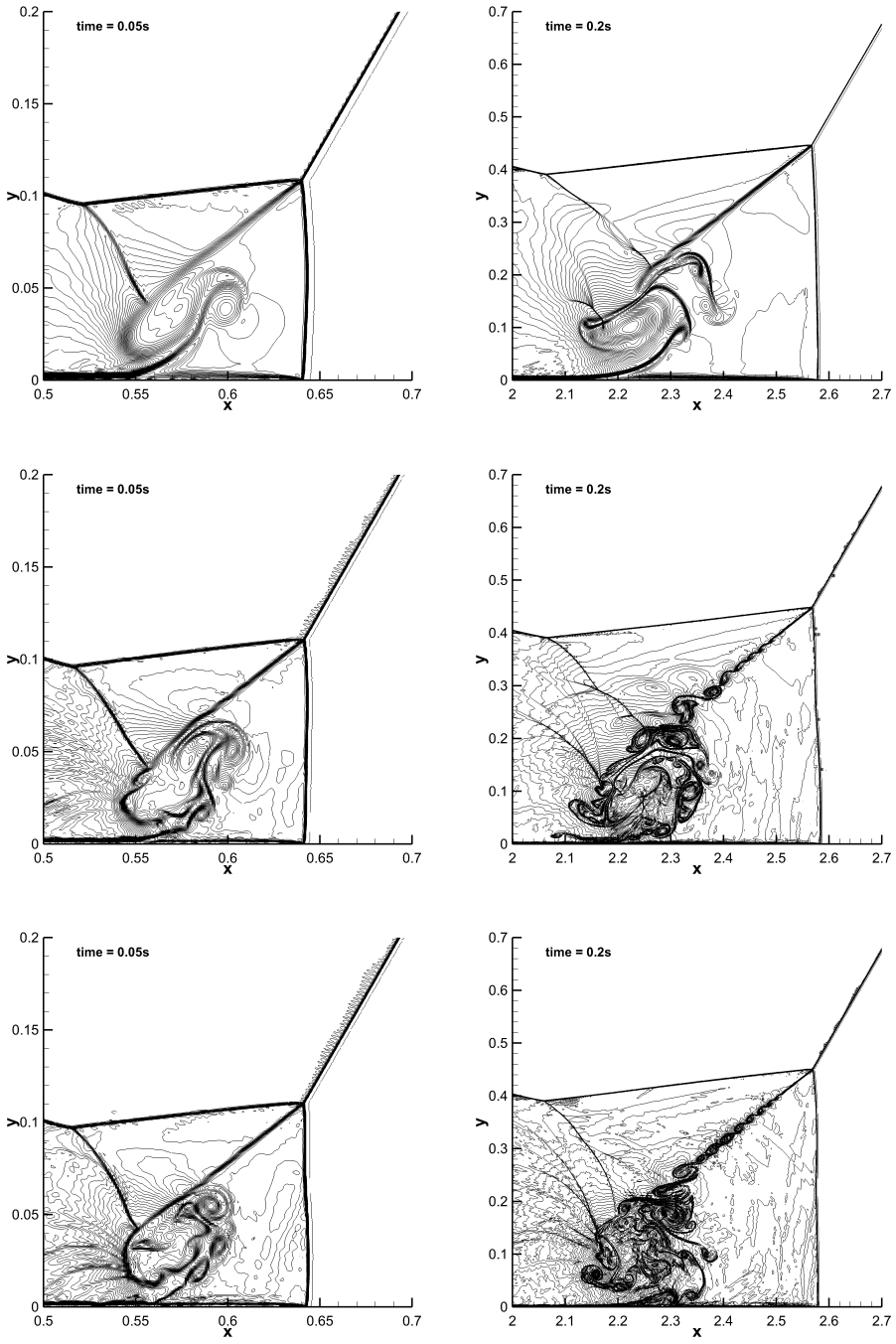

Figure 22: Contour lines of the density for the viscous double Mach reflection test for viscosity $\mu = 10^{-3}$, 10^{-4} and the inviscid limit 10^{-8}, from top to bottom, at different times $t = 0.05$ (left) and 0.20 (right), obtained with ADER-DG-P_5 and *a posteriori* SCL WENO3.

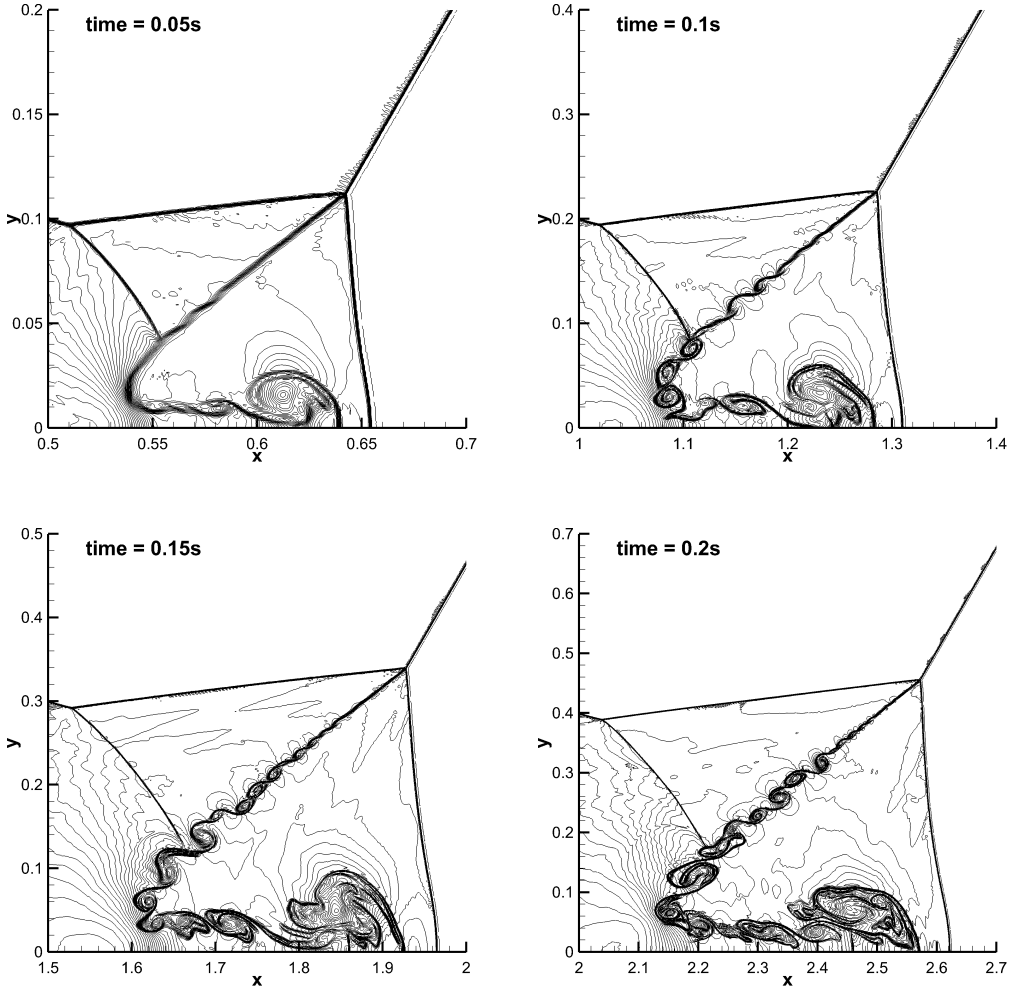

Figure 23: Contour lines of the density for the viscous double Mach reflection test **with purely reflective wall boundary conditions** for viscosity 10^{-4} at different times $t = 0.05, 0.10, 0.15$ and 0.20, from top left to bottom right, obtained with ADER-DG-P_5 and *a posteriori* SCL WENO3.

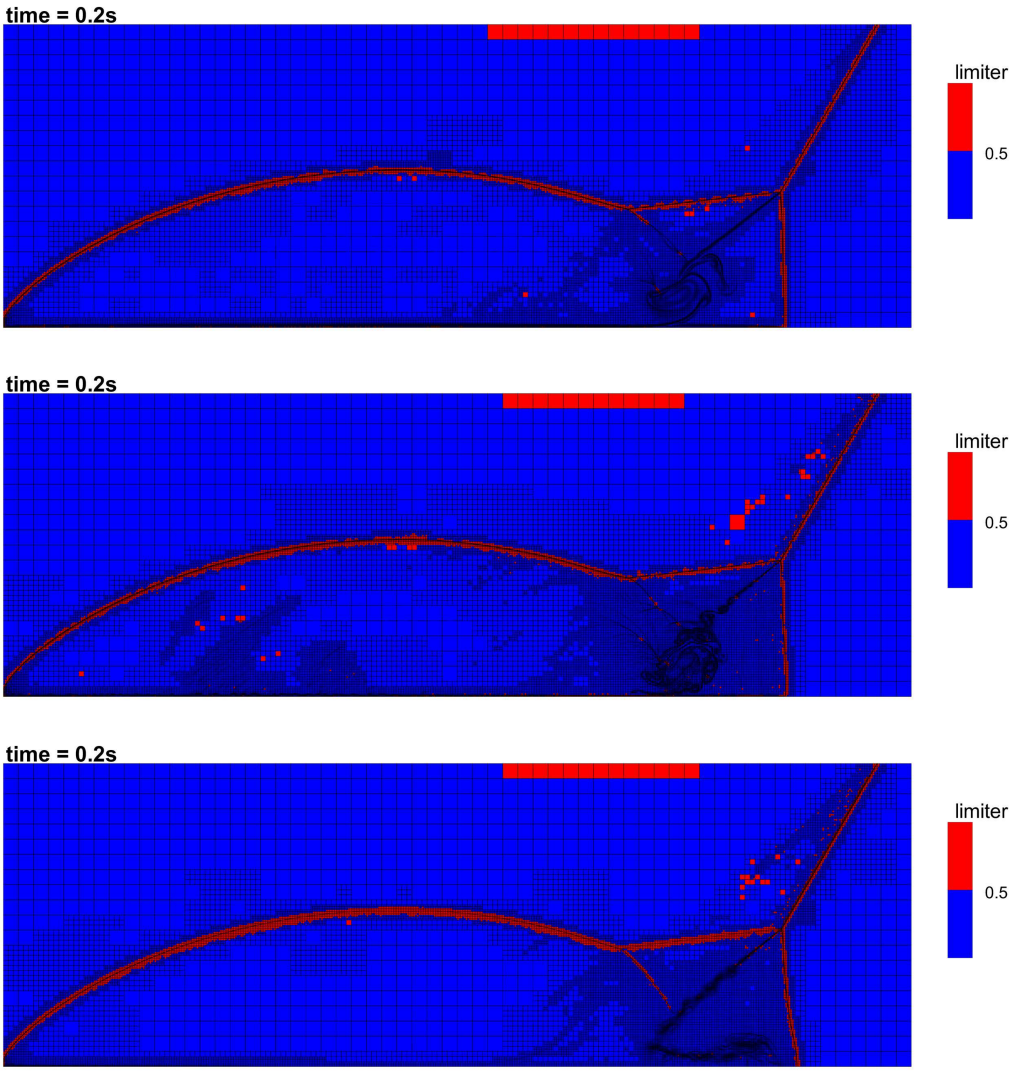

Figure 24: Plot of the AMR grid for ADER-DG-P_5 polynomials (blue) and the ADER-WENO3 *sub-cell* averages, i.e. the limited cells (red), for the viscous double Mach reflection test at the final time $t = 0.2$ obtained by choosing $\mu = 10^{-3}$ and no-slip walls (top), $\mu = 10^{-4}$ and no-slip walls (center) and $\mu = 10^{-4}$ with slip walls (bottom).

is compared with the maximally refined uniform grid composed of $800 \times 800 = 640,000$ elements, corresponding to a total resolution of $4800 \times 4800 = 23,040,000$ spatial degrees of freedom on the uniform grid for the augmented MHD equations. Transmissive boundary conditions are applied at the borders. Following [17], a linear taper is applied in the range $0.1 \leqslant r \leqslant 0.105$ to allow continuity of the physical variables between the internal rotor and the fluid at rest at $r = 0.105$. The divergence cleaning velocity is set equal to $c_h = 4$, while the adiabatic index is $\gamma = 1.4$.

Figures 25-26 shows the solution for density, pressure, Mach number and magnetic pressure fields at time $t = 0.25$. An excellent agreement between the AMR computation (reported in the left panels) and the uniform grid computation (reported in the right panels) is observed. Moreover, the numerical results are in very good agreement both with [17], and with the results of the ADER-WENO scheme with space-time adaptive mesh refinement presented in [107]. We would like to stress that spurious oscillations are absent in the density and the magnetic pressure fields, because of the adopted divergence cleaning procedure. In fact, without divergence cleaning, Godunov's schemes would suffer of unphysical oscillations as reported by [17]. Finally, figure 27 shows the AMR mesh in the left panel and in the right panel the troubled zones in red, for which activation of the sub-cell limiter became necessary.

4.3.10 *Orszag-Tang vortex system (MHD)*

The second test that we have considered concerns the well known Orszag-Tang vortex problem, presented in [218], and later investigated by [223] and [81]. The adopted parameters refer to the computation performed by [158]. Because of the chosen normalization of the magnetic field, our initial conditions are

$$(\rho, \boldsymbol{v}, p, \mathbf{B}) = \left(\gamma^2, -\sin(y), \sin(x), 0, \gamma, -\sqrt{4\pi}\sin(y), \sqrt{4\pi}\sin(2x), 0\right), \quad (4.24)$$

where $\gamma = 5/3$. The computational domain $\Omega = [0, 2\pi] \times [0, 2\pi]$ is discretized with 30×30 elements on the coarsest refinement level at $t = 0$. Periodic boundary conditions are applied along each edge. By using $r = 3$ and $\ell_{max} = 2$, the associated maximally refined uniform grid is formed of $270 \times 270 = 72,000$ elements, that correspond to a total resolution of $2,624,400$ spatial degrees of freedom. The resulting solution for density, pressure, Mach number and magnetic pressure is plotted at times $t = 0.5, 2.0, 3.0, 5.0$ in figure 28, both for the AMR and for the uniform grid. The AMR results appear to be in very good agreement with the reference solution represented by the calculation over the uniform grid. Moreover, our computations are in agreement with the the fifth order WENO finite difference results presented by [158], with the solution of [105] obtained with an unstructured third order WENO scheme, and also with the ADER-WENO solution computed with space-time adaptive mesh refinement in [107].

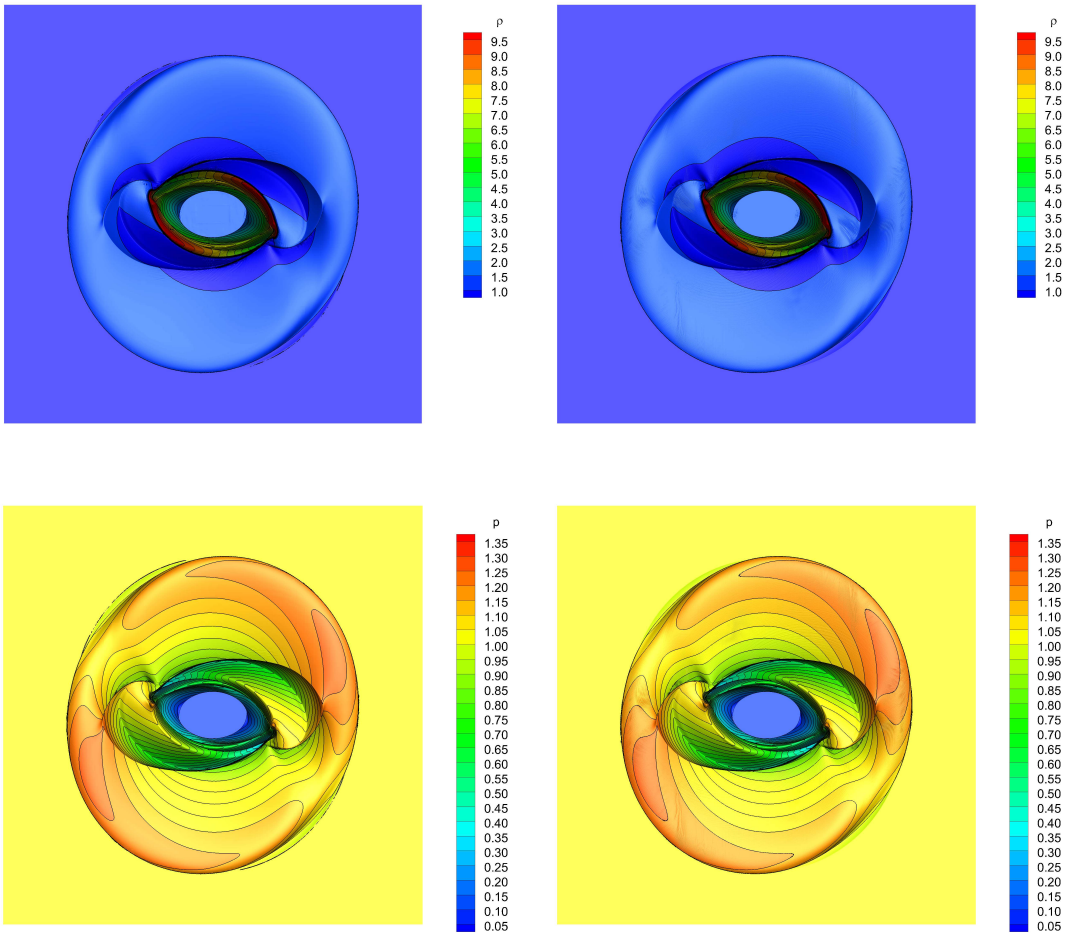

Figure 25: MHD rotor problem at time $t = 0.25$ solved with ADER-DG-P_5. Left panels: solution obtained on the AMR grid. Right panels: solution obtained on a fine uniform grid corresponding to the finest AMR grid level.

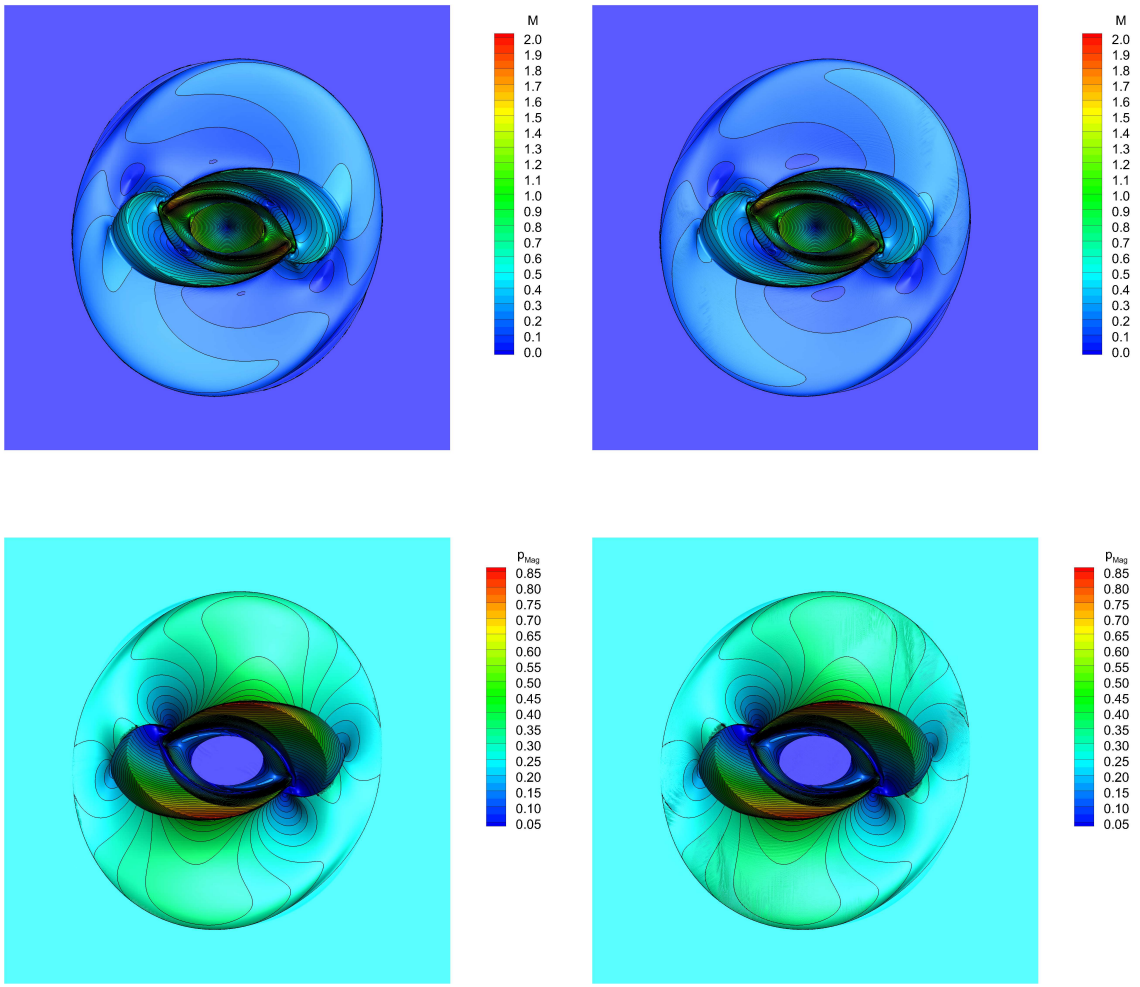

Figure 26: MHD rotor problem at time $t = 0.25$ solved with ADER-DG-P_5. Left panels: solution obtained on the AMR grid. Right panels: solution obtained on a fine uniform grid corresponding to the finest AMR grid level.

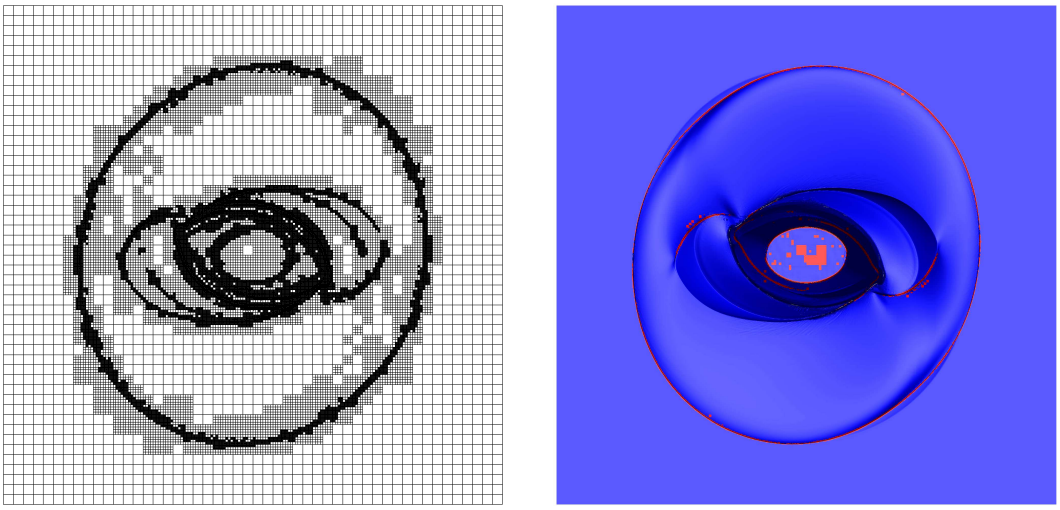

Figure 27: MHD rotor problem at time $t = 0.25$: AMR grid on the left; troubled cells (red) and unlimited cells (blue) on the right.

4.3.11 *The rotor problem (SR-MHD)*

As a first genuinely two dimensional test we consider the relativistic version of the MHD rotor problem, originally proposed by [17], and solved by a number of authors over the years, including [83], [101], [194] and [167]. The computational domain is chosen to be $\Omega = [-0.6, 0.6] \times [-0.6, 0.6]$, discretized on a coarse initial grid formed by 40×40 elements. The AMR framework is activated with a refinement factor $r = 3$ and a number of refinement levels $\ell_{max} = 2$. In this problem a cylinder of a high density fluid is rotating rapidly with angular velocity ω, surrounded by a low density fluid at rest. The initial conditions are in fact given by

$$\rho = \begin{cases} 10 & \text{for } 0 \leqslant r \leqslant 0.1; \\ 1 & \text{otherwise;} \end{cases}, \qquad \omega = \begin{cases} 9.95 & \text{for } 0 \leqslant r \leqslant 0.1; \\ 0 & \text{otherwise;} \end{cases}, \tag{4.25}$$

$$\mathbf{B} = \begin{pmatrix} 1.0, & 0, & 0 \end{pmatrix}^T, \qquad p = 1, \tag{4.26}$$

which imply an initial maximum Lorentz factor $\Gamma_{max} \approx 10$ at $r = 0.1$. Transmissive boundary conditions are applied at the borders. The spinning of the rotor produces torsional Alfvén waves that are launched outside the cylinder, transferring amounts of its initial angular momentum into the external medium. The simulation is performed without any linear taper, that means the physical variables between the internal rotor and the fluid at rest are really discontinuous. The adiabatic index is $\gamma = 4/3$. For this test, the P_5 version of our ADER-DG scheme was used, combined with the Rusanov Riemann solver. Due to the challenging nature of the problem, a robust second-order TVD scheme, rather then the standard WENO scheme, has been used on the sub-grid where the limiter is activated.

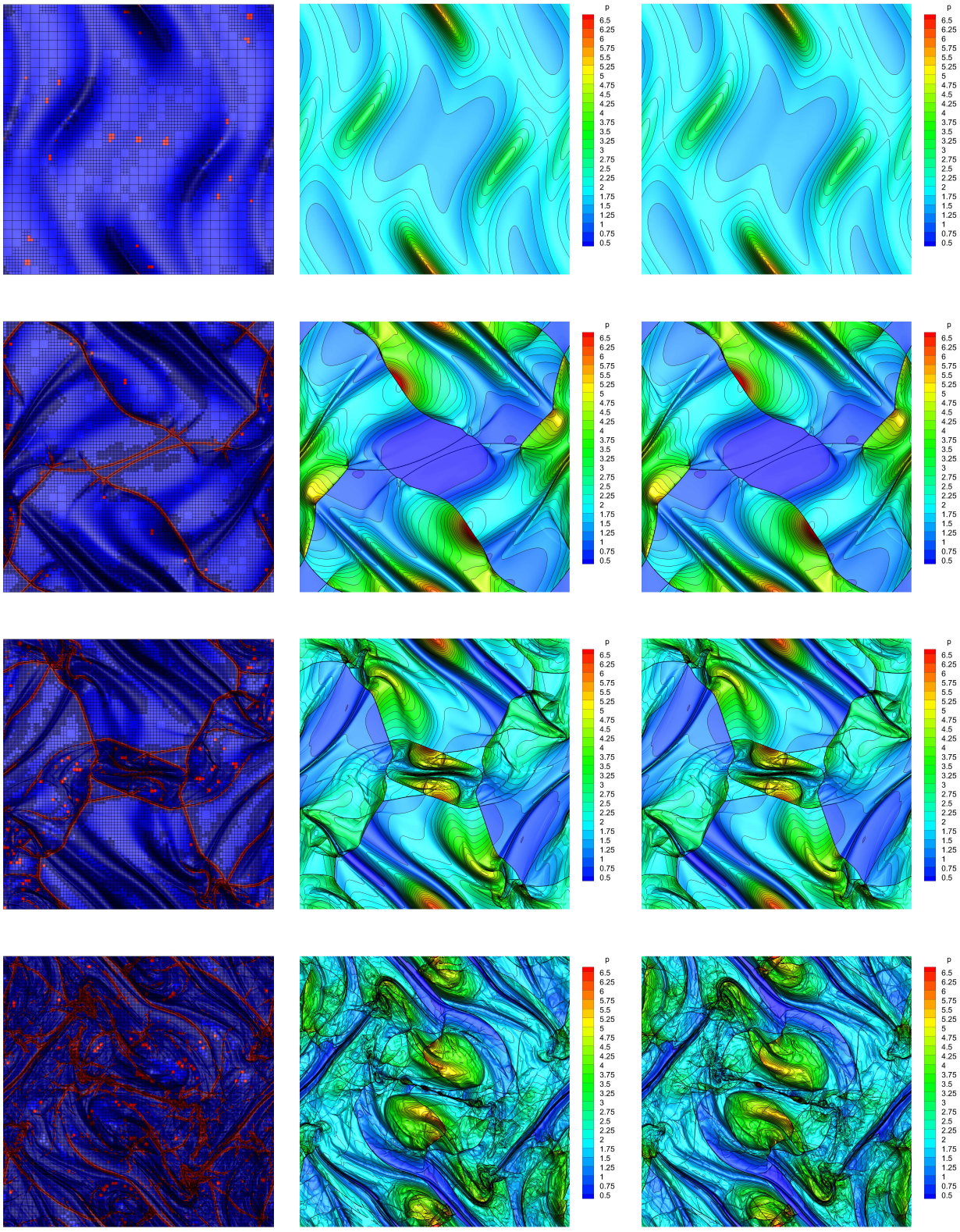

Figure 28: Orszag-Tang vortex problem at times $t = 0.5$, $t = 2.0$, $t = 3.0$, $t = 5.0$ (from top to bottom) obtained through the ADER-DG-P_5 scheme supplemented with *a posteriori* ADER-WENO3 sub-cell limiter. Left panels: AMR-grid, troubled cells (red) and unlimited cells (blue). Central panels: P_5-solution obtained on the AMR grid. Right panels: P_5-solution obtained on the uniform grid corresponding to the finest AMR grid level.

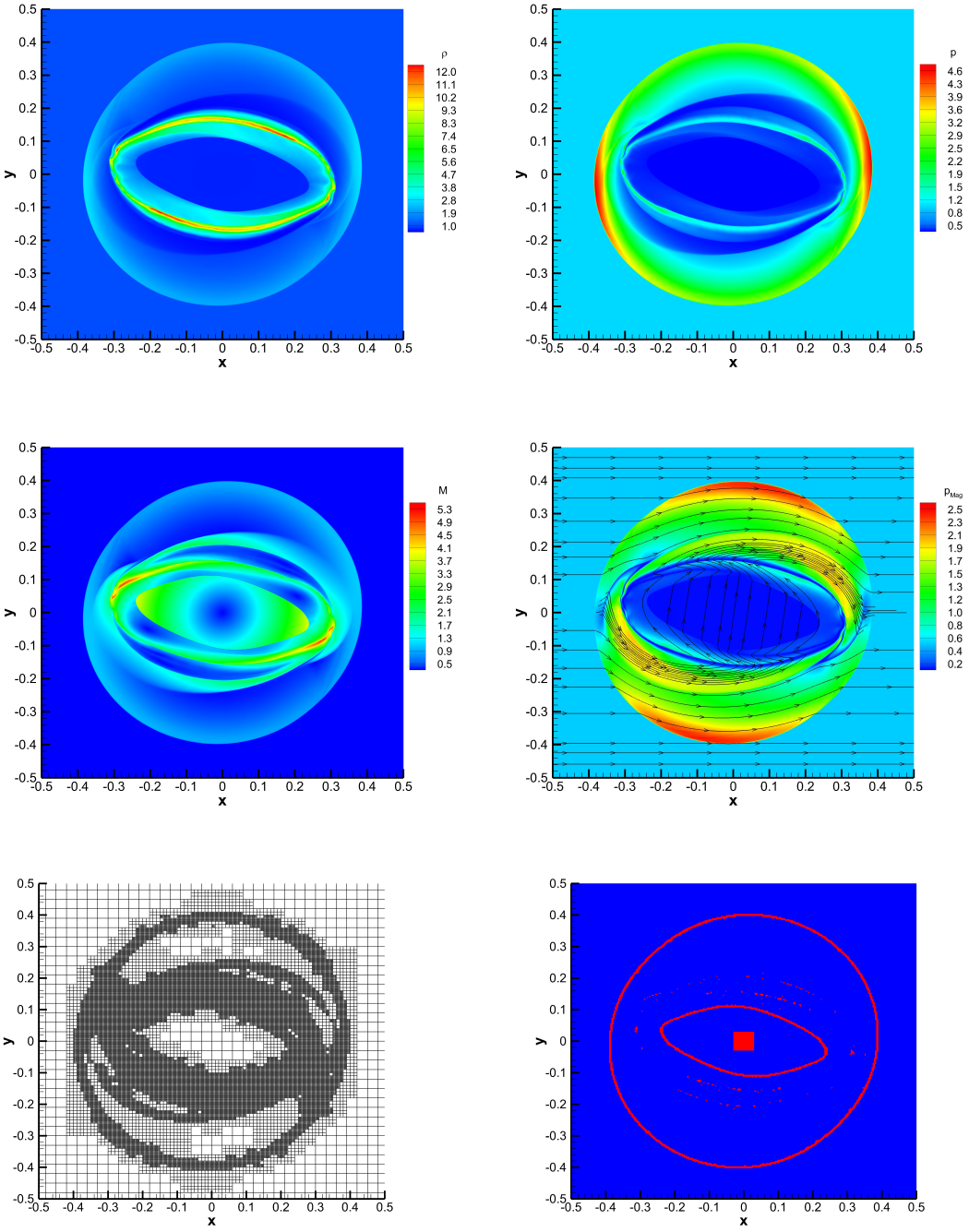

Figure 29: Solution of the SR-MHD rotor problem at time t = 0.4, obtained with the ADER-DG P_5 scheme supplemented with the *a posteriori* second order TVD sub-cell limiter. Top panels: rest-mass density (left) and thermal pressure (right). Central panels: Mach number (left) and magnetic pressure (right). Bottom panels: AMR grid (left) and limiter map (right) with troubled cells marked in red and regular unlimited cells marked in blue.

Figure 29 shows the rest-mass density, the thermal pressure, the relativistic Mach number M and the magnetic pressure $p_{\rm Mag}$ at time $t = 0.4$. The latter are computed according to

$$M = \frac{Wv}{W_s v_s}, \qquad p_{\rm Mag} = \frac{1}{2} b^2 = \frac{B^2/W + (\mathbf{v}\cdot\mathbf{B})^2}{2}, \tag{4.27}$$

where v_s is the speed of sound and $\Gamma_s = (1 - v_s^2)^{-1/2}$ is the corresponding Lorentz factor. Although an analytic solution is not available for this test, the results shown are in very good qualitative agreement with those already reported in the literature. In particular, the maximum Lorentz factor of the rotor, which is considerably slowed down by magnetic braking, is $\Gamma_{\rm max} \approx 2.1$. Moreover, the adopted divergence-cleaning approach works accurately as expected, with no appreciable spurious oscillations generated in the rest mass density or in the magnetic field. Lastly, the behavior of the space-time AMR and of the *a posteriori* limiter is depicted in the two bottom panels of figure 29: the final mesh is shown in the left panel, whereas in the right the troubled zones are represented in red. Clearly, the activation of the limiter becomes necessary only in a limited number of cells, and precisely where discontinuities are stronger.

4.3.12 *Cylindrical blast wave (SR-MHD)*

As a second two dimensional academic test we have considered the cylindrical expansion of a blast wave in a plasma with an initially uniform magnetic field. This is notoriously a severe test, which became canonical after [173], and it has been solved by several authors, including [186, 84, 101]. The initial conditions are prescribed by assuming that, within a radius $R = 1.0$, the rest-mass density and the pressure are $\rho = 0.01$ and $p = 1$, while outside the cylinder $\rho = 10^{-4}$ and $p = 5 \times 10^{-4}$. Like in [173] and in [84], the inner and outer values are joined through a smooth ramp function between $r = 0.8$ and $r = 1$, to avoid a sharp discontinuity in the initial conditions. The plasma is initially at rest and subject to a constant magnetic field along the x-direction. In our tests we have considered two different magnetizations, the first one with $B_x = 0.1$, corresponding to the intermediate value chosen by [173], and the second one with $B_x = 0.5$. We have solved this problem over the computational domain $\Omega = [-6, 6] \times [-6, 6]$, with 40×40 elements on the coarsest refinement level, $r = 3$ and $\ell_{\rm max} = 2$. We have used the Rusanov Riemann solver with the P_3 version of the ADER-DG scheme. Also for this test, a robust second-order TVD scheme has been used on the subgrid where the limiter is activated. The results for $B_x = 0.1$ are shown in figure 30, which reports the rest-mass density, the thermal pressure, the Lorentz factor and the magnetic pressure at time $t = 4.0$. The wave pattern of the configuration at this time is composed by two main waves, an external fast shock and a reverse shock, the former being almost circular, the latter being somewhat elliptic. The magnetic field is essentially confined between them, while the inner region is almost devoid of magnetization. We have detected a maximum Lorentz factor $\Gamma_{\rm max} \approx 4.3$ along the x axis just on the back of the reversed shock. The two bottom panels show

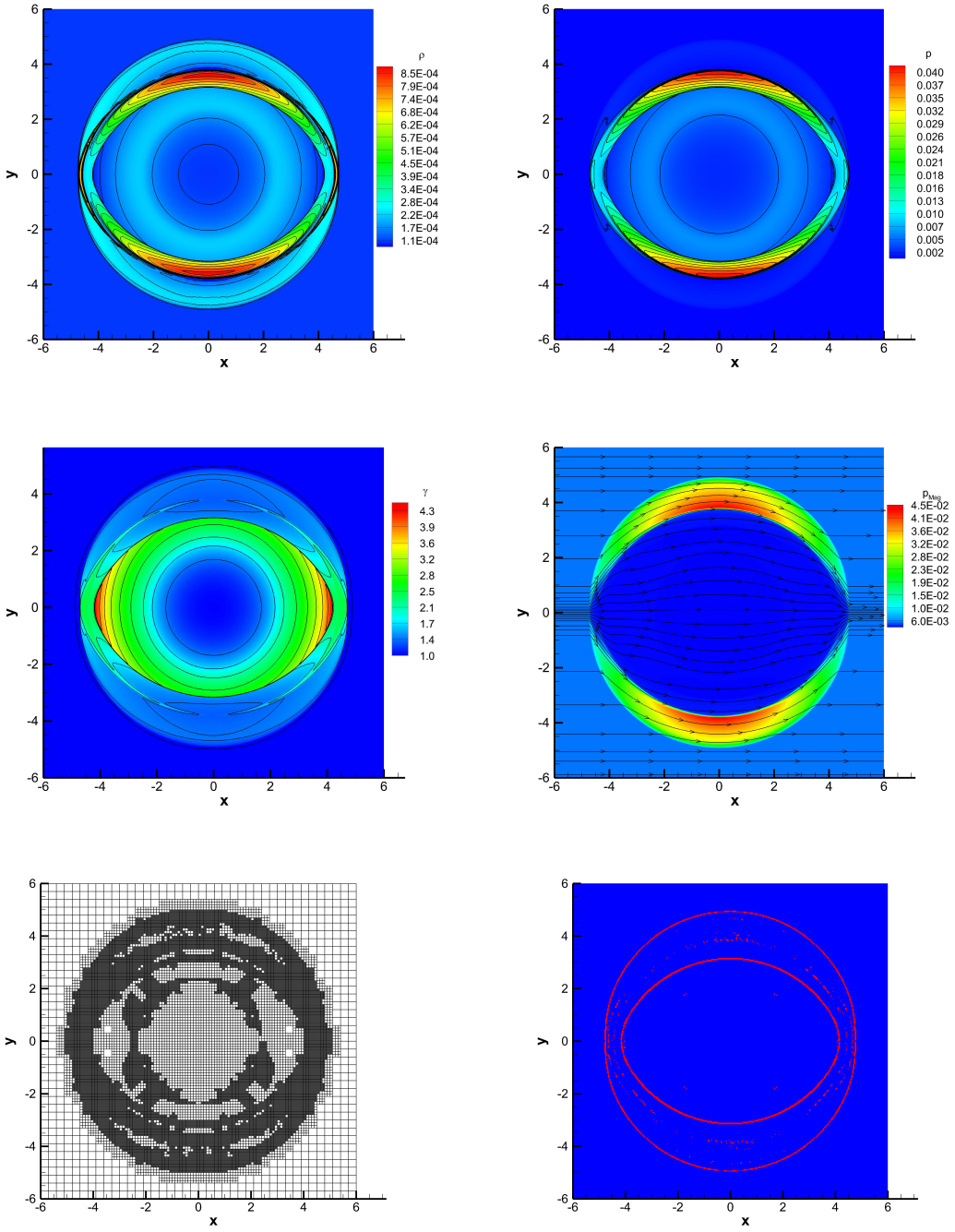

Figure 30: Solution of the SR-MHD blast wave with $B_x = 0.1$ at time $t = 4.0$, obtained with the ADER-DG P_3 scheme supplemented with the *a posteriori* second order TVD sub-cell limiter. Top panels: rest-mass density (left) and thermal pressure (right). Central panels: Lorentz factor (left) and magnetic pressure (right), with magnetic field lines reported. Bottom panels: AMR grid (left) and limiter map (right) with troubled cells marked in red and regular unlimited cells marked in blue.

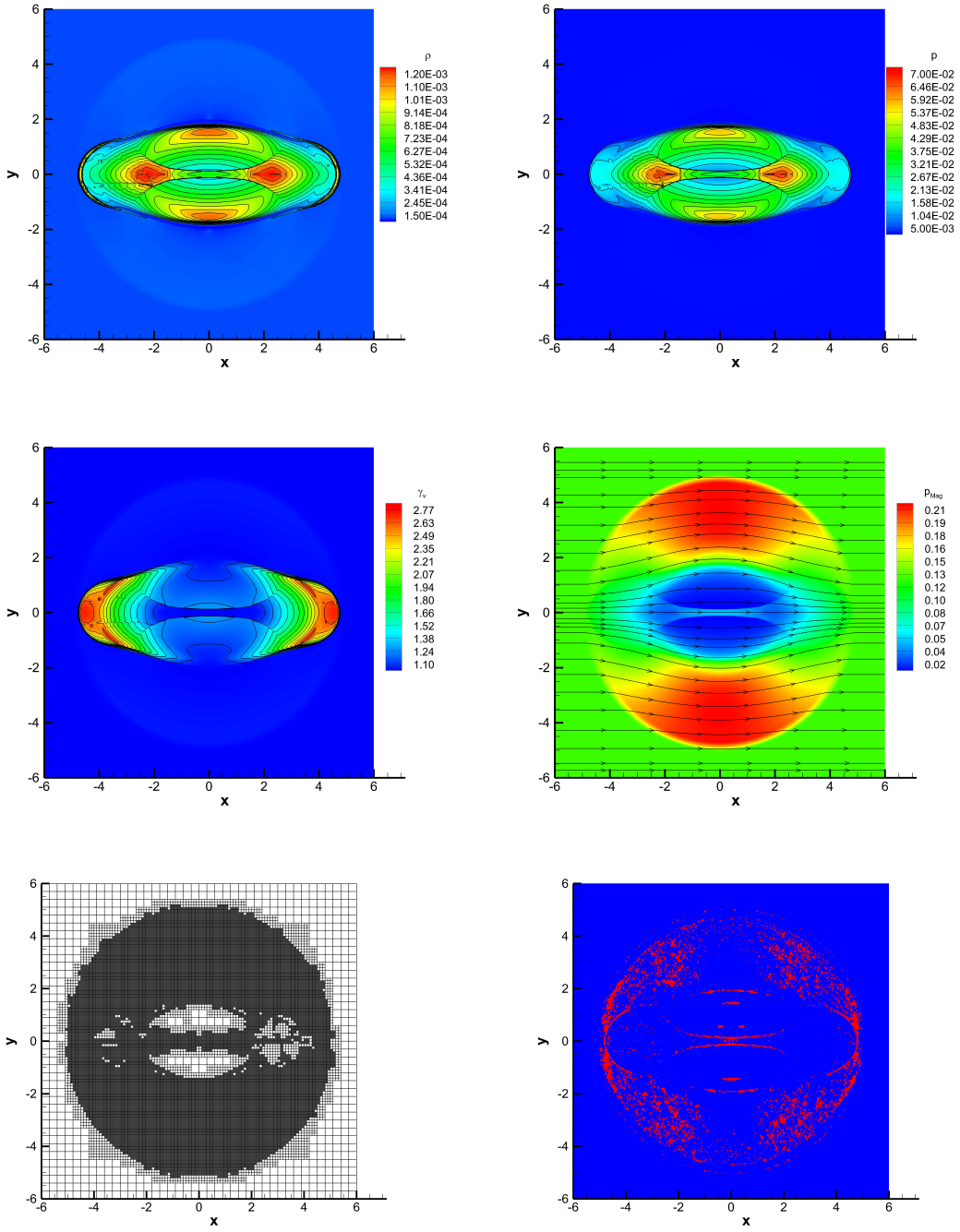

Figure 31: Solution of the SR-MHD blast wave with $B_x = 0.5$ at time $t = 4.0$, obtained with the ADER-DG P_3 scheme supplemented with the *a posteriori* second order TVD sub-cell limiter. Top panels: rest-mass density (left) and thermal pressure (right). Central panels: Lorentz factor (left) and magnetic pressure (right), with magnetic field lines reported. Bottom panels: AMR grid (left) and limiter map (right) with troubled cells marked in red and regular unlimited cells marked in blue.

the AMR grid and the map of the limiter, which is activated along the two main shock fronts. In Fig. 31, on the other hand, we have reported the results obtained for $B_x = 0.5$, again at $t = 4.0$. In this case, the external circular fast shock, which is visible in the rest-mass density and in the magnetic pressure, is very weak, while the magnetic confinement of the plasma is increased. The maximum Lorentz factor detected in this case is $\Gamma_{max} \approx 2.8$.

4.3.13 *Orszag-Tang vortex system (SR-MHD)*

Next, we have chosen the relativistic version of the well known Orszag-Tang vortex problem, proposed by [218], and later considered by [223] and [81]. The resistive case of this relativistic MHD problem has been investigated by [101]. The initial conditions are given by

$$(\rho, \boldsymbol{v}, p, \mathbf{B}) = \left(1, -\frac{3}{4\sqrt{2}}\sin(y), \frac{3}{4\sqrt{2}}\sin(x), 0, 1, -\sin(y), \sin(2x), 0\right), \quad (4.28)$$

while the adiabatic index is $\gamma = 4/3$. The equations are discretized over the computational domain $\Omega = [0, 2\pi] \times [0, 2\pi]$, with 30×30 elements on the coarsest refinement level at the initial state. Periodic boundary conditions are imposed at the borders and the Rusanov Riemann solver is adopted. The relevant AMR parameters are $r = 3$ and $\ell_{max} = 2$. We note that the maximally refined AMR mesh corresponds to a uniform grid formed of $270 \times 270 = 72,900$ elements. Moreover, the P_5 version of the ADER-DG scheme that we have adopted uses 6 degrees of freedom per spatial dimension, amounting to a total resolution of $2,624,400$ spatial degrees of freedom. The computed solution for the rest-mass density is shown in the central column of figure 32, at times $t = 0.5, 2.0, 3.0, 4.0$ respectively. For comparison, the panels on the right column show the results of a simulation performed over the maximally refined uniform mesh, which can be used as a reference solution. Clearly, an excellent agreement between the AMR results and this reference solution is obtained. As before, this test confirms the ability of the proposed method for solving complex two dimensional problems and, by showing the critical cells which required the activation of the limiter, it provides an immediate visual sketch of the most delicate regions over the computational domain.

4.3.14 *The SR-MHD Kelvin-Helmholtz instability (SR-MHD)*

A two-dimensional test that is not only academic but may be relevant to explain the observed phenomenology of extended radio-jets [see Martí and Müller [201] and references therein], we consider the Kelvin–Helmholtz (KH) instability with an initially uniform magnetic field. Following the works of Mignone et al. [206],

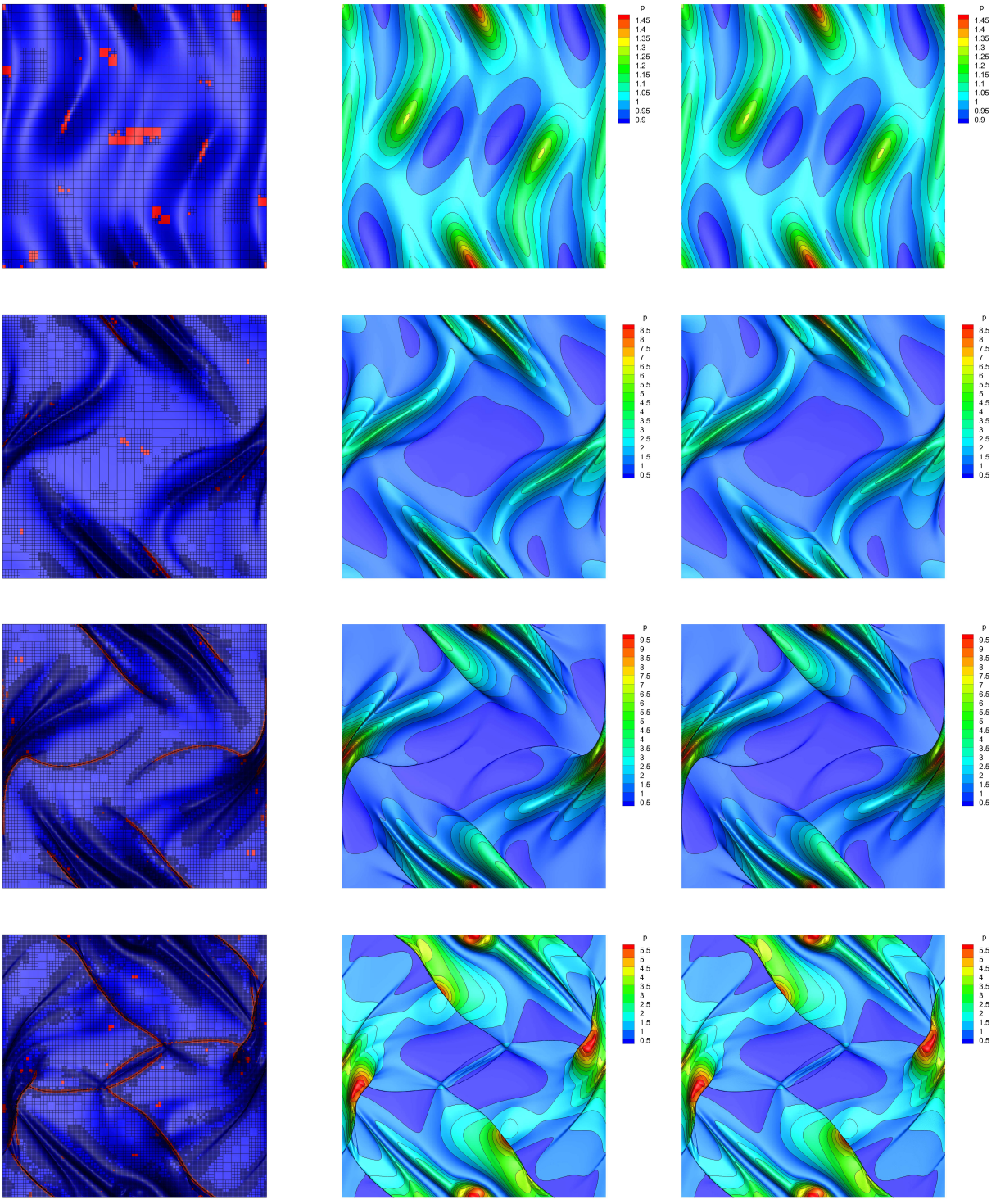

Figure 32: SR-MHD Orszag-Tang vortex problem at times $t = 0.5$, $t = 2.0$, $t = 3.0$, $t = 4.0$, from top to bottom, obtained through the ADER-DG-P_5 scheme supplemented with the third order *a posteriori* ADER-WENO sub-cell limiter. Left panels: AMR-grid, troubled cells (red) and unlimited cells (blue). Central panels: P_5-solution obtained on the AMR grid. Right panels: P_5-solution obtained on the fine uniform grid corresponding to the finest AMR grid level.

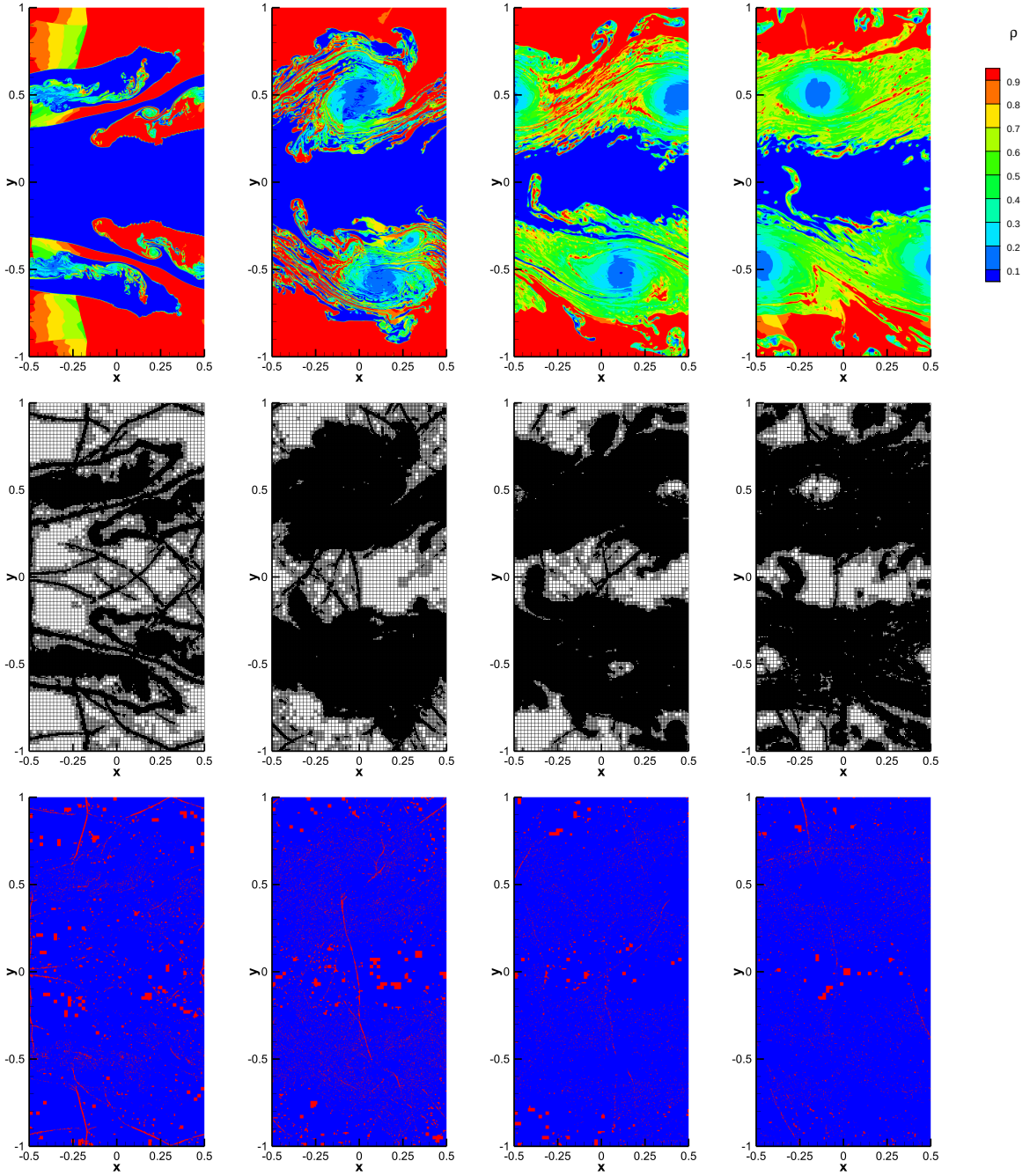

Figure 33: SR-MHD Kelvin–Helmholtz instability at times $t = 5.0$, $t = 10.0$, $t = 20.0$, $t = 30.0$ from left to right, obtained through the ADER-DG-P_3 scheme supplemented with the second order *a posteriori* ADER-TVD sub-cell limiter. The computed solution of density (top), AMR grid (center) and limiter map (bottom) are shown.

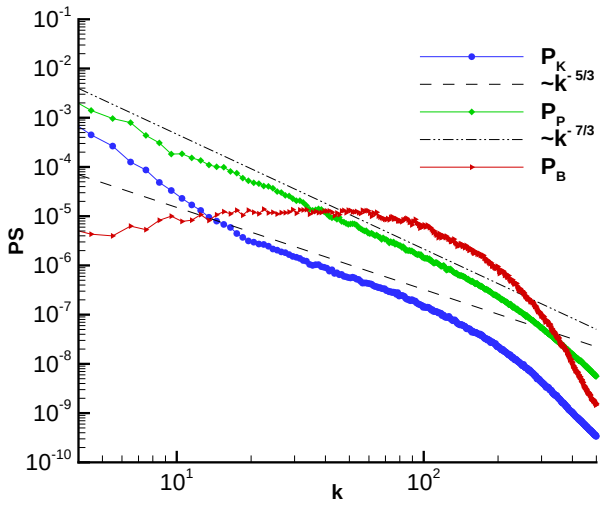

Figure 34: Power spectra for the SR-MHD Kelvin–Helmholtz instability at time $t = 30.0$ obtained through the ADER-DG-P_3 scheme.

Beckwith and Stone [33] and Radice and Rezzolla [231], we choose the initial conditions as

$$v_x = \begin{cases} v_s \tanh\left[(y-0.5)/a\right] & y > 0\,, \\ -v_s \tanh\left[(y+0.5)/a\right] & y \leqslant 0\,, \end{cases} \tag{4.29}$$

where $v_s = 0.5$ is the velocity of the shear layer and $a = 0.01$ is its characteristic size. Although not necessary in principle, it is convenient to introduce a small transverse velocity to trigger the instability, hence fixing

$$v_y = \begin{cases} \eta_0 v_s \sin(2\pi x) \exp\left[-(y-0.5)^2/\sigma\right] & y > 0\,, \\ -\eta_0 v_s \sin(2\pi x) \exp\left[-(y+0.5)^2/\sigma\right] & y \leqslant 0\,, \end{cases} \tag{4.30}$$

where $\eta_0 = 0.1$ and $\sigma = 0.1$. Finally, the rest-mass density is chosen as

$$\rho = \begin{cases} \rho_0 + \rho_1 \tanh\left[(y-0.5)/a\right] & y > 0\,, \\ \rho_0 - \rho_1 \tanh\left[(y+0.5)/a\right] & y \leqslant 0\,, \end{cases} \tag{4.31}$$

with $\rho_0 = 0.505$ and $\rho_1 = 0.495$. The adiabatic index is $\gamma = 4/3$, the pressure is $p = 1$ everywhere, and we add a weak uniform magnetic field along the $x-$ direction, namely $B_x = 0.001$. The simulations are run with the ADER-DG-P_3 scheme over the computational domain $\Omega = [-0.5, 0.5] \times [-1, 1]$, using 50×100 elements on the coarsest refinement level at the initial state. Periodic boundary conditions

are imposed along all borders and the Rusanov Riemann solver is adopted. AMR is activated with $r = 3$ and $\ell_{max} = 2$. In this simulation the solution on the subgrid has been evolved through a second order TVD scheme, which turned out to be more robust than the usual third order WENO method. Figure 33 shows the rest-mass density field at various times, up to $t = 30$, and the corresponding development of the KH instability. Since no physical viscosity or resistivity is present, it is very difficult to judge about the physical nature of the tiny structures, especially secondary instabilities, which are produced during the evolution, and which have been shown to depend sensibly on the order of accuracy of the scheme and on the Riemann solver used [33, 231, 279]. As the instability proceeds, the transition to a turbulent state occurs. Although our final time is not large enough to allow for a fully developed turbulent state, and although this thesis is not devoted to a detailed study of relativistic MHD turbulence (see instead the works by [284, 285, 123]), we have nevertheless computed the power spectra of a few relevant quantities to confirm that the transition to turbulence is indeed taking place. Figure 34, in particular, shows the power spectra of the velocity field, of the pressure field and of the magnetic field, which have been computed according to

$$P_v(k) = \frac{1}{2}\int_{|\mathbf{k}|=k} |\hat{v}(\mathbf{k})|^2 \, d\mathbf{k}, \quad P_p(k) = \int_{|\mathbf{k}|=k} |\hat{p}(\mathbf{k})|^2 \, d\mathbf{k}, \quad P_B(k) = \int_{|\mathbf{k}|=k} |\hat{B}(\mathbf{k})|^2 \, d\mathbf{k}, \tag{4.32}$$

where $\mathbf{k}$ is the wave-number, while $\hat{v}(\mathbf{k})$, $\hat{B}(\mathbf{k})$, $\hat{p}(\mathbf{k})$ are the two-dimensional Fourier-transforms of $\boldsymbol{v}$, p and $\mathbf{B}$, respectively. For $k \approx [20, 70]$, in the so-called *inertial range* where the dynamics of the turbulence is not affected by large scale energy inputs nor by dissipation, we approximately recover Kolmogorov's trends, namely $P_v(k) \propto k^{-5/3}$ and $P_p(k) \propto k^{-7/3}$ [39]. The power spectrum of the magnetic field is instead in qualitative agreement with results obtained by [284] for fully turbulent configurations. A dedicated analysis to astrophysical SR-MHD turbulence will be presented in a separate work.

4.3.15 *Kelvin Helmholtz instability for the CNS and the VRMHD equations (CNS and VRMHD)*

In this two-dimensional test the well known physical instability that takes the name from William Thomson (named Lord Kelvin) and Hermann von Helmholtz is simulated both for the compressible Navier-Stokes and the viscous-resistive MHD equations. The Kelvin-Helmholtz instability plays important roles in dissipative processes and momentum/energy transfer in atmospheric processes, fluvial engineering, oceanography, but also solar physics and astrophysics. In general, it is the physical instability that arises in the nonlinear interaction of the relative motion of two parallel fluids, as in the compressible mixing layer problem solved before. The spatial domain $\Omega = [-0.5, 0.5] \times [-1, 1]$ is discretized on the zeroth level with only 20×40 elements. The AMR framework is used up to $\ell_{max} = 2$ maximum number of refinement levels and a refine factor $r = 3$. Periodic boundary

conditions are assumed at the borders. The fluid flow is initialized following [206], [33], [231] and [280], i.e.

$$u = \begin{cases} v_s \tanh\left[(y - 0.5)/a\right] & y > 0\,, \\ -v_s \tanh\left[(y + 0.5)/a\right] & y \leqslant 0\,, \end{cases} \tag{4.33}$$

where $v_s = 1.0$ is the velocity of the shear layer and $a = 0.01$ is its characteristic size. A small transverse velocity has been conveniently introduced to trigger the instability by choosing

$$v = \begin{cases} \eta_0 v_s \sin(2\pi x) \exp\left[-(y - 0.5)^2/\sigma\right] & y > 0\,, \\ -\eta_0 v_s \sin(2\pi x) \exp\left[-(y + 0.5)^2/\sigma\right] & y \leqslant 0\,, \end{cases} \tag{4.34}$$

with $\eta_0 = 0.1$ and $\sigma = 0.1$. Finally, the fluid density is

$$\rho = \begin{cases} \rho_0 + \rho_1 \tanh\left[(y - 0.5)/a\right] & y > 0\,, \\ \rho_0 - \rho_1 \tanh\left[(y + 0.5)/a\right] & y \leqslant 0\,, \end{cases} \tag{4.35}$$

with $\rho_0 = 1.005$ and $\rho_1 = 0.995$. The dynamic viscosity coefficient has been chosen to be $\mu = 10^{-3}$. For the MHD case the electric resistivity is $\eta = 10^{-2}$ and a constant magnetic field is initialized horizontally oriented as

$$(B_x, B_y, B_z) = (0.1, 0, 0)\,. \tag{4.36}$$

Figures 35 and 36 show the numerical results obtained with our ADER-DG-P_3 scheme supplemented with the *a posteriori* sub-cell WENO3 limiter for the compressible NS and the resistive MHD equations, respectively, up to the time $t_e = 7$. It becomes evident how the initial magnetic field drastically influences the dynamics of the electrically conducting fluid (see figure 36). At first, the hydrodynamical forces between the two layers are in mutual unstable equilibrium. By introducing the nonzero vertical velocity component we upset the balance and the fluid state starts falling, looking for a new equilibrium state through the generation of mixing-breaking waves and diffusion processes (see figure 35). When a non-negligible magnetic field is active, every minimal distortion in the fluid flow corresponds to a deformation in the magnetic field. In this sense an amount of work is necessary to the magnetic-field lines to distort, and therefore also to the streamlines. Consequently, the resulting mixing process is weakened with respect to the non-charged fluid flow. Notice how a non-negligible magnetic pressure gradient pushes the fluid flow from the inner lower-density core to the outer zones (see figure 36), causing the shear layer to remain spatially confined for longer times. Thus the magnetic field plays the role of stabilizer of the initial unstable equilibrium, leading to a longer life-time of the double shear layer flow.

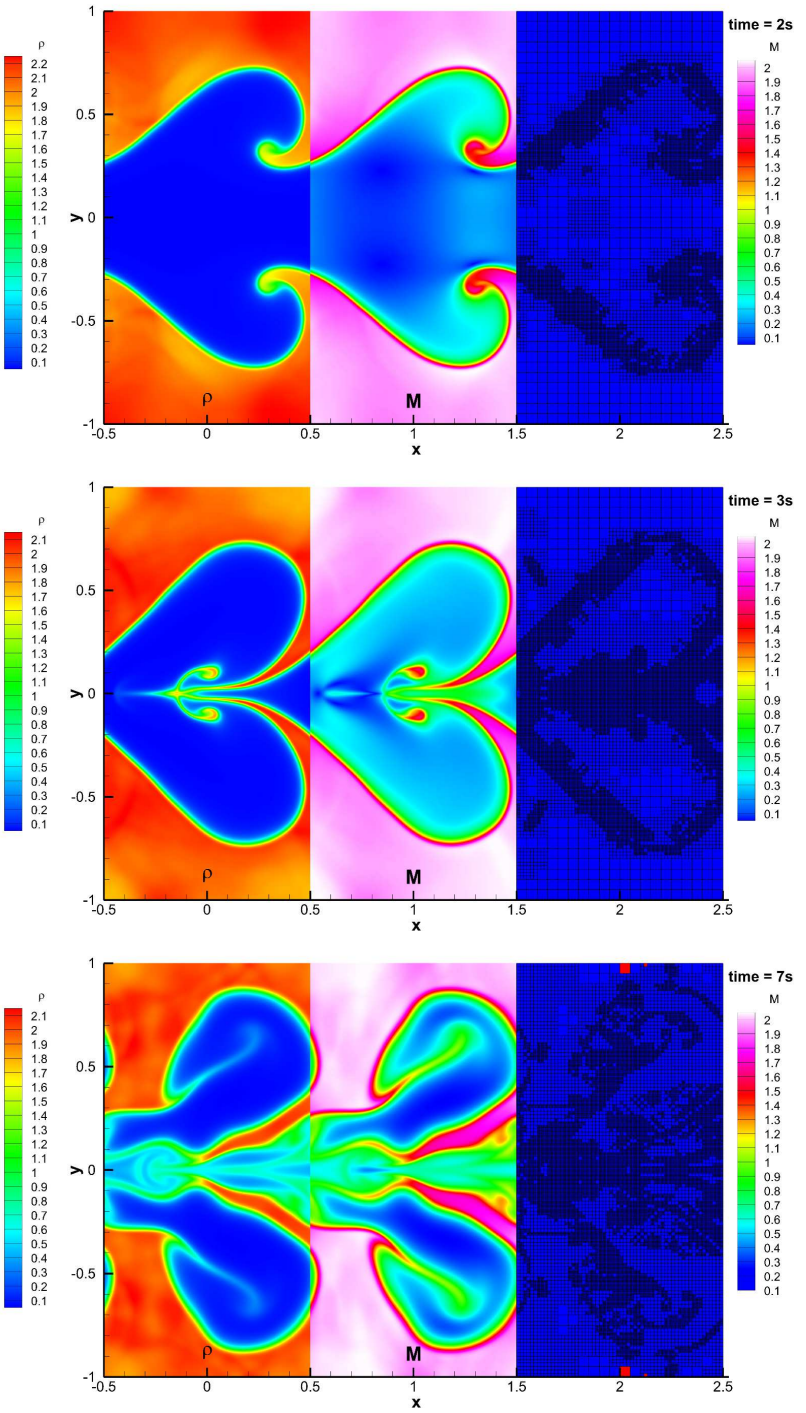

Figure 35: Numerical solution of the compressible Navier-Stokes equations for the two dimensional Kelvin-Helmholtz instability our ADER-DG-P_3 supplemented by the *a posteriori* SCL using 20×40 elements on the coarsest level, up to $\ell_{max} = 2$ maximum number of refinement levels with a refine factor $\mathfrak{r} = 3$. The density (left), the local Mach number (center) and the active-mesh colored by the limiter-status are plotted at times $t = 2.0$, 3.0 and 7.0 from the top to the bottom, respectively.

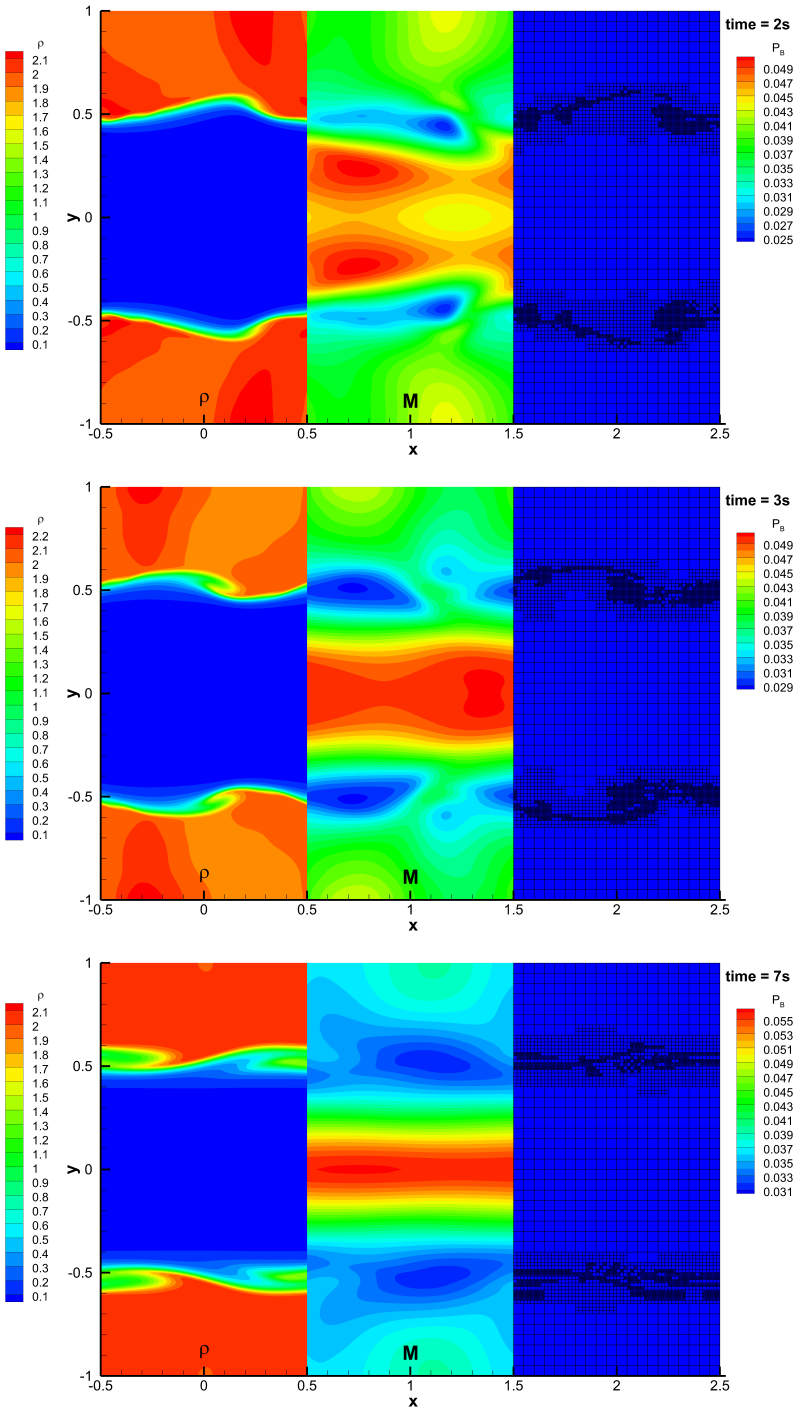

Figure 36: Numerical solution of the viscous and resistive MHD equations for the two dimensional Kelvin-Helmholtz instability our ADER-DG-P_3 supplemented by the *a posteriori* SCL using 20×40 elements on the coarsest level, up to $\ell_{max} = 2$ maximum number of refinement levels with a refine factor $r = 3$. The density (left), the magnetic pressure $|\mathbf{B}|/8\pi$ (center) and the active-mesh colored by the limiter-status are plotted at times $t = 2.0$, 3.0 and 7.0 from the top to the bottom, respectively.

4.3.16 *Magnetic reconnection (VRMHD)*

In this test we consider the classical problem of magnetic reconnection, which consists of the re-adjustment of the magnetic field topology due to a non-vanishing resistivity, typically occurring through sheet-like structures of length L and width a. The classical Sweet–Parker (SP) reconnection model predicts a dissipation of magnetic energy with a reconnection timescale $\tau_{rec} \sim \tau_A S^{1/2}$, where S is the Lundquist number. Since both in astrophysical context and in laboratory conditions the Lundquist number is very large ($S \sim 10^{12}$ in the solar corona and $S \sim 10^8$ in tokamaks), the interest towards simple resistive MHD reconnection has been frustrated for a long time. However, a novel attention has been triggered by the discovery that current sheets with large aspect ratios L/a become violently unstable [38, 196, 243, 182], generating plasmoid chains on smaller and smaller scales.

Here we reproduce a representative case of magnetic reconnection with our ADER-DG scheme, focusing on the *ideal tearing mode* investigated recently by [182]. The numerical domain is $[-20a, 20a] \times [-L/2, L/2]$, where $a = L/S^{1/3}$ is the width of the current sheet, while the Lundquist number S, which is given by the ratio between the diffusion timescale $\tau_D = L^2/\eta$ and the advection timescale $\tau_A = L/v_a$, is $S = Lv_a/\eta$. The magnetic field in the (x, y) plane follows the typical Harris model, with, in addition, a perpendicular component, in order to have a globally uniform magnetic field at time $t = 0$, i.e.

$$\mathbf{B} = B_0 \left[\tanh(x/a)\hat{\mathbf{y}} + \operatorname{sech}(x/a)\hat{\mathbf{z}}\right] , \tag{4.37}$$

where B_0 is related to the Alfven-speed by the usual expression $v_a^2 = B_0^2/(4\pi\rho)$. The thermal pressure, which is also initially uniform over the computational domain, is determined through a condition on the magnetic Mach number $M = v_a/c_s$. For an ideal gas equation of state $p = \rho\epsilon(\gamma - 1)$, this allows to obtain $p = \rho/(\gamma M^2)$. In our test we have chosen $v_a = L = 1$, $\gamma = 5/3$, $M = 0.7$ and $S = 10^6$, corresponding to a current sheet thickness $a = 0.01$ and to an asymptotic plasma parameter $\beta = 2.4$. Like in [182], the instability is triggered by inserting a perturbation in the velocity field at time $t = 0$, i.e.

$$v_x = \varepsilon \tanh\xi \exp(-\xi^2)\cos(ky) \tag{4.38}$$

$$v_y = \varepsilon(2\xi\tanh\xi - \operatorname{sech}^2\xi)\exp(-\xi^2)S^{1/2}\sin(ky)/k , \tag{4.39}$$

where $\varepsilon = 10^{-3}$, $\xi = xS^{1/2}$, while the wave-number is computed from $kL = 2\pi m$, with $m = 10$. Free outflow and periodic boundary conditions are chosen along x and y, respectively. The time evolution of the numerical solution for the density current $j_z = \partial_x B_y - \partial_y B_x$ obtained with our ADER-DG-P_5 supplemented by the *a posteriori* WENO3 SCL is plotted in figure 37 next to the active-mesh contour plot. The computational domain has been discretized between 20×50 coarsest elements, up to $\ell_{max} = 2$ maximum number of refinement levels with a refine factor $r = 3$. The initial condition consists in a positive (exiting) current density j_z localized within a thin vertical layer centered in $x = 0$. Because of Ampere's law, there is a magnetic tension acting along the thin current density (along y) and,

therefore, this system can be seen as a *tighten string* that owes its instability to the compressible nature of the fluid. The present test is often referred indeed to as the 'tearing instability' process. Due to the initial perturbation, the symmetry of the system breaks and a higher current density-segment follows up next to a lower one. Simultaneously, the magnetic field aims to maintain the divergence free condition and the lower current density-segment is consequently *bifurcated* (see the first plot in figure 37 keeping in mind the periodic boundary conditions). In this way, the first main *reconnection island* (or *major plasmoid*) is generated and it takes the form of an *harmonic perturbation* of the current density j_z. Then, the higher current density-segment behaves like a source of new smaller reconnection islands that are attracted to the center of the major plasmoid. Throughout this non-linear process the successively generated smaller islands collide and merge with the major plasmoid, leading to the so called *plasmoid coalescence*. The major plasmoid broadens out, resulting in a larger *onion* like structure of alternating positive/negative current density interfaces (see figures 37 and 38).

4.4 THREE-DIMENSIONAL TESTS

4.4.1 *Spherical explosion problem (Euler)*

In addition to the two dimensional case, presented in previous section 4.3.4, we have also solved the spherical explosion problem in three spatial dimensions. In this case a very coarse initial mesh has been adopted, consisting of $13 \times 13 \times 13$ cells, which is subsequently refined using $r = 3$ and $\ell_{max} = 2$. The problem has been solved with the ADER-DG-P_3 scheme, Rusanov flux and reconstruction in characteristic variables. The results are shown in figure 39. As it is apparent from the top-left panel of this figure, the limiter has bee activated only at the shock front, at the contact discontinuity and at the head of the rarefaction wave. The comparison with the reference solution is also good.

4.4.2 *3D Taylor-Green vortex at low Mach number (M=0.1)*

A very intriguing three-dimensional flow that drives the larger to the smallest physical scales is the turbulence-decaying process that is generated in the Taylor-Green vortex problem. The initial condition of the fluid variables is given by

$$\rho(x, y, z, 0) = 1, \tag{4.40}$$
$$u(x, y, z, 0) = \sin(x)\cos(y)\cos(z), \tag{4.41}$$
$$v(x, y, z, 0) = -\cos(x)\sin(y)\cos(z), \tag{4.42}$$
$$w(x, y, z, 0) = 0, \tag{4.43}$$
$$p(x, y, z, 0) = \rho c_0^2/\gamma + (\cos(2x) + \cos(2y))(\cos(2z) + 2)/16. \tag{4.44}$$

where c_0 is the adiabatic sound speed. The reference solution is widely accepted to be the DNS solution presented by [43] through both a direct spectral method (up to 256^3 modes) and a rigorous power series analysis (up to order t^{80}), see

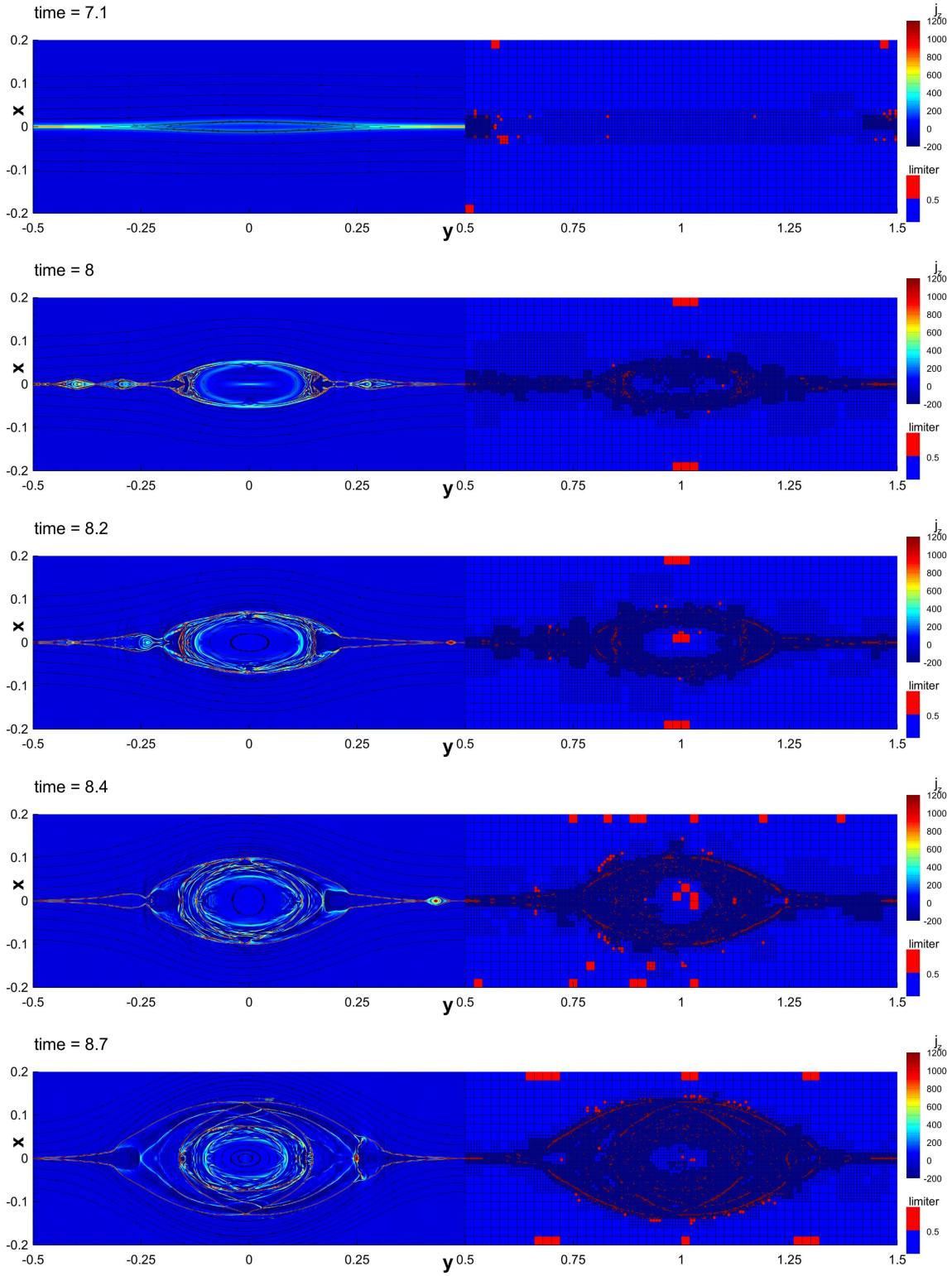

Figure 37: Numerical solution of the resistive MHD equations for the two dimensional magnetic reconnection test problem at several time-step obtained with our ADER-DG-P_5 supplemented by the *a posteriori* WENO3 SCL using 20×50 elements on the coarsest level, up to $\ell_{max} = 2$ maximum number of refinement levels with a refine factor $r = 3$. The density current j_z (left) and the active-mesh colored by the limiter-status (right) are plotted at times $t = 7.1$, 8.0, 8.2, 8.4 and 8.7 from the top to the bottom, respectively.

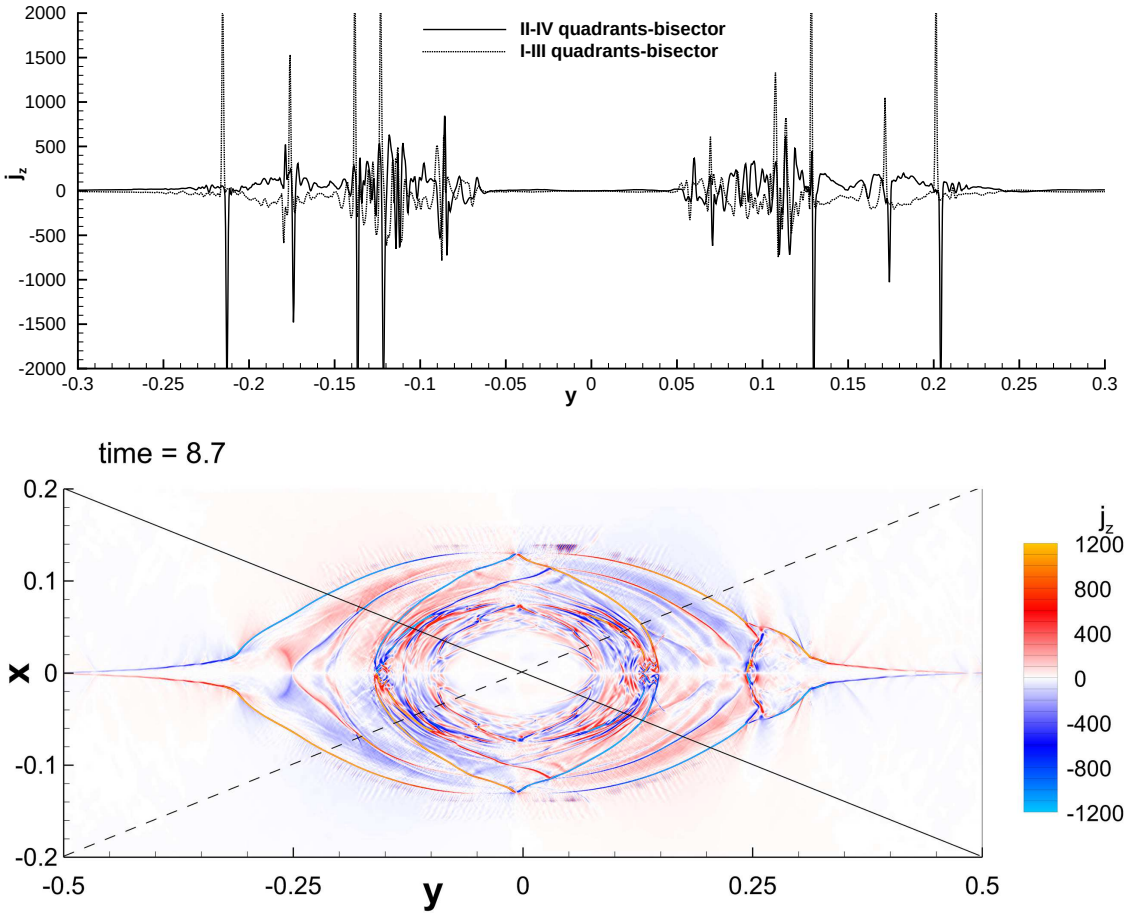

Figure 38: Interpolation of the current density j_z for the two dimensional magnetic reconnection test problem at time $t = 8.7$ along the two bisectors of the rectangular computational domain (top), highlighting the *tree-ring* structure of the alternately-positive/negative current density of the major plasmoid. At the bottom the corresponding current density j_z is shown and the two considered bisector have been highlighted in white continuous and dashed lines.

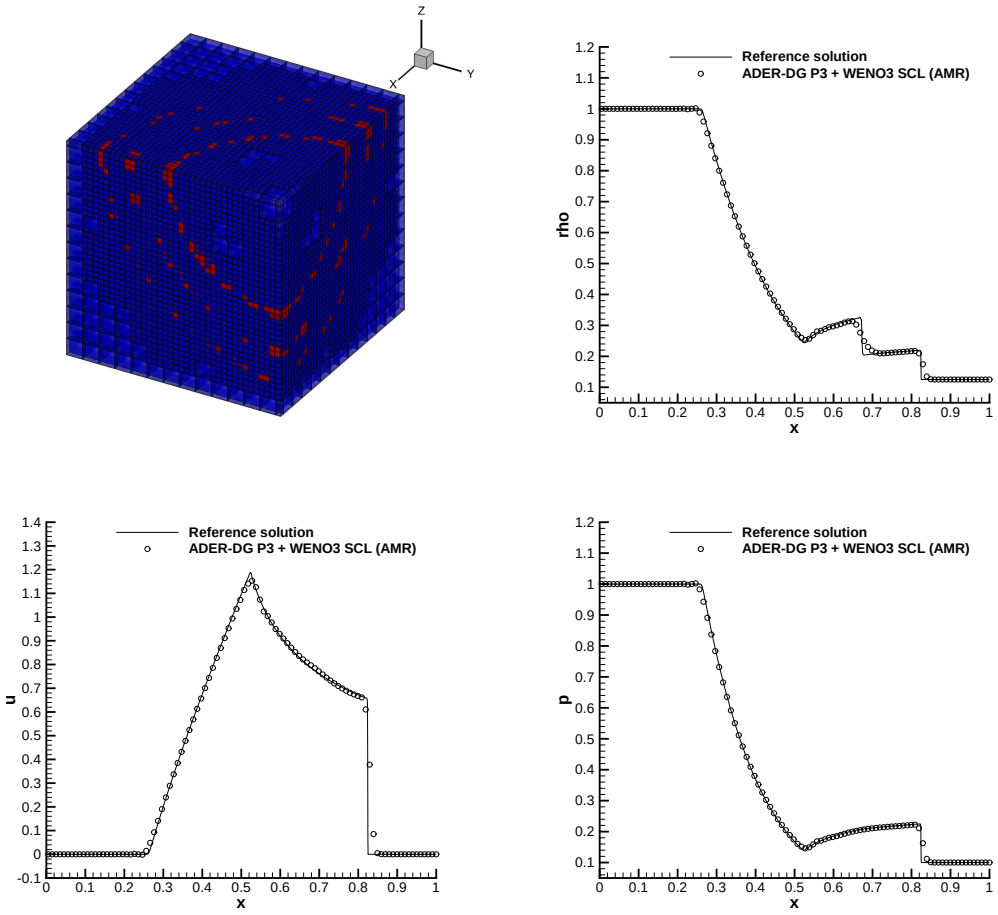

Figure 39: Three-dimensional explosion problem. 3D view of the AMR grid together with limited and unlimited cells (top left). One dimensional cuts of the numerical solution for density ρ (top right), velocity u (bottom left) and fluid pressure p (bottom right) on 120 equidistant sample points along the positive $x-$axis obtained at $t_{\text{final}} = 0.20$ with the space-time adaptive ADER-DG-P_5 scheme, supplemented with *a posteriori* ADER-WENO3 sub-cell limiter.

also [212]. Periodic boundary conditions are assumed everywhere with respect to the cubic spatial domain $\Omega = [0, 2\pi]^3$. Figure 67 shows the results for the kinetic energy dissipation rate

$$\epsilon(t) = -\frac{\partial K}{\partial t} = -\frac{1}{||\Omega||}\frac{\partial}{\partial t}\int_{\Omega}\frac{1}{2}\rho \mathbf{v}^2 d\mathbf{x} \tag{4.45}$$

for different Reynolds numbers $Re \in [100, 1600]$ evaluated in the time interval $t \in [0, 10]$. A direct comparison with the reference solution of [43] shows that an excellent agreement has been obtained. Notice that for larger Reynolds numbers, smaller dissipative vortex structures can be generated and, consequently, a higher numerical resolution is needed. Since we use a dissipative scheme (due to the Riemann solver), a too low resolution would generate an excess of numerical diffusion. The initial condition is the same for all the different test cases, but the time series of the kinetic energy dissipation strongly depends on the chosen Reynolds number. At $t = 0$ a very smooth solution is initialized, then the diffusive decaying begins slowly. Once the peak of dissipation is reached ($t \sim 4$ for $Re = 100$, $t \sim 6$ for $Re = 200$, $t \sim 9$ for $Re = 800$ and $Re = 1600$) then the kinetic energy dissipation rate decreases asymptotically and inexorably to the trivial stationary solution with $K = 0$. For this test the third order P_2 version of our ADER-DG scheme supplemented with the third order ADER-WENO3 sub-cell limiter has been used. The AMR grid is activated using the 32^3 elements of the coarsest level zero grid. A refinement factor of $r = 2$ is used and up to $\ell_{max} = 2$ maximum number of refinement levels are admitted. Figure 68 shows the iso-surfaces of pressure, density and velocity at different times $t \in [0, 10]$ and gives a better qualitative comprehension of the flow dynamics.

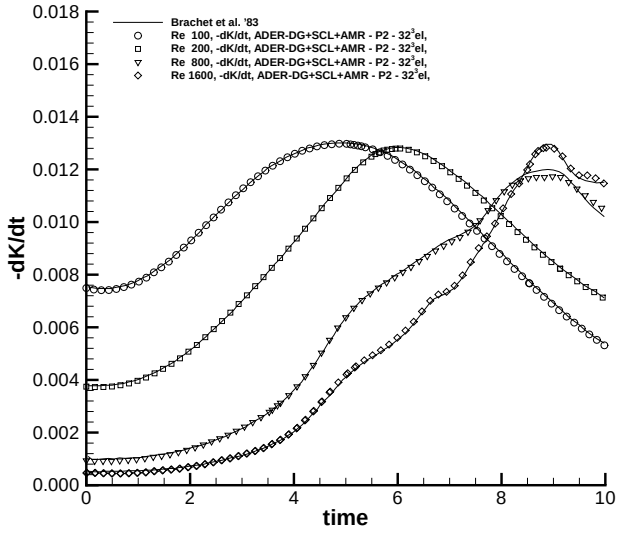

Figure 40: Time evolution of the kinetic energy dissipation rate $\epsilon(t)$ obtained with our ADER-DG-P_2 supplemented with the *a posteriori* WENO3 SCL at different Reynolds numbers $Re = 100$, 200 and 800. The DNS reference solutions of Brachet et al. [43] are plotted as continuous lines. Up to $\ell_{max} = 2$ maximum number of refinement levels with a refine factor $r = 2$ are used along the 32^3 elements of the coarsest grid.

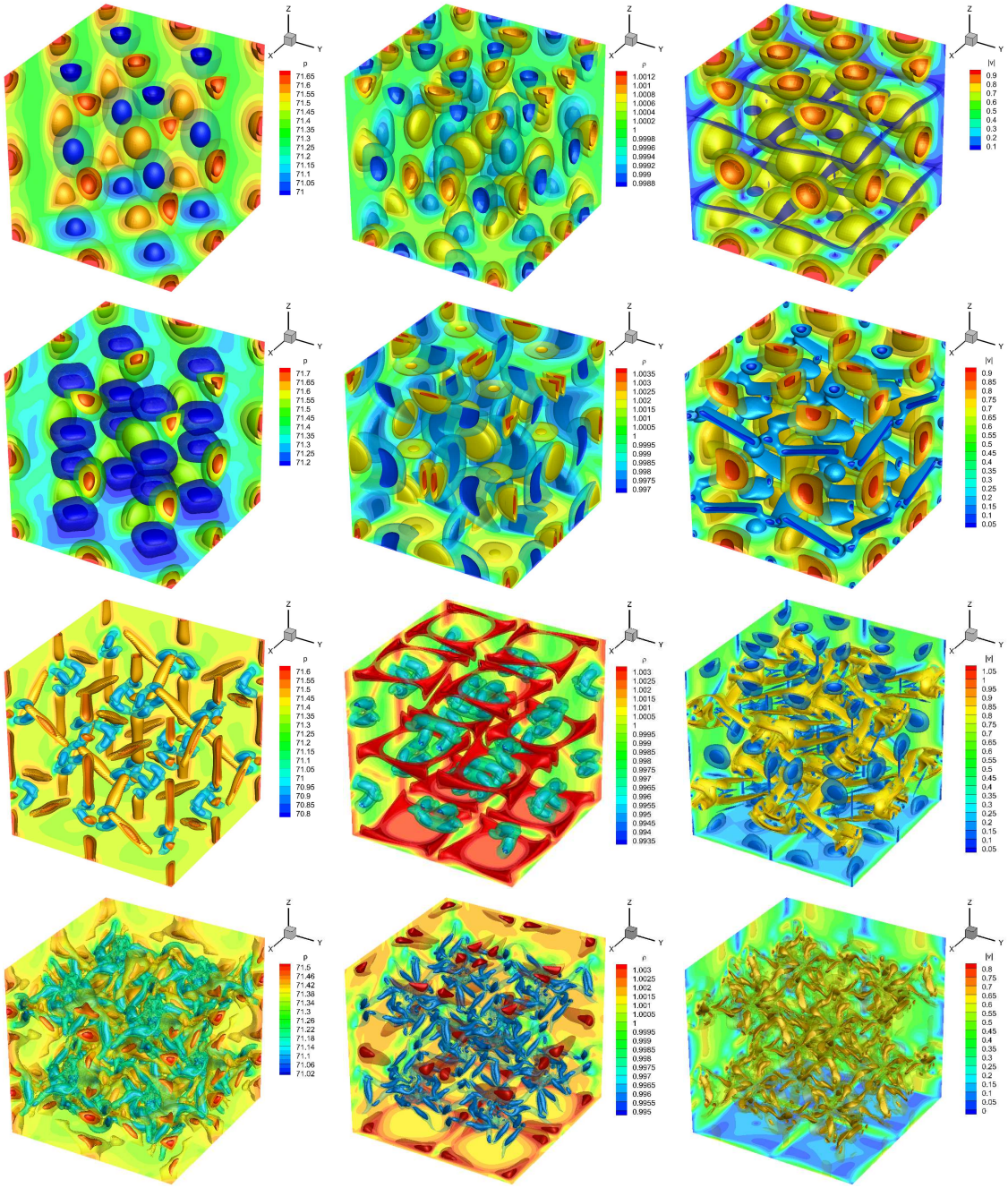

Figure 41: Numerical solution for the three dimensional Taylor-Green vortex flow at $\mathrm{Re} = 800$ computed with our ADER-DG-P_2 supplemented by the *a posteriori* SCL using 32^3 elements on the coarsest level, up to $\ell_{\max} = 2$ maximum number of refinement levels with a refine factor $\mathrm{r} = 2$. The iso-surfaces of the pressure (left), the density (center) and the velocity (right) are plotted at times $\mathrm{t} = 0.5$, 2.0, 6.0 and 10.0 from the top to the bottom, respectively.

Part III

DG METHODS FOR INCOMPRESSIBLE FLUIDS

The third part of the thesis is organized in two chapters, presenting the published research-contributions of the author concerning semi-implicit DG, see [115, 114], and space-time DG methods, see [115], for the incompressible Navier-Stokes equations on staggered Cartesian grids. Chapter 5 outlines the theoretical description of our SI-DG on AMR meshes, and the respective space-time formulation, i.e. the st-DG method. In chapter 6 we present a numerical validation.

5

SPECTRAL DG METHODS ON STAGGERED CARTESIAN MESHES

5.1 SEMI-IMPLICIT DG METHODS FOR FLUID DYNAMICS

In this chapter a novel semi-implicit discontinuous Galerkin method for solving the incompressible Navier-Stokes equations is derived within the framework of *staggered adaptive* meshes (staggered AMR), in two and three space dimensions. The governing equations for an incompressible fluid, see (2.52), read

$$\frac{\partial \mathbf{v}}{\partial t} + \nabla \cdot \mathbf{F} + \nabla p = 0, \tag{5.1}$$

$$\nabla \cdot \mathbf{v} = 0, \tag{5.2}$$

where $\mathbf{v}(\mathbf{x}, t)$ is the velocity vector field, $p(\mathbf{x}, t)$ is the pressure and $\mathbf{F}$ takes into account non-linear convection $\mathbf{F}_c = \mathbf{v} \otimes \mathbf{v}$ as well as the viscous stress tensor $\boldsymbol{\sigma} = -\nu \nabla \mathbf{v}$, i.e.

$$\mathbf{F} = \mathbf{F}_c + \boldsymbol{\sigma} = \mathbf{v} \otimes \mathbf{v} - \nu \nabla \mathbf{v}, \tag{5.3}$$

ν being the kinematic viscosity of the considered fluid. The great interest of the here considered governing partial differential equations has been largely discussed in the previous chapters, ranging from ocean-river modeling, industrial flows in aerospace-naval and mechanical engineering, but also to high energy astrophysics whenever high density plasma are approximated to behave similarly to an incompressible fluid.

As it has been mentioned, the importance of resolving the smallest spatial scales appearing in the flow within large domains requires a higher-order accurate method with very low numerical diffusion and dispersion errors. Over the years, finite-difference (FD) and finite-volume (FV) methods have been widely used for solving many different families of partial differential equations. Very high order of accuracy at low computational cost can be easily reached for FD schemes whenever regular structured grids are used. In contrast to FD methods, FV schemes are particularly suitable for general unstructured meshes, but the expensive and rather cumbersome *recovery* or *reconstruction* step that is needed for obtaining high order of accuracy in the FV framework constitutes a clear drawback. In all cases, higher order formulations of FD and FV methods require large stencils, leading to a deterioration of the parallel scalability of the algorithms. In this context, the excellent parallel scalability properties of discontinuous Galerkin (DG) finite element methods make this class of finite element (FE) schemes well suited for large-scale simulations.

Typically, a stable higher order time discretization was reached by means of the method of lines (MOL) approach in combination with explicit TVD Runge Kutta schemes, leading to the well known family of RKDG schemes, although also other explicit time-discretizations are possible, see e.g. the family of ADER-DG and Lax-Wendroff DG schemes presented in [99, 229]. On the other hand, one of the major drawbacks for any *explicit* DG scheme is represented by the severe CFL stability condition that limits the time-step of the simulations to be proportional to $h/(2N+1)$ for hyperbolic PDE or even proportional to $h^2/(2N+1)^2$ for parabolic PDE, where h is the characteristic mesh size and N is the degree of the polynomial basis. Van der Vegt et al. have extended the DG method to an elegant space-time formalism [268, 269, 169], providing a fully implicit and *unconditionally stable* DG scheme for the compressible Euler and Navier-Stokes equations, and later also for the incompressible Navier-Stokes equations, see [238]. The drawback is that a fully implicit time-discretization leads to a highly coupled non-linear system for the complete set of the degrees of freedom of the physical variables to be solved at every time-step. In this case large scale simulations in two and three space-dimensions can become computationally very demanding. Alternative families of *linearly implicit* time discretizations for DG schemes have been considered recently in [28].

In their pioneering work [26] Bassi and Rebay have presented the first DG scheme for the solution of the compressible Navier-Stokes equations, and shortly after Baumann and Oden [30, 31] have formulated a DG scheme based on penalty terms for the treatment of convection-diffusion equations. Indeed, whenever parabolic (second order) or higher order spatial derivatives appear in the considered PDE, obtaining a DG finite-element formulation is not straightforward, see [75, 274]. High order DG methods are actually a very active field of the ongoing research and several different formulation for the Navier-Stokes equations have been provided in the meantime, see [27, 124, 125, 95, 143, 144, 80, 171] to mention a few.

In this work we adopt a specific technique for circumventing a direct approach for solving the saddle point problem of the incompressible Navier-Stokes equations, which goes back to a family of very efficient semi-implicit finite difference methods developed by Casulli et al. in the context of simulating hydrostatic and non-hydrostatic gravity-driven free-surface flows on staggered grids, see [59, 61, 55, 56]. A theoretical analysis of this approach has been provided in [57, 47, 48, 63]. In this family of methods, exact mass conservation is ensured via a conservative finite-volume formulation of the discrete continuity equation and the nonlinear convective terms are discretized *explicitly*, in order to obtain a well-behaved pressure system that is at most mildly nonlinear (i.e. with non-linearities only on the diagonal) and whose linear part is at least symmetric and positive semi-definite. The common point of the numerical methods mentioned above consist in the application of the Schur complement for the solution of the discrete saddle point problem that results after a semi-implicit discretization of the PDE within a staggered-mesh framework. Characterized by a high computational efficiency, these methods have been extended to other problems, e.g. blood flow in the

human cardiovascular system [64, 117], compressible gas dynamics in compliant tubes [110] and the dynamics of compressible fluids with general equation of state [98].

The first direct extension of staggered semi-implicit finite volume and finite difference schemes to the DG framework has been derived in [97, 252] for the shallow water equations on Cartesian and unstructured triangular grids. The resulting staggered semi-implicit DG method has furthermore been extended to the incompressible Navier-Stokes equations in two and three space dimensions on uniform Cartesian and conforming unstructured simplex meshes, see [115, 253, 254, 255]. Concerning the uniform Cartesian grid case [115], a rigorous theoretical analysis of the corresponding algebraic systems has been very recently presented in [102] by employing the theory of matrix-valued symbols and Generalized Locally Toeplitz (GLT) algebras, see [245, 140, 246].

Actually, there exist several different alternative formulations that combine the stability properties of semi-implicit methods and the high order of accuracy of DG schemes within *collocated grids*. Some important examples are provided by Dolejsi et al. [90, 92, 89] for compressible gas dynamics and convection-diffusion equations, as well as the work of [131, 266] for shallow water systems. Concerning staggered-meshes, relevant research has been carried out by Chung et al. in [70, 68] for *edge-based* staggered meshes, and by Liu et al. for the analysis of a DG finite element method based on the alternative *vertex-based* staggering approach, see [190, 189].

Concerning implicit time discretizations, Kopera and Giraldo [175] presented an interesting implicit-explicit (IMEX) DG method on AMR meshes for the compressible Euler equations with application to atmospheric flow simulations. For further references see also [126, 197].

In this chapter, the family of *spectral* semi-implicit DG methods for the solution of the two and three dimensional Navier-Stokes equations on *edge-based staggered* Cartesian grids [115] is extended to staggered grids with adaptive mesh refinement (AMR). The main novelty of the paper consists in the development of the first high order DG scheme on *staggered AMR meshes*. Similar to the uniform Cartesian case, even within staggered AMR grids, an important achievement in terms of computational efficiency has been obtained by succeeding in writing all discrete operators as a combination of simple one-dimensional operators thanks to the use of tensor-products of one-dimensional operators. The method is tested on a large set of test problems in two and three space dimensions, employing polynomial degrees up to $N = 9$. To the knowledge of the authors, this is the *first time* that a high order accurate semi-implicit DG scheme is derived on *staggered adaptive grids*.

The rest of the chapter is structured as follows: section 5.2 defines the adopted *staggered AMR mesh*; section 5.3 defines the solution space for the adopted discrete formulation of the governing equations within our staggered DG framework; section 5.4 outline the details of our SI-DG discretization procedure on AMR grids; section 5.5 outline the details of our SI-DG discretization procedure.

The numerical validation of the SI-DG and st-DG schemes is outlined in chapter 6, providing comparisons with available analytical, numerical or experimen-

tal reference solution for several non-trivial test cases in two and three space-dimensions.

5.2 THE SPATIALLY STAGGERED AMR MESHES

Chosen a main Cartesian mesh Ω_h, with or without AMR, there are basically two different strategies for choosing a staggered Cartesian dual mesh Ω_h^*: the 'node-based' and the 'edge-based' staggering, i.e. the *B*- and the *C-grid*, respectively, according to the nomenclature of Arakawa & Lamb [7]. In this work the *edge*-based staggering has been selected to be the optimal one in terms of numerical efficiency for the resolution of the resulting system of discrete equations. A d-dimensional uniform Cartesian element $T_i \in \Omega_h$ is defined as the Cartesian product

$$T_i = \prod_{s=x,y,z} \Delta s(\mathbf{x}_i), \quad \forall\, i = 1, 2, \ldots, N_{elem},$$

where $\Delta s(\mathbf{x}_i)$ are the spatial discretization-steps, centered in $\mathbf{x}_i = (x_i, y_i, z_i)$, i.e. the barycenter of T_i. Then, in order to treat hanging-nodes in the chosen AMR-mesh, one can define $N^{(k)}_{i-faces}$ being the total number of *faces* (or *edges* in two space dimensions) of T_i that are oriented in the k-th space direction, i.e. $\Gamma^{(k)}_{i,l}$ with $l = 1, 2, \ldots, N^{(k)}_{i-faces}$, having $N^{(k)}_{i-faces} = 2$ (backward and forward) for uniform grids. Then, the complete set for the faces of T_i will be $\Sigma_i = \left\{\Gamma_{i,1}, \Gamma_{i,2}, \ldots, \Gamma_{i,N_{i-faces}}\right\}$, where $N_{i-faces}$ is the total number of faces of T_i with

$$N_{i-faces} = \sum_{k=1}^{d} N^{(k)}_{i-faces} \qquad\qquad \partial T_i \equiv \Sigma_i = \bigcup_{j=1}^{N_{i-faces}} \Gamma_{ij}$$

The resulting edge-based Cartesian *staggered* (or '*dual*', or '*starred*') elements are identified by T^*_{ij}, $j = 1, 2, \ldots, N_{i-faces}$ and $i = 1, 2, \ldots, N_{elem}$. It becomes useful to distinguish up to d sets of non-overlapping Cartesian staggered-elements $T^{*(k)}_{ij}$ $j = 1, 2, \ldots, N^{(k)}_{i-faces}$, and $i = 1, 2, \ldots, N_{elem}$, referring to the k-th space-direction of the staggering, $k = x, y, z$. Since every internal face Γ is shared by two distinct *neighbor* elements $T_{r(\Gamma)}$ and $T_{l(\Gamma)}$, the chosen two-index notation is *surjective*, i.e. exists j_1 and j_2 such that $T^*_{l(\Gamma),j_1} \equiv T^*_{r(\Gamma),j_2}$, or equivalently $\Gamma_{l(\Gamma),j_1} \equiv \Gamma_{r(\Gamma),j_2} \equiv \Gamma$. Here, $r(\Gamma)$ and $l(\Gamma)$ are defined to be the integer indexes for the right and the left space element, with respect to the oriented face Γ, which orientation is well definite and no sign-function is needed, because the mesh is Cartesian.

Then, in the aim of simplicity, a one-index *injective* notation can be obtained after an adequate surjective reordering map ρ

$$\begin{array}{rccl} \mathbb{N} \times \mathbb{N} \supset & A & \xrightarrow{\quad\rho\quad} & B = \{1, 2, \ldots, N_{faces}\} \subset \mathbb{N} \\ & \cup & & \cup \\ & (i, j) & \longrightarrow & m = \rho(i, j), \end{array}$$

$$\forall\, i = 1, 2, \ldots, N_{elem};\ j = 1, 2, \ldots, N_{i-faces};$$

so that exists $m = \rho(l(\Gamma), j_1) = \rho(r(\Gamma), j_2)$ and the following equivalence holds

$$T^*_{l(\Gamma),j_1} \equiv T^*_{r(\Gamma),j_2} \equiv T^*_m = \prod_{s=x,y,z} \Delta s(\mathbf{x}^*_m), \quad \forall\, m = 1, 2, \ldots, N_{\text{faces}}$$

where $\Delta s(\mathbf{x}^*_m)$ are the spatial discretization-steps centered in $\mathbf{x}^*_m$, i.e. the barycenter of face Γ_m; N_{faces} is the total number of faces of Ω_h. Then, it follows the injectivity property

$$T^*_{m_1} \neq T^*_{m_2}, \quad \forall m_1 \neq m_2, \quad m_1, m_2 \in \{1, 2, \ldots, N_{\text{faces}}\}$$

or alternatively

$$T^{*(k)}_{m_1} \neq T^{*(k)}_{m_2}, \quad \forall m_1 \neq m_2, \quad m_1, m_2 \in \left\{1, 2, \ldots, N^{(k)}_{\text{faces}}\right\}, \quad k = x, y, z$$

$N^{(k)}_{\text{faces}}$ being the total number of faces in the k-th space direction in the computational domain. In the following, the two-index notation will be used only whenever strictly necessary. In this notation, one can distinguish the $d+1$ (the main Ω_h and the d dual meshes $\Omega^{*(k)}_h$, $k = x$, y or z if $d = 3$) spatially staggered non-overlapping meshes with the property

$$\Omega = \bigcup_i T_i = \bigcup_i T^{*(k)}_i, \tag{5.4}$$

$$\varnothing = \bigcup_{i \neq j} \left(T^\circ_i \cap T^\circ_j\right) = \bigcup_{i \neq l} \left(T^{*(k)\circ}_i \cap T^{*(k)\circ}_j\right), \tag{5.5}$$

$$T \in \Omega_h,\ T^{*(k)} \in \Omega^{*(k)}_h\ k = x, y, z.$$

Figure 42 depicts the staggered meshes $\Omega^{*(k)}_h$ next to the main grid Ω_h in two and three space-dimensions in the purely Cartesian case, i.e. $\ell_{\max} = 0$ and $N^{(k)}_{i-\text{faces}} = 2$.

Whenever AMR is considered the starred notation for the refinement meshes is used, i.e. $\Omega^{*(k)}_h$ for the dual-staggered active grid and $\Omega^{\ell*(k)}_h$ for the dual-staggered grid of refinement level ℓ. Furthermore, for $\Omega^{*(k)}_h$ a simple trick becomes necessary in order to satisfy condition (5.4). Indeed, if uniform Cartesian elements are used for the dual elements T^*_m, centered in $\mathbf{x}^*_m$, then some *new kind of elements*, characterized by a different mesh size ratio, need to be defined. An u.s. element T^*_u appears in the dual computational domain Ω^*_h wherever two *neighbor* and *active* elements T_i and T_j belong to adjacent refinement levels, i.e. $T_i \in \Omega^\ell_h$, $T_j \in \Omega^{\ell+1}_h$ with $\beta_i = \beta_j = 0$. Figure 43 gives an illustration of the resulting staggered adapted grid $\Omega^{*(x)}_h$ next to Ω_h. The peculiarity of such *unusual staggered* (u.s.) elements will arise in the definition of the discrete solution. For the sake of simplicity, N_{faces} will take account also of the number of u.s. dual elements belonging to Ω^*_h. An auxiliary value for labeling the refinement level of the u.s. elements T^*_u is given by the fractional intermediate index $\ell(T^*_u) = (\ell(T_i) + \ell(T_j))/2$. Finally, referring to an u.s. element T^*_u, the corresponding face Γ_u should not exist, but is can be imposed to be equal to the void set $\varnothing$. Similarly the right and left element of Γ_u are chosen to be $l(u) = r(u) \equiv i$, where $T^*_u \subset T_i$.

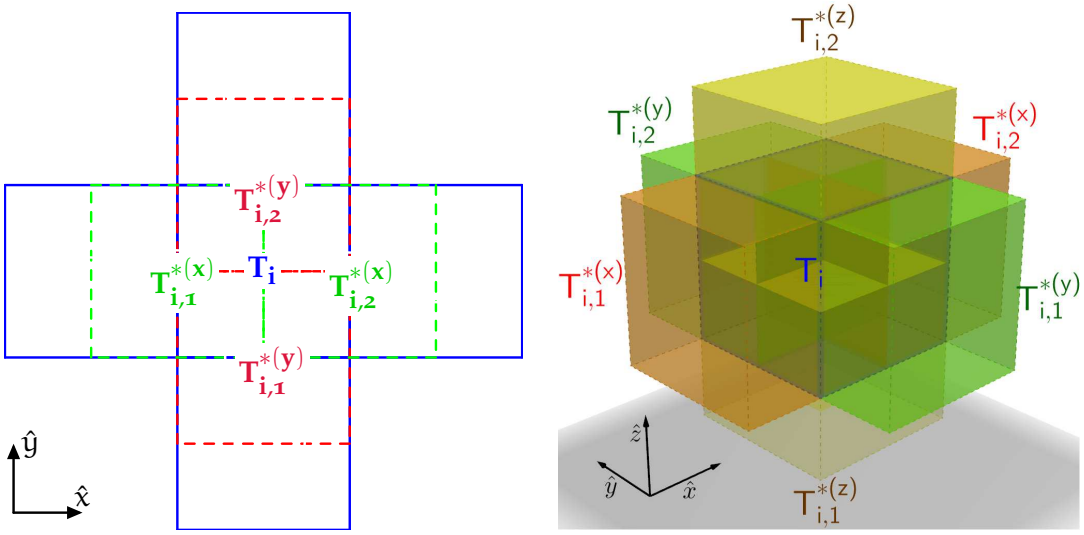

Figure 42: Mesh-staggering for the two dimensional (left) and for the three-dimensional (right) purely-Cartesian case, i.e. in our notation $\ell_{max} = 0$ and consequently $\Omega_h \equiv \Omega_h^{\ell=0}$ and $N^{(k)}_{i-faces} = 2$, with $k = x, y, z$. The staggered elements $T^{*(k)} \in \Omega_h^{*(k)}$ corresponding to the faces of $T_i \in \Omega_h$ in the x-th, y-th (for d=2) and z-th (for d=3) direction are shown and highlighted in red, green and ocher, respectively. For the 2d case, the nearest neighbor elements of T_i are shown and highlighted in blue. In our notation the following correspondence holds $(T^{*(x)}_{i,1}, T^{*(x)}_{i,2}, T^{*(y)}_{i,1}, T^{*(y)}_{i,2}, T^{*(z)}_{i,1}, T^{*(z)}_{i,2}) = (T^*_{i,1}, T^*_{i,2}, T^*_{i,3}, T^*_{i,4}, T^*_{i,5}, T^*_{i,6})$ for the $d = 3$ case. (See colored version online)

Similarly, also the faces of the dual elements, i.e. the *dual faces* $\Gamma^{*(k)}_i \in \partial T^{*(k)}_m$, can be defined, and the respective *dual right* $r^*(i)$ and *dual left* $l^*(i)$ elements can be identified. These set of dual faces are slightly sophisticated and are used rarely in the text. Then, in order to simplify the notation, we define only the dual edges whose points lie within a given space element, i.e. the faces $\Gamma^{*(k)}_i \in \partial T^{*(k)}_m$ for $k = x$, y, z such that $\Gamma^{*(k)}_i \subset \partial T_i$ Once the main and staggered adaptive meshes are fully defined, in the following section the space of discrete solutions of our SI-DG-P_N method is outlined.

5.3 SPACE OF SOLUTIONS P_N ON STAGGERED AMR MESHES

In the DG framework, the discrete solution is defined in the space of piecewise polynomials of maximum degree N with discontinuities along the faces of the elements of the computational mesh. Then, given a reference mesh $\tilde{\Omega}$, the corresponding vector space of piecewise polynomials of maximum degree $N \in \mathbb{N}_0^+$ is called $P_N(\tilde{\Omega})$. In particular, in the staggered-DG formulation with adaptive mesh refinement, we look for piecewise polynomials $P(\mathbf{x})$, $\mathbf{x} \in \tilde{\Omega}$ where $\tilde{\Omega}$ is one of the considered meshes, i.e. $\tilde{\Omega} \in \{\Omega_h, \Omega_h^{*(k)}\}_{k=x,y,z}$. Similar to [115, 97], the discrete solution in every single space element $\tilde{T}_i \in \tilde{\Omega}$ is written according to the same but

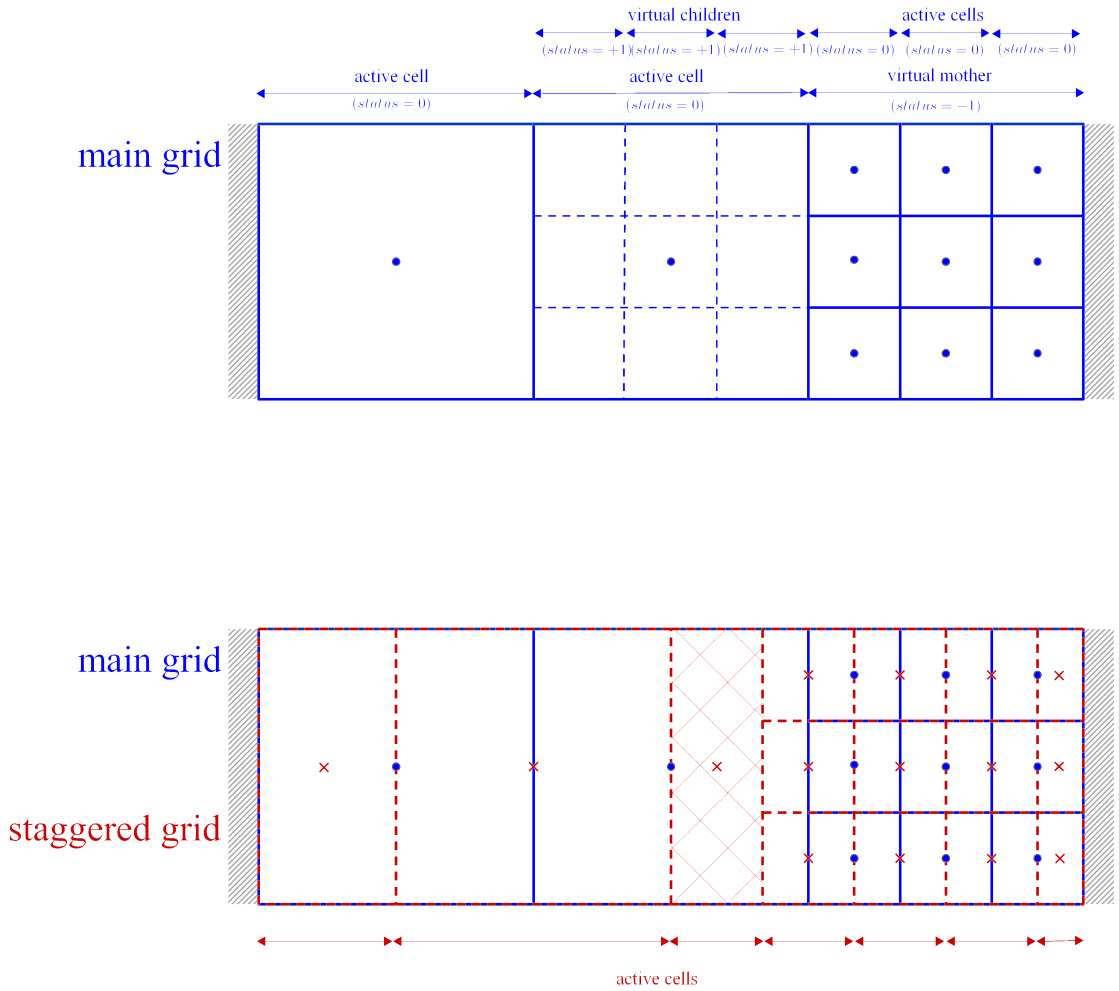

Figure 43: Schematic two dimensional view of the adopted cell by cell AMR framework (top), and the chosen spatially staggered and adaptively refined grid, e.g., in the in x direction $\Omega_h^{*(x)}$ (highlighted in red at the bottom). In particular, the *anomalous* dual element, over which the pressure is continuous, is highlighted by a checkered texture (See colored version online)

shifted *one-dimensional* polynomial basis $\mathcal{B}_N = \{\varphi_l(x)\}_{l=0,N}$ along its own control volume $x \in \Delta\tilde{s}_k(\tilde{\mathbf{x}}_i)$, for *each* spatial dimension $k = x, y, z$.

In order to transform the numerical solution from a coarser level ℓ to the finer $\ell+1$ and *vice versa* (see figure 44) suitable L_2 *projection* $\mathcal{P}$ and *average* $\mathcal{A}$ operators are defined in the form

$$P_N(\Omega_h^{\ell+1}) \ni P_c^{\ell+1} = \mathcal{P}\left(P_i^{\ell}\right): \qquad \left\langle \omega^{\ell+1}, P_c^{\ell+1}\right\rangle_{T_c} = \left\langle \omega^{\ell+1}, P_i^{\ell}\right\rangle_{T_c}, \quad \forall T_c \subset T_i,\ T_c \in \Omega_h^{\ell+1},\ T_i \in \Omega_h^{\ell}; \tag{5.6}$$

$$P_N(\Omega_h^{\ell}) \ni P_i^{\ell} = \mathcal{A}\left(\{P_c^{\ell+1}\}\right): \qquad \left\langle \omega^{\ell}, P_i^{\ell}\right\rangle_{T_i} = \sum_{T_c \subset T_i} \left\langle \omega^{\ell}, P_c^{\ell+1}\right\rangle_{T_c}, \quad T_c \in \Omega_h^{\ell+1},\ T_i \in \Omega_h^{\ell}; \tag{5.7}$$

where $\langle\cdot,\cdot\rangle$ is the scalar product

$$\langle f, g\rangle_{T_i} = \int_{T_i} f\, g\, d\mathbf{x} \qquad f, g \in L^2 \tag{5.8}$$

and

$$\omega_{|_{T_i}}(s) = \varphi(\xi_1) \otimes \varphi(\xi_2) \otimes \varphi(\xi_3),$$
$$\text{with} \qquad s = \mathbf{x}_i + \sum_k \left(\xi_k - \frac{1}{2}\right) \Delta x_k^{\ell(T_i)}(\mathbf{x}_i)\hat{x}^{(k)}. \quad 0 \leqslant \xi_1, \xi_2, \xi_3 \leqslant 1,$$

defines the *shifted* basis polynomials, centered in the barycenter $\mathbf{x}_i$ of $T_i \in \Omega_h^{\ell}$ and written in tensor form. If φ is the vector of the basis elements $(\varphi_1, \varphi_2, \ldots, \varphi_{N+1})$, then $\omega_{|_{T_i}}$ is the vector of the *shifted* basis elements $(\omega_1, \omega_2, \ldots, \omega_{(N+1)^d})_{|_{T_i}}$ generating the three dimensional basis $\mathcal{B}_{N,i}^d \equiv \mathcal{B}_{N,i} \otimes \mathcal{B}_{N,i} \otimes \mathcal{B}_{N,i}$, for any $T_i \in \Omega_h^{\ell}$, for any piecewise polynomial $P^{\ell} \in P_N(T_i)$. Then P can be expanded along the basis in the form

$$P(x) = \sum_l \frac{\langle \omega_l(x), P(x)\rangle_{T_i}}{\|\omega_l\|^2_{T_i}} \omega_l \equiv \sum_l P_l \omega_l \equiv \mathbf{P} \cdot \omega(x) \tag{5.9}$$

where $\mathbf{P}$ is called to be the vector of the *degrees of freedom* of P, $\|\cdot\|$ is the norm related to the chosen scalar product. Moreover, if one chooses $\mathcal{B}_N^d$ to be a *nodal* basis then the following equivalence holds: $P_l \equiv P(x_l^{GL})$ with a large gain in computational effort, specially at higher space-dimensions when three-dimensional coefficient matrices can be written in a tensor combination of one dimensional matrices. In our scheme, the basis functions are given by the Lagrange interpolation polynomials passing through the Gauss-Legendre quadrature nodes.

In this work, although each physical variable will be defined referring to *a proper and given computational mesh* (main or dual), it becomes useful defining the transformation rules for projecting from one vector space $P \in P_N(\Omega_h)$ to a corresponding

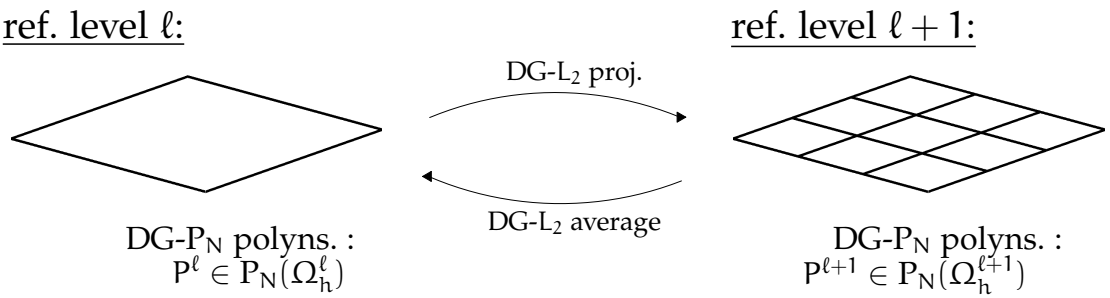

Figure 44: Simple sketch of the polynomial mapping between two adjacent refinement levels ℓ and $\ell+1$, i.e. the L_2 projection and average.

staggered one $P^* \in P_N(\Omega_h^{*(k)})$, i.e. satisfying the classical L_2 projection equations, i.e.

$$P^* = \pi^{*(k)}(P): \qquad \langle \psi, P^* \rangle_{T_m^{*(k)}} = \langle \psi, P \rangle_{T_m^{*(k)}} \qquad \forall T_m^{*(k)} \in \Omega_h^{*(k)} \tag{5.10}$$

$$P = \pi(P^*): \qquad \langle \omega, P \rangle_{T_i} = \langle \omega, P^* \rangle_{T_i}; \qquad \forall T_i \in \Omega_h \tag{5.11}$$

where the vectors of the *shifted* polynomial basis element ψ are given by

$$\psi_{|_{T_{ij}^{*(k)}}}(s) = \varphi(\xi_1) \otimes \varphi(\xi_2) \otimes \varphi(\xi_3), \tag{5.12}$$

$$\text{with } s = \mathbf{x}_m^{*(k)} + \sum_k \left(\xi_k - \frac{1}{2}\right) \Delta x_k^{\ell(T_{ij}^{*(k)})}(\mathbf{x}_m^{*(k)}) \hat{\mathbf{x}}^{(k)}, \quad 0 \leqslant \xi_1, \xi_2, \xi_3 \leqslant 1,$$

i.e. polynomials $\psi(\mathbf{s} \in T_{ij}^{*(k)})$ centered in the barycenter $\mathbf{x}_m^{*(k)}$ of $T_m^{*(k)} \in \Omega_h^{*(k)}$ and written in tensor form; k labels the direction of the staggering for $\Omega_h^{*(k)}$ ($k = x$, y or z).

Because of the tensor definition of the polynomial basis, a generic coefficient matrix $\mathbf{A}$ operating over a generic vector of degrees of freedom X can be written as

$$\mathbf{A} \equiv \mathbf{A}^{xyz} \equiv \mathbf{A}^x \otimes \mathbf{A}^y \otimes \mathbf{A}^z,$$
$$\widehat{\mathbf{x}} \equiv \{\hat{x}_l\}_{l=1,..,(N+1)^d} \equiv \{\hat{x}_{ll'l''} \equiv \hat{x}_l \otimes \hat{x}_{l'} \otimes \hat{x}_{l''}\}_{l,l',l''=1,..,N+1},$$

where the components $\mathbf{A}^k$ operate along the respective k-th index of the generic vector of degrees of freedom $\widehat{\mathbf{X}}$. Whenever a k-th direction is specified, an identity operator is assumed in the other directions, i.e.

$$'\mathbf{A}^{x\prime} \equiv \mathbf{A}^x \otimes \mathbb{I} \otimes \mathbb{I}, \qquad '\mathbf{A}^{y\prime} \equiv \mathbb{I} \otimes \mathbf{A}^y \otimes \mathbb{I}, \qquad '\mathbf{A}^{z\prime} \equiv \mathbb{I} \otimes \mathbb{I} \otimes \mathbf{A}^z,$$
$$'\mathbf{A}^{xy\prime} \equiv '\mathbf{A}^x \cdot \mathbf{A}^{y\prime} = (\mathbf{A}^x \cdot \mathbb{I}) \otimes (\mathbb{I} \cdot \mathbf{A}^y) \otimes (\mathbb{I}^2) = \mathbf{A}^x \otimes \mathbf{A}^y \otimes \mathbb{I},$$
$$'\mathbf{A}^{xz\prime} \equiv '\mathbf{A}^x \cdot \mathbf{A}^{z\prime} = (\mathbf{A}^x \cdot \mathbb{I}) \otimes (\mathbb{I}^2) \otimes (\mathbb{I} \cdot \mathbf{A}^z) \equiv \mathbf{A}^x \otimes \mathbb{I} \otimes \mathbf{A}^z,$$
$$'\mathbf{A}^{yz\prime} \equiv '\mathbf{A}^y \cdot \mathbf{A}^{z\prime} = (\mathbb{I}^2) \otimes (\mathbf{A}^y \cdot \mathbb{I}) \otimes (\mathbb{I} \cdot \mathbf{A}^z) \equiv \mathbb{I} \otimes \mathbf{A}^y \otimes \mathbf{A}^z, \tag{5.13}$$

where $\mathbb{I}$ is the identity operator. Then, after evaluating the definite integrals of the known basis functions, one gets from the definitions (5.6-5.7)

$$\left.\begin{aligned} \langle \omega_l, P \rangle_{T_i} &= \mathbf{M}_{lm|_{T_i}} \hat{P}_m \\ \langle \omega_l, P^* \rangle_{T_i} &= \sum_{\Gamma_j \in \partial T_i^{(k)}} \mathbf{M}_{lm}^{\sigma(i,j,k)} \hat{P}^*_{m|_{T_{ij}^{(k)}}} \end{aligned}\right\} \quad \Rightarrow \quad \hat{P}_l = \mathbf{M}^{-1}_{lm|_{T_i}} \sum_{\Gamma_j \in \partial T_i^{(k)}} \mathbf{M}_{mn}^{\sigma(i,j,k)} \hat{P}^*_{n|_{T_{ij}^{(k)}}} \tag{5.14}$$

$$\left.\begin{aligned} \langle \psi_l, P^* \rangle_{T_c^{*(k)}} &= \mathbf{M}_{lm|_{T_c^{*(k)}}} \hat{P}^*_m \\ \langle \psi_l, P \rangle_{T_c^{*(k)}} &= \sum_{\Gamma_j^* \in \partial T_c^{*(k)}} \mathbf{M}_{lm}^{\sigma^*(c,j,k)} \hat{P}_{m|_{T_{cj}^{*(k)}}} \end{aligned}\right\} \quad \Rightarrow \quad \hat{P}^*_l = \mathbf{M}^{-1}_{lm|_{T_c^{*(k)}}} \sum_{\Gamma_j^* \in \partial T_i^{*(k)}} \mathbf{M}_{mn}^{\sigma^*(c,j,k)} \hat{P}_{n|_{T_{cj}^{*(k)}}} \tag{5.15}$$

where the summation is intended over the j-th faces of T_i in the direction of the staggering, i.e. the k-th, backward and forward; $\sigma(i,j,j)$ labels the mutual position and refinement of T_i and the corresponding dual element $T_{ij}^{(k)}$. Some new matrices have been defined to be

$$\begin{aligned} \mathbf{M}_{|_{T_i}} &= \left\{ M_{pq|_{T_i}} \right\}_{p,q=1,..,(N+1)^d} = \left\{ \frac{1}{|T_i|} \int_{T_i} \omega_{p|_{T_i}}(\xi)\, \omega_{q|_{T_i}}(\xi)\, d\xi \right\}_{p,q=1,..,(N+1)^d} \\ \mathbf{M}_{|_{T_c^{*(k)}}} &= \left\{ M_{pq|_{T_c^{*(k)}}} \right\}_{p,q=1,..,(N+1)^d} \equiv \mathbf{M}_{|_{T_i}} \\ \mathbf{M}^{\sigma(i,j,k)} &= \left\{ \mathbf{M}_{pq}^{\sigma(i,j,k)} \right\}_{p,q=1,..,(N+1)^d} \\ &= \left\{ \frac{1}{\min(|T_i|, |T_{ij}^{*(k)}|)} \int\limits_{T_i \cap T_{ij}^{*(k)}} \omega_{p|_{T_i}}(\xi)\, \psi_{q|_{T_{ijk}^{*(k)}}}(\xi)\, d\xi \right\}_{p,q=1,..,(N+1)^d} \\ \mathbf{M}^{\sigma^*(c,j,k)} &= \left\{ \mathbf{M}_{pq}^{\sigma^*(c,j,k)} \right\}_{p,q=1,..,(N+1)^d} \\ &= \left\{ \frac{1}{\min(|T_c^*|, |T_{cj}^{(k)}|)} \int\limits_{T_c^* \cap T_{cj}^{(k)}} \psi_{p|_{T_c^*}}(\xi)\, \omega_{q|_{T_{cjk}^{(k)}}}(\xi)\, d\xi \right\}_{p,q=1,..,(N+1)^d} \end{aligned} \tag{5.16}$$

where $|\cdot|$ denotes the volume of the corresponding space-element, $\mathbf{M}$ is the *mass matrix* which is diagonal according to the chosen polynomial basis, it is positive definite and it gives the projection coefficients between the piecewise polynomials of $P_N(T_i)$; $\mathbf{M}^{-1}$ is its inverse; ω_q is the p-th basis polynomial centered for $P_N(T_i)$; ψ_p is the p-th basis polynomial for $P_N(T_{ij}^{*(k)})$; p ranging from $p = 1, 2, \ldots (N+1)^d$; $\mathbf{M}^\sigma$ or $\mathbf{M}^{\sigma^*}$ are the so-called '*swap-mass matrices*', and give the projection coefficients between the piecewise polynomial basis of $P_N(T_i)$ and $P_N(T_{ij}^{*(k)})$. Notice that a swap-matrix is defined as the integral of the respective basis elements, within the shared (swap) space domain $T_i \cap T_{ij}^{*(k)}$, which spatial characteristic size is of the same order of the *minimum* between the characteristic sizes of the two intersected elements. Indeed, in principle, the two elements T_i and $T_{ij}^{*(k)}$ are allowed to belong to different refinement level. It is important to stress the fact that, with

a little linear algebra, the aforementioned three-dimensional tensors can be written in a simpler and versatile composition of one-dimensional $(N+1)\times(N+1)$ matrices. It can be shown that then the following symmetry property holds

$$\mathbf{M}^{\sigma^*(c,j,k)} = \left(\mathbf{M}^{\sigma(i,\tilde{j},\tilde{k})}\right)^T \qquad \text{if } T_c^* \equiv T_{ij}^{*(\tilde{k})} \text{ and } T_i \equiv T_{cj}^{(k)}.$$

5.4 A SEMI-IMPLICIT TIME DISCRETIZATION

Since our SI-DG method on adaptive Cartesian staggered meshes collapses to the uniform-grid case after setting maximum refinement levels $\ell_{max} = 0$, then in this section the numerical strategy for the semi-implicit time discretization is outlined directly within the AMR framework. Once the main and the staggered grids have been defined, the space of discrete solutions P_N is outlined, then the numerical method follows the procedure of [115].

5.4.1 *Spectral SI-DG on staggered AMR grids*

A weak formulation of the governing equations (5.1-5.2) is considered in the form

$$\int_{T_m^{*(k)}} \psi_q \left(\frac{\partial v_k}{\partial t} + \nabla\cdot\mathbf{F}_{v_k} + \partial_{x_k} p \right) d\mathbf{x} = 0, \tag{5.17}$$

$$\int_{T_i} \omega_q \ (\nabla\cdot\mathbf{v})\, d\mathbf{x} = 0, \tag{5.18}$$

$$(x_k, v_k) = (x, v_x), (y, v_y), (z, v_z), \qquad T_m^{*(k)} \in \Omega_h^{*(k)}, \ \ T_i \in \Omega_h$$

where it is important to highlight that the momentum equations are integrated along the *dual* AMR meshes $\Omega_h^{*(k)}$ according to the k-th space-direction, and the incompressibility condition along the main AMR mesh Ω_h; $\psi_q \in \mathcal{B}_N(T_{ij}^{*(k)})$, i.e. the q-th element of the basis for the *dual* vector space $P_N(T_{ij}^{*(k)})$; $\omega_q \in \mathcal{B}_N(T_i)$, i.e. the q-th element of the basis for the vector space $P_N(T_i)$. In this formalism, it is clear that the chosen weak formulation of our staggered DG scheme consists in an L_2 projection of the incompressible Navier-Stokes equations onto the chosen vector space of staggered piecewise polynomials P_N. Then, according to [97, 115], the discrete solution of the staggered DG discretization is defined as follows: the velocity components v_k are approximated in the respective vector spaces of the staggered dual meshes $P_N(\Omega_h^{*(k)})$, while the pressure is defined on the main grid, i.e. in $P_N(\Omega_h)$. Therefore, the respective expansion over the polynomial basis reads

$$v_h^{(k)}(\mathbf{x},t)|_{T_m^{*(k)}} = v_m^{*(k)}(\mathbf{x},t) = \sum_{l=1}^{(N+1)^d} \psi_l(\mathbf{x})\,\hat{v}_l(t)$$
$$\text{for } \mathbf{x} \in T_m^{*(k)}, \quad m = 1,\dots,N_{faces}^{(k)}, \ \ \psi_k \in \mathcal{B}_N(T_m^{*(k)}), \ \ \hat{v}_l \in \mathbb{R} \tag{5.19}$$

$$\boxed{\begin{aligned} p_h(\mathbf{x},t)|_{T_i} &= p_i(\mathbf{x},t) = \sum_{l=1}^{(N+1)^d} \omega_l(\mathbf{x})\,\hat{p}_l(t) \\ &\text{for } \mathbf{x}\in T_i, \quad i=1,\dots,N_{elem}, \quad \omega_l\in\mathcal{B}_N(T_i), \quad \hat{p}_l\in\mathbb{R} \end{aligned}} \tag{5.20}$$

After substituting (5.19) into the incompressibility condition (5.18) one obtains

$$0 = \int_{\partial T_i} \omega_l(\mathbf{x})\,\mathbf{v}_h\cdot\vec{n}\,dS - \int_{T_i}\nabla\omega_l(\mathbf{x})\cdot\mathbf{v}_h\,d\mathbf{x} =$$

$$= \sum_k \left[\int_{\Gamma_m^{(k)}\in\partial T_i} \omega_l(\mathbf{x})\,\mathbf{v}_h\cdot\vec{n}\,dS - \int_{T_m^{*(k)}\cap T_i}\nabla\omega_l(\mathbf{x})\cdot\mathbf{v}_h\,d\mathbf{x}\right]. \tag{5.21}$$

Indeed, exactly because of the chosen C-staggering, $\mathbf{v}_h\cdot\vec{n}$ is well defined along ∂T_i, i.e. all the velocity components are *continuous* along the respective faces $\Gamma_m^{(k)}$; moreover ω_k is continuous in T_i. On the other hand, due to the staggering, the pressure p_h is discontinuous within $T_m^{*(k)}$. Then, after substituting the *ansatz* (5.20) into the momentum equation (5.17), the pressure gradient terms can be written as

$$\int_{T_m^{*(k)}} \psi_l\partial_{x_k}p_h d\mathbf{x} \equiv \int_{T_m^{*(k)}\cap T_{l(m)}} \psi_l\partial_{x_k}p_{l(m)}\,d\mathbf{x} + \int_{T_m^{*(k)}\setminus T_{l(m)}} \psi_l\partial_{x_k}p_{r(m)}\,d\mathbf{x} + \tag{5.22}$$

$$+ \int_{\Gamma_m^{*(k)}} \psi_l\left(p_{r(m)}-p_{l(m)}\right)dS \tag{5.23}$$

where $l(m)$ is the index of the left element with respect to $\Gamma_m^{(k)}$.

Notice that, whenever $T_m^{*(k)}$ is an u.s. element, then $r(m)=l(m)\equiv i$ and then: (i) the surface integral of equation (5.21) vanishes because $\Gamma_m^{(k)}=\varnothing$; (ii) the second volume integral vanishes because $(T_m^{*(k)}\setminus T_{l(m)})\equiv\varnothing$; (iii) the jump term vanishes because $\Gamma_m^{*(k)}\equiv\varnothing$ [1]. Otherwise, if $T_m^{*(k)}$ is a *standard* dual element, the second volume integral is evaluated exactly along the right element of $\Gamma_m^{(k)}$, i.e. $T_{r(m)}\equiv(T_m^*\setminus T_{l(m)})$ independently of the refinement level.

Then, after evaluating the definite integrals of system (5.17-5.18), a semi-implicit higher order DG finite element formulation of the incompressible Navier-Stokes equations on staggered AMR grids reads[2]

$$\boxed{\begin{aligned} &\mathbf{M}^{x_1x_2x_3}\cdot\left(\widehat{\mathbf{V}}_m^{n+1}-\widehat{\mathbf{Fv}}_m^{n}\right)+ \\ &+\frac{\Delta t}{\Delta x_1}\mathbf{M}^{x_2x_3}\cdot\left(\mathbf{R}_v^{x_1\sigma(m,r(m))}\cdot\widehat{\mathbf{P}}_{r(m)}^{n+\theta}-\mathbf{L}_v^{x_1\sigma(m,l(m))}\cdot\widehat{\mathbf{P}}_{l(m)}^{n+\theta}\right)=0, \\ &\qquad\forall T_m^{*(x_1)}\in\Omega_h^{*(x_1)},\ \forall(x_1,x_2,x_3)\in\left\{{}^{x}_{z}\circlearrowright{}^{y}\right\} \end{aligned}} \tag{5.24}$$

1 In principle, for u.s. elements, $\Gamma_m^{*(k)}$ is something indefinite, and it can be set to be $\Gamma_m^{*(k)}\equiv\varnothing$. This definition is a way of stating the pressure of being continuous inside $T_m^{*(k)}$. Indeed, for u.s. elements it holds $T_m^{*(k)}\subset T_{r(m)\equiv l(m)}$.

2 Symbol $\left\{{}^{a}_{c}\circlearrowright{}^{b}\right\}$ denotes the standard cyclic (or circular) permutations of (a,b,c): i.e. $\{(a,b,c),(b,c,a),(c,a,b)\}$.

$$\boxed{\sum_{x_1=x,y,z}\ \sum_{\Gamma_i^{*(x_1)}\subset T_i} \Delta x_2\Delta x_3\ \mathbf{M}^{x_2x_3}\left(\mathbf{R}_p^{x_1\sigma^*(i,r^*(i))}\cdot\widehat{\mathbf{V}}_{r^*(i)}^{n+1}-\mathbf{L}_p^{x_1\sigma^*(i,l^*(i))}\cdot\widehat{\mathbf{V}}_{l^*(i)}^{n+1}\right)=0,\quad \text{with}\ \ (x_1,x_2,x_3)\in\left\{{}^{x_1}_{x_3}\bigcirc^{x_2}\right\}} \tag{5.25}$$

The momentum equation (5.24) has been normalized with respect to the volume of $T_m^{*(k)}$ divided by the time step Δt which is intended in the classical sense $\Delta t = t^{n+1}-t^n$; $\widehat{\mathbf{V}}$ is the vector of the degrees of freedom of the x_1-th velocity component; $l^*(i)$ and $l^*(i)$ are the integer indexes of the right and left *dual* elements $T_m^{*(x_1)}$ and $T_n^{*(x_1)}$ that shares[3] the dual face $\Gamma_i^{*(x_1)}$. $\sigma(m,j)$ and $\sigma^*(j,m)$ labels the mutual position and refinement of face $\Gamma_m^{(x_1)}$ respect to element T_j, the dual face $\Gamma_i^{*(x_1)}$ respect to the dual element $T_m^{*(x_1)}$, respectively; the implicitness factor $\theta\in[0.5,1]$ has been introduced for the implicit time-discretization of the pressure gradients in the form $X^\theta=\theta X^{n+1}+(1-\theta)X^n$; note that if $\theta=1/2$ the well known second order Crank-Nicolson time discretization is obtained. $\widehat{\mathbf{Fv}}^n$ collects the advective-diffusive terms that can be approximated by means of a fully explicit or a proper semi-implicit discretization within am operator-splitting scheme. Further details will appear in the next sections. The following three-dimensional *swap*-matrices have been introduced

$$\begin{aligned}\mathbf{R}_v^{\sigma(m,r(m))} &= \left\{\frac{\int_{\Gamma_m}\psi_p|_{T_m^*}\,\omega_q|_{T_{r(m)}}\,dS}{|\Gamma_m|}+\frac{\int_{T_m^*\cap T_{r(m)}}\psi_p|_{T_m^*}\,\frac{\partial\omega_q}{\partial x_1}|_{T_{r(m)}}\,dx}{\min(|T_m^*|,|T_{r(m)}|)}\right\}_{p,q=1,..,(N+1)^d}\\ &\equiv \left\{\tilde{\mathcal{R}}_{pq}\right\}_{p,q=1,..,(N+1)^d}\equiv\mathbf{M}^{x_2x_3}\mathbf{R}_v^{x_1\sigma(m,r(m))}\end{aligned} \tag{5.26}$$

$$\begin{aligned}\mathbf{L}_v^{\sigma(m,l(m))} &= \left\{\frac{\int_{\Gamma_m}\psi_p|_{T_m^*}\,\omega_q|_{T_{l(m)}}\,dS}{|\Gamma_m|}-\frac{\int_{T_m^*\cap T_{l(m)}}\psi_p|_{T_m^*}\,\frac{\partial\omega_q}{\partial x_1}|_{T_{l(m)}}\,dx}{\min(|T_m^*|,|T_{l(m)}|)}\right\}_{p,q=1,..,(N+1)^d}\\ &\equiv \left\{\tilde{\mathcal{L}}_{pq}^{\sigma(m,l(m))}\right\}_{p,q=1,..,(N+1)^d}\equiv\mathbf{M}^{x_2x_3}\mathbf{L}_v^{x_1\sigma(m,l(m))}\end{aligned} \tag{5.27}$$

3 In this notation the integrals of eq. (5.21) break into the summations

$$\int_{\partial T_i}\longrightarrow\sum_{x_1}\ \int_{\Gamma_m^{(x_1)}\in\partial T_i}\longrightarrow\sum_{x_1}^{(0)}\ \sum_{\Gamma_i^{*(x_1)}\subset T_i}^{(1)}\ \sum_{n=l^*(i),r^*(i)}^{(2)}\ \int_{\Gamma_n^{(x_1)}},$$

where the first summation (1) is intended over all the dual faces $\Gamma_i^{*(x_1)}$ within T_i; the second summation (2) is intended over the right and left (or forward and backward) dual elements $T_{r^*(i)}^{*(x_1)}$ and $T_{l^*(i)}^{*(x_1)}$ that shares the corresponding dual face $\Gamma_i^{*(x_1)}$.

$$\begin{aligned}
\mathbf{R}_p^{\sigma(i,r^*(i))} &= \left\{ \frac{\int_{\Gamma_i^*} \omega_{p|_{T_i}} \psi_{q|_{T^*_{r^*(i)}}} \, dS}{|\Gamma_i^*|} - \frac{\int_{T_i \cap T^*_{r^*(i)}} \omega_{p|_{T_i^*}} \frac{\partial \psi_q}{\partial x_1}|_{T^*_{r^*(i)}} \, dx}{|T_i|, \min(|T^*_{r^*(i)}|)} \right\}_{p,q=1,..,(N+1)^d} \\
&\equiv \left\{ \bar{\mathcal{R}}_{pq}^{\sigma^*(i,r^*(i))} \right\}_{p,q=1,..,(N+1)^d} \equiv \mathbf{M}^{x_2 x_3} \mathbf{R}_p^{x_1 \sigma^*(i,r^*(i))}
\end{aligned} \tag{5.28}$$

$$\begin{aligned}
\mathbf{L}_p^{\sigma(i,l^*(i))} &= \left\{ \frac{\int_{\Gamma_i^*} \omega_{p|_{T_i}} \psi_{q|_{T^*_{l^*(i)}}} \, dS}{|\Gamma_i^*|} + \frac{\int_{T_i \cap T^*_{l^*(i)}} \omega_{p|_{T_i}} \frac{\partial \psi_q}{\partial x_1}|_{T^*_{l^*(i)}} \, dx}{\min(|T_i|, |T^*_{l^*(i)}|)} \right\}_{p,q=1,..,(N+1)^d} \\
&\equiv \left\{ \bar{\mathcal{L}}_{pq}^{\sigma^*(i,l^*(i))} \right\}_{p,q=1,..,(N+1)^d} \equiv \mathbf{M}^{x_2 x_3} \mathbf{L}_p^{x_1 \sigma^*(i,l^*(i))}.
\end{aligned} \tag{5.29}$$

where x_1 is the normal direction with respect to edge Γ_m and Γ_i^*, x_2 and x_3 the rest orthogonal directions. The most-significant property of the above-defined matrices is the symmetry

$$\begin{aligned}
\mathbf{R}_p^{\sigma(i,r^*(i))} &= \left(\mathbf{L}_v^{\sigma(m,l(m))} \right)^T \qquad \text{if } T_m^* \equiv T^*_{r^*(i)} \text{ and } T_i \equiv T_{l(m)}, \\
\mathbf{L}_p^{\sigma(i,l^*(i))} &= \left(\mathbf{R}_v^{\sigma(m,r(m))} \right)^T \qquad \text{if } T_m^* \equiv T^*_{l^*(i)} \text{ and } T_i \equiv T_{r(m)}.
\end{aligned}$$

Because of the symmetry between the aforementioned matrices (see also [115] for the purely Cartesian case), it becomes simpler to introduce the following notation

$$\mathcal{R} \equiv \mathbf{R}_v \equiv \mathbf{L}_p^T, \qquad \mathcal{L} \equiv \mathbf{L}_v \equiv \mathbf{R}_p^T. \tag{5.30}$$

It should be noticed that equations (5.24-5.25) constitute a particular coupled equation system with a typical *saddle point structure* which is typical for any discrete formulation of the incompressible Navier-Stokes equations. The total number of unknowns of the system is large, since we have N_{elem} space-elements, each element with $(N+1)^d$ degrees of freedom. In principle, a direct solution can become cumbersome, since it involves four unknown quantities per degree of freedom: three velocity components and the scalar pressure. The complexity of the problem can be considerably reduced with a very simple manipulation.

A well known numerical strategy, widely used for solving such a complex linear systems, is the application of the *Schur complement* to the saddle point system (5.24-5.25). In the context of staggered grids, this procedure has been successfully adopted in the field of ocean modeling and free-surface dynamics [61, 55, 56], physiological fluid flows in the arterial system [64, 117], compressible fluids [110, 98] and a novel family of higher order DG methods [97, 252, 253, 254, 255, 115]

which inspired this work. After multiplying equation (5.17) by the inverse of the element mass matrix $\mathbf{M}$, i.e.

$$\widehat{\mathbf{V}}_m^{n+1} = \widehat{\mathbf{Fv}}_m^n - \frac{\Delta t}{\Delta x_1}(\mathbf{M}^{x_1})^{-1} \cdot \left(\mathbf{R}_v^{x_1\sigma(m,r(m))} \cdot \widehat{\mathbf{P}}_{r(m)}^{n+\theta} - \mathbf{L}_v^{x_1\sigma(m,l(m))} \cdot \widehat{\mathbf{P}}_{l(m)}^{n+\theta}\right), \quad \forall T_m^{*(x_1)} \in \Omega_h^{*(x_1)},\ \forall (x_1,x_2,x_3) \in \{{}^{x}_{y}\bigcirc_{z}\} \tag{5.31}$$

and a direct substitution of equation (5.17) into (5.18), the following linear algebraic system for the pressure degrees of freedom as the only unknowns is obtained:

$$\boxed{\mathbb{H} \cdot \mathcal{P}^{n+\theta} \equiv \mathcal{b}^n} \tag{5.32}$$

in which operator $\mathbb{H}$ is the block coefficient matrix representing the discrete Laplace operator for the pressure Poisson equation in the space of solutions P_N within the chosen staggered-mesh framework; $\mathcal{P}^{n+\theta} = \theta\mathcal{P}^{n+1} + (1-\theta)\mathcal{P}^n$ is the complete vector of the degrees of freedom for the pressure; $\mathcal{b}^n$ collects all the known terms, i.e. the non-linear advection and diffusion, see Section 5.4.2. In particular, $\mathcal{P}^{n+\theta}$ multiplied by the i-th row of $\mathbb{H}$ reads

$$\boxed{\mathbb{H}^i \cdot \mathcal{P}^{n+\theta} \equiv \sum_{\{{}^{x_1}_{x_3}\bigcirc_{x_2}\}} \sum_{\Gamma_i^{*(x_1)} \subset T_i} \frac{\Delta x_2 \Delta x_3}{\Delta x_1} \mathbf{M}^{x_2x_3} \left(\mathbb{R}_i^{x_1} \cdot \widehat{\mathbf{P}}_{r(r^*(i))}^{n+\theta} + \mathbb{L}_i^{x_1} \cdot \widehat{\mathbf{P}}_{l(l^*(i))}^{n+\theta} + \mathbb{C}_i^{x_1} \cdot \widehat{\mathbf{P}}_i^{n+\theta}\right).} \tag{5.33}$$

where

$$\begin{aligned}
\mathbb{R}_i &= -\mathcal{L}^T\mathbf{M}^{x_1}\mathcal{R} &&= -\mathbf{R}_p^{x_1\sigma^*(i,r^*(i))}\mathbf{M}^{x_1}\mathbf{R}_v^{x_1\sigma(r^*(i),r(r^*(i)))} &&\equiv \mathbb{L}_{i+1}^T \\
\mathbb{L}_i &= -\mathcal{R}^T\mathbf{M}^{x_1}\mathcal{L} &&= -\mathbf{L}_p^{x_1\sigma^*(i,l^*(i))}\mathbf{M}^{x_1}\mathbf{L}_v^{x_1\sigma(l^*(i),l(l^*(i)))} &&\equiv \mathbb{R}_{i-1}^T \\
\mathbb{C}_i &= \mathcal{L}^T\mathbf{M}^{x_1}\mathcal{L} + \mathcal{R}^T\mathbf{M}^{x_1}\mathcal{R} &&= \mathbf{R}_p^{x_1\sigma^*(i,r^*(i))}\mathbf{M}^{x_1}\mathbf{L}_v^{x_1\sigma(r^*(i),l(r^*(i)))} + \\
& && \quad + \mathbf{L}_p^{x_1\sigma^*(i,l^*(i))}\mathbf{M}^{x_1}\mathbf{R}_v^{x_1\sigma(l^*(i),r(l^*(i)))} &&\equiv \mathbb{C}_i^T
\end{aligned} \tag{5.34}$$

Notice that $l(l^*(i))$ labels the space-element $T_{l(l^*(i))}$ at the left of edge $\Gamma_{l^*(i)}$, corresponding to the *dual* space-element $T^*_{l^*(i)}$ at the left of the *dual* edge Γ_i^*, corresponding to T_i. In the one-dimensional and purely Cartesian case, $l(l^*(i))$ corresponds to the T_{i-1} left element, $l^*(i)$ to the $T^*_{i-1/2}$ left *dual* element. Moreover, it holds $r(l^*(i)) \equiv l(r^*(i)) \equiv i$. In AMR meshes, several neighbors element in one single direction could exist. It can be explicitly shown that the Laplace operator $\mathbb{H}$ can be decomposed into a more familiar composite matrix product, i.e.

$$\mathbb{H} \equiv \mathcal{D}^T\mathbb{M}^{-1}\mathcal{D},$$

where $\mathcal{D}$ is the *discrete-weak gradient* operator obtained after an L_2 projection of the gradient ∇ in the vector space $P_N(\Omega_h^*)$, i.e.

$$\mathcal{D}_{x_1}^m \mathcal{P} \equiv \frac{\langle \psi, \partial_{x_1} p_h\rangle_{T_m^{*(x_1)}}}{\langle \psi, \psi\rangle_{T_m^{*(x_1)}}} = \frac{\mathcal{R}\cdot\widehat{\mathbf{P}}_{r(m)} - \mathcal{L}\cdot\widehat{\mathbf{P}}_{l(m)}}{\Delta x_1}, \quad \forall T_m^{*(x_1)} \in \Omega_h^*,\ x_1 = x,y,z; \tag{5.35}$$

and the transposed $\mathcal{D}^T$ is the *discrete-weak divergence* $(\nabla\cdot)$. Indeed, matrix $\mathbb{H}$ can be written in the form of a tensor product of the matrices $\mathbb{H} = \mathbb{H}^{xyz} = \mathbb{H}^x\mathbb{H}^y\mathbb{H}^z$. Next, the positive semi-definiteness is shown to be valid for the one-dimensional case $\mathbb{H} = \mathbb{H}^x$, then the extension to $\mathbb{H} = \mathbb{H}^{xyz}$ is straightforward. If $d = 1$, periodic boundary conditions are assumed and dropping the indexing of the coefficient matrices for simplicity, then, the global system can be written as

$$
\begin{aligned}
&\mathbb{H}\cdot\mathcal{P}^{n+1} \equiv \\
&\begin{pmatrix}
\mathbb{C}_1 & \mathbb{R}_1 & 0 & \ddots & 0 & \mathbb{L}_1 \\
\mathbb{L}_2 & \mathbb{C}_2 & \mathbb{R}_2 & 0 & \cdot & 0 \\
0 & \mathbb{L}_3 & \mathbb{C}_3 & \mathbb{R}_3 & \ddots & \vdots \\
\vdots & \ddots & \ddots & \ddots & \ddots & 0 \\
0 & \cdot & 0 & \mathbb{L}_{N_x-1} & \mathbb{C}_{N_x-1} & \mathbb{R}_{N_x-1} \\
\mathbb{R}_{N_x} & 0 & \cdots & 0 & \mathbb{L}_{N_x} & \mathbb{C}_{N_x}
\end{pmatrix}
\cdot
\begin{pmatrix}
\widehat{\mathbf{P}}_1^{n+1} \\ \widehat{\mathbf{P}}_2^{n+1} \\ \vdots \\ \vdots \\ \widehat{\mathbf{P}}_{N_x-1}^{n+1} \\ \widehat{\mathbf{P}}_{N_x}^{n+1}
\end{pmatrix} \equiv \\
&\begin{pmatrix}
-\mathcal{L}^T & 0 & \cdots & 0 & \mathcal{R}^T \\
\mathcal{R}^T & -\mathcal{L}^T & 0 & 0 & 0 \\
0 & \mathcal{R}^T & -\mathcal{L}^T & \ddots & \vdots \\
\vdots & 0 & \ddots & \ddots & 0 \\
0 & \cdots & 0 & \mathcal{R}^T & -\mathcal{L}^T
\end{pmatrix}
\cdot \mathbb{M}^{-1} \cdot
\begin{pmatrix}
-\mathcal{L} & \mathcal{R} & 0 & \cdots & 0 \\
0 & -\mathcal{L} & \mathcal{R} & 0 & 0 \\
\vdots & 0 & -\mathcal{L} & \ddots & 0 \\
0 & 0 & \ddots & \ddots & \mathcal{R} \\
\mathcal{R} & 0 & \cdots & 0 & -\mathcal{L}
\end{pmatrix}
\cdot
\begin{pmatrix}
\widehat{\mathbf{P}}_1^{n+1} \\ \widehat{\mathbf{P}}_2^{n+1} \\ \vdots \\ \widehat{\mathbf{P}}_{N_x-1}^{n+1} \\ \widehat{\mathbf{P}}_{N_x}^{n+1}
\end{pmatrix},
\end{aligned}
\tag{5.36}
$$

where the *diagonal* mass matrix $\mathbb{M}$ has been introduced. Equation (5.36) shows matrix $\mathbb{H}$ for uniform meshes, i.e. in its tri-diagonal formulation. Notice that

$$
\mathcal{D} = \begin{pmatrix}
-\mathcal{L} & \mathcal{R} & 0 & \cdots & 0 \\
0 & -\mathcal{L} & \mathcal{R} & 0 & 0 \\
\vdots & 0 & -\mathcal{L} & \ddots & 0 \\
0 & 0 & \ddots & \ddots & \mathcal{R} \\
\mathcal{R} & 0 & \cdots & 0 & -\mathcal{L}
\end{pmatrix}
\tag{5.37}
$$

is precisely the weak form of the gradient operator. In principle, with AMR in multi-space dimensions, the number of non zero blocks grows. The following results are valid in general, even after mesh refinement. Matrix $\mathbb{H}$ is proved to be ***positive semi-definite*** because it can be decomposed into the matrix product

$$
v^T\mathbb{H}v \equiv v^T\mathcal{D}^T\mathbb{M}^{-1}\mathcal{D}v = w^T\mathbb{M}^{-1}w \geqslant 0, \quad \text{with} \quad w = \mathcal{D}v \qquad \forall\ v
$$

because the mass matrix is positive definite. This is an interesting property because the problem of the uniqueness of the solutions of the pressure system is shifted to the uniqueness of the solutions of

$$
\mathcal{D}\,\mathcal{P} = \text{right hand side.} \tag{5.38}
$$

that in ensured in general *up to the solutions of* $\mathcal{D}\,\mathcal{P} = 0$. This means that (for periodic boundaries) the discrete pressure $\mathcal{P}$ is defined up to weak solutions of $\partial_x p = 0$, which is exactly what one could expect from a discrete formulation of the incompressible Navier-Stokes equations. If pressure boundary conditions are specified, it can be verified easily that the resulting system for the pressure is indeed *symmetric* and *positive-definite*.

The real advantages of the chosen staggered framework are shown in the properties of $\mathbb{H}$, which defined the discrete pressure Poisson system, which is at the same time the most complex linear system to be solved in our algorithm. Indeed, the resulting discrete Laplace operator $\mathbb{H}$ satisfies the following peculiar properties:

(i) $\mathbb{H}$ is **symmetric**, i.e. $\mathbb{H} \equiv \mathbb{H}^T$;

(ii) $\mathbb{H}$ is **always** *at least* **positive semi-definite**, independent of the chosen boundary conditions; in particular, $\mathbb{H}$ is *positive definite up to the solutions of*

$$\mathcal{D}\,\mathcal{P}' = 0 \qquad \Longleftrightarrow \qquad \mathcal{P}' \in \mathrm{Ker}(\mathcal{D}), \tag{5.39}$$

where $\mathrm{Ker}(\cdot)$ is the kernel set;

(iii) for *uniform Cartesian grids*, $\mathbb{H}$ is **block hepta-diagonal** for the three-dimensional case, only **block penta-diagonal** for the two dimensional case and only **block tri-diagonal** for the one dimensional case.

(iv) whenever any *pressure boundary condition* is imposed, then $\mathbb{H}$ is shown to be **strictly positive definite**.

It should be mentioned the resulting algebraic system (5.32) would occur also after choosing a different mesh staggering, but the corresponding non-zero blocks (*stencil*) of the local equation (5.33) would be larger and the computational effort needed for solving the discrete Poisson equation (5.32) would presumably increase.[4] Table 5 shows the stencil-sizes (number of non-zero blocks) of the resulting algebraic systems for the pressure, varying for different choices of the grid type and for different numbers of space dimensions.

Finally, once the equation system for the degrees of freedom of the pressure (5.33) has been solved by means of a classical matrix-free conjugate gradient method, then the velocity components can be updated directly via (5.24). In all numerical examples shown in this paper no preconditioner has been used.

4 Without staggering (A-grid case), the integral of the pressure gradients in the momentum equations (5.23), after integrating by parts, would generate a three-point stencil of dependence between the elements by means of some numerical flux functions that are necessary for approximating the pressure at the element interfaces, i.e. $p(x_{i+1/2}) = \mathcal{G}(p_i, p_{i+1})$. With the same argument, further flux functions are needed also in the incompressibility condition (5.18) for evaluating the velocities at the interfaces and the resulting discrete pressure system would become: block 5-*diagonal* for the 1d case, instead of being block 3-*diagonal*; block 9-*diagonal* for the two dimensional case, versus our block 5-*diagonal* system; block 13-*diagonal* for the three dimensional case, versus our block 7-*diagonal* system. Concerning the vertex-based staggered grids (B-grid), Riemann solvers or numerical flux functions are not necessary. However, with a vertex based staggering, a block 9-*diagonal system* or a block 27-*diagonal system* are obtained for the two and for the three dimensional case, respectively, see also Table 5

space dimensions	Collocated grid (A–grid)	Vertex-based staggered grid (B–grid)	Edge-based staggered grid (C–grid)
1D	5	3	3
2D	9	9	5
3D	13	27	7

Table 5: Total stencil-size for the resulting pressure systems for semi-implicit DG schemes on *uniform* Cartesian meshes using different grid types for different numbers of space dimensions. In all cases it is assumed that the discrete momentum equation is substituted into the discrete continuity equation, in order to yield one single equation system for the scalar pressure.

Spectral Analysis of $\mathbb{H}$

It should be mentioned that in the uniform Cartesian case, a rigorous theoretical analysis of $\mathbb{H}$ for the design of specific preconditioners, using the theory of matrix-valued symbols and Generalized Locally Toeplitz (GLT) algebras (see [245, 140, 246]) has been very recently provided with promising results in terms of numerical efficiency [102] and showing beneficial properties of the respective condition number.

5.4.2 *Advection and diffusion*

Any stable explicit DG scheme can be adopted for solving the advective-diffusive terms $\widehat{\mathbf{Fv}}$ in equation (5.24). In order to simplify the computation, in this work we considered a DG formulation on the collocated grid, with $v_h \in P_N(\Omega_h)$, having

$$\widehat{\mathbf{Fv}}_i^n = \widehat{\mathbf{V}}_i^n - \frac{\Delta t}{|T_i|}\left(\mathbf{M}^{xyz}\right)^{-1} \cdot \left(\int_{\partial T_i} \boldsymbol{\omega}\mathbf{F}_v \cdot \vec{n}\, dS - \int_{T_i} \nabla\boldsymbol{\omega} \cdot \mathbf{F}_v \, d\mathbf{x} \right). \tag{5.40}$$

Because of the discontinuities of the piecewise polynomials along the element faces, a very simple and classical Rusanov flux (or local Lax-Friedrichs flux - LLF) [241, 259] has been used for evaluating the surface integral of (5.40) in the form

$$\mathbf{F}_q \cdot \vec{n} = \frac{1}{2}\left(\mathbf{F}_q^+ + \mathbf{F}_q^-\right) \cdot \vec{n} - \frac{1}{2} s_q \left(q^+ - q^-\right) \quad \text{with } q = u, v, w. \tag{5.41}$$

in which the penalty term s_q is the maximum value of the Jacobian of the flux tensor $\mathbf{F}_q$

$$s_q = 2\max\left(|q^+|, |q^-|\right) + 2\nu\frac{2N+1}{\Delta x_q\sqrt{\pi/2}} \qquad \text{with } (q, \Delta x_q) = (u, \Delta x), (v, \Delta y), (w, \Delta z). \tag{5.42}$$

The chosen Rusanov flux has been modified in order to account for both hyperbolic and parabolic terms (see [124, 95, 145]). In this context, it should be emphasized that although the advection-diffusion equation contains parabolic terms, an appropriate numerical flux can be defined by the solution of the corresponding generalized Riemann problem, see [124] for details.

Since equation (5.40) is an explicit DG scheme, then a rather severe CFL time restriction with $CFL \in (0,1)$ becomes necessary for ensuring stability:

$$\Delta t = CFL \left[(2N+1) \left(\frac{|u_{max}|}{\Delta x_{min}} + \frac{|v_{max}|}{\Delta y_{min}} + \frac{|w_{max}|}{\Delta z_{min}} \right) + \right.$$
$$\left. + (2N+1)^2 \left(\frac{2\nu}{\Delta x_{min}^2} + \frac{2\nu}{\Delta y_{min}^2} + \frac{2\nu}{\Delta z_{min}^2} \right) \right]^{-1}. \tag{5.43}$$

Once $\widehat{\mathbf{Fv}}_i^n$ has been computed on the main grid Ω_h, the numerical solution is projected back to the dual space of solutions $p_N(\Omega_h^{*(k)})$ according to the L_2 projection operators (5.10-5.11), with the projection matrices (5.16).

Notice that, the parabolic nature of the viscous terms introduces a quadratic dependence of the minimum step-size on $h/(2N+1)$, which can become extremely severe when more than one refinement level is considered for a viscous fluid flow at low Reynolds number. In such circumstances, the stability condition (5.43) can become too restrictive. Then, following [115], an implicit discretization of the diffusive fluxes is taken for the advection diffusion system

$$\boldsymbol{\sigma} = -\nu \nabla \mathbf{v}. \tag{5.44}$$
$$\frac{\partial \mathbf{v}}{\partial t} + \nabla \cdot \mathbf{F_c} - \nabla \cdot \boldsymbol{\sigma} = 0. \tag{5.45}$$

In particular, the velocity components and the stress tensor components are the unknowns of the system. The velocity components are discretized within the piecewise polynomials of maximum degree N along the main grid Ω_h, the component of the stress tensor along the *dual grid* $\Omega_h^{*(k)}$. Then the final algorithm is obtained following exactly the same strategy adopted for the incompressible Navier-Stokes equations:

1. the governing equations (5.44) and (5.45) are projected along the chosen space of solutions, i.e. $P_N(\Omega_h)$ and $P_N(\Omega_h^{*(k)})$ respectively;

2. the unknown variables are assumed to live in the corresponding space of solutions, i.e. $v_h^{(k)} \in P_N(\Omega_h)$ and $F_h^{(k)} \in P_N(\Omega_h^{*(k)})$, and then substituted into the discrete DG equations:

$$\mathbf{M}^{x_1 x_2 x_3} \cdot \widehat{\mathbf{F}}_m^{n+1} =$$
$$= -\frac{\nu}{\Delta x_1} \mathbf{M}^{x_2 x_3} \cdot \left(\mathbf{R}_v^{x_1 \sigma(m,r(m))} \cdot \widehat{\mathbf{V}}_{r(m)}^{n+1} - \mathbf{L}_v^{x_1 \sigma(m,l(m))} \cdot \widehat{\mathbf{V}}_{l(m)}^{n+1} \right),$$
$$\forall T_m^{*(x_1)} \in \Omega_h^{*(x_1)}, \ \forall (x_1, x_2, x_3) \in \left\{ {}^{x}_{z} \bigcirc^{y} \right\} \tag{5.46}$$

$$\mathbf{M}^{x_1x_2x_3}\cdot\left[\widehat{\mathbf{V}}_i^{n+1}-\widehat{\mathbf{Fv}}_i^{n}\right]=$$
$$=\sum_{x_1=x,y,z}\sum_{\Gamma_i^{*(x_1)}\subset T_i}\frac{\Delta t}{\Delta x_1}\,\mathbf{M}^{x_2x_3}\left(\mathbf{R}_p^{x_1\sigma^*(i,r^*(i))}\cdot\widehat{\mathbf{F}}_{r^*(i)}^{n+1}-\mathbf{L}_p^{x_1\sigma^*(i,l^*(i))}\cdot\widehat{\mathbf{F}}_{l^*(i)}^{n+1}\right)=0,$$
$$\text{with}\quad(x_1,x_2,x_3)\in\left\{{}^{x_1}\!\bigcirc^{x_2}_{x_3}\right\}\tag{5.47}$$

3. the Schur complement of the resulting algebraic coupled system is solved, after substituting the equation (5.46) for the tensor components $F_h^{(k)}$ into the momentum equations (5.46); then the decoupled system for the only velocity components $v_h^{(k)}$ is obtained, in a very familiar structure, i.e.

$$(\mathbb{M}+\nu\mathbb{H})\cdot\mathcal{V}_{(k)}^{n+\frac{1}{2}}=\mathcal{b}_{(k)},\qquad k=x,y,z,\tag{5.48}$$

where $\mathbb{M}^i\equiv\mathbf{M}$ is the mass matrix, $\mathbb{H}$ is exactly the afore-defined discrete Laplace operator, $\mathcal{V}_{(k)}^{n+1/2}$ is the vector of the complete set of degrees of freedom for the k-th velocity component; $\mathcal{b}_{(k)}$ collects all the known terms, i.e. the explicit advective terms of equation (5.40) multiplied by a mass matrix; $n+1/2$ labels a *fictitious time step* $t^{n+1/2}$, labeling the intermediate stage within the global algorithm;

4. system (5.48) is very efficiently solved by means of a classical conjugate gradient method. Throughout this paper, we do not employ any preconditioner;

5. the velocity components are projected back to the dual space $P_N(\Omega_h^{*(k)})$ into $\widehat{\mathbf{Fv}}_m^n$ of equation (5.24).

Notice that, although equation system (5.48) must be solved for each velocity component, the coefficient matrix $(\mathbb{M}+\nu\mathbb{H})$ has even better properties than $\mathbb{H}$: (i) it is **symmetric**; (ii) it is **strictly positive definite**; (iii) for the *purely Cartesian case*, $(\mathbb{M}+\nu\mathbb{H})$ is only **block hepta-diagonal** for the three-dimensional case and only **block penta-diagonal** for the two dimensional case. (iv) the viscosity acts as a perturbation coefficient of the mass matrix, which is **purely diagonal** (not only block diagonal); then the system is surely much better behaved compared to the discrete pressure system. After the aforementioned operator-splitting procedure for the semi-implicit time discretization, since the parabolic terms are treated fully implicitly, the final CFL time-restriction relaxes to

$$\Delta t=\frac{CFL}{(2N+1)}\left(\frac{|u_{max}|}{\Delta x_{min}}+\frac{|v_{max}|}{\Delta y_{min}}+\frac{|w_{max}|}{\Delta z_{min}}\right)^{-1}.\tag{5.49}$$

5.4.3 *Final algorithm*

Finally, even in the staggered AMR framework, the resulting numerical scheme can be summarized, similar to [115], as follows:

1. the velocity is projected to the pressure grid Ω_h with π defined in equation (5.11); advection terms are discretized explicitly while the viscous terms are treated implicitly for each velocity component within $P_N(\Omega_h)$

$$(\mathbb{M} + \nu\mathbb{H}) \cdot \mathcal{V}^{n+\frac{1}{2}}_{(x_1)\#} = \mathbb{M} \cdot \mathcal{F}v^{n}_{(x_1)\#}, \qquad x_1 = x, y, z \tag{5.50}$$

   symbol '#' labels the degrees of freedom respect to the main space of solutions $P_N(\Omega_h)$;

2. the velocity is projected back to the dual space $P_N(\Omega^{*(k)}_h)$ according to the projection operator $\pi^{*(k)}$ defined in equation (5.10) and the system for the discrete pressure Poisson equation is solved

$$\begin{aligned} &\mathbb{H} \cdot \mathcal{P}^{n+\theta}_{\#} = \mathcal{b}^{n+\frac{1}{2}}_{\#}, \\ &\text{with} \quad \mathcal{b}^{n+\frac{1}{2}}_{\#} \equiv \sum_{\{x_1 \bigcirc^{x_2}_{x_3}\}} \Delta x_2 \Delta x_3 \mathbb{M}^{x_2 x_3} \left(\mathcal{D}^{x_1}\right)^{T} \cdot \mathcal{V}^{n+\frac{1}{2}}_{(x_1)*}, \end{aligned} \tag{5.51}$$

   symbol '$*$' denotes the degrees of freedom with respect to the dual space of solutions $P_N(\Omega^{*(x_1)}_h))$;

3. the velocity components are directly updated according to

$$\mathcal{V}^{n+1}_{(x_1)*} = \mathcal{V}^{n+\frac{1}{2}}_{(x_1)*} - \frac{\Delta t}{\Delta x_1} \left(\mathbb{M}^{-1}\mathcal{D}\right)^{(x_1)} \cdot \mathcal{P}^{n+\theta}_{\#}, \tag{5.52}$$

5.5 A SPECTRAL-DG TIME DISCRETIZATION

In this section the high-order DG formulation is extended to the time dimension by looking for discrete solutions (u_h, v_h, w_h, p_h) under the form of linear combinations of *piecewise space-time polynomials* of maximum degree N in space and M in time with respect to a reference basis $\mathcal{B}_N$ for the spatial dependency and $\mathcal{B}_M$ for the time dependency. In the following, the general mathematical framework is outlined, and several numerical tests are performed in two and three space dimensions, with the aim of assessing the efficiency and the accuracy of the proposed high order accurate staggered spectral space-time DG scheme. Since the development of the space-time extension of our SI-DG on adaptive staggered grids in still under construction, in this section we limit our-self to depict the space-time extension of the *only uniform-grid case*.

5.5.1 *Spectral st-DG on uniform meshes*

Here, the discrete solutions are defined within the more general space-of-solution $\mathbb{P}_{N_\otimes M}$, defined as the vector space of piecewise polynomials of maximum degree $N \in \mathbb{N}$ in space, $M \in \mathbb{N}$ in time, identified by the tensor product

$$\mathbb{P}_{N_\otimes M} = \mathbb{P}_{N_\otimes M}\left(\tilde{\Omega}_h \otimes \tau_{n+1}\right) \equiv P_N\left(\tilde{\Omega}_h\right) \otimes P_M\left(\tau_{n+1}\right), \tag{5.53}$$

where $\tilde{\Omega}_h \in \{\Omega_h, \Omega_h^{*(k)}\}$, $k = x, y$ and z; $\tau_{n+1} = [t_n, t_{n+1}]$ is the future time-step where the solution is unknown. The fundamental basis of Lagrangian polynomials interpolating the Gauss-Legendre quadrature points within a local space-time element $T_i \otimes \tau_{n+1}$ is denoted by the tensor product $\mathcal{B}_N(T_m^{*(k)}) \otimes \mathcal{B}_M(\tau_{n+1})$. Therefore, the respective expansion over the polynomial basis (5.19-5.20) are augmented by

$$\boxed{\begin{array}{ll} \left\{ \begin{array}{rcl} \hat{v}_l(t) & = & \sum_{s=1}^{M+1} \theta_s(t)\, \hat{v}_{ls}, \\ \hat{p}_l(t) & = & \sum_{s=1}^{M+1} \theta_s(t)\, \hat{p}_{lm}, \end{array} \right. & \begin{array}{l} \text{with } \ t \in \tau_{n+1}, \\ n = 1, \ldots, N_t, \\ \hat{v}_{ls}, \hat{p}_{lm} \in \mathbb{R}, \end{array} \\ \\ \theta_{|_{\tau_{n+1}}}(t) = \varphi(\xi), \qquad \text{with} & t = t_n + \xi \Delta t^{n+1}, \quad 0 \leqslant \xi \leqslant 1, \end{array}} \tag{5.54}$$

where symbol θ, that was the implicitness factor for the semi-implicit method, now refers to the vector of time basis-polynomials $\theta \in \mathcal{B}_M(\tau_{n+1})$.

By using the same nomenclature as before, the weak formulation of the governing equations (5.17-5.18) in *space-time* reads

$$\boxed{\begin{array}{l} \displaystyle\int_{T_m^{*(k)} \times \tau_{n+1}} \psi_q \theta_r \left(\frac{\partial v_k}{\partial t} + \nabla \cdot \mathbf{F}_{v_k} + \partial_{x_k} p \right) d\mathbf{x}\, dt = 0, \\ \displaystyle\int_{T_i \times \tau_{n+1}} \omega_q \theta_r \ (\nabla \cdot \mathbf{v})\, d\mathbf{x}\, dt = 0, \\ (x_k, v_k) = (x, v_x), (y, v_y), (z, v_z), \qquad T_m^{*(k)} \in \Omega_h^{*(k)}, \ \ T_i \in \Omega_h \end{array}} \tag{5.55}$$

where $\tau_{n+1} = [t_n, t_{n+1}]$ is the future time interval where the solution is unknown, with $t^{n+1} = t^n + \Delta t$ given by the stability condition of explicit terms, i.e. or (5.43) or (5.49). Since the only time-dependent operator of the incompressible Navier-Stokes equations is the time-derivative, and thanks to the chosen dimension-by-dimension tensor definition of $\mathbb{P}_{N_\otimes M}$, then all space integrals can be factorized into the same coefficient matrices of equations (5.24-5.25) in the previous sections, yielding to

$$\begin{aligned} \int_{\tau_{n+1}} \theta(t) \ \Bigg[& \mathbf{M}^{x_1 x_2 x_3} \cdot \left(\frac{\partial}{\partial t} \widehat{\mathbf{V}}^{n+1}(t) \right) + \\ & + \frac{\Delta t}{\Delta x_1} \mathbf{M}^{x_2 x_3} \cdot \left(\mathbf{R}_v^{x_1 \sigma(m, r(m))} \cdot \widehat{\mathbf{P}}_{r(m)}^{n+1}(t) - \mathbf{L}_v^{x_1 \sigma(m, l(m))} \cdot \widehat{\mathbf{P}}_{l(m)}^{n+1}(t) \right) \Bigg] \ dt = 0, \\ & \forall T_m^{*(x_1)} \in \Omega_h^{*(x_1)}, \ \forall (x_1, x_2, x_3) \in \{ {}^{x}_{z} \bigcirc^{y} \} \end{aligned} \tag{5.56}$$

$$\begin{aligned} \int_{\tau_{n+1}} \theta(t) \cdot \sum_{x_1 = x,y,z} \sum_{\Gamma_i^{*(x_1)} \subset T_i} & \Delta x_2 \Delta x_3 \ \mathbf{M}^{x_2 x_3} \left(\mathbf{R}_p^{x_1 \sigma^*(i, r^*(i))} \cdot \widehat{\mathbf{V}}_{r^*(i)}^{n+1}(t) + \right. \\ & \left. - \mathbf{L}_p^{x_1 \sigma^*(i, l^*(i))} \cdot \widehat{\mathbf{V}}_{l^*(i)}^{n+1}(t) \right) \ dt = 0 \\ & \text{with } \ (x_1, x_2, x_3) \in \left\{ {}^{x_1}_{x_3} \bigcirc^{x_2} \right\}. \end{aligned} \tag{5.57}$$

On the other hand, after substituting the polynomial definition (5.54) and integration over time, a *time*-mass matrix $\mathbf{M} = \int \theta\theta$ can be factorized as well. The only real changes with respect to the previous formulation arise in the integration of the time derivatives that, after integrating by parts in time and introducing the known solution at time t^n (*upwinding in time*, according to the causality principle), read

$$\begin{aligned}\int_{T_m^{*(k)}\times\tau_{n+1}} \psi\theta\frac{\partial v_k}{\partial t}\,dx\,dt = &\int_{T_m^{*(k)}} \psi\left[\theta(t^{n+1})v_k^{n+1}(x,t^{n+1}) - \theta(t^n)v_k^n(x,t^n)\right]dx \\ &- \int_{T_m^{*(k)}\times\tau_{n+1}} \psi\left(\frac{\partial}{\partial t}\theta(t)\right)v_k^{n+1}(x,t^{n+1})dxdt = \\ &\mathbf{M}^{xyz}\left[\left(\mathbf{M}_1^t - \mathbf{M}_V^t\right)\cdot\widehat{\mathbf{V}}^{n+1} - \mathbf{M}_0^t\cdot\widehat{\mathbf{V}}^n\right]\times|T_m^{*(k)}|\end{aligned} \tag{5.58}$$

where

$$\mathbf{M}_1^t = \left\{M_{1\,pq}^t\right\}_{p,q=1,..,M+1} = \left\{\varphi_p(1)\varphi_q(1)\right\}_{p,q=0,..,M}, \tag{5.59}$$

$$\mathbf{M}_0^t = \left\{M_{0\,pq}^t\right\}_{p,q=1,..,M+1} = \left\{\varphi_p(0)\varphi_q(1)\right\}_{p,q=0,..,M}, \tag{5.60}$$

$$\mathbf{M}_V^t = \left\{M_{V\,pq}^t\right\}_{p,q=1,..,M+1} = \left\{\int_0^1 \varphi_p'(\xi)\varphi_q(\xi)\,d\xi\right\}_{p,q=0,..,M+1}. \tag{5.61}$$

Here the spatial *xyz*-formalism of the tensor products (5.13) to the space-time case by defining a generic vector of space-time degrees of freedom as can be written as

$$\begin{aligned}&\mathbf{A} \equiv \mathbf{A}^{xyzt} \equiv \mathbf{A}^x \otimes \mathbf{A}^y \otimes \mathbf{A}^z \otimes \mathbf{A}^t, \\ &\widehat{\mathbf{x}} \equiv \left\{\hat{x}_{ll_0}\right\}_{l=1,..,(N+1)^d;l_0=1,..,M+1} \\ &\quad\equiv \left\{\hat{x}_{l_1l_2l_3l_0} \equiv \hat{x}_{l_1}\otimes\hat{x}_{l_2}\otimes\hat{x}_{l_3}\otimes\hat{x}_{l_0}\right\}_{l_1,l_2,l_3=1,..,N+1;l_0=1,..,M+1}.\end{aligned}$$

In this notation the mass matrix that corresponds to the time coordinate can be written as $\mathbf{M}^t$, according to the definition of the mass matrix in equations (5.16). Then, from equations (5.56-5.57) the following system is obtained:

$$\boxed{\begin{aligned}&\mathbf{M}^{x_1x_2x_3}\left[\left(\mathbf{M}_1^t - \mathbf{M}_V^t\right)\cdot\widehat{\mathbf{V}}_m^{n+1} - \mathbf{M}_0^t\cdot\widehat{\mathbf{Fv}}_m^n\right] + \\ &+\frac{\Delta t}{\Delta x_1}\mathbf{M}^{x_2x_3t}\cdot\left(\mathbf{R}_v^{x_1\sigma(m,r(m))}\cdot\widehat{\mathbf{P}}_{r(m)}^{n+1} - \mathbf{L}_v^{x_1\sigma(m,l(m))}\cdot\widehat{\mathbf{P}}_{l(m)}^{n+1}\right) = 0, \\ &\qquad\qquad \forall T_m^{*(x_1)} \in \Omega_h^{*(x_1)},\ \forall(x_1,x_2,x_3) \in \{{}^x{}_z^y\}\end{aligned}} \tag{5.62}$$

$$\boxed{\begin{aligned}\sum_{x_1=x,y,z}\ \sum_{\Gamma_i^{*(x_1)}\subset T_i} \Delta x_2\Delta x_3\ \mathbf{M}^{x_2x_3t}\Big(\mathbf{R}_p^{x_1\sigma^*(i,r^*(i))}\cdot\widehat{\mathbf{V}}_{r^*(i)}^{n+1}+\\ -\mathbf{L}_p^{x_1\sigma^*(i,l^*(i))}\cdot\widehat{\mathbf{V}}_{l^*(i)}^{n+1}\Big)\,dt=0\\ \text{with}\quad (x_1,x_2,x_3)\in\left\{{}^{x_1}_{x_3}\!\!\bigcirc^{x_2}\right\}.\end{aligned}} \tag{5.63}$$

which is analogous to the system of equations (5.24-5.25), where now the advective-diffusive terms are computed according to

$$\mathbf{M}_0^t\cdot\widehat{\mathbf{Fv}}_i^n=\mathbf{M}_0^t\cdot\widehat{\mathbf{V}}_i^n-\frac{\Delta t}{|T_i|}\left(\mathbf{M}^{xyz}\right)^{-1}\mathbf{M}^t\cdot\left(\int_{\partial T_i}\omega\mathbf{F}_v\cdot\vec{n}\,dS-\int_{T_i}\nabla\omega\cdot\mathbf{F}_v\,d\mathbf{x}\right). \tag{5.64}$$

The adopted numerical strategy for the implicit diffusion is actually the higher order time extension of the aforementioned implicit approach and it will be described later in this section. Following the philosophy of section 5.4, after multiplying equation (5.62) by the inverse of the matrix $\mathbf{M}^{xyz}\left(\mathbf{M}_1^t-\mathbf{M}_V^t\right)$, which is simply the matrix product of three $(N+1)^2$ space-matrices and one $(M+1)^2$ time-matrix, the following direct definitions of the degrees of freedom of the velocity components are obtained

$$\begin{aligned}\widehat{\mathbf{V}}_m^{n+1}=&\left(\mathbf{M}_1^t-\mathbf{M}_V^t\right)^{-1}\mathbf{M}_0^t\cdot\widehat{\mathbf{Fv}}_m^n+\\ &-\frac{\Delta t}{\Delta x_1}\left(\mathbf{M}_1^t-\mathbf{M}_V^t\right)^{-1}\mathbf{M}^t\left(\mathbf{M}^{x_1}\right)^{-1}\cdot\left(\mathbf{R}_v^{x_1\sigma(m,r(m))}\cdot\widehat{\mathbf{P}}_{r(m)}^{n+\theta}-\mathbf{L}_v^{x_1\sigma(m,l(m))}\cdot\widehat{\mathbf{P}}_{l(m)}^{n+\theta}\right),\end{aligned}$$

$$\forall T_m^{*(x_1)}\in\Omega_h^{*(x_1)},\ \forall(x_1,x_2,x_3)\in\left\{{}^{x}_{z}\!\!\bigcirc^{y}\right\} \tag{5.65}$$

Then, after substitution of the resulting equations in the discrete incompressibility condition (5.63), one obtains

$$\left[\mathbf{M}^t\left(\mathbf{M}_1^t-\mathbf{M}_V^t\right)^{-1}\mathbf{M}^t\ \ \mathbb{H}^i\right]\cdot\mathcal{P}^{n+1}=\left[\mathbf{M}^t\left(\mathbf{M}_1^t-\mathbf{M}_V^t\right)^{-1}\mathbf{M}_0^t\right]\cdot\mathcal{b}_i^n \tag{5.66}$$

that is the higher order time-accurate version of the pressure equation, analogous to (5.32). The right hand side $\mathcal{b}_i^n$ collects all the known terms, i.e. the advective and diffusive terms $\{\widehat{\mathbf{Fu}}^n\}$, $\{\widehat{\mathbf{Fv}}^n\}$ and $\{\widehat{\mathbf{Fw}}^n\}$. This system is not symmetric because of the non-symmetric time-matrices (5.59) and (5.61). After multiplication by the inverse of $\mathbf{M}^t\left(\mathbf{M}_1^t-\mathbf{M}_V^t\right)^{-1}$, the non-symmetric contribution of the time-matrix can be *removed*, and the same well suited coefficient matrix $\mathbb{H}$ of section 5.4 is obtained, i.e.

$$\boxed{\mathbf{M}^t\mathbb{H}^i\cdot\mathcal{P}^{n+1}=\left[\mathbf{M}_0^t\right]\cdot\mathcal{b}_i^n} \tag{5.67}$$

and consequently, the resulting system is **symmetric** and **strictly positive definite** (for appropriate pressure boundary conditions). Hence, it can be solved very efficiently by means of a classical conjugate gradient method. Once the system for

the higher order accurate space-time expansion coefficients of the pressure $\mathcal{P}^{n+1}$ has been solved, the velocity can be readily updated according to equation (5.65). Note, however, that although the presented space-time DG framework is formally high order accurate in time, the final numerical scheme is strongly influenced by the time-splitting between advection, diffusion and incompressibility condition, which constrains the final method to be only first order accurate in time. In section 5.5.3 a very simple numerical procedure based on the Picard iteration is outlined in order to circumvent the order limitation induced by the time-splitting and to enable the final solution to preserve the original high-order time accuracy of the presented spectral staggered space-time DG discretization.

5.5.2 *Implicit diffusion*

Following the same procedure outlined in section 5.4, the high-order time accurate version of the implicit scheme for diffusion (5.46-5.47) reads

$$\begin{aligned}
&\mathbf{M}^{x_1x_2x_3t}\cdot\widehat{\mathbf{F}}_m^{n+1} = \\
&= -\frac{\nu}{\Delta x_1}\mathbf{M}^{x_2x_3}\cdot\left(\mathbf{R}_v^{x_1\sigma(m,r(m))}\cdot\widehat{\mathbf{V}}_{r(m)}^{n+1} - \mathbf{L}_v^{x_1\sigma(m,l(m))}\cdot\widehat{\mathbf{V}}_{l(m)}^{n+1}\right), \\
&\qquad\qquad \forall T_m^{*(x_1)}\in\Omega_h^{*(x_1)},\ \forall(x_1,x_2,x_3)\in\left\{{}^{x}{}_{z}^{y}\right\}
\end{aligned} \tag{5.68}$$

$$\begin{aligned}
&\frac{|T_i|\,\mathbf{M}^{x_1x_2x_3}}{\Delta t}\cdot\left[(\mathbf{M}_1^t-\mathbf{M}_V^t)\cdot\widehat{\mathbf{V}}_i^{n+1} - \mathbf{M}_0^t\cdot\widehat{\mathbf{Fv}}_i^{n}\right] = \\
&= \sum_{x_1=x,y,z}\ \sum_{\Gamma_i^{*(x_1)}\subset T_i}\Delta x_2\Delta x_3\ \mathbf{M}^{x_2x_3t}\left(\mathbf{R}_p^{x_1\sigma^*(i,r^*(i))}\cdot\widehat{\mathbf{F}}_{r^*(i)}^{n+1} - \mathbf{L}_p^{x_1\sigma^*(i,l^*(i))}\cdot\widehat{\mathbf{F}}_{l^*(i)}^{n+1}\right) = 0, \\
&\qquad\qquad \text{with}\ \ (x_1,x_2,x_3)\in\left\{{}^{x_1}{}_{x_3}^{x_2}\right\}
\end{aligned} \tag{5.69}$$

Then, after substituting the definitions of the velocity derivatives (5.68) into the discrete advection-diffusion equation (5.69), the high-order accurate space-time DG version of (5.48) can be written as

$$\left[\left(\mathbb{M}_1^t-\mathbb{M}_V^t\right)\mathbb{M}^{x_1x_2x_3}+\nu\mathbb{M}^t\mathbb{H}\right]\cdot\mathcal{V} = \mathbb{M}_0^t\mathbb{M}^{x_1x_2x_3}\cdot\mathcal{F}v^n, \tag{5.70}$$

that is *non-symmetric* because of the time-matrices

$$\left(\mathbb{M}_1^t-\mathbb{M}_V^t\right) = \left\{\left(\mathbf{M}_1^t-\mathbf{M}_V^t\right)_i\right\}, \qquad \mathbb{M}_0^t = \left\{\mathbf{M}_{0\,i}^t\right\} \tag{5.71}$$

and can be efficiently solved by means of a classical GMRES method [242]. Notice that the non-symmetric component of system (5.70) can be shifted to the viscous terms, i.e. the second term on the left-hand-side, by multiplying the equations with the inverse of $\left(\mathbb{M}_1^t-\mathbb{M}_V^t\right)$ from the left. In that case, for small viscosity, the system can be seen as a non-symmetric perturbation of the inviscid case.

5.5.3 *Space-time pressure correction algorithm*

In Section 5.4 the final staggered semi-implicit DG scheme (5.50-5.52) consists of two main blocks that are solved sequentially by the use of a fractional time-step

approach. If only high order of accuracy in space is needed, such a splitting is possible. The first fractional block is described by the discrete advection-diffusion equations (5.50), which itself contains a first fractional step for the purely explicit advection and a second fractional step for the implicit discretization of the diffusive terms. Then, the second fractional block (5.51-5.52) contains the solution of the discrete pressure Poisson equation that results from substituting the discrete momentum equations into the discrete incompressibility condition. The important fact is that *the chosen fractional time discretization is only first order accurate*. In principle, higher order schemes for fractional time-stepping or other more sophisticated techniques could be adopted in defiance of simplicity or generality [162, 277, 168, 199]. In this work a simple *Picard method* has been implemented. In this manner, the first order time-splitting approach of system (5.50-5.52) can then be generalized to arbitrary high order of accuracy in time at the aid of the Picard procedure. We emphasize that at the moment we have no rigorous mathematical proof for the fact that the Picard iterations actually increase the order of accuracy by one per iteration. We only have numerical evidence which support this claim in the context of high order ADER schemes, see [105], as well as the numerical convergence tables shown later in this paper for a set of test cases. The final version of the spectral staggered space-time DG scheme, which is written in terms of a *space-time pressure correction algorithm*, reads: for $k = 0, \dots, M$ do

$$\left[\left(\mathbb{M}_1^t - \mathbb{M}_V^t\right)\mathbb{M}^{x_1x_2x_3} + \nu\mathbb{M}^t\mathbb{H}\right]\cdot \mathcal{V}_{(x_1)\#}^{n+1,[k+\frac{1}{2}]} = \\ = \mathbb{M}^{x_1x_2x_3}\cdot\left[\mathbb{M}_0^t\cdot\mathcal{F}v_{(x_1)\#}^{n+1,[k]} - \pi\left(\frac{\Delta t}{\Delta x_1}\mathbb{M}^t\cdot\left(\mathbb{M}^{-1}\mathcal{D}\right)^{(x_1)}\cdot\mathcal{P}_{\#}^{n+1,(k)}\right)\right], \tag{5.72}$$

$$\mathbb{M}^t\mathbb{H}^{xyz}\cdot\left(\mathcal{P}_{\#}^{n+1,[k+1]} - \mathcal{P}_{\#}^{n+1,[k]}\right) = \mathcal{b}_{\#}^{n+1,[k+\frac{1}{2}]}, \\ \text{with}\quad \mathcal{b}_{\#}^{n+1,[k+\frac{1}{2}]} \equiv \sum_{\{x_1 \bigcirc x_3^{x_2}\}} \Delta x_2\Delta x_3\mathbb{M}^{x_2x_3}\left(\mathcal{D}^{x_1}\right)^T\cdot\mathcal{V}_{(x_1)*}^{n+\frac{1}{2}}, \tag{5.73}$$

$$\mathcal{V}_{(x_1)*}^{n+1,[k+1]} = \left(\mathbb{M}_1^t - \mathbb{M}_V^t\right)^{-1}\cdot\left[\mathbb{M}_0^t\cdot\mathcal{V}_{(x_1)*}^{n+1,[k+\frac{1}{2}]} + \right. \\ \left. -\frac{\Delta t}{\Delta x_1}\mathbb{M}^t\cdot\left(\mathbb{M}^{-1}\mathcal{D}\right)^{(x_1)}\cdot\left(\mathcal{P}_{\#}^{n+1,[k+1]} - \mathcal{P}_{\#}^{n+1,[k]}\right)\right], \tag{5.74}$$

where M is the maximum degree of the time-polynomials and k is the Picard iteration number. Note that the Picard process allows to gain one order of accuracy in time per Picard iteration when applied to an ODE, see [183, 208, 209]. $\mathcal{F}v_{(x_1)} = \{\widehat{\mathbf{Fv}}_i^{(x_1)}\}$ collects the advective terms computed according to (5.64), without taking into account the diffusive flux. We furthermore set

$$\mathcal{F}v_{(x_1)}^{n+1,(0)} = \mathcal{F}v_{(x_1)}^{n}, \tag{5.75}$$

and $\mathcal{P}^{n+1,(k)}$ is the k-th iterate for the discrete pressure, for which we use the trivial initial guess

$$\mathcal{P}_{\#}^{n+1,(0)} = 0. \tag{5.76}$$

Thanks to the Picard procedure the desired properties of the presented spectral space-time DG method are re-established, so that the final algorithm (5.72)-(5.74) is arbitrary high-order accurate both in space and time. Finally, it is important to stress that the proposed iterative solution of the non-trivial system of equations (5.72)-(5.74) is feasible in practice, thanks to the fact that the coefficient matrix $\mathbb{H}$ that enters into the discrete Poisson equation (i.e. the incompressibility condition) and the discrete diffusion equation is well conditioned and can be solved in a very efficient way via modern matrix-free Krylov subspace methods, even *without the use of any preconditioner*. Finally, note that when the degree of the time-polynomials M is set to be zero, then

$$\mathbf{M}_1^t \equiv 1, \quad \mathbf{M}_0^t \equiv 1, \quad \mathbf{M}_V^t \equiv 0,$$

and the method collapses to the previous spectral staggered semi-implicit DG scheme with a classical first order backward Euler discretization in time. Moreover, if at the same time the spatial and the temporal polynomial approximation degrees are chosen to be zero ($M = N = 0$), then the following equalities arise from (5.26-5.29)

$$\mathbf{M} \equiv 1, \quad \mathbf{R}_v \equiv 1, \quad \mathbf{L}_v \equiv 1, \quad \mathbf{R}_p = 1, \quad \mathbf{L}_p \equiv 1,$$

and the method collapses to a classical staggered semi-implicit finite-difference finite-volume method for the incompressible Navier-Stokes equations, where the pressure field is defined at the barycenters of the main grid and the velocity components are defined at the middle points of the cell interfaces, i.e. the classical family of efficient semi-implicit methods on staggered grids of Casulli et al. [64, 41, 61, 54, 58, 53, 117, 110, 55, 63, 62, 57, 60] is obtained.

5.5.4 *A different framing: time-dependence of divergence-free errors*

In the following rows an alternative and equivalent derivation of the pressure Poisson equations is briefly outlined. By operating the time derivative of the incompressibility condition, i.e.

$$\nabla \cdot \mathbf{v} = 0 \qquad \Longrightarrow \qquad \frac{\partial}{\partial t} (\nabla \cdot \mathbf{v}) = 0. \tag{5.77}$$

and by operating the same aforementioned space-time higher order DG discretization, the following semi-discrete equation is obtained

$$\int_{d\Omega_{ijk}} \omega_m(x)\omega_{m'}(y)\omega_{m''}(z) \left[\left(\mathbf{M}_1^t - \mathbf{M}_V^t\right) \cdot (\nabla \cdot \mathbf{v}_h)^{n+1} - \mathbf{M}_0^t \cdot (\nabla \cdot \mathbf{v}_h)^n \right] = 0, \tag{5.78}$$

where the complete time dependency is summarized into the time coefficient-matrices. Only after forcing the incompressibility condition to be valid at the older time-slice $t = t^n$, i.e.

$$\int_{d\Omega_{ijk}} \omega_m(x)\omega_{m'}(y)\omega_{m''}(z) \left[\mathbf{M}_0^t \cdot (\nabla \cdot \mathbf{v}_h)^n\right] = 0, \qquad \forall\, t^n < t_{end}, \tag{5.79}$$

then equation (5.78) becomes

$$\left(\mathbf{M}_1^t - \mathbf{M}_V^t\right) \cdot \left[\int_{d\Omega_{ijk}} \omega_m(x)\omega_{m'}(y)\omega_{m''}(z) \left(\nabla \cdot \mathbf{v}_h\right)^{n+1}\right] = 0. \tag{5.80}$$

After integrating in space and substitution of equations (5.65), equation (5.80) yields directly to equation (5.67), reported here for convenience

$$\mathbf{M}^t \mathbb{H}^{ijk} \cdot \mathcal{P}^{n+1} = \left[\mathbf{M}_0^t\right] \cdot \mathcal{b}_{ijk}^n, \tag{5.81}$$

without the misleading intermediate step (5.66), misleading because it shows *non-symmetric* matrix coefficients. This means that the dynamic condition (5.77) is weaker with respect to the original static version. Indeed, even if a proper divergence-free solution is chosen for the initial state, numerical errors on $\nabla \cdot \boldsymbol{\nu} = 0$ are accumulated in time within equation (5.78). Since the our adopted formulation is compatible to the constraint (5.80), this means that *the incompressibility condition is satisfied at every time-step within the chosen tolerance threshold for the iterative resolution of system* (5.81).

6 NUMERICAL VALIDATION AND RESULTS

In order to verify the accuracy and robustness of the presented methods together with the AMR framework, a series of non-trivial numerical tests is chosen. The test problems have been selected according to the following criteria: (i) an analytical, numerical or experimental reference solution exists; (ii) the test problem involves all terms of the incompressible Navier-Stokes equations, i.e. the nonlinear convective terms as well as the viscous and pressure forces are equally important; (iii) physical instabilities and energy dissipation from the largest to the smallest spatial scales are present (see the three-dimensional Taylor-Green vortex problem); (iv) pressure, velocity and wall boundary conditions are considered; (v) the AMR framework should provide a remarkable benefit in terms of resolution without introducing spurious mesh-effects; (vi) whenever possible, a convergence table should be provided according to a smooth *analytical* reference solution.

6.1 CONVERGENCE TESTS

In this section the higher-order capabilities of our new spectral semi-implicit and space-time DG (SI-DG and st-DG) method are tested against several numerical benchmark problems in two and three space dimensions for which an analytical reference solutions exist. In particular, three different numerical convergence tables are produced, with the aim of assuring that the presented methods, i.e. SI-DG-$\mathbb{P}_N$ with AMR and st-DG-$\mathbb{P}_{N_\otimes M}$. are really arbitrary high-order accurate in space (SI-DG and st-DG) *and* time (st-DG). Note that achieving high order time accuracy for the incompressible Navier-Stokes equations is far from being straightforward. Here, the nomenclature st-DG-$\mathbb{P}_N$ refers to our spectral space-time DG method (st-DG-$\mathbb{P}_{N_\otimes M}$) with $N = M$.

6.1.1 *Oscillatory viscous flow between two flat plates (st-DG)*

In this test, the fluid flow between two parallel flat plates is driven by a time harmonic pressure gradient. According to [181, 179, 195], by neglecting the nonlinear convective terms, the resulting axial velocity profile is only a function of time and the distance from the plates. The flow furthermore depends only on one single dimensionless parameter, known as the Womersley number $\alpha_W = R\sqrt{\omega/\nu}$, see [271], where R is the half distance between the two plates, ω is the frequency of

2D Womersley problem — Spectral-DG-$\mathbb{P}_N$

N_{el}	ϵ_{L^2}	ϵ_{L^∞}	$\mathcal{O}_{L^2}$	$\mathcal{O}_{L^\infty}$	N_{el}	ϵ_{L^2}	ϵ_{L^∞}	$\mathcal{O}_{L^2}$	$\mathcal{O}_{L^\infty}$
$N = M = 1$			($t_{end} = 0.5$)		$N = M = 2$				
40^2	1.6288E-03	3.1562E-03	—	—	20^2	1.1014E-04	4.7994E-04	—	—
50^2	1.3100E-03	2.5073E-03	0.98	1.03	25^2	5.5799E-05	2.5608E-04	3.05	2.82
60^2	1.0947E-03	2.0868E-03	0.98	1.00	30^2	3.1934E-05	1.5173E-04	3.06	2.87
70^2	9.3992E-04	1.7923E-03	0.99	0.99	35^2	1.9913E-05	9.6986E-05	3.06	2.90
$N = M = 3$					$N = M = 4$				
16^2	2.0842E-05	7.7657E-05	—	—	15^2	2.9044E-06	1.6983E-05	—	—
20^2	8.9568E-06	3.1298E-05	3.78	4.07	20^2	7.3904E-07	4.9121E-06	4.76	4.31
24^2	4.4439E-06	1.6255E-05	3.84	3.60	25^2	2.3730E-07	1.7422E-06	5.09	4.65
28^2	2.4474E-06	9.0529E-06	3.87	3.80	30^2	9.2319E-08	7.2933E-07	5.18	4.78
$N = M = 5$					$N = M = 6$				($t_{end} = 2.2$)
8^2	4.1408E-06	2.1569E-05	—	—	9^2	1.7483E-07	1.0630E-06	—	—
12^2	7.1268E-07	4.5893E-06	4.34	3.82	10^2	8.4841E-08	5.1637E-07	6.86	6.85
16^2	1.7093E-07	1.2088E-06	4.96	4.64	11^2	4.3911E-08	2.6415E-07	6.91	7.03
20^2	5.0328E-08	3.6841E-07	5.48	5.32	12^2	2.3925E-08	1.4122E-07	6.98	7.20

Table 6: Numerical convergence table for the two dimensional oscillatory flow between two flat plates computed with staggered spectral space-time DG schemes for $N = M = 1, \dots, 6$.

the oscillations and ν is the kinematic viscosity. In particular the fluid velocity and pressure are given by

$$u(x,y) = \frac{A}{i\,\omega}\left[1 - \frac{\cosh\left(\alpha_W\sqrt{i}\,y/R\right)}{\cosh\left(\alpha_W\sqrt{i}\right)}\right],$$
$$\frac{\partial p}{\partial x} = \frac{p(x_R) - p(x_L)}{L} = -A\,e^{i\omega t},$$

where $i = \sqrt{-1}$ is the imaginary unit, $L = x_R - x_L$ is the total length of the duct and the amplitude has been chosen equal to $A = 1$. The exact solution has been chosen as initial condition at $t = 0$, then pressure conditions are imposed on the left and right boundaries, while no-slip boundary conditions have been imposed at the upper and lower walls. The other parameters of this test problem were chosen as $L = 1$, $R = 0.5$ and $\omega = 1$. Figures 45 and 46 show the numerical results obtained for $\nu = 2 \cdot 10^{-2}$ with our spectral staggered space-time DG scheme using only ***one single*** P_{11} *space-time* element (M=N=11), completing the entire simulation within the time interval $t \in [0, 2.2]$ in one single time step. The results are compared with the exact analytical solution at different intermediate output times. In particular, for this test problem, two periods of oscillation are resolved within a single time-step, and the complete velocity profile is resolved within a single spatial cell. From the obtained results one can conclude that the proposed staggered spectral space-time DG scheme is indeed very accurate in both space and time, since it is able to resolve all flow features within *one single* space-time element.

Furthermore, table 6 contains the results of a numerical convergence study that we have performed with this smooth unsteady two-dimensional flow problem, for

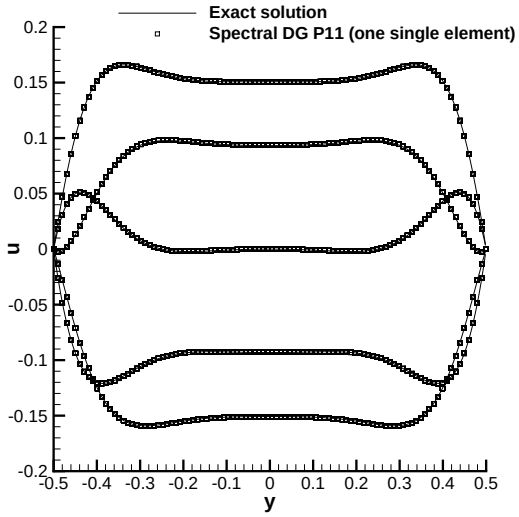

Figure 45: The numerical solution interpolated along 100 equidistant spatial points obtained for the unsteady Womersley problem compared with the exact solution [271, 195] at different times for $\nu = 2 \cdot 10^{-2}$: $t = 1.8, 1.6, 2.0, 1.4, 2.2$, respectively, from the bottom to the top. A staggered spectral space-time DG-$\mathbb{P}_{11}$ method has been run using only *one single* space-time element.

which an exact solution is available. The order of accuracy has been verified up to order 7 in space and time by evaluating the L_2 and L_∞ errors

$$\epsilon_{L_2} = \sqrt{\int_\Omega (u_h - u)^2}, \quad \text{and} \quad \epsilon_{L_\infty} = \max_\Omega |u_h - u|,$$

at different discretization numbers for the polynomial degrees $N = M = 1, \ldots, 6$. From the obtained results we conclude that the designed order of accuracy of the scheme has been reached in both space and time. For the polynomial degree $N = M = 1$, only sub-optimal convergence rates have been verified experimentally, and will be subject of future research.

6.1.2 *2D Taylor-Green vortex (SI-DG with AMR, and st-DG)*

The two dimensional Taylor-Green vortex problem is widely used for testing the accuracy of numerical schemes, because it offers another smooth unsteady analytical solution of the incompressible Navier-Stokes equations with periodic boundary conditions. The exact solution of this problem is given by

$$u(x, y, t) = \sin(x)\cos(y)e^{-2\nu t}, \qquad v(x, y, t) = -\cos(x)\sin(y)e^{-2\nu t},$$
$$p(x, y, t) = \frac{1}{4}\left(\cos(2x) + \cos(2y)\right)e^{-4\nu t}.$$

The computational domain is $\Omega = [0, L]^2$ with periodic boundary conditions. The initial sinusoidal velocity field is smoothed in time by the viscous dissipative

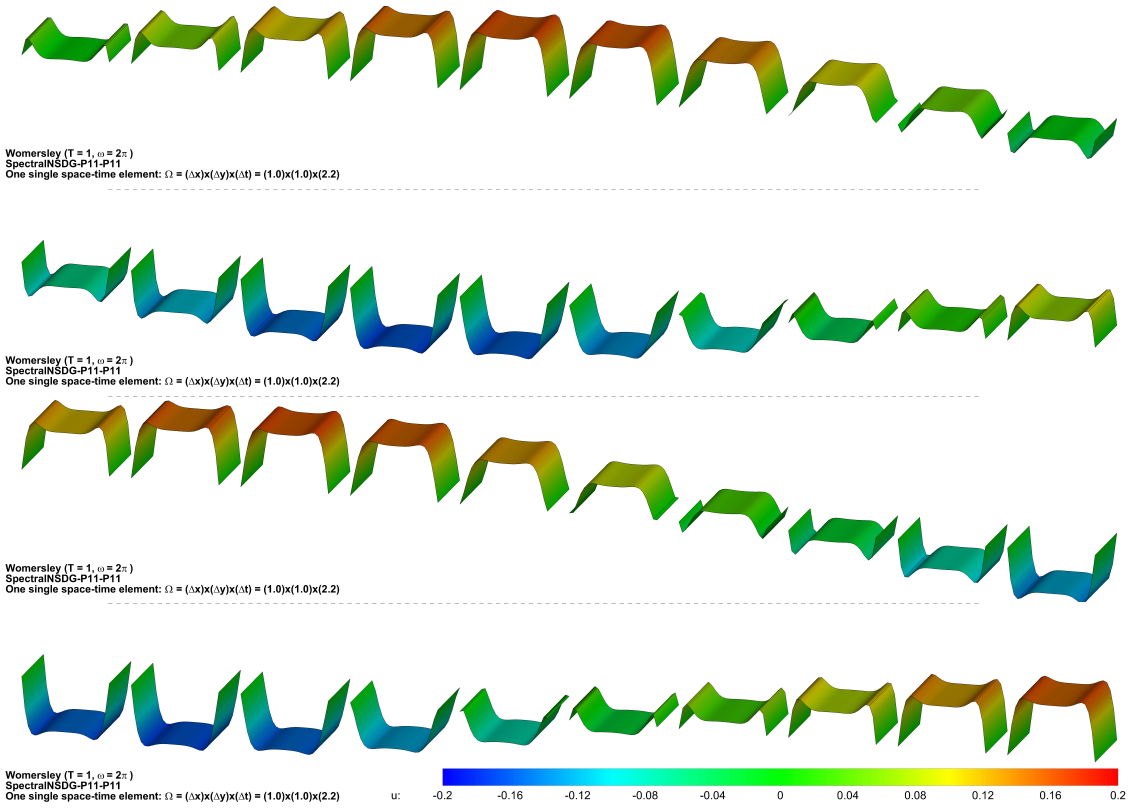

Figure 46: The numerical solution obtained for the two-dimensional oscillatory flow between two flat plates with the staggered spectral space-time DG-$\mathbb{P}_{11}$ scheme. The computational domain in space and time $\Omega = \Delta x \times \Delta y \times \Delta t = 1.0 \times 1.0 \times 2.2$ has been discretized by using only ***one single space time element***, and the plotted numerical solution for the velocity field has been interpolated along 40 time slices with $t \in [0, 2.2]$, respectively, from top left to bottom right.

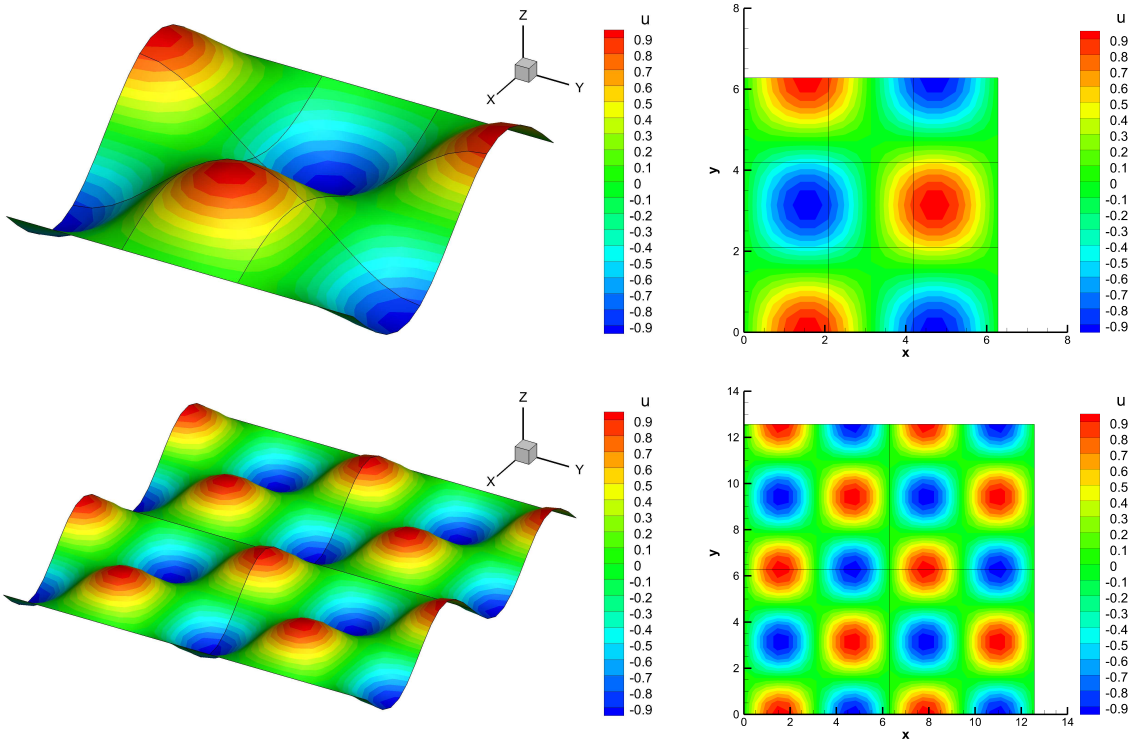

Figure 47: Numerical solution of the u velocity component for the two dimensional Taylor-Green vortex problem computed with the staggered spectral space-time DG-$\mathbb{P}_5$ method using 3^2 elements with $L = 2\pi$ (top) and the staggered spectral space-time DG-$\mathbb{P}_{12}$ scheme using 2^2 elements with $L = 4\pi$ (bottom).

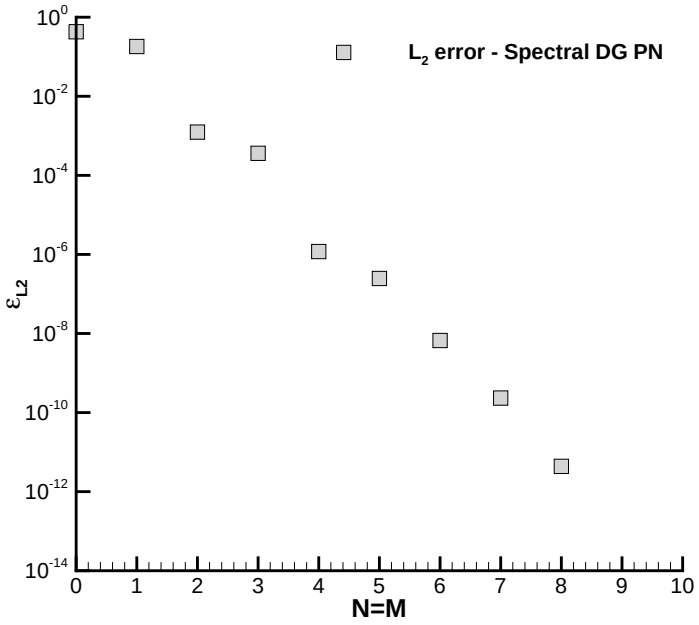

Figure 48: Numerical L_2 error ϵ_{L_2} of the u velocity component for the two dimensional Taylor-Green vortex problem computed with staggered spectral space-time DG-$\mathbb{P}_N$ schemes as a function of the polynomial degree $N = M$ on a fixed grid of 12^2 elements.

forces. The convergence study for this test is summarized in table 8. The accuracy of our staggered spectral space-time DG scheme is verified for polynomial degrees $N = M = 1, \dots, 8$. Figure 47 shows the numerical solution obtained by setting $L = 2\pi$ for the staggered spectral space-time DG-$\mathbb{P}_5$ scheme, using a very coarse mesh composed of only 3^2 spatial elements. Furthermore, we repeat this test with $L = 4\pi$ using a staggered spectral space-time DG-$\mathbb{P}_{12}$ scheme using only 2^2 spatial elements. Moreover, figure 48 shows the behavior of the error ϵ_{L_2} as a function of the polynomial degree ($N = M$) for a fixed mesh: *the exponential decay* of the error, i.e. the *spectral convergence* obtained with our scheme by increasing the polynomial approximation degree in space and time, is explicitly verified. The results confirm the designed accuracy in space and time and show how the presented numerical method works properly even when using very high order approximation polynomials and very coarse meshes. Also in this two dimensional test, for the polynomial degree $N = M = 1$ a non-optimal convergence has been experimentally verified.

2D TAYLOR-GREEN VORTEX WITH AMR. Then, in order to compute properly a convergence table within the AMR framework in our SI-DG method, the ratio between finer and coarser elements should remain approximately constant in time and also for increasing mesh resolution. In this particular test the L_1, L_2 and L_∞ errors have been evaluated at a final time $t_{end} = 0.1$. The resulting convergence study is summarized in table 7 for polynomial degrees $N = 1, \dots, 6$, fixing a refinement factor $r = 3$ and using up to $\ell_{max} = 1$ refinement levels. Since the SI-DG method is higher order accurate only in space, very small time-steps have been used. Furthermore, figure 48 shows the dependence of the L_2 error on the polynomial degree N for a given mesh. One can notice that the *spectral decay* is verified. These results indicate that for smooth problems the present algorithm works properly even when using very high order approximation polynomials and very coarse meshes. It should be emphasized that with very few higher order elements, e.g. $N = 6$, the resulting numerical error is much smaller than the error obtained with an extremely refined grid at lower polynomial degrees (see table 7 and figure 49).

6.1.3 *3D Arnold-Beltrami-Childress flow (st-DG)*

In order to test the accuracy of our staggered spectral space-time DG scheme also against an unsteady three dimensional benchmark problem, the Arnold-Beltrami-Childress (ABC) flow, proposed by Arnold [9] and Childress in [69], is considered. For this smooth unsteady test problem, the exact solution reads

$$\begin{aligned} u(x, y, z, t) &= [\sin(z) + \cos(y)]\, e^{-\nu t}, \\ v(x, y, z, t) &= [\sin(x) + \cos(z)]\, e^{-\nu t}, \\ w(x, y, z, t) &= [\sin(y) + \sin(x)]\, e^{-\nu t}. \end{aligned} \tag{6.1}$$

The computational domain is the cube $\Omega = [0, 2\pi]^3$, with periodic boundary conditions everywhere. Given the initial condition (6.1) at time $t = 0$, the corresponding

2D Taylor-Green vortex problem – SI-DG-P_N scheme with AMR

	N_x	L_1 error	L_2 error	L_∞ error	L_1 order	L_2 order	L_∞ order	Theor.
SI-DG-P_1	12^2	1.133E-00	2.374E-01	8.664E-02	—	—	—	2
	24^2	3.785E-01	7.630E-02	3.250E-02	1.58	1.64	1.41	
	36^2	2.935E-01	6.074E-02	2.489E-02	0.63	0.56	0.66	
	48^2	2.085E-01	4.29E-02	1.74E-02	1.19	1.21	1.25	
SI-DG-P_2	6^2	3.938E-01	8.213E-02	3.511E-02	—	—	—	3
	12^2	4.015E-02	8.997E-03	4.312E-03	3.29	3.19	3.03	
	18^2	1.744E-02	4.012E-03	2.420E-03	2.06	1.99	1.42	
	24^2	5.898E-03	1.495E-03	1.057E-03	3.77	3.43	2.88	
SI-DG-P_3	3^2	1.91E-01	4.19E-02	1.72E-02	—	—	—	4
	6^2	1.27E-02	2.81E-03	1.48E-03	3.92	3.90	3.54	
	9^2	3.05E-03	6.32E-04	5.10E-04	3.51	3.68	2.63	
	15^2	5.18E-04	1.13E-04	8.34E-05	3.47	3.37	3.55	
SI-DG-P_4	3^2	4.33E-02	1.04E-02	5.84E-03	—	—	—	5
	6^2	1.88E-03	4.20E-04	3.10E-04	4.53	4.63	4.23	
	9^2	3.08E-04	7.05E-05	5.52E-05	4.46	4.40	4.25	
	12^2	9.18E-05	2.04E-05	1.68E-05	4.20	4.32	4.14	
SI-DG-P_5	3^2	6.40E-03	1.45E-03	5.97E-04	—	—	—	6
	6^2	1.01E-04	2.24E-05	1.05E-05	5.99	6.02	5.82	
	9^2	9.98E-06	2.42E-06	1.68E-06	5.71	5.48	4.52	
	12^2	2.99E-06	7.14E-07	4.04E-07	4.19	4.24	4.96	
SI-DG-P_6	3^2	5.37E-04	1.27E-04	6.91E-05	—	—	—	7
	4^2	1.61E-04	3.47E-05	1.34E-05	4.20	4.50	5.71	
	6^2	7.96E-06	1.81E-06	9.86E-07	7.41	7.28	6.43	
	9^2	1.15E-06	2.37E-07	1.16E-07	4.78	5.01	5.28	
	8^2	1.59E-06	3.23E-07	1.73E-07	5.59	5.99	6.05	

Table 7: Numerical convergence table computed for the two dimensional Taylor-Green vortex problem using staggered SI-DG-P_N schemes with AMR for polynomial degrees $N = 1, \dots, 6$; $\ell_{max} = 1$; $r = 3$.

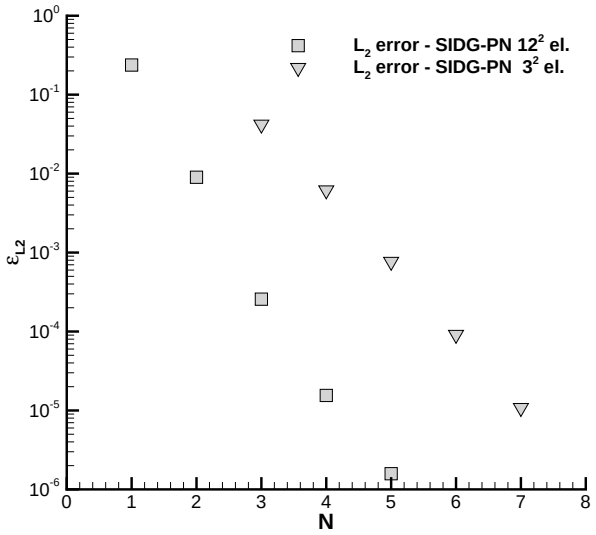

Figure 49: Numerical L_2 error ϵ_{L_2} of the u velocity component for the two dimensional Taylor-Green vortex problem computed with our SI-DG-P_N schemes as a function of the polynomial degree N on a fixed grid of 12^2 elements (squares) and 3^2 elements (triangles).

2D Taylor-Green vortex problem $L = 2\pi$ — Staggered spectral space-time DG-$\mathbb{P}_N$

N_{el}	L_2 error	L_∞ error	$\mathcal{O}_{L^2}$	$\mathcal{O}_{L^\infty}$	N_{el}	L_2 error	L_∞ error	$\mathcal{O}_{L^2}$	$\mathcal{O}_{L^\infty}$
$N = M = 1$					$N = M = 2$				
20^2	6.8094E-02	2.0375E-02	—	—	10^2	2.9023E-03	1.3592E-03	—	—
25^2	5.2703E-02	1.5419E-02	1.15	1.25	15^2	6.6991E-04	3.2999E-04	3.62	3.49
30^2	4.2541E-02	1.2114E-02	1.17	1.32	20^2	2.1652E-04	9.4734E-05	3.93	4.34
35^2	3.5663E-02	1.0062E-02	1.14	1.20	25^2	9.2092E-05	5.0350E-05	3.83	2.83
$N = M = 3$					$N = M = 4$				
16^2	1.3626E-04	7.8999E-05	—	—	16^2	1.0519E-06	6.1297E-07	—	—
20^2	6.5874E-05	3.7886E-05	3.26	3.29	20^2	2.7970E-07	1.6271E-07	5.94	5.94
24^2	3.6213E-05	2.0085E-05	3.28	3.48	24^2	9.1334E-08	5.3150E-08	6.14	6.14
28^2	2.1887E-05	1.1756E-05	3.27	3.47	28^2	3.4806E-08	2.0411E-08	6.26	6.21
$N = M = 5$					$N = M = 6$				
12^2	2.9725E-07	2.1057E-07	—	—	12^2	3.9994E-09	2.4762E-09	—	—
15^2	8.4575E-08	6.3046E-08	5.63	5.40	15^2	9.2671E-10	5.6882E-10	6.55	6.59
18^2	2.9174E-08	2.2565E-08	5.84	5.64	18^2	2.6783E-10	1.7230E-10	6.81	6.55
21^2	1.1910E-08	9.4502E-09	5.81	5.65	21^2	8.9312E-11	6.0292E-11	7.12	6.81
$N = M = 7$					$N = M = 8$				
6^2	1.0586E-08	6.3735E-09	—	—	4^2	3.4616E-08	2.4849E-08	—	—
9^2	4.8791E-10	2.6452E-10	7.59	7.85	6^2	1.5605E-09	7.1039E-10	7.64	8.77
12^2	7.2738E-11	3.8053E-11	6.62	6.74	8^2	6.1523E-11	3.3955E-11	11.24	10.57
15^2	1.2830E-11	7.5665E-12	7.78	7.24	10^2	5.7787E-12	4.9803E-12	10.60	8.60

Table 8: Numerical convergence table computed for the two dimensional Taylor-Green vortex problem using staggered spectral space-time DG schemes with $N = M = 1, \ldots, 8$.

3D ABC flow problem — SI-DG-$\mathbb{P}_N$

N_{el}	L_2 error	L_∞ error	$\mathcal{O}_{L^2}$	$\mathcal{O}_{L^\infty}$	N_{el}	L_2 error	L_∞ error	$\mathcal{O}_{L^2}$	$\mathcal{O}_{L^\infty}$
$N = M = 1$					$N = M = 2$				
12^2	8.6905E-02	1.0949E-02	—	—	12^2	6.9061E-03	1.7183E-03	—	—
16^2	4.8615E-02	6.6433E-03	2.02	1.74	15^2	3.3559E-03	8.2081E-04	3.23	3.31
20^2	3.2626E-02	4.7890E-03	1.79	1.47	18^2	1.7856E-03	4.2641E-04	3.46	3.59
24^2	2.3886E-02	3.6992E-03	1.71	1.42	21^2	1.0316E-03	2.4384E-04	3.56	3.63
$N = M = 3$					$N = M = 4$				
4^2	1.2102E-02	2.3277E-03	—	—	4^2	1.2102E-02	2.3277E-03	—	—
6^2	2.1258E-03	4.9684E-04	4.29	3.81	6^2	2.1258E-03	4.9684E-04	4.29	3.81
8^2	6.4822E-04	1.6790E-04	4.13	3.77	8^2	6.4822E-04	1.6790E-04	4.13	3.77
10^2	2.6346E-04	7.5594E-05	4.03	3.58	10^2	2.6346E-04	7.5594E-05	4.03	3.58
$N = M = 5$					$N = M = 6$				
2^2	4.6766E-03	9.2223E-04	—	—	2^2	2.4587E-04	8.9231E-05	—	—
4^2	6.6120E-05	1.9076E-05	6.14	5.60	4^2	4.2976E-06	1.2496E-06	5.84	6.16
6^2	5.7711E-06	2.1200E-06	6.01	5.42	6^2	3.6205E-07	1.0417E-07	6.10	6.13
8^2	1.1153E-06	5.0069E-07	5.71	5.02	8^2	5.6088E-08	1.6526E-08	6.48	6.40
$N = M = 7$					$N = M = 8$				
2^2	5.4083E-05	1.4183E-05	—	—	1^2	1.5955E-03	5.0110E-04	—	—
3^2	2.1818E-06	7.6077E-07	7.92	7.22	2^2	2.1017E-06	1.0666E-06	9.57	8.88
4^2	2.1037E-07	6.2486E-08	8.13	8.69	3^2	9.7717E-08	3.5484E-08	7.57	8.39
5^2	3.5196E-08	1.3221E-08	8.01	6.96	4^2	1.0666E-08	3.4279E-09	7.70	8.12

Table 9: Numerical convergence table for the three dimensional Arnold-Beltrami-Childress (ABC) flow problem computed with staggered spectral space-time DG schemes for $N = M = 1, \dots, 8$.

analytical solution decays exponentially in time according to the chosen kinematic viscosity. Also for this three dimensional time-dependent test problem, the designed high order of accuracy of our staggered spectral space-time DG scheme has been confirmed up to order 9 by a numerical convergence study that is summarized in table 9. Similar to the two dimensional Taylor-Green vortex, in the 3D ABC flow the advective terms, the pressure forces and the incompressibility condition are highly coupled. The numerical solution for $\nu = 0.1$ at time $t = 10$ is depicted in figure 50.

6.2 TWO-DIMENSIONAL TESTS

6.2.1 *Blasius boundary layer (SI-DG)*

In this test, a steady laminar boundary layer over a flat plate is considered. According to the theory of Prandtl [226, 244], convective terms are of the order 1 in the boundary layer along the horizontal direction, whereas the vertical accelerations are of the order of the boundary layer thickness. The spatial domain under consideration is $\Omega = [-1, 1] \times [0, 0.25]$ and the chosen kinematic viscosity is $\nu = 10^{-3}$. The flat-plate boundary is imposed at $y = 0$ for $x > 0$. Constant velocity $\mathbf{v} = (1, 0)$ is imposed at the left inflow boundary, constant pressure $p = 0$ at the right outflow, no-slip boundary conditions along the wall and no-jump condition in the rest.

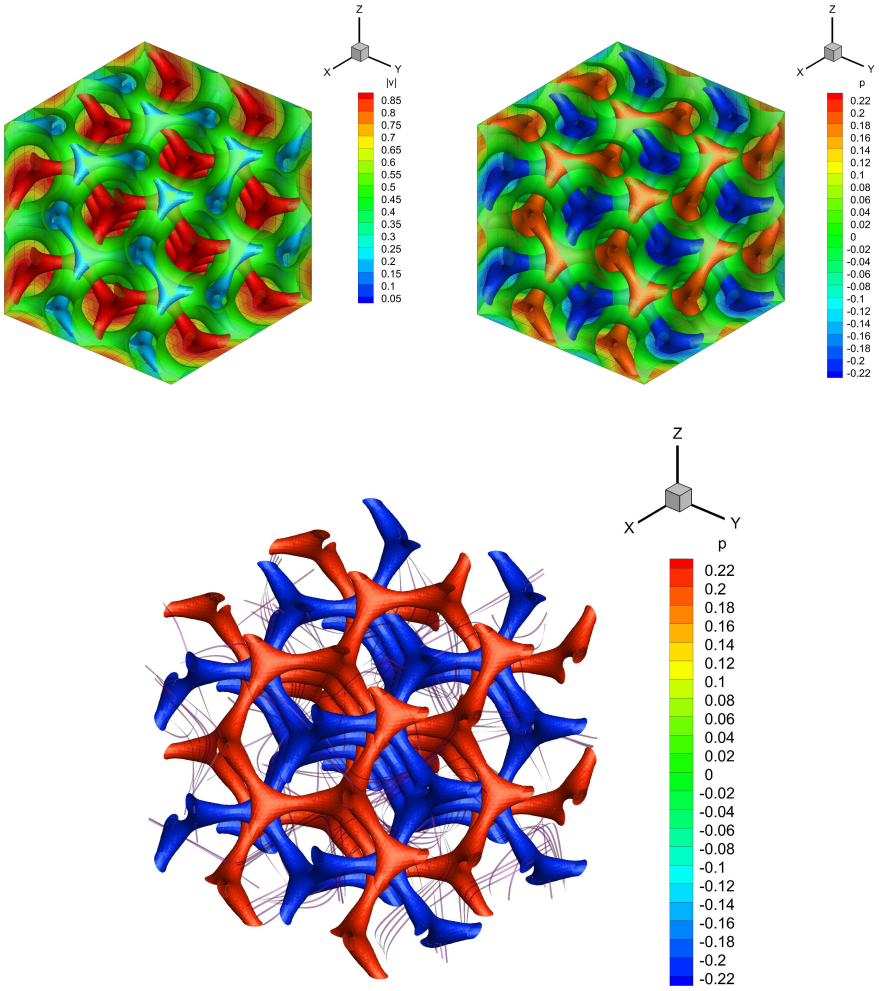

Figure 50: Numerical solution for the three dimensional Arnold-Beltrami-Childress (ABC) flow at time $t = 1.0$ computed with the staggered spectral space-time DG-$\mathbb{P}_5$ scheme using only 7^3 elements in space. The periodic solution has been replicated along the three dimensional cube of edge $L_c = 4\pi$ for giving a better view of the field variables. At the top of the figure the velocity is plotted on the left and the pressure is depicted on the right; at the bottom the 3D stream-traces together with the pressure iso-surfaces are plotted.

Results are shown in figure 51, obtained with our SIDG-P_7 method using $\theta = 1$ and a very coarse grid of only 18×6 elements. A very good agreement between the numerical solution obtained with the semi-implicit spectral DG scheme and the Blasius reference solution can be observed. Notice that the complete boundary layer is well resolved inside a single element close to $x = 0$.

BLASIUS BOUNDARY LAYER WITH AMR. Regarding to the SI-DG-P_N method with AMR, a rectangular domain $\Omega = [-1, 1] \times [0.0, 0.5]$ is initialized with a 20×10 grid at the coarsest AMR level $\ell = 0$. Figure 52 shows the numerical results obtained with the P_4 version of our SI-DG method using an adaptive mesh with $\ell_{max} = 1$ and a refinement factor of $r = 3$. The grid is refined according to the gradient of the velocity magnitude $|\mathbf{v}|$.

A very good agreement between the reference solution and the numerical solution obtained with the semi-implicit staggered DG scheme is observed. As it is shown in figure 52, the refinement only takes place in the region of large velocity gradients, in particular at the leading edge of the boundary layer, as expected.

6.2.2 *Lid-driven cavity: 2D (SI-DG)*

An interesting standard benchmark problem for numerical methods applied to the incompressible Navier-Stokes equations is the lid-driven cavity, see [127]. In this test, a closed square cavity is filled with an incompressible fluid and the flow is driven by the upper wall that moves with velocity $\mathbf{v} = (1, 0)$. The main difficulties in solving this problem arise from the singularities of the velocity gradient at the top right and at the top left corners, where the horizontal velocity component is a double valued function: $u = 0$ at the left (or right) wall boundary and $u = 1$ at the upper moving boundary. Moreover, the pressure is determined only up to a constant, because there are only velocity boundary conditions. The physical domain is $\Omega = [-0.5, 0.5] \times [-0.5, 0.5]$, the initial condition for velocity and pressure is set to $\mathbf{v} = (0, 0)$ and $p = 0$. Figure 54 shows the computed results compared with the reference solution of Ghia et al. [127] next to the two-dimensional view of the velocity magnitude at different Reynolds numbers from Re=100 to Re=3200, obtained with the P_6 version of our staggered semi-implicit spectral DG scheme. The implicitness factor has been chosen equal to $\theta = 1$, since only a steady solution is sought for this test problem. Notice that the computed results match the reference solution very well, despite the presence of the corner singularities and the use of a very coarse mesh. A possibility to avoid the corner singularities in this test problem is the use the unified first order *hyperbolic* formulation of viscous Newtonian fluids, recently proposed and used in [222, 111], which does not need the computation of velocity gradients in the numerical fluxes.

LID-DRIVEN CAVITY WITH AMR. Figures 55 and 56 show the numerical results in two space dimensions obtained at different Reynolds numbers in the range $Re \in [100, 3200]$. The horizontal and vertical velocity profiles, interpolated along the vertical and the horizontal axes respectively, are plotted and compared

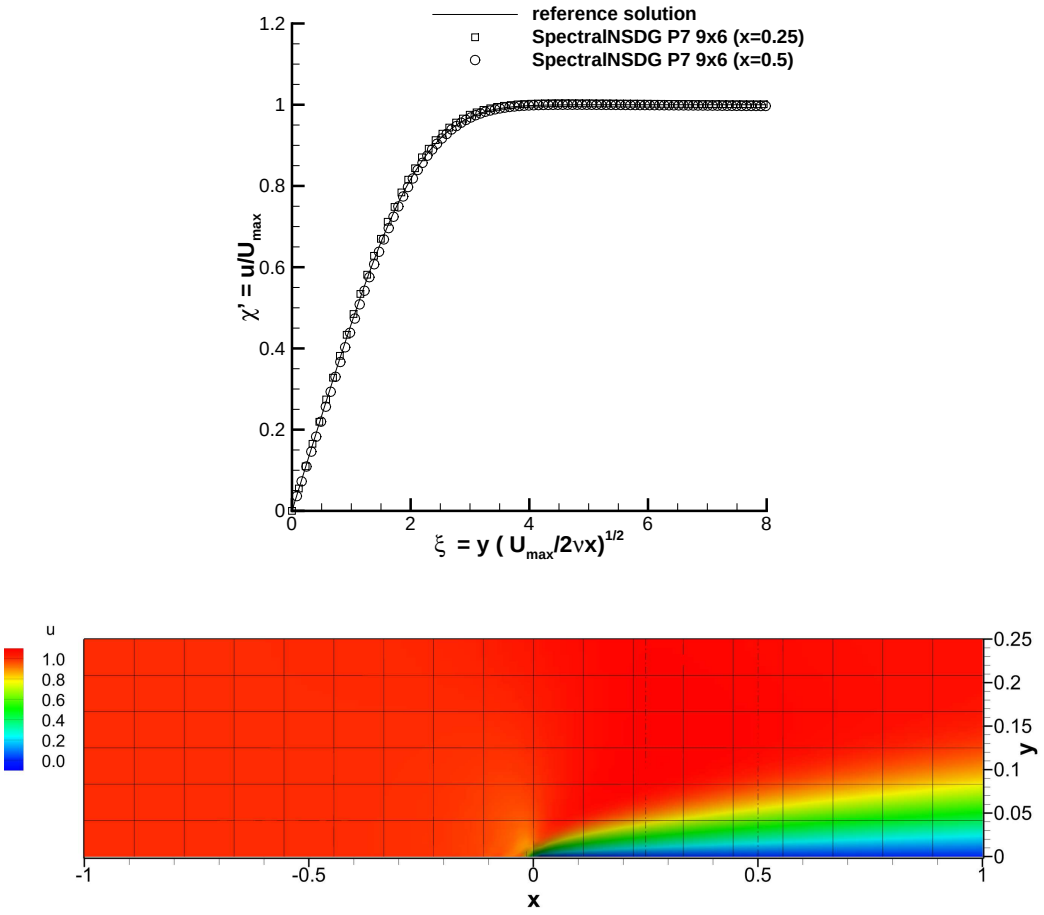

Figure 51: Top: Comparison of the reference solution of Blasius with the numerical results at $t = 5$ for different axial positions $x = 0.25$ and $x = 0.50$ obtained with a staggered semi-implicit spectral DG-P_7 scheme on a very coarse grid of 18×6 elements. Bottom: numerical solution for the horizontal velocity field computed at time $t = 5$; the high-order elements of the main grid are depicted with solid lines; the vertical cuts at $x = 0.25$ and $x = 0.50$ with dash-dotted lines.

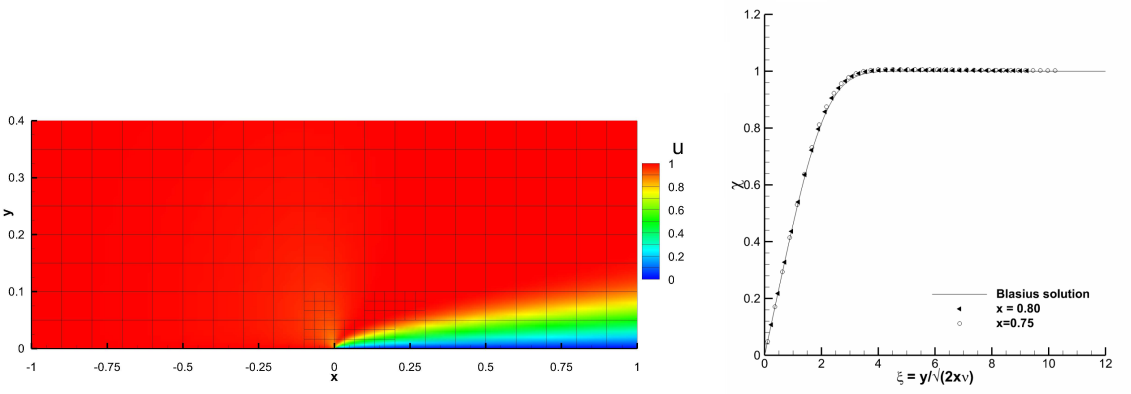

Figure 52: The numerical solution obtained for the two dimensional laminar boundary layer test. The two dimensional view of the horizontal velocity field is shown on the left. The velocity profile interpolated along the vertical direction at two different axial position, i.e. $x = 0.75, 0.80$, is plotted next to the reference Blasius solution on the right. The results have been obtained with our staggered semi-implicit AMR-DG-P_5 together with a refinement factor of $r = 3$ and $\ell_{max} = 1$ levels.

with the reference solution given by Ghia et al. [127]. The AMR grid is adapted according to a refinement factor $r = 3$ and up to one single maximum refinement level ($\ell_{max} = 1$). As shown in figures 55 and 56, the computed results match the reference solution very well and the automatic adaptation is well-driven along the higher velocity gradients close to the walls. In this case the SI-DG-P_4 scheme has been used, corresponding to a total number of degrees of freedom of $N_{dof} = 5^2 = 25$ per space-element. On the level zero grid (ℓ_0), the two-dimensional domain has been discretized within $6^3 = 36$ elements for Reynolds numbers 100, 400 and 1000, while $16^2 = 256$ elements have been used for Reynolds number 3200.

6.2.3 *Backward facing step: 2D (SI-DG)*

Another typical benchmark problem for testing the accuracy of numerical methods in computational fluid dynamics is the backward facing step problem. In this test a flow separation is induced by a sudden backward step inside a two dimensional duct. A main recirculation zone is generated next to the step, starting already at low Reynolds numbers. Then, by increasing the Reynolds number, new secondary recirculations are generated. A non-zero velocity $u = 1$ is imposed at the entrance, a constant pressure $p = 0$ is imposed at the outflow. In this case the axial spatial domain is $x \in [-10, 20]$, the height of the two dimensional duct is $h_{in} = 0.5$ at the entrance and $h_{out} = h_{in} + h_s = 1.0$ at the exit, with an expansion ratio ER$= h_{out}/h_{in} = 2$ at $x = 0$, i.e. a backward facing step of height $h_s = 0.5$. The spatial domain is discretized with elements of dimension $\Delta x = 1$, $\Delta y = 0.25$, the implicitness factor in time is taken as $\theta = 0.6$. Figure 57 shows the streamlines and the recirculation patterns obtained for different Reynolds number up to $Re = 800$

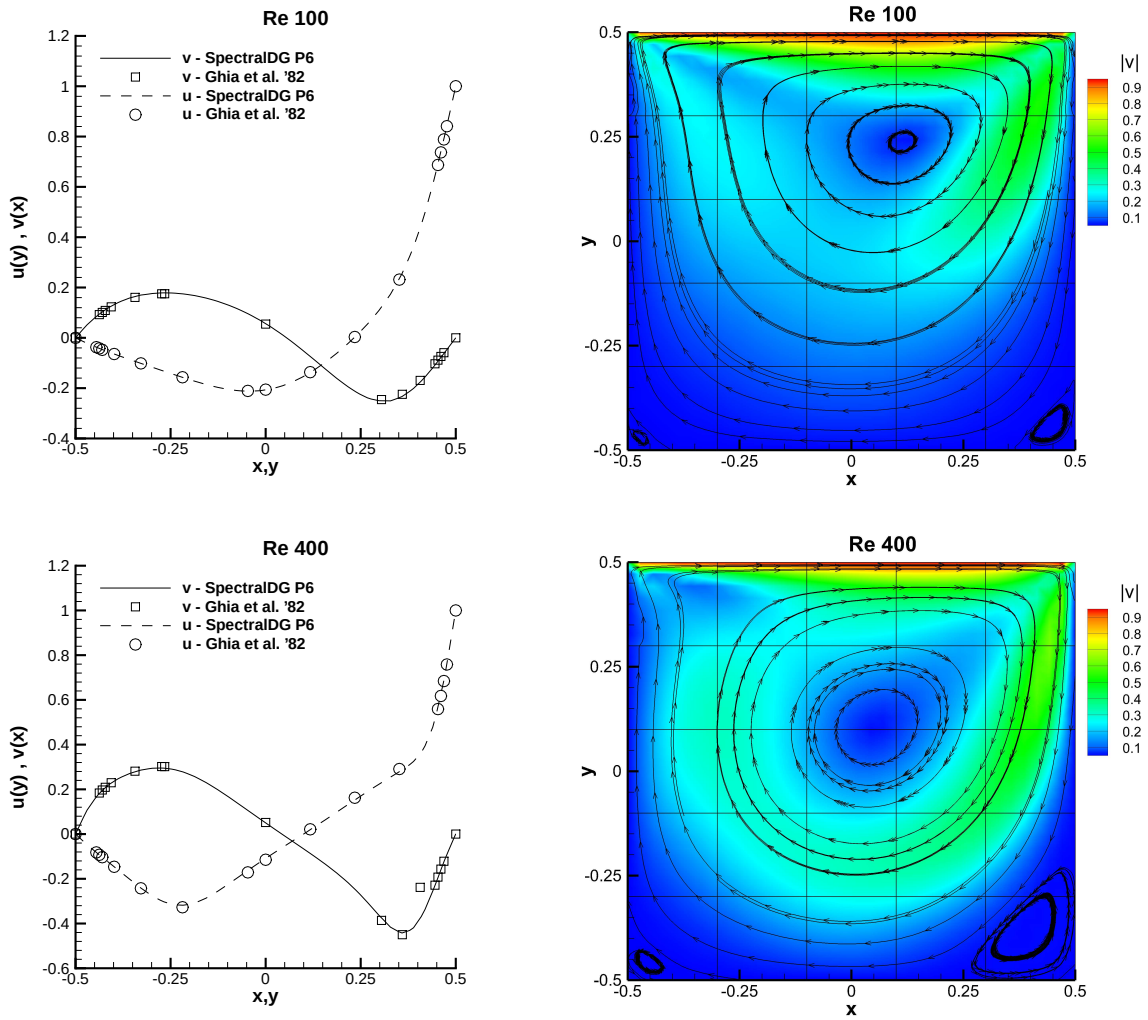

Figure 53: The numerical solution obtained for the two dimensional lid-driven cavity problem compared with the numerical results of [127] at different Reynolds numbers, respectively, from the top to the bottom: Re=100 and Re=400 using 5x5 elements, obtained with a staggered semi-implicit spectral DG-P_6 method.

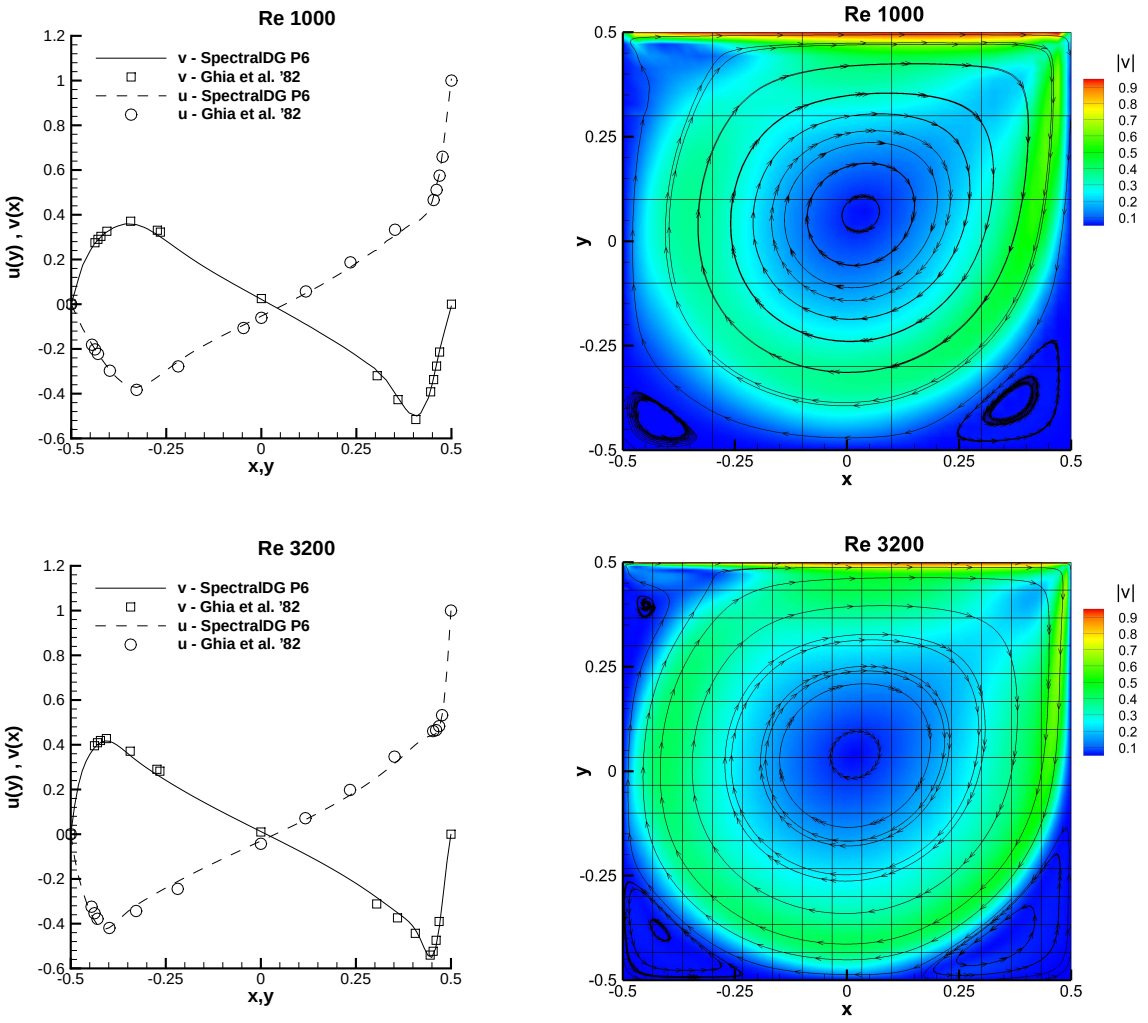

Figure 54: The numerical solution obtained for the two dimensional lid-driven cavity problem compared with the numerical results of [127] at different Reynolds numbers, respectively, from the top to the bottom: Re=1000 using 5x5 elements and Re=3200 using 15x15 elements, obtained with a staggered semi-implicit spectral DG-P_6 method.

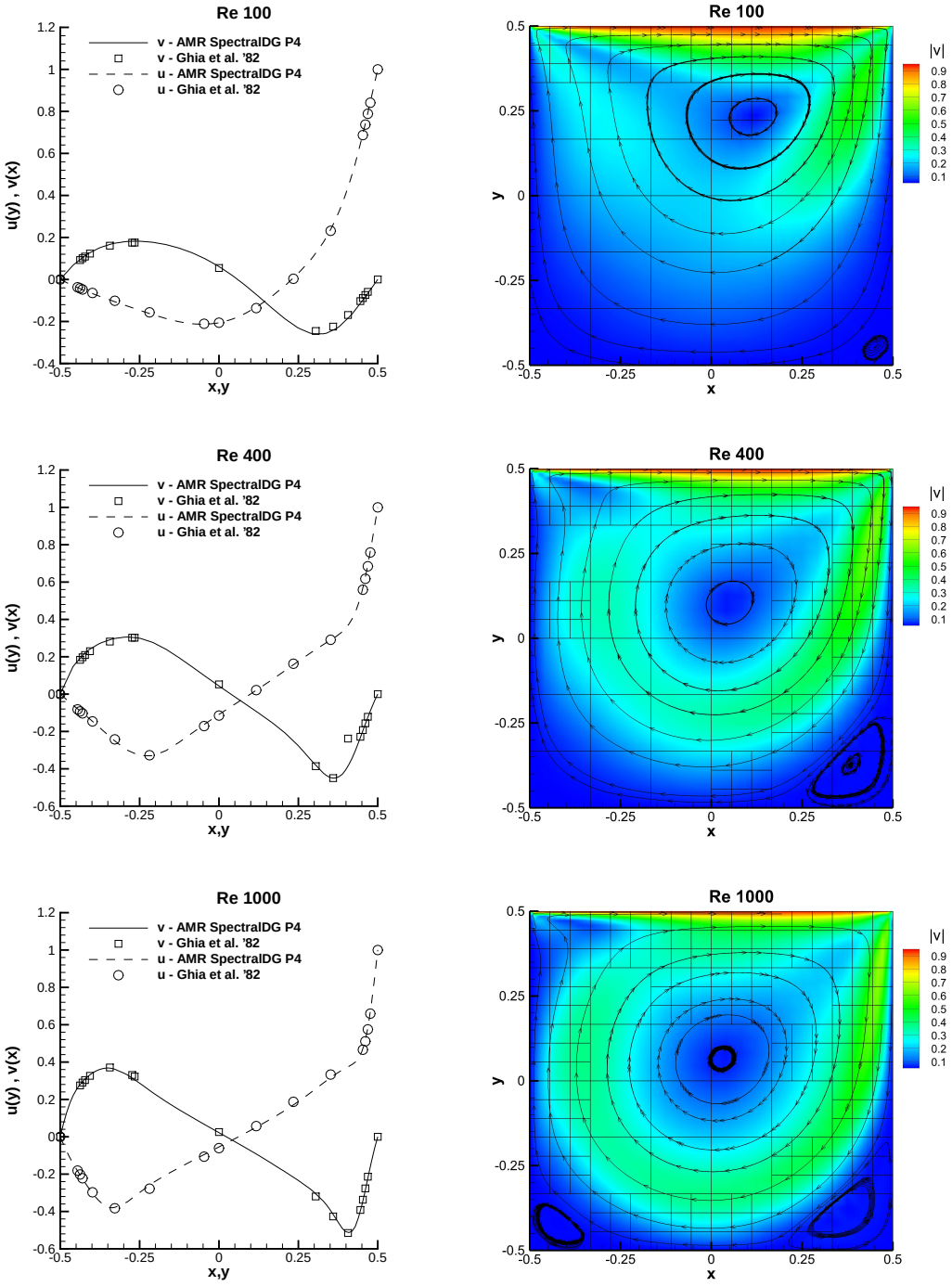

Figure 55: The numerical solution obtained for the two dimensional lid-driven cavity problem compared with the numerical results of [127] at different Reynolds numbers, respectively, from the top to the bottom: Re=100, Re=400 and Re=1000 using 6x6 elements on the coarsest grid level. These results have been obtained with the P_4-version of our staggered semi-implicit spectral DG method.

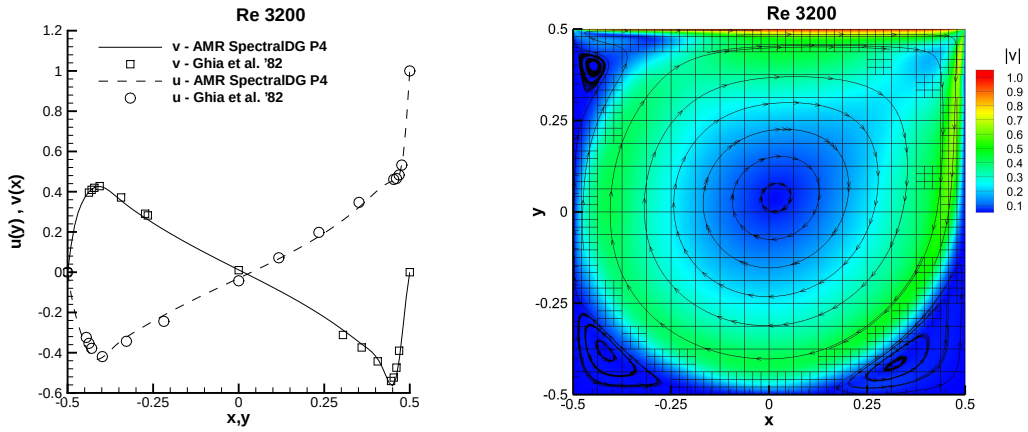

Figure 56: The numerical solution obtained for the two dimensional lid-driven cavity problem compared with the numerical results of [127] at Reynolds number Re=3200 using 16x16 elements on the coarsest grid level. These results have been obtained with the P_4-version of our staggered semi-implicit spectral DG method.

with the P_6 version of our staggered semi-implicit spectral DG method. The numerical results are compared with the two dimensional reference data provided in [112] and with the experimental measurements of [184]. A good agreement is achieved. The plotted data in figure 57 show some discrepancies between the two dimensional simulations and the experimental data [184] that become more visible at higher Reynolds number. These differences are due to three dimensional effects that are introduced by the sidewalls at higher Reynolds numbers, as discussed in [267, 8, 213, 232].

BACKWARD FACING STEP WITH AMR. The physical domain is discretized with elements of size $\Delta x_{\ell=0} = 5/12$ and $\Delta y_{\ell=0} = 1/6$ on the coarsest main grid. For testing the staggered AMR framework we use a maximum number of refinement levels $\ell_{max} = 2$ and a refine factor of $r = 3$, corresponding to a mesh size on the finest grid of $\Delta x_{\ell=2} = 5/108$ and $\Delta y_{\ell=2} = 1/54$. Figure 59 shows the numerical results obtained ad different Reynolds numbers within $Re \in [100, 800]$, where the main recirculations together with the active AMR grid are highlighted. Corresponding reference solutions, i.e. [184] (experimental study) and [112] (numerical study), are compared with the computed results obtained through our adaptive SI-DG-P_4 scheme in figure 60. As it is shown, our numerical results match the two-dimensional numerical reference data of [112] very well, as well as the experimental data of [184] in the low Reynolds number regime. The correct discrepancies with the experimental results arise for higher Reynolds numbers also in this case.

6.2.4 *2D double shear layer (SI-DG with AMR)*

A classical two dimensional test that is well-suited for demonstrating the resolution of high order methods and the usefulness of adaptive grids is the double

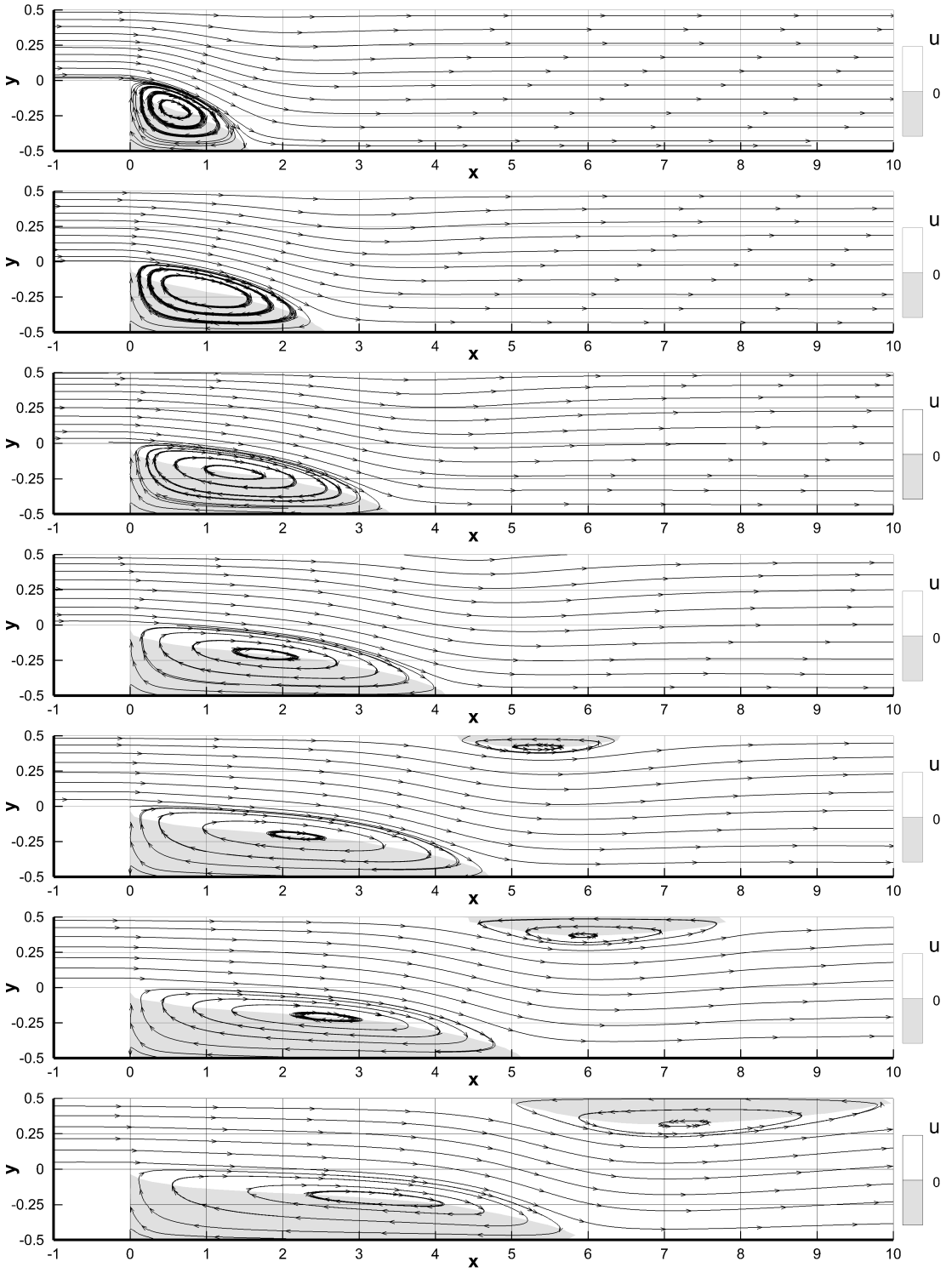

Figure 57: The numerical solution obtained for the two-dimensional backward facing step problem at different Reynolds numbers, respectively, from the top to the bottom: Re=100, Re=200, Re=300, Re=400, Re=500, Re=600, and Re=800 obtained with the staggered semi-implicit spectral DG-P_6 method. Recirculations are highlighted by the sign of the axial velocity u.

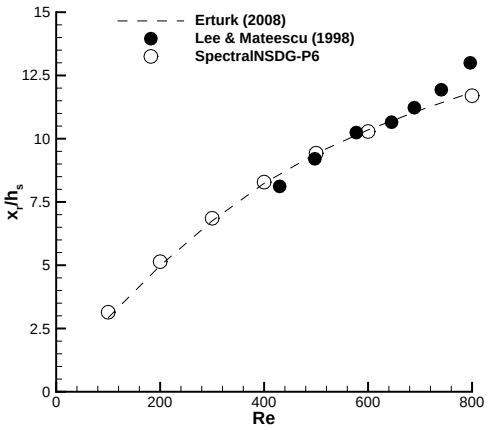

Figure 58: Position of the reattachment point obtained with the staggered semi-implicit spectral DG-P_6 method for the two dimensional backward facing step problem compared with the two dimensional numerical results of [112] and the experimental measurements of [184] at different Reynolds numbers, in the range $Re \in (0, 800)$.

shear layer. In this work, the so called '*thin*' double shear layer is chosen to be the initial and unstable state at $t = 0$ given by

$$u = \begin{cases} u_0 \tanh\left((y - 0.5)/\delta\right) & y > 0 \\ -u_0 \tanh\left((y + 0.5)/\delta\right) & y \leqslant 0 \end{cases} \tag{6.2}$$

with a perturbation in the vertical velocity component in the vicinity of the shear layer that reads

$$v = \begin{cases} v_0 \sin(2\pi x)\, e^{-(y-0.5)^2/2\sigma^2} & y > 0 \\ -v_0 \sin(2\pi x)\, e^{-(y+0.5)^2/2\sigma^2} & y \leqslant 0 \end{cases} \tag{6.3}$$

The rectangular spatial domain $\Omega = [-0.5, 0.5] \times [-1, 1]$ has been discretized by a grid composed of 20×40 elements at the coarsest level $\ell = 0$. We use up to $\ell_{max} = 2$ refinement levels and a refine factor of $r = 2$ in this test problem. In the present test the chosen parameters are $\delta = 10^{-2}$ for the shear layer thickness, $u_0 = 10$, $v_0 = 0.5$ and $\sigma^2 = 0.05$ for the variance of the Gaussian perturbation. The example has been run with a kinematic viscosity of $\nu = 10^{-4}$.

As mentioned in [46, 210] a not sufficiently accurate solution of the flow field may cause spurious oscillations that arise in different locations along the shear layers. Figure 61 shows the time evolution of the z-component of vorticity ω_z obtained with our SI-DG-P_9 scheme, next to the active main AMR grid. The computed results show to be in agreement with previously published results in literature. Moreover, in this test the space-time AMR is shown to give major benefits, resulting in a very high resolution obtained with a still rather coarse mesh at $\ell = 0$. Notice that the coarsest level corresponds to a total number of $N_0 = 800$ elements,

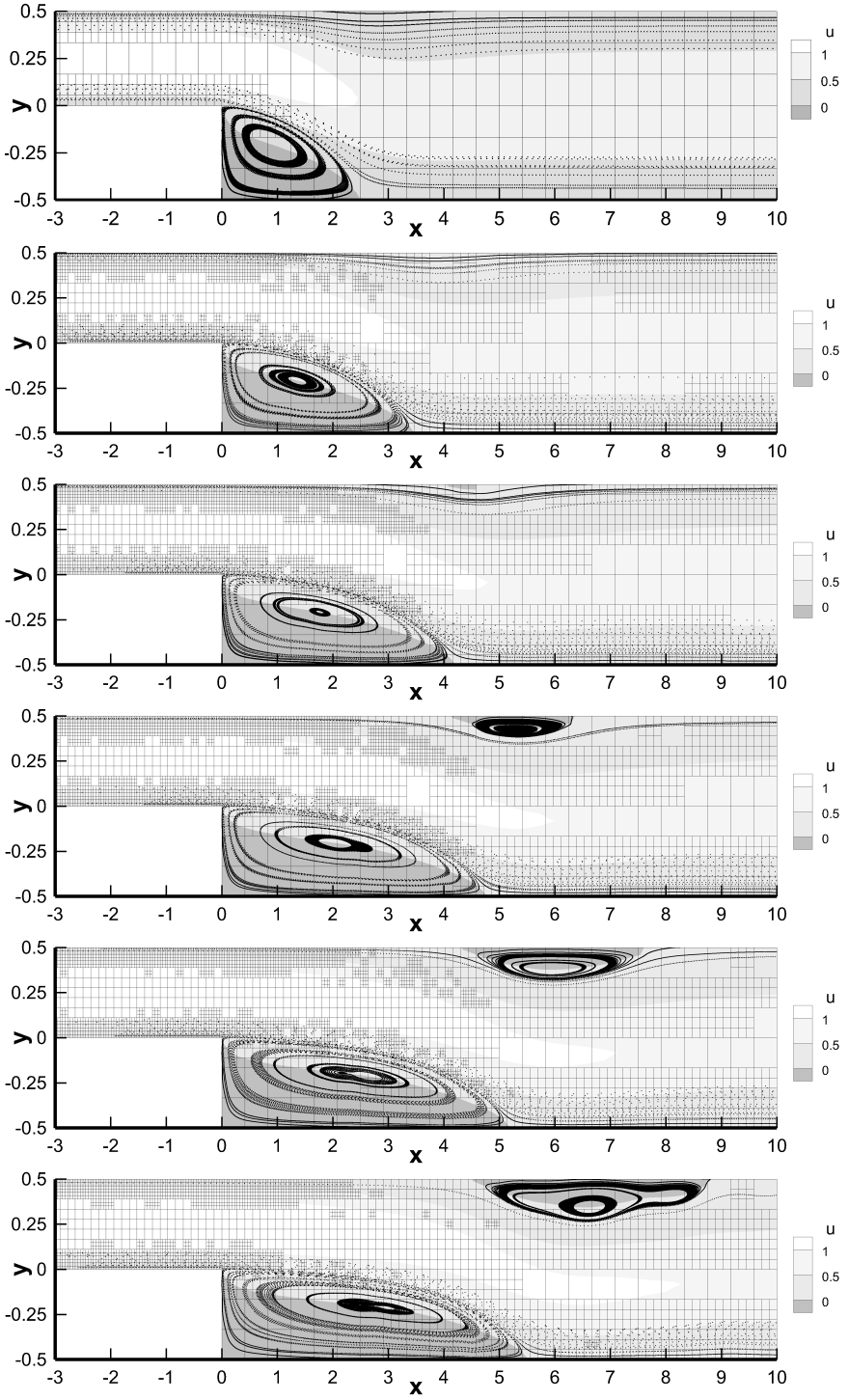

Figure 59: Numerical solution obtained for the 2D backward facing step problem with the staggered semi-implicit AMR-DG-P_4 method at different Reynolds numbers, from top to bottom, respectively: Re=200, Re=300, Re=400, Re=500, Re=600, and Re=700.

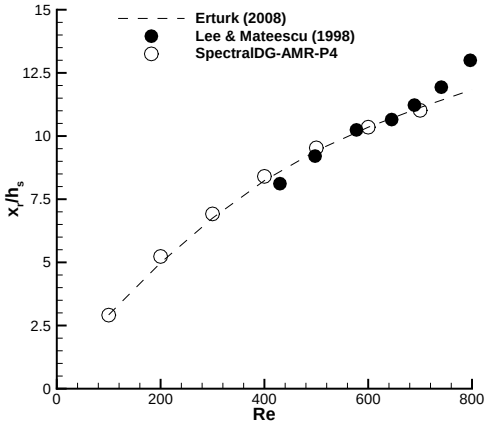

Figure 60: Total lengths of the main recirculations obtained with the staggered semi-implicit spectral AMR-DG-P_4 method for the 2D backward facing step problem next to the 2D numerical results of [112] and the experimental measurements of [184] at different Reynolds numbers, up to $Re = 800$.

a total number of degrees of freedom of $N_0^{dof} = 80'000$ and a characteristic mesh size of $h_0 = 1/20 = 0.05$, while a uniform grid on the finest level corresponds to $N_2 = 64'800$, $N_2^{dof} = 6'480'000$ and $h_2 = h_0/9$. No spurious oscillations are generated in our simulation, which means that the non-conforming elements that appear in the AMR framework are treated properly by our numerical method.

6.3 THREE-DIMENSIONAL TESTS

6.3.1 *Lid-driven cavity: 3D (SI-DG)*

In this section we present the three-dimensional version of the previous test case. A cubic cavity is filled by an incompressible fluid, and the upper wall boundary drives the fluid flow with a non-zero velocity $\mathbf{v} = (1, 0, 0)$. The presence of a third spatial dimension introduces a new degree of freedom to dynamics of the flow and the resulting flow field is different compared to the 2D case discussed before. The physical domain $\Omega = [-0.5, 0.5]^3$ has been divided into only $5 \times 5 \times 5$ spatial elements, with the implicitness factor $\theta = 1$ chosen for the time discretization. Figure 62 shows the computed results compared with the reference data provided by [177] and [2] next to the three-dimensional view of the flow field at Reynolds numbers Re=100 and Re=400, obtained with the P_6 and P_8 version of our staggered semi-implicit spectral DG scheme. Also for the three-dimensional cavity flow, our numerical results are in very good agreement with the reference data. At the bottom of figure 62 the numerical solution for the case $Re = 400$ has been projected onto the three orthogonal planes $x - y$, $x - z$ and $y - z$. The expected secondary

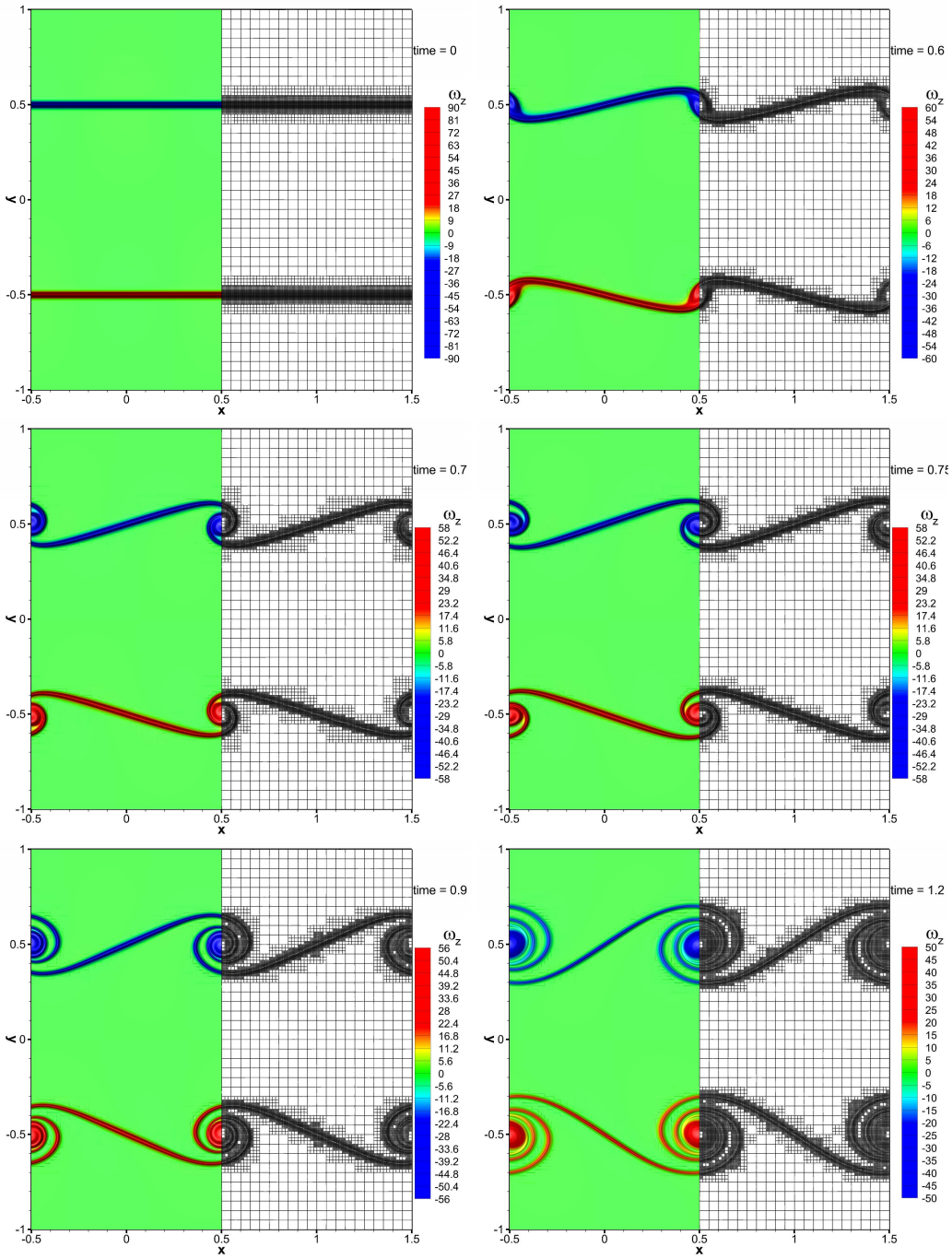

Figure 61: The numerical solution obtained for the two dimensional *'thin'* double shear layer problem at different time steps. The staggered SI-DG-P9 method has been used together with a refinement factor $\mathfrak{r} = 3$ and $\ell_{\max} = 2$ refinement levels. Every figure depicts the vorticity field ω_z next to the respective AMR grid.

recirculations, which distinguish the three dimensional flow field from the two dimensional one, are clearly visible.

LID-DRIVEN CAVITY WITH AMR. Figures 63-64 show the respective numerical results obtained at Reynolds numbers $Re = 100$ and $Re = 1000$ with our SI-DG-P_4 scheme, corresponding to a total number of degrees of freedom of $N_{dof} = 5^3 = 125$ per space-element. The velocity profile interpolated along the vertical and horizontal axes, i.e. $(x, y, z) \in [-0.5, 0.5] \times \{0\} \times \{0\}$ and $(x, y, z) \in \{0\} \times [-0.5, 0.5] \times \{0\}$, is shown and compared with the reference solutions of [2, 177] next to the corresponding three-dimensional view of the fluid flow. A very good match between our numerical results and the reference data is obtained. The three dimensional recirculation together with the active AMR grid are highlighted in figure 63, where the numerical solution is interpolated along the three orthogonal panes $x-y$, $y-z$ and $x-z$. In this case, the physical domain has been discretized on the zeroth level using only $8^3 = 512$ elements. For the AMR framework we set $\ell_{max} = 1$ and $r = 2$.

6.3.2 *Backward facing step: 3D (SI-DG)*

In this section, the numerical results of the simulation of the three dimensional extension of the backward facing step problem are shown and discussed. The physical domain is described by an expansion-ratio ER= 2, and an aspect-ratio AR= $L_z/H = 40$, where L_z is the width of the duct in the third spatial dimension. As mentioned above, the two dimensional results are show differences compared to the experimental data for higher Reynolds numbers. The main reason is that the lateral boundary layers developing on the side walls interact with the main recirculations of the two-dimensional flow. This interpretation is justified by the fact that at lower Reynolds numbers and higher aspect ratio, i.e. when the aforementioned interactions are negligible, the two-dimensional results actually match the three dimensional ones and the experimental data (see figure 58). The numerical solutions for $Re = 100$ (laminar regime) and Re=1000 (transitional regime) at time $t = 25.0$ obtained with our spectral SIDG-P_3 scheme give an overview of the 3D flow field, see figures 65-66. The friction forces at the lateral boundary layers constrict the axial velocity profile and the main recirculation to the center of the duct. A non-zero w velocity component is generated consequently.

6.3.3 *Three dimensional Taylor-Green vortex problem (SI-DG)*

A classical fully three-dimensional flow that is widely used for testing the ability of a numerical method in solving the smallest scales in turbulent flows is the three

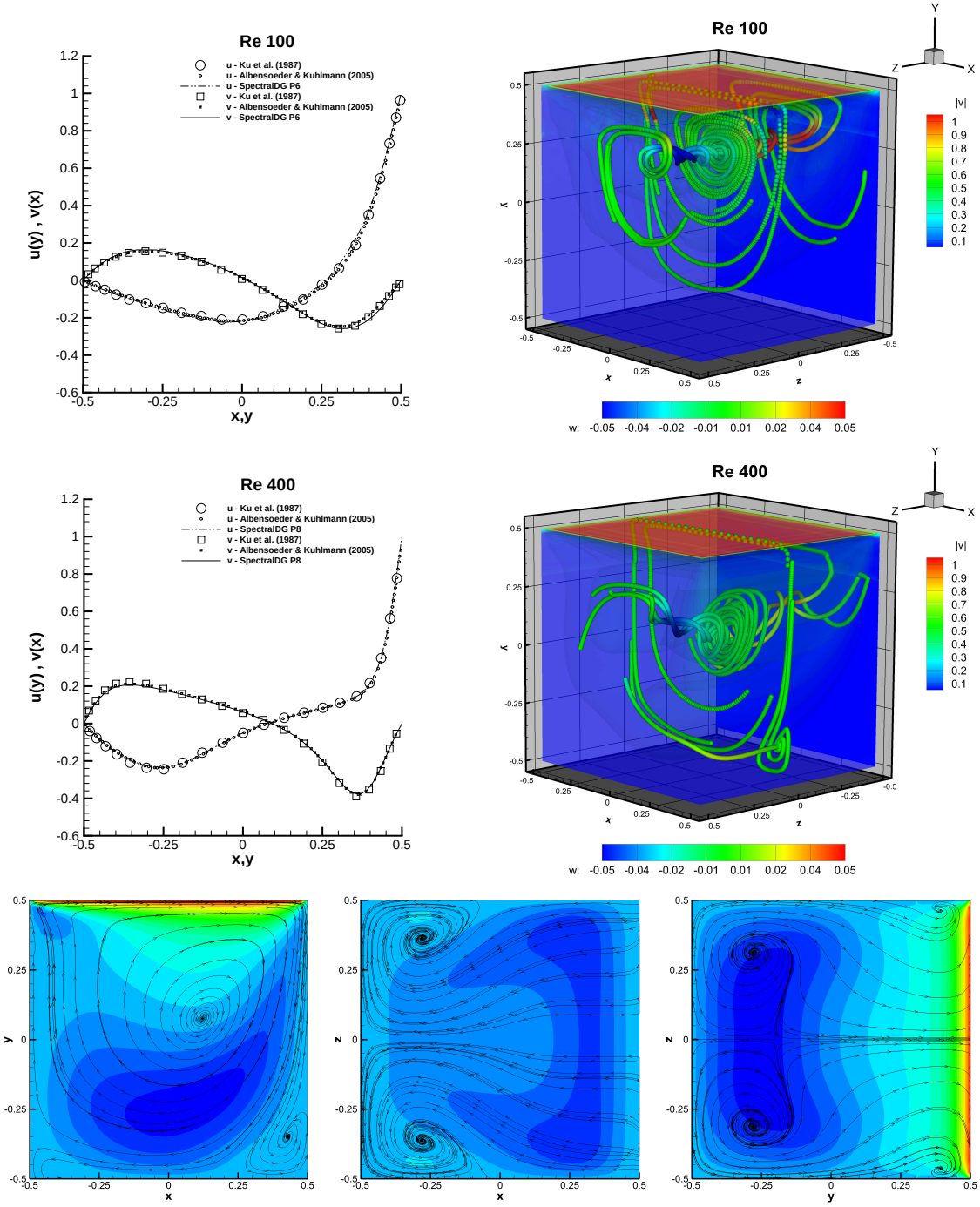

Figure 62: The numerical solution obtained for the three dimensional lid-driven cavity problem compared with the numerical results of [2, 177] at different Reynolds numbers, respectively, from the top to the center: Re=100 and Re=400 using $5 \times 5 \times 5$ elements. The results have been obtained with a staggered semi-implicit spectral DG-P_6 and DG-P_8 method. The streamlines are colored with the w velocity magnitude. The numerical solution for the case $Re = 400$ has been interpolated along the three orthogonal planes $x - y$, $x - z$ and $y - z$ at the bottom: streamlines and the u velocity are depicted.

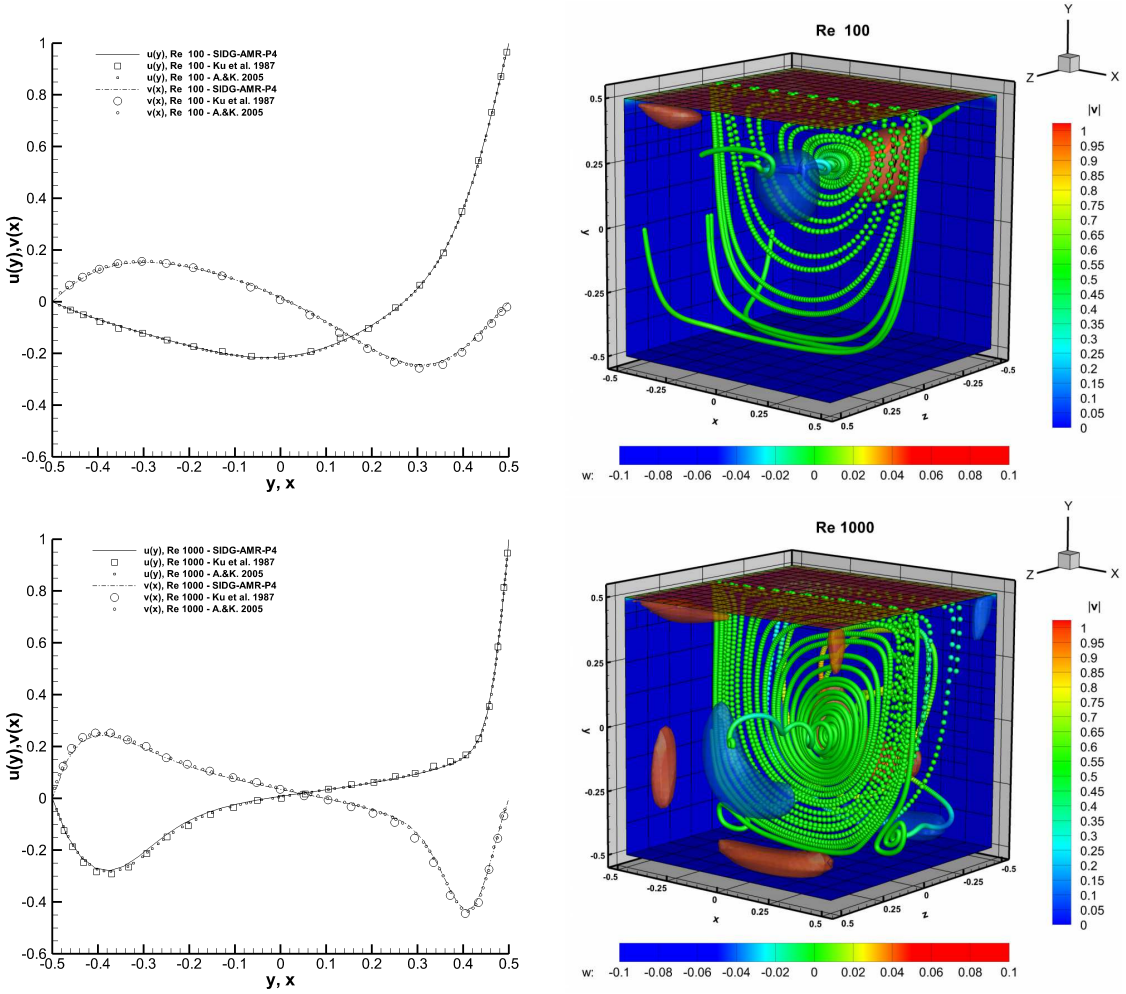

Figure 63: The numerical solution obtained for the three dimensional lid-driven cavity problem compared with, at the left, the numerical results of [2, 177] at Reynolds numbers Re=100 (top) and Re=1000 (bottom) using $8 \times 8 \times 8$ elements. The results have been obtained with our staggered semi-implicit DG-P_4 method with AMR. In the 3d-view on the right, streamlines are colored with the w velocity magnitude, w-peak iso-surfaces are shown, the boundary-slices are colored by the velocity magnitude $|\mathbf{v}|$ together with the *main* AMR-grid.

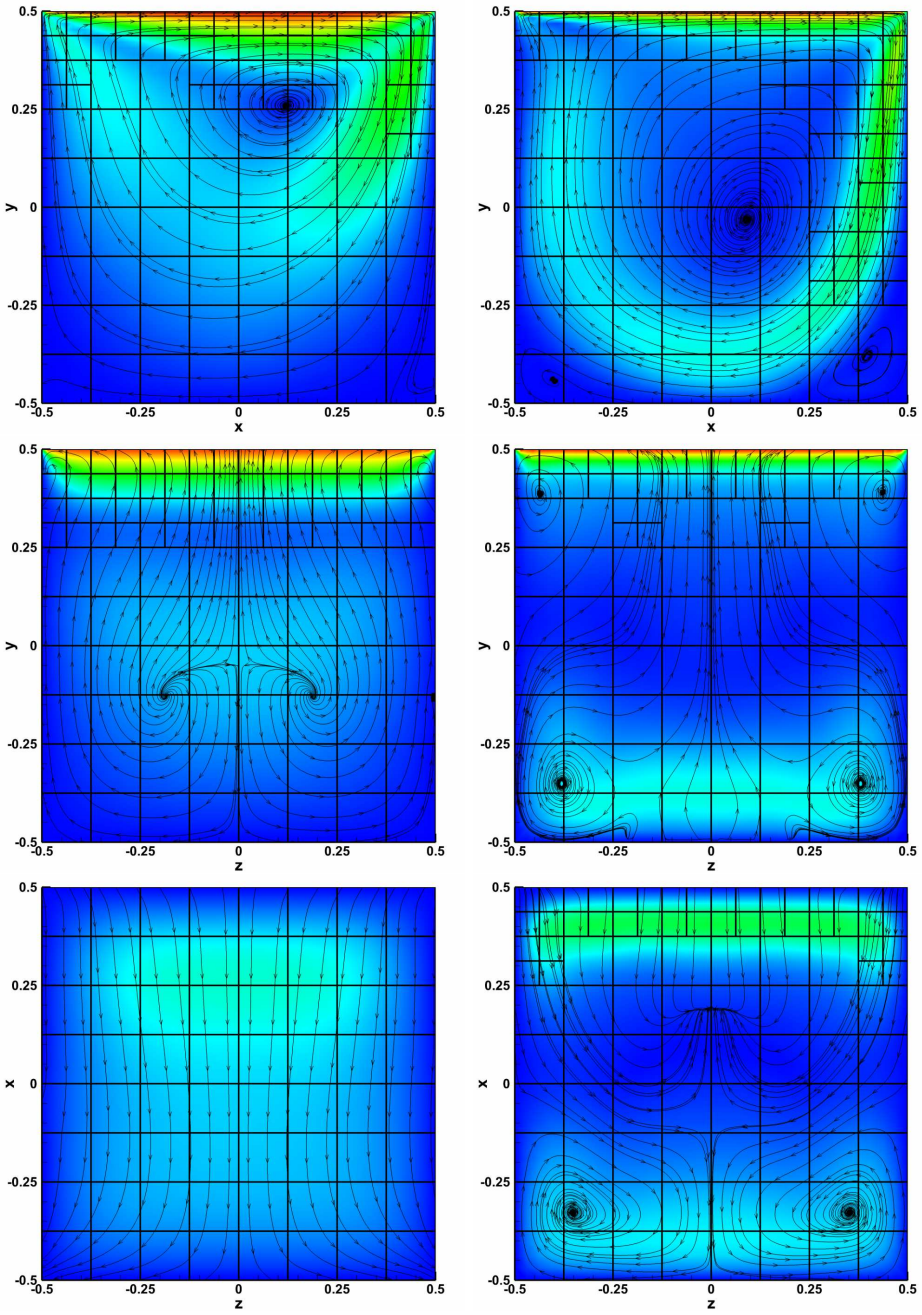

Figure 64: The numerical solution obtained for the three dimensional lid-driven cavity problem interpolated along the three orthogonal planes $x-y$, $z-x$ and $z-y$ from the top the bottom, at Reynolds numbers Re=100 (left) and Re=1000 (right) using $8\times8\times8$ elements. Tangential streamlines and the velocity magnitude $|\mathbf{v}|$ are depicted. The results have been obtained with our staggered semi-implicit AMR-DG-P_4 method.

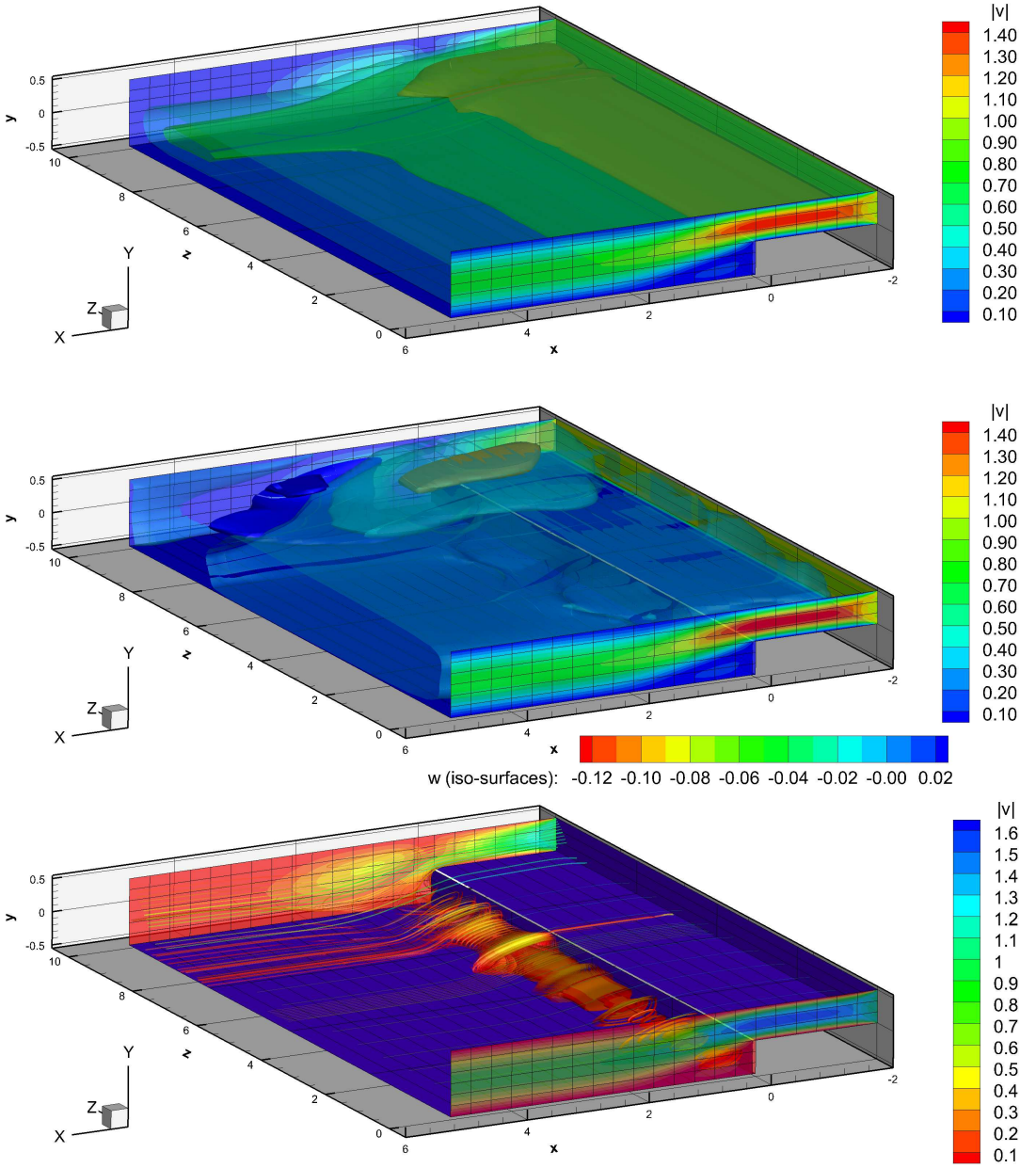

Figure 65: Numerical solution for the three dimensional backward facing step problem at time $t = 25.0$ computed with the staggered semi-implicit spectral DG-$\mathbb{P}_3$ method for $Re = 100$. The iso-surfaces of the velocity magnitude (top), the iso-surfaces of the w velocity component (center) and the streamtraces of the fluid flow (bottom) are plotted for the first half of the spatial domain $z > 0$.

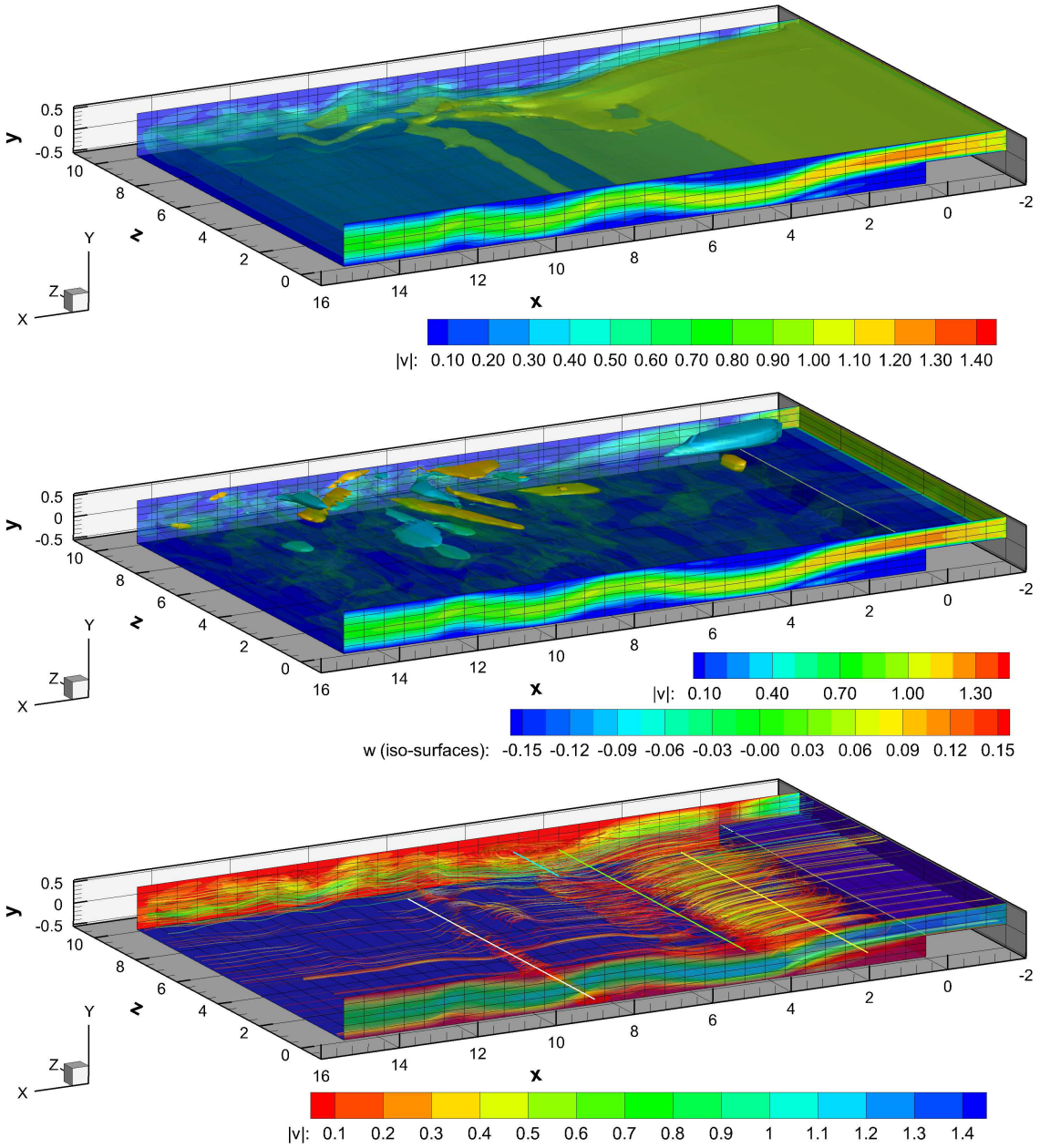

Figure 66: Numerical solution for the three dimensional backward facing step problem at time $t = 25.0$ computed with the staggered semi-implicit spectral DG-$\mathbb{P}_3$ method for $Re = 1000$. The iso-surfaces of the velocity magnitude (top), the iso-surfaces of the w velocity component (center) and the streamtraces of the fluid flow (bottom) are plotted for the first half of the spatial domain $z > 0$. The main recirculation axes are highlighted in the figure at the bottom.

dimensional Taylor-Green vortex problem. In this test the velocity and pressure field are initialized with

$$u(x,y,z,0) = \sin(x)\cos(y)\cos(z), \tag{6.4}$$
$$v(x,y,z,0) = -\cos(x)\sin(y)\cos(z), \tag{6.5}$$
$$w(x,y,z,0) = 0, \tag{6.6}$$
$$p(x,y,z,0) = \frac{1}{16}(\cos(2x)+\cos(2y))(\cos(2z)+2). \tag{6.7}$$

The resulting fluid flow is initially smooth and laminar, but the non-linearity in the governing PDE due to the convective terms combined with a small viscosity quickly generates complex small-scale flow structures after finite times. Indeed, depending on the kinematic viscosity ν, the fluid flow goes through a highly non-linear decaying process, in which the kinetic energy $E = \mathbf{v}^2/2$ is transported from the lower (large scale processes) to higher modes (smallest scales) until reaching the dissipative viscous regime. A widely accepted reference solution for the rate of kinetic energy dissipation has been computed for this test problem by Brachet et al. in [43] through both a direct spectral method based on up to 256^3 modes and a rigorous power series analysis up to order t^{80} (see also [212]). The computational domain is chosen as $\Omega = [0, 2\pi]^3$, with periodic boundary conditions everywhere. The smaller the expected flow scales, the higher the necessary grid resolution. The time evolution of the main physical variables of the fluid flow is represented in figure 68 at times $t = 0.4$, 2.0, 6.0 and 10.0 for the case $Re = 800$. The streamlines along the three orthogonal planes $x-y$, $x-z$ and $y-z$ are presented in figure 69. The complexity of the resulting small scale flow structures is clearly visible. In order to compare our results quantitatively with those of Brachet et al. [43], we compute the rate of kinetic energy dissipation

$$\epsilon(t) = -\frac{\partial K}{\partial t} = -\frac{1}{\|\Omega\|}\frac{\partial}{\partial t}\int_\Omega \frac{1}{2}\mathbf{v}^2 d\mathbf{x}. \tag{6.8}$$

Especially when the rate ϵ reaches its maximum, a high-resolution method together with a sufficiently fine grid is needed in order to resolve the flow physics properly. Figure 67 shows the time evolution of the rate of the global kinetic energy dissipation $\epsilon(t)$ for different Reynolds numbers $Re = 100$, Re=200, Re=400, Re=800 and Re=1600, obtained with our semi-implicit staggered spectral DG-P_4 and -P_6 schemes, along with 20^3 and 50^3 elements, respectively, see figure 67. The computed results fit the DNS reference data very well, confirming that our scheme is able to resolve even the smallest flow scales properly up to $Re = 1600$.

THREE DIMENSIONAL TAYLOR-GREEN VORTEX PROBLEM WITH AMR. Figure 71 shows the time evolution of pressure, velocity and vorticity magnitude obtained with our SI-DG-P_4 at Reynolds $Re = 800$, within a main mesh Ω_h made of only 20^3 space-elements at the coarsest level Ω_h^0, with a refinement factor $r = 2$ and $\ell_{max} = 1$ refinement levels. When the dissipation rate $\epsilon(t)$ reaches its peak at a given time $t = t_p$, this means the higher modes reach the highest population, entering into

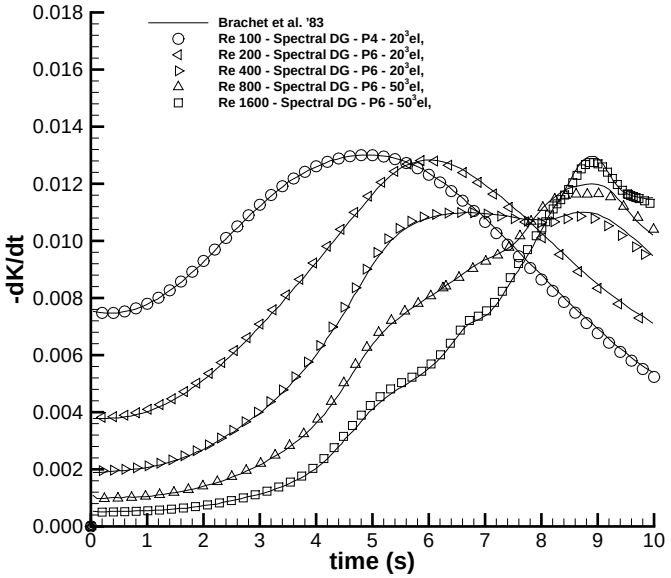

Figure 67: Time evolution of the kinetic energy dissipation rate $\epsilon(t)$ obtained with staggered semi-implicit spectral DG-P_N schemes at different Reynolds numbers $100 < Re < 1600$. The DNS reference solutions of Brachet et al. [43] are plotted as continuous lines.

the viscous regime and being soon destroyed by dissipative forces. At this crucial point, the higher resolution provided by the AMR framework is needed for allowing the smallest scales to dissipate properly. Whenever an under-resolved solution is computed, then the kinetic energy dissipation rate behaves improperly: if the numerical method is non-dissipative, then at higher Reynolds numbers ϵ is expected to be *under-estimated* leading to possible spurious oscillations, i.e. the higher modes saturate the computational domain for the wave numbers $\mathcal{F}[\Omega_h]$, far both from the physical and from the numerical viscous regimes, $\mathcal{F}$ denoting the Fourier operator; if the numerical method is over-dissipative, then ϵ is expected to be *over-estimated*, meaning the numerical viscous regime appears sooner in $\mathcal{F}[\Omega_h]$ with respect to the physical one. From Figure 70 we can conclude that the results obtained with our adaptive semi-implicit staggered DG scheme are in good agreement with the DNS reference solution.

6.3.4 *Vortex ring dynamics (SI-DG with AMR)*

For describing the physical state of an incompressible fluid, vorticity and velocity are essentially interchangeable quantities. On the other hand, higher Reynolds numbers and turbulent flow regimes are typically characterized by localized higher vorticity zones. This fact leads to think that a deeper comprehension in the vortex dynamics could allow a deeper comprehension of high Reynolds fluid dynamics. The visualization and measurement of vorticity constitutes a non-trivial problem

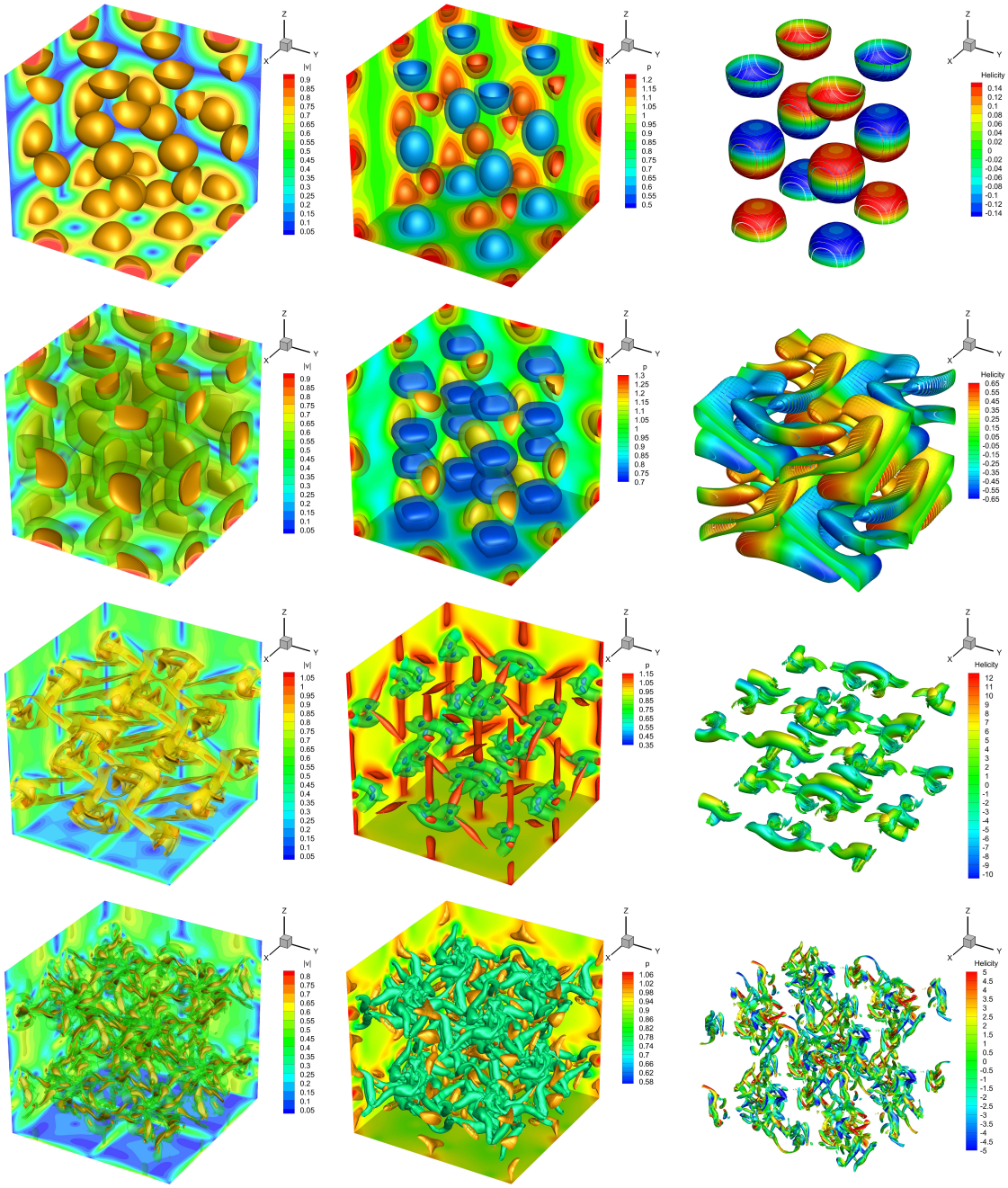

Figure 68: Numerical solution for the three dimensional Taylor-Green vortex flow at $\mathrm{Re} = 800$ computed with the staggered semi-implicit spectral DG-P_6 method using 50^3 elements. The iso-surfaces of the velocity (left), the iso-surfaces of the pressure (center) and the iso-surfaces of the vorticity colored by the helicity field (right) are plotted at times $\mathrm{t} = 0.4$, 2.0, 6.0 and 10.0 from the top to the bottom, respectively.

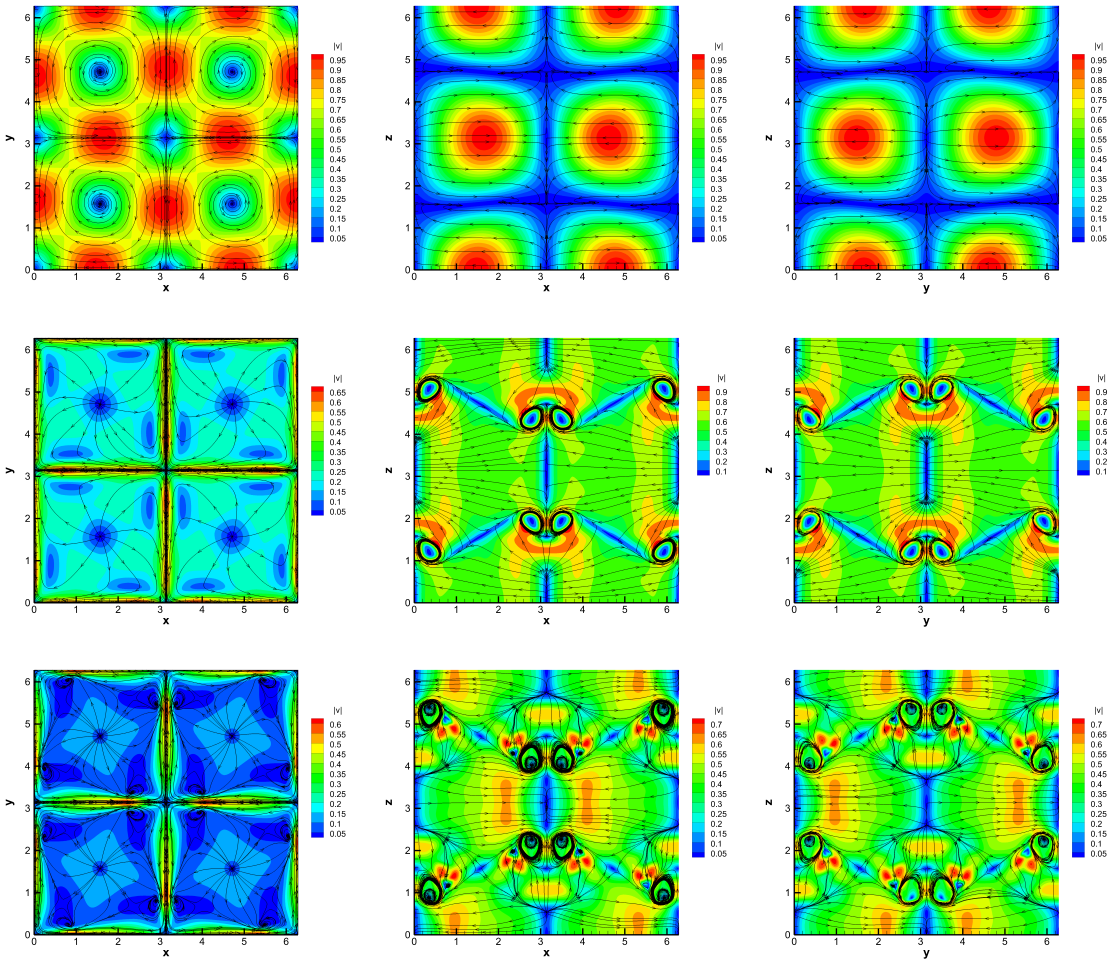

Figure 69: Numerical solution for the three dimensional Taylor-Green vortex flow at $Re = 800$ computed with our spectral DG-P_6 along 50^3 elements with $L = 2\pi$. The numerical solution has been interpolated along the three orthogonal planes $x\hat{O}y$ (left), $x\hat{O}z$ (center) and $y\hat{O}z$ (right): streamlines and the u velocity are shown at times $t = 0.4$, 2.0, 6.0 and 10.0 from the top to the bottom, respectively.

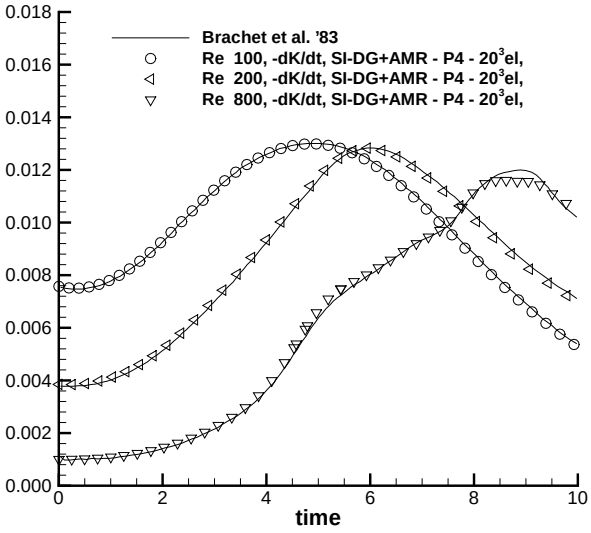

Figure 70: Time evolution of the kinetic energy dissipation rate $\epsilon(t)$ obtained with our SI-DG-P_4 scheme at Reynolds numbers $Re = 100$, 200 and 800. The DNS reference solutions of Brachet et al. [43] are plotted as continuous lines.

in experimental studies. Then, over the years, several experiments, theoretical analysis and numerical investigations provided typical test problems that nowadays can be used for testing the ability of a numerical method to give an accurate description of vortex dynamics. In the following tests the initial conditions are given in terms of vorticity, then the *real* initial condition for the numerical simulations are computed after recycling exactly the same discrete operators depicted in the previous theoretical sections.

Indeed, for incompressible fluids a vector potential $\mathbf{A}$ can be introduced by defining the velocity vector as $\mathbf{v} = \nabla \times \mathbf{A}$. Then the vorticity can be written in terms of $\mathbf{A}$ as

$$\omega = \nabla \times \mathbf{v} = \nabla \times (\nabla \times \mathbf{A}) \equiv \nabla(\nabla \cdot \mathbf{A}) - \nabla^2 \mathbf{A}. \tag{6.9}$$

Notice that any divergence-free component of vector $\mathbf{A}$ would not contribute to the corresponding velocity field. Then, by looking for solutions satisfying the divergence-free condition for $\mathbf{A}$, a very simple Poisson equation follows for $\mathbf{A}$, yielding a very familiar system of equations for the potential vector components A_k, $k = x, y, z$, i.e.

$$\mathbf{B} = \nabla A^{(k)} \tag{6.10}$$

$$\nabla \cdot \mathbf{B} = -\omega^{(k)} \tag{6.11}$$

where vector $\mathbf{B}$ is an auxiliary variable. Indeed, this system shows to be very similar to our governing equations (5.1-5.2) and a consistent discrete DG-P_N formula-

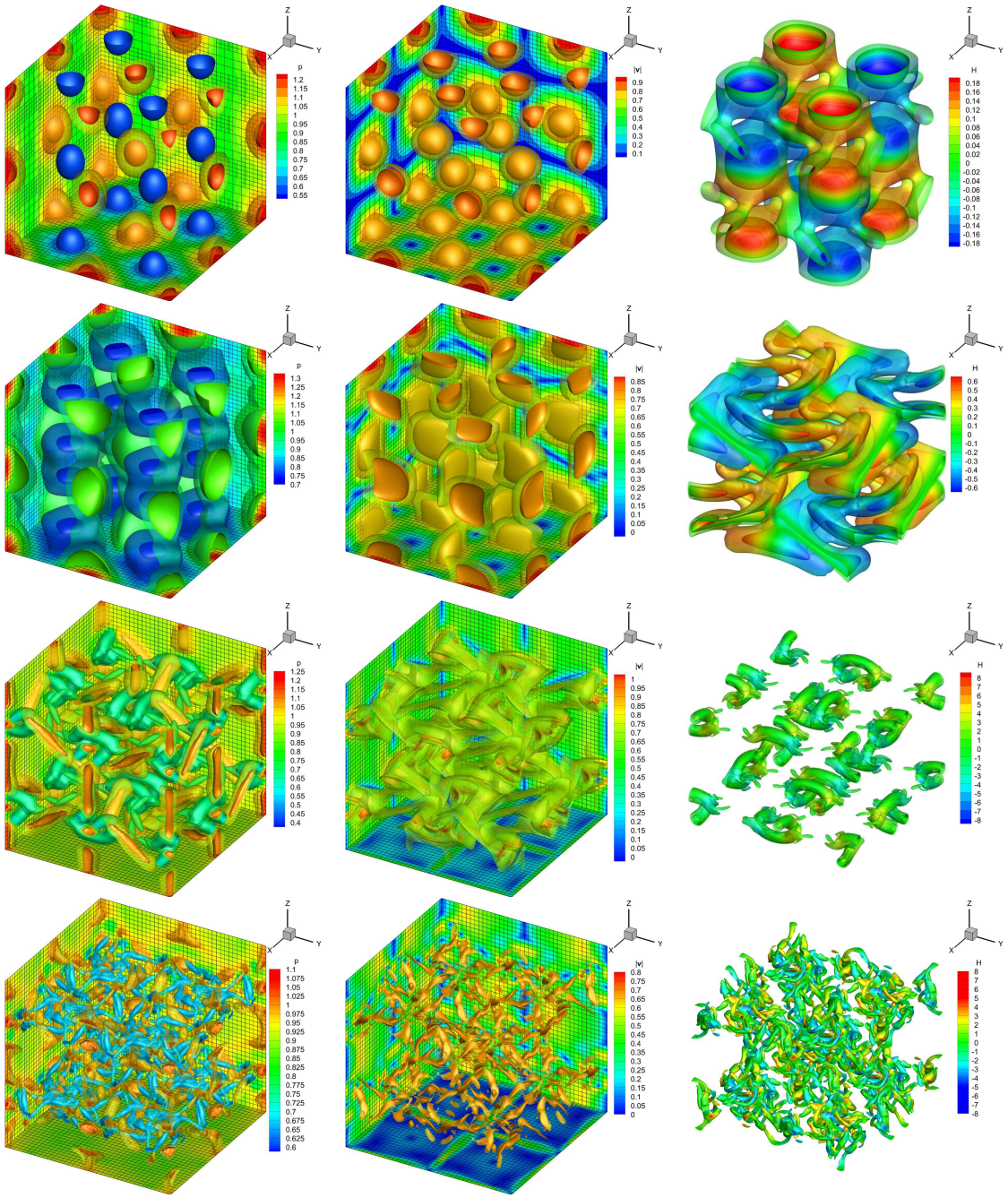

Figure 71: Numerical solution for the three dimensional Taylor-Green vortex flow at $Re = 800$ computed with our SI-DG-P_4 method using 20^3 elements on the coarsest level Ω_h^0, a refinement factor $\tau = 2$, $\ell_{max} = 1$ maximum refinement levels. The iso-surfaces of the velocity (left), the iso-surfaces of the pressure (center) and the iso-surfaces of the vorticity colored by the helicity field (right) are plotted at times $t = 0.5$, 2.0, 6.0 and 10.0 from the top to the bottom, respectively.

tion on the presented staggered grids, $A_h^{(k)}, \omega_h^{(k)} \in P_N(\Omega_h)$ and $B_h^{(k)} \in P_N(\Omega_h^{*(k)})$, reads

$$\mathbb{H}\tilde{A}^{(k)} = \mathbb{M}\tilde{\omega}^{(k)} \tag{6.12}$$

after setting $\Delta t = 1$, $\tilde{\omega}^{(k)}$ and $\tilde{A}^{(k)}$ are respectively the vector of the degrees of freedom for the k-th vorticity and potential vector components. After the three equivalent discrete Poisson systems are solved for the potential vector, then the velocity is updated accordingly to the L_2 projection over P_N of the definition $\mathbf{v} = \nabla \times \mathbf{A}$.

6.3.4.1 *Vortex ring pair collision*

In this three-dimensional test, two coplanar vortex rings are initialized within a cubic spatial domain $\Omega = [-\pi, \pi]^3$ with periodic boundary condition everywhere, centered in $C_{1,2} = \pm(D\cos(\pi/4)/2, D\cos(\pi/4)/2)$ with $D = 1.83$, a major radius $R = 0.491$, centered along the $x - y$ plane, according to a Gaussian distribution in the ring core (matches case II of [166])

$$|\omega|(r) = \omega_0 \exp\left[-\left(\frac{r}{a}\right)^2\right], \tag{6.13}$$

where r is the radial direction, $a = 0.196$ is the effective thickness of the core, $\omega_0 = 23.8$ the vorticity amplitude. For the present test the Reynolds number is $Re_\gamma = \gamma/\nu = 577$, $\gamma = \pi\omega_0 a^2$ being the circulation of the vortex ring, yielding a kinematic viscosity $\nu \sim 5 \times 10^{-3}$. The two ring vortices proceed in the vertical direction because of *self-induction* and, at the same time, the two rings are attracted towards the $x = y$ plane by *mutual-induction*. At around $t = 3$ the two vortex rings collide. Notice that vortex lines are anti-parallel at the contact point, and consequently dissipated by viscous interactions. Then, the resulting dynamics becomes highly non linear, with very complex effects due to both self- and mutual-induced interaction (see a review for vortex reconnection [165] and [166] for an almost complete overview of the vortex collision process). Figure 72 shows the dynamics of the vortex interaction by means of the selected iso-surfaces for the vorticity magnitude $|\omega|$, showing the main evolution phases before the ring collision, the collision phase and the post-collision phase, with a good description of the *bridging mechanism*. The computed results show to be in good agreement with the provided reference solution in literature, e.g. see [166, 128, 141]. For this test, the computational domain has been discretized using 30^3 space-elements on the coarsest grid Ω_h^0 within the space of solutions of our SI-DG-P_4 method, a refinement factor $\tau = 2$ and a maximum number of refinement levels $\ell_{max} = 1$. The mesh is shown to be automatically refined only next to the vorticity cores, saving much computational effort compared to a uniform fine grid. Figure 72 shows the time evolution of the vorticity field interpolated along the two orthogonal vertical planes $x = y$ and $x = -y$. At $t = 4.5$, some spurious oscillations arise in the vorticity field along the collision plane $x = y$, reflecting the fact that, in the vorticity formulation, a potentially dangerous steep gradient is generated. Indeed, it is a

well known fact that vortex reconnection is allowed only for viscous fluids. This means that, in the high Reynolds regime, the vortex rings would approach to be conserved in time, leading, probably, to a highly non-linear inviscid interaction in the collision phase. In this case, very high resolution methods are needed and a limiting strategy would become necessary for a pure DG method for resolving the physics of the fluid flow.

6.3.4.2 *Vortex ring pair leapfrogging*

In this section the interaction between two coaxial vortex rings is simulated within the spatial domain $\Omega = [-1.5, 1.5]^2 \times [-4.4]$ with periodic boundary conditions everywhere. Two vortex rings are initialized according to the Gaussian distribution (6.13), following [249], with a Reynolds number $Re_\Gamma = 1000$, a ratio of major and minor radius of $R/r = 10$, the ring centers being *one radius* R away from each other. In particular the chosen parameters are $R_0 = 0.5$, $a = 0.05$, vorticity amplitude $\omega_0 = 1$, and kinematic viscosity $\nu = 10^{-3}$. In this case, the self-induction leads the ring pair to move vertically in the z direction, the mutual-induction leads the last (backward) vortex to accelerate, being scaled down and going past the second vortex through the inner orifice, i.e. *'leapfrogging'*. The time evolution for the computed vorticity magnitude interpolated along the two arbitrary (central symmetry holds) vertical and orthogonal planes is shown in figures 74 and 75. Also in this case, good agreement with the provided reference solution of [249, 67] is verified. The physical domain Ω has been discretized within a mesh of $30 \times 30 \times 80$ space elements on the coarsest grid Ω_h^0 within the space of solutions of our SI-DG-P_4 method, refinement factor $r = 2$, up to one single refinement level $\ell_{max} = 1$. The chosen AMR grid corresponds to a maximum number of $N_{dof}^{max} = N_{elem}^{max} \times (N+1)^3 = 72\ 000\ 000$ of degrees of freedom per physical variable if a uniform fine grid was used. Notice that, thanks to the AMR framework the real total number of degrees of freedom per physical variable is reduced approximately by a factor of $r^d = 8$. Indeed, the mesh is dynamically refined only close to the vortex rings.

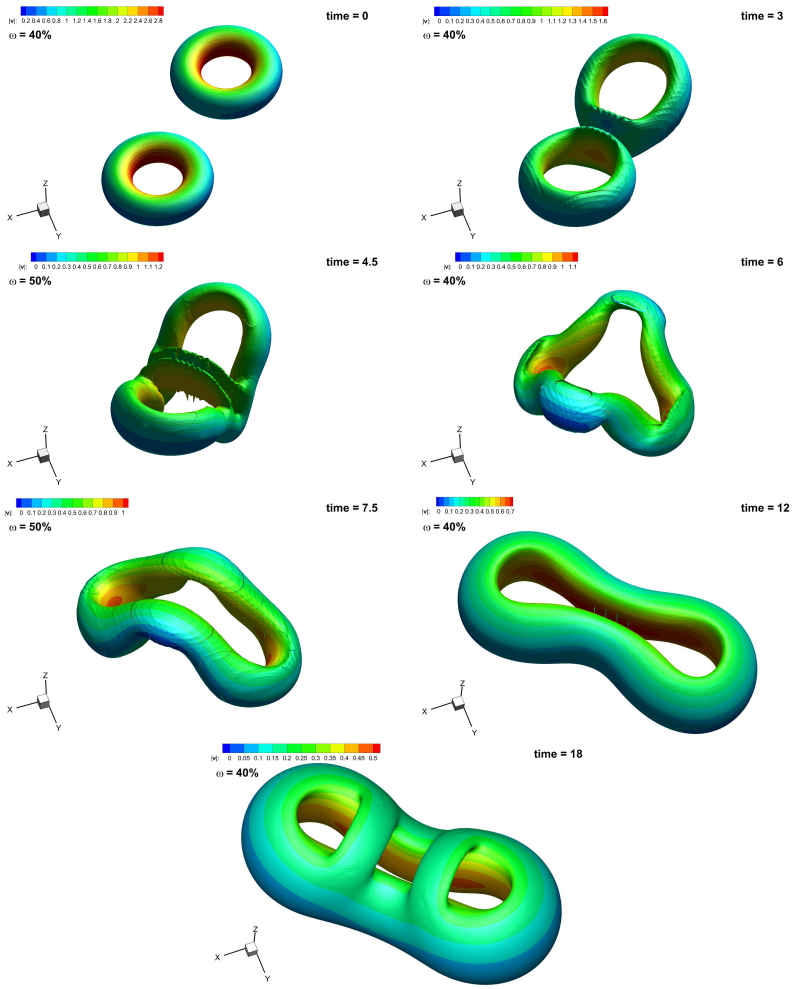

Figure 72: Time evolution of the iso-surfaces for the vorticity magnitude $|\omega|$ in the three-dimensional vortex-ring pair interaction problem at different times, respectively, from left to right, from the top to the bottom: t=0.0, 3.0, 4.5, 6.0, 7.5, 12.0 and 18.0, using 30^3 elements on the coarsest grid with periodic boundary conditions; these results are obtained with the P_4-version of our SI-DG method. The iso-vorticity values has been chosen accordingly to the percentage referred to the maximum $|\omega|_{max}$ accordingly to [166].

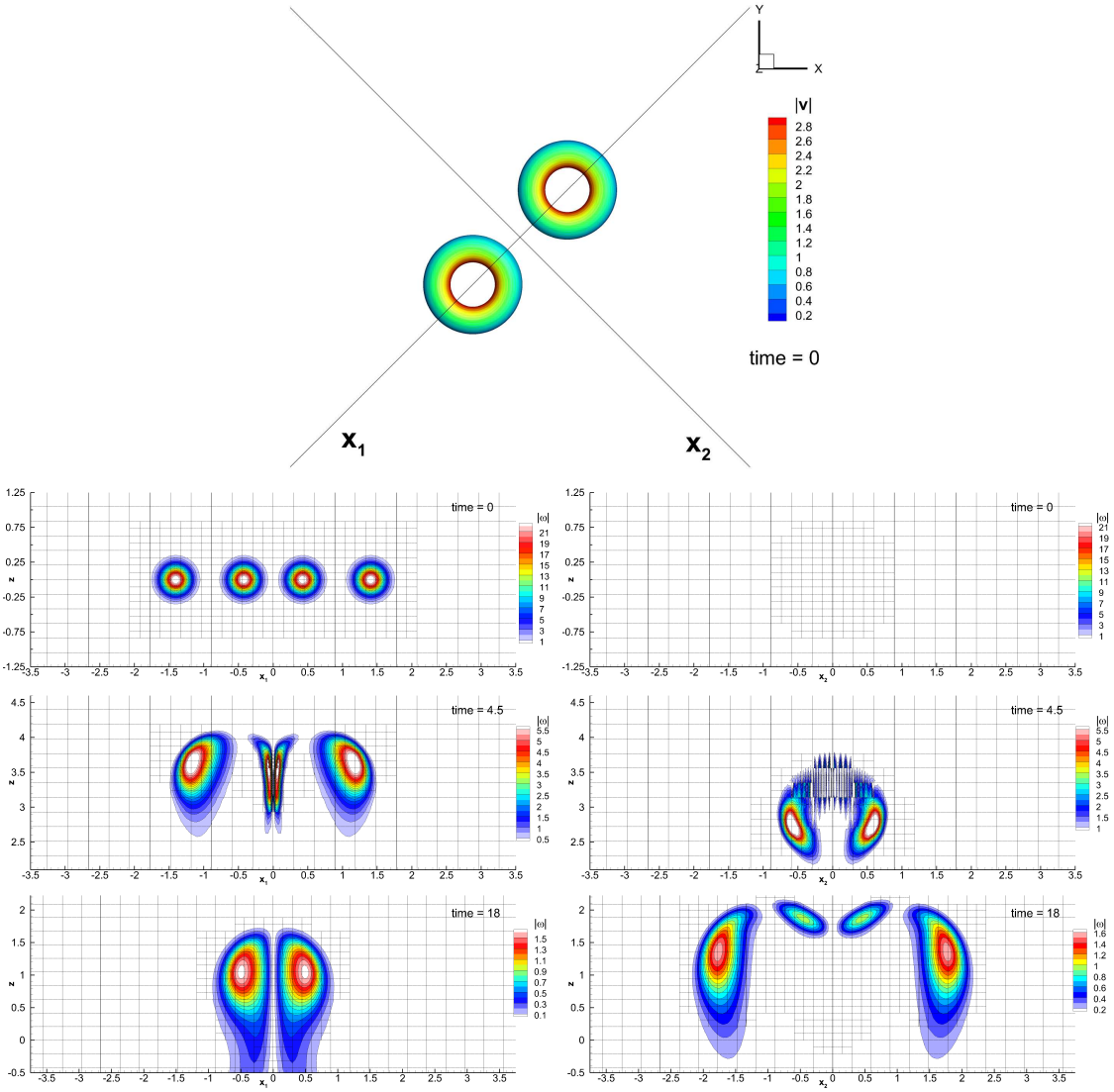

Figure 73: Time evolution of the iso-surfaces for the vorticity magnitude $|\omega|$ in the three-dimensional vortex-ring pair interaction problem at different times; the numerical solution has been interpolated along the two-dimensional orthogonal planes $x_1 - z$ (left) and $x_2 - z$ (right), passing through the two bisectors x_1 and x_2 of $x - y$, respectively (see image at the top); these results are obtained with the P_4-version of our SI-DG method using 30^3 elements on the coarsest grid with periodic boundary conditions at times t=0.0, 4.5 and 18.0.

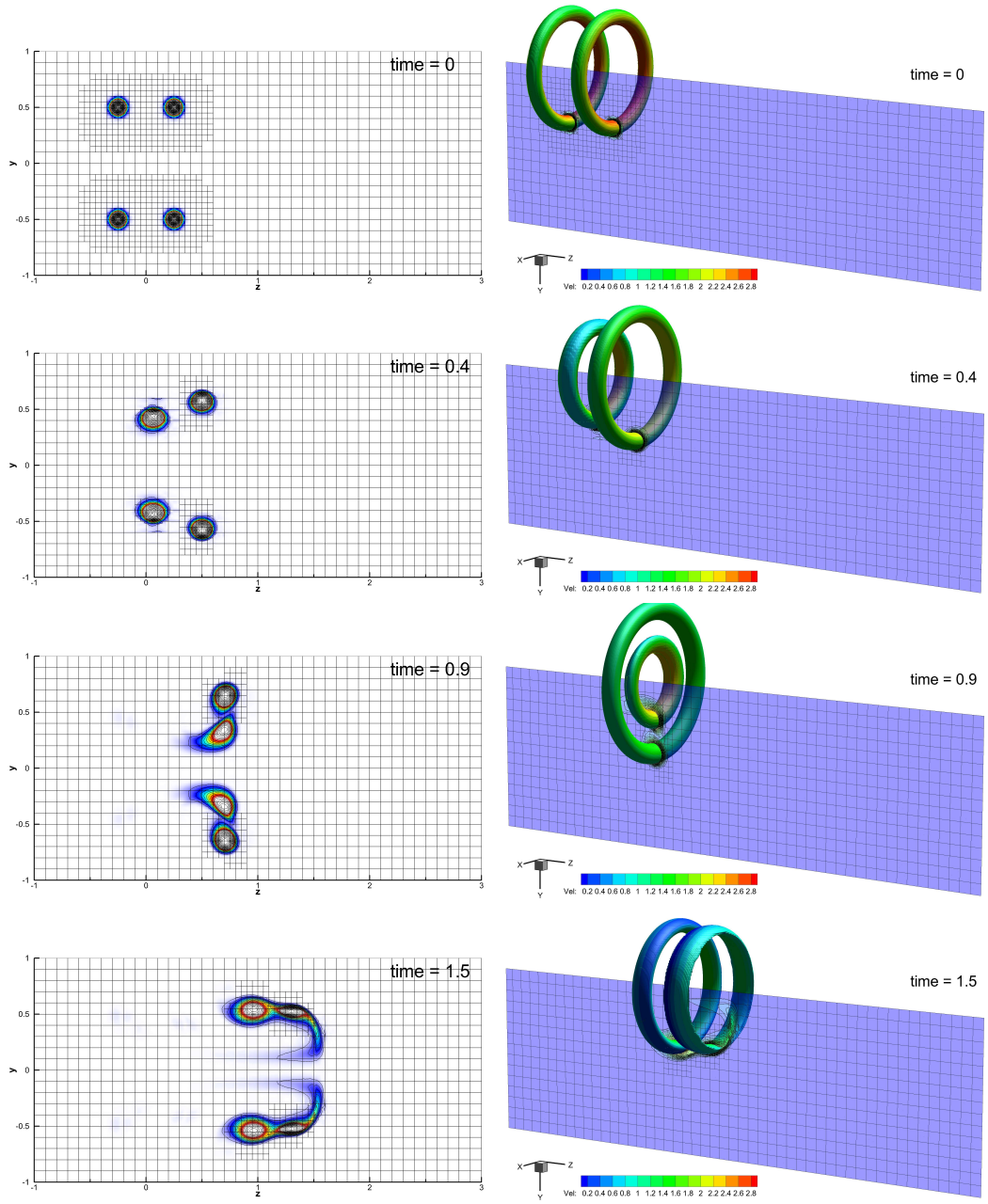

Figure 74: Time evolution of the vorticity field for the three-dimensional vortex-ring pair 'leapfrog' problem, respectively, from the top to the bottom: t=0.0, 0.4, 0.9, and 1.5, using $30 \times 30 \times 80$ elements on the coarsest grid with periodic boundary conditions; at the left the numerical solution interpolated along the two-dimensional $y - z$ plane, at the right the three-dimensional view of the iso-surfaces of the vorticity magnitude $|\omega|$; these results are obtained with the P_4-version of our SI-DG method.

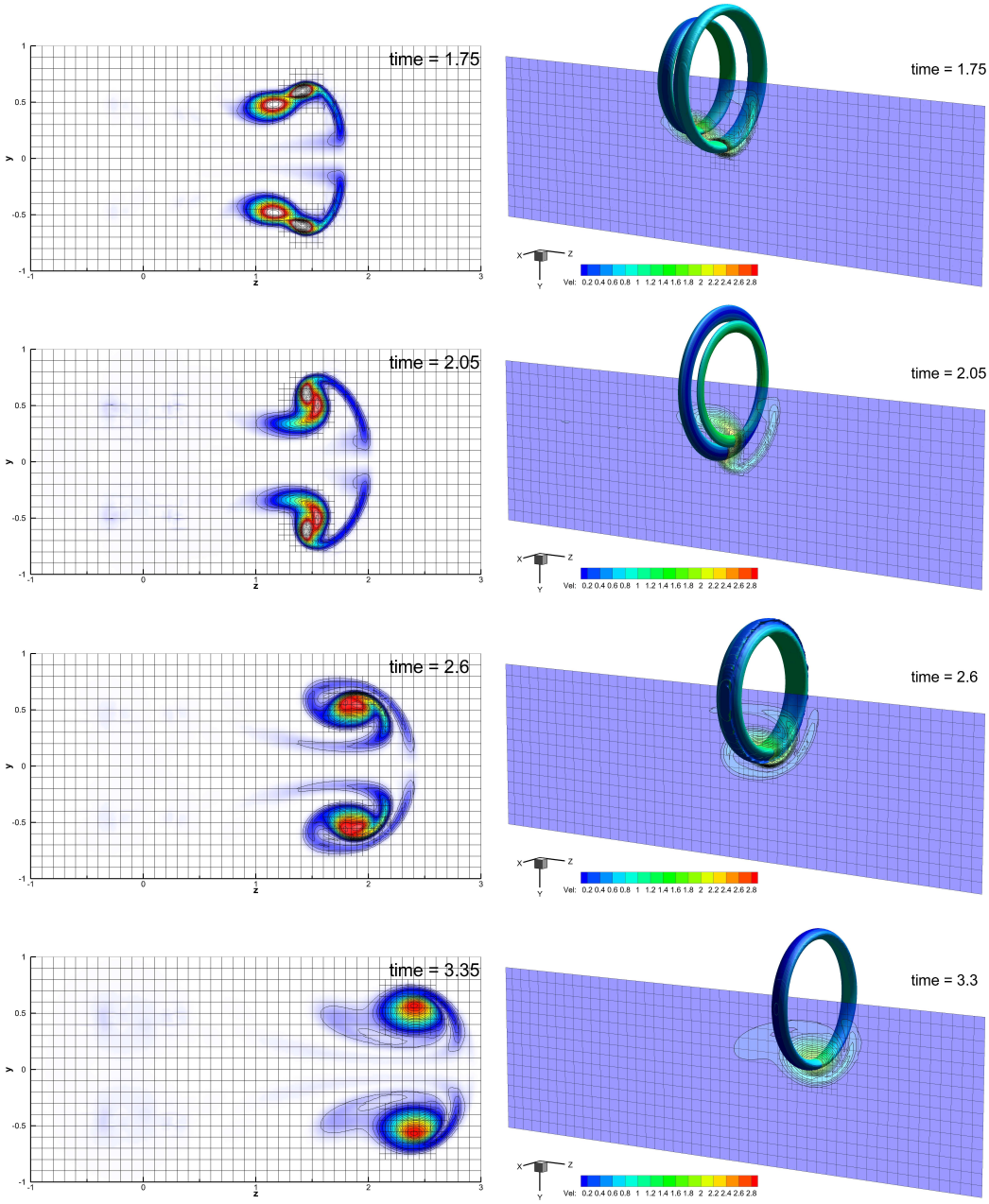

Figure 75: Time evolution of the vorticity field for the three-dimensional vortex-ring pair 'leapfrog' problem, respectively, from the top to the bottom: t=1.75, 2.05, 2.60, and 3.35, using $30 \times 30 \times 80$ elements on the coarsest grid with periodic boundary conditions; at the left the numerical solution interpolated along the two-dimensional $y - z$ plane, at the right the three-dimensional view of the iso-surfaces of the vorticity magnitude $|\omega|$; these results are obtained with the P_4-version of our SI-DG method.

Part IV

CONCLUSIONS

Here we present a summary of the theoretical results. Then, some possible and auspicious future research trends are given.

7

CONCLUSION AND PERSPECTIVES

7.1 ADER-DG

7.1.1 *Summary*

Their high order of accuracy combined with their locality (no reconstruction step needed) make DG methods very attractive for solving a wide range of spatial flow scales in fluid dynamics when used within an adaptive mesh refinement framework (AMR). However, it is a well known fact that pure DG methods are unable to properly resolve discontinuous waves or very sharp flow profiles without introducing unphysical spurious oscillations (Gibbs phenomenon). To cope with this problem, in this work an arbitrary high-order unlimited ADER-DG method has been supplemented with a high-order accurate and very robust ADER-WENO finite-volume method. The adopted limiting method, based on an *a posteriori* survey of troubled zones and, when necessary, a complete re-computation of the solution by means of a more robust finite volume scheme within a proper finer sub-grid, i.e. the SCL, has been introduced for the first time by [109]. The primordial version of the adopted *a posteriori* limiting method is due to the series of papers concerning the multi-dimensional optimal order detection (MOOD) criteria for finite-volume methods introduced in [71, 86, 87, 194]. The SCL procedure for DG methods has been extended to adaptive meshes in [281, 280], but only for inviscid fluids. Finally, in [116], the cited numerical method has been extended for the first time to solve the fluid dynamics of dissipative flows, i.e. the *viscous* compressible Navier-Stokes equations and the *resistive* magneto-hydrodynamic equations (VRMHD).

The numerical method has been thoroughly tested on a large set of non-trivial numerical benchmark problems, from low to high Mach number flows, from low to high Reynolds number regimes, for which a reference solution or published reference results exist. In particular, the higher order of accuracy combined with the shock-capturing capabilities of the method have been successfully demonstrated.

7.1.2 *Perspectives*

The presented fully explicit finite-element ADER-DG-P_N method, supplemented by a proper higher order finite-volume sub-cell limiter on AMR grids showed to be a validate numerical engine for solving general hyperbolic systems. In the next we propose some possible developments and applications of the model for the purpose of finalizing possible next research topics.

7.1.2.1 *Extensions and corrections*

Whenever highly non-linear, low-dissipative and poorly-smooth problems are simulated, then the limited computational domain is expected to enlarge, letting in those specific cases to the finite-volume ADER-WENO the main computational effort. Even in such complicated test-problems, the same high-resolution properties are expected. On the other hand, the highly scalability of DG methods is expected to be damaged due to the non-linear polynomial reconstruction of the sub-cell WENO limiter. This fact introduces the possibility of extending the presented sub-cell limiter to *new higher-scalable and robust methods*. For instance, the central-WENO (CWENO) method could become part of future extensions. Indeed, in CWENO methods, originally introduced by Levy, Puppo and Russo, see [188], the stencil-size for the reconstruction is minimized and seems to be a good candidate alternative to our ADER-WENO, reducing considerably the amount of total MPI communication, in particular for multi-dimensional problems. Moreover, one of the purposes of choosing space-time adaptive meshes is to increase the numerical resolution only where and when it is necessary. Looking forward to multi-scale applications, an efficient MPI-parallel implementation is a must. In this sense, a *dynamical-redistribution of the active computational cells* is needed in order to obtain a balanced computational charge between the MPI-cores, even in the presence of refined AMR-elements, even in the presence of limited sub-grid cells.

7.1.2.2 *PDE systems and applications*

Since the mathematical formulation of the presented problem are quite general, concerning the ADER-DG-P_N method, the future possible application are several, for example the seismic wave propagation in anelastic media (linear and non-linear elasticity equations), a further extension to the viscous-resistive special-relativistic MHD equations (VR-SR-MHD), where a special treatment *stiff source terms* becomes necessary, but in principle one could introduce also the *Hall-interaction* (Hall-MHD). Some extra computational effort could be done for resolving multi-fluid systems, e.g. the *Baer-Nunziato equations* for multi-phase flows and chemical-reaction problems, but also the *multi-fluid equations for plasma physics*. In this context, a proper strategy for simulating different fluid-interfaces is needed, e.g. *immersed boundary* or *cut-cell* methods.

At this stage, another PDE system should be mentioned. Indeed, in a very recent work of Peshkov & Romenski and collaborators [222, 111] dissipative effects in fluids have been successfully described within the more general and unified framework of *first order* symmetric *hyperbolic* thermodynamically compatible systems of Godunov & Romenski, see [134, 135, 240, 136]. In this new unified approach, a *single* PDE system shows the ability of describing at the same time viscous fluids as well as elastic and elasto-plastic solid media. An application of our ADER-DG and sub-cell limiting framework to this innovative PDE system is part of future research.

7.2 SPECTRAL SEMI-IMPLICIT AND SPACE-TIME DG

7.2.1 *Summary and conclusive remarks*

In chapter 5 the novel family of staggered spectral semi-implicit DG methods for the incompressible Navier-Stokes equations recently proposed in [115] for uniform Cartesian grids, and *staggered AMR meshes* in [114], has been outlined in two and three space dimensions. A similar formulation for staggered DG schemes on conforming *unstructured* simplex meshes has been recently outlined in [252, 253, 254], but there the chosen staggered grid was slightly different, and the use of unstructured meshes did *not* allow to produce a spectral DG scheme based on simple tensor products of one-dimensional operators. Of course, unstructured meshes as those used in [252, 253, 254] allow to fit very complicate geometries and complex physical boundaries, however, by choosing staggered Cartesian grids, some interesting advantages follow, in particular:

1. Cartesian grids allow the use of *tensor-products* of the basis and test functions; this means that the weak formulation of the governing equations can be written as a very handy combination of one dimensional integrals over the canonical reference element $\xi \in [0, 1]$;

2. this fact significantly minimizes the computational costs and difficulties for evaluating integrals, because the defined matrices are the same for all the elements in the Cartesian framework;

3. by using basis functions that are built from the Lagrange interpolation polynomials passing through the Gauss-Legendre quadrature points, the basis functions are *orthogonal* and thus the resulting mass matrices are *diagonal*; this fact reduces significantly the computational cost for a mass-matrix multiplication;

4. in our staggered Cartesian framework, each velocity component is defined on a different staggered dual control volume; consequently, the computation of convective and viscous terms on the main grid by interpolating from the dual grids to the main grid and vice versa is simpler and more natural than a discretization of these terms on the dual grids;

5. the resulting numerical method achieves a *spectral convergence* property, i.e. the computational error decreases exponentially when increasing the degree of the approximation polynomials in space and time.

It has been shown that the main advantage of edge/face-based staggered grid methods is to improve substantially the sparsity of the main linear system compared to traditional DG schemes on collocated grids. In particular the discrete Laplace operator $\mathbb{H}$ is shown to be symmetric and positive-definite and has maximum sparsity, since it only involves the element and its direct edge/face neighbors. On uniform meshes, it is block penta-diagonal (in 2D) or block hepta-diagonal (in

3D). This has to be compared to classical DG methods on collocated grids: those are characterized by discrete operators with either larger computational stencils, if a discrete pressure Poisson equation is solved, since in this case the discrete pressure will also depend on neighbors of neighbors; or, one solves directly the saddle point problem associated with the PDE system and thus keeps the small stencil, but in that case there are much more unknowns, namely the scalar pressure and the components of the velocity vector. Moreover, in our scheme $\mathbb{H}$ is shown to be the Schur complement of the discrete saddle point system of the incompressible Navier-Stokes equations. From another point of view, $\mathbb{H} \equiv \mathcal{D}^T \mathbb{M}^{-1} \mathcal{D}$ accounts for the jumps of the piecewise polynomials in the discrete gradients $\mathcal{D}$ resembling a Bassi-Rebay-type lifting operator *evaluated on the dual grid* Ω_h^*, see equation (5.35). The same well-conditioned coefficient matrix $\mathbb{H}$ appears both in the pressure Poisson equation, but also in the linear system arising from the implicit discretization of the viscous terms, with only one additional symmetric positive definite block diagonal term coming from the element mass matrix associated with the time derivative of the velocity. As a consequence, the pressure system and the viscous systems can be solved very efficiently by means of a classical matrix-free conjugate gradient method without recurring, in this paper, to any preconditioner. The spectral properties of the system matrix have been theoretically analyzed in [102] for the uniform Cartesian grid case.

The final algorithm is verified to be high order accurate in both space (SI-DG) and time (st-DG) with spectral convergence property after completing a thorough numerical convergence test that accounts also for the AMR grid refinement. The presented SI-DG-$\mathbb{P}_N$ with AMR and st-DG-$\mathbb{P}_{N_\otimes M}$ methods have been observed to be stable, robust and very accurate. The performance of the method has been shown on a large set of non-trivial test cases in two and three space-dimensions.

7.2.1.1 *Extensions and corrections*

The first extension of our SI-DG with AMR is surely the *space-time formulation* of the here presented st-DG for uniform-grid case. In principle, a proper DG-time integration within a Picard recursive correction procedure seems to be feasible.

7.2.1.2 *PDE systems and applications*

Further work will also concern the extension to the *compressible Euler and Navier-Stokes equations*, following the ideas put forward in [98] for pressure-based semi-implicit finite volume schemes on staggered grids. In this case, a proper limiter will be needed, not only for the treatment of shock waves, but also in order to avoid spurious oscillations in the presence of steep gradients or under-resolved flow features, for example following the novel ideas on *a posteriori* sub-cell finite volume limiters outlined in chapter 3, see [109, 281, 280, 116].

Another research topic is inspired by the linkage between divergence-free condition of incompressible fluids and MHD equations. Indeed, the here presented implicit treatment of the elliptic Poisson equation could inspire *a novel semi-implicit DG discretization of the MHD equations within staggered grids*.

As a matter of fact, the main computational costs in our SI-DG or st-DG simulations are due to the solution of the pressure and viscous systems, characterized by our staggered-discrete Laplace operator $\mathbb{H}$. Since it has been developed a rigorous spectral analysis of $\mathbb{H}$ with very promising results in terms of condition number, see [102], the *design of an optimal specific preconditioner* belongs auspiciously to the next future extensions. In this sense, the novel family of semi-implicit and space-time DG methods represents a validate candidate for a very efficient algorithm suitable for *realistic large-scale problems*. An application of the presented semi-implicit or space-time DG methods for resolving *free-surface hydrodynamics* or the *seismic-wave equations* on *large computational domain* becomes consequently a moral-numerical duty. Also in this case a proper treatment of *boundary conditions* is needed, specially in the aim of applying these methods within complex-domains, which is the case for example of *naval-engineering applications* or *weather forecasting*.

BIBLIOGRAPHY

[1] G. Agbaglah, S. Delaux, D. Fuster, J. Hoepffner, C. Josserand, S. Popinet, P. Ray, R. Scardovelli, and S. Zaleski. Parallel simulation of multiphase flows using octree adaptivity and the volume-of-fluid method. *Compte-rendus de l'Académie des Sciences, Paris*, 339:194–207, 2011.

[2] S. Albensoeder and H.C. Kuhlmann. Accurate three-dimensional lid-driven cavity flow. *Journal of Computational Physics*, 206(2):536 – 558, 2005. ISSN 0021-9991.

[3] Matthew Anderson, Eric Hirschmann, Steven L. Liebling, and David Neilsen. Relativistic MHD with Adaptive Mesh Refinement. *Classical Quantum Gravity*, 23:6503–6524, 2006.

[4] A. M. Anile. *Relativistic Fluids and Magneto-fluids*. Cambridge University Press, 1990.

[5] L. Antón, O. Zanotti, J. A. Miralles, J. M. Martí, J. M. Ibáñez, J. A. Font, and J. A. Pons. Numerical 3+1 general relativistic magnetohydrodynamics: a local characteristic approach. *Astrophys. J.*, 637:296, 2006.

[6] L. Antón, J. A. Miralles, J. M. Martí, J. M. Ibáñez, M. A. Aloy, and P. Mimica. Relativistic Magnetohydrodynamics: Renormalized Eigenvectors and Full Wave Decomposition Riemann Solver. *Astrophys. J. Suppl.*, 188:1–31, 2010.

[7] A. Arakawa and V.R. Lamb. Computational design of the basic dynamical processes of the UCLA general circulation model. *Methods of Computational Physics*, 17:173–265, 1977.

[8] B. F. Armaly, F. Durst, J. C. F. Pereira, and B. Schönung. Experimental and theoretical investigation of backward-facing step flow. *Journal of Fluid Mechanics*, 127:473–496, 1983. ISSN 1469-7645.

[9] V. I. Arnold. Sur la topologic des écoulements stationnaires des fluides parfaits. *Comptes Rendus Hebdomadaires des Séances de l'Académie des Sciences*, 261:17–20, 1965.

[10] F. Assous, P. Degond, E. Heintze, P.A. Raviart, and J. Segre. On a finite-element method for solving the three-dimensional Maxwell equations. *Journal of Computational Physics*, 109(2):222–237, 1993. ISSN 0021-9991.

[11] A. Babucke, M. Kloker, and U. Rist. DNS of a plane mixing layer for the investigation of sound generation mechanisms. *Computers & Fluids*, 37:360–368, 2008.

[12] A. Baeza and P. Mulet. Adaptive mesh refinement techniques for high–order shock capturing schemes for multi-dimensional hydrodynamic simulations. *International Journal for Numerical Methods in Fluids*, 52:455–471, 2006.

[13] D. Balsara. Total Variation Diminishing Scheme for Adiabatic and Isothermal Magnetohydrodynamics. *Astrophysical Journal Suppl. Series*, 116:133–153, 1998.

[14] D. Balsara. Total Variation Diminishing Scheme for Relativistic Magnetohydrodynamics. *Astrophysical Journal Suppl. Series*, 132:83–101, 2001.

[15] D. Balsara. Second-order accurate schemes for magnetohydrodynamics with divergence-free reconstruction. *The Astrophysical Journal Supplement Series*, 151:149–184, 2004.

[16] D. Balsara and C.W. Shu. Monotonicity preserving weighted essentially non-oscillatory schemes with increasingly high order of accuracy. *Journal of Computational Physics*, 160:405–452, 2000.

[17] D. Balsara and D. Spicer. A staggered mesh algorithm using high order godunov fluxes to ensure solenoidal magnetic fields in magnetohydrodynamic simulations. *Journal of Computational Physics*, 149:270–292, 1999.

[18] D. S. Balsara. Divergence-Free Adaptive Mesh Refinement for Magnetohydrodynamics. *Journal of Computational Physics*, 174:614–648, 2001.

[19] D. S. Balsara, C. Altmann, C.-D. Munz, and M. Dumbser. A sub-cell based indicator for troubled zones in RKDG schemes and a novel class of hybrid RKDG+HWENO schemes. *Journal of Computational Physics*, 226:586–620, 2007.

[20] D.S. Balsara. Divergence-free adaptive mesh refinement for magnetohydrodynamics. *Journal of Computational Physics*, 174(2):614–648, 2001.

[21] D.S. Balsara. A two-dimensional HLLC Riemann solver for conservation laws: Application to Euler and magnetohydrodynamic flows. *Journal of Computational Physics*, 231:7476–7503, 2012.

[22] D.S. Balsara and M. Dumbser. Divergence-free MHD on unstructured meshes using high order finite volume schemes based on multidimensional Riemann solvers. *Journal of Computational Physics*, 299:687–715, 2015.

[23] D.S. Balsara, C. Meyer, M. Dumbser, H. Du, and Z. Xu. Efficient implementation of ADER schemes for euler and magnetohydrodynamical flows on structured meshes – speed comparisons with runge–kutta methods. *Journal of Computational Physics*, 235:934 – 969, 2013.

[24] D.S. Balsara, M. Dumbser, and R. Abgrall. Multidimensional HLLC Riemann Solver for Unstructured Meshes - With Application to Euler and MHD Flows. *Journal of Computational Physics*, 261:172–208, 2014.

[25] M. Barkov, S. S. Komissarov, V. Korolev, and A. Zankovich. A multidimensional numerical scheme for two-fluid relativistic magnetohydrodynamics. *Mon. Not. R. Astron. Soc.*, 438:704–716, 2014.

[26] F. Bassi and S. Rebay. A high-order accurate discontinuous finite element method for the numerical solution of the compressible Navier-Stokes equations. *Journal of Computational Physics*, 131:267–279, 1997.

[27] F. Bassi, A. Crivellini, D.A. Di Pietro, and S. Rebay. An implicit high-order discontinuous Galerkin method for steady and unsteady incompressible flows. *Computers & Fluids*, 36(10):1529 – 1546, 2007.

[28] F. Bassi, L. Botti, A. Colombo, A. Ghidoni, and F. Massa. Linearly implicit Rosenbrock-type Runge-Kutta schemes applied to the discontinuous Galerkin solution of compressible and incompressible unsteady flows. *Computers & Fluids*, 118:305 – 320, 2015.

[29] G.K. Batchelor. *An Introduction to Fluid Dynamics*. Cambridge Mathematical Library. Cambridge University Press, 2000.

[30] C.E. Baumann and J.T. Oden. A discontinuous hp finite element method for convection-diffusion problems. *Computer Methods in Applied Mechanics and Engineering*, 175:311–341, 1999.

[31] C.E. Baumann and J.T. Oden. A discontinuous hp finite element method for the Euler and Navier-Stokes equations. *International Journal for Numerical Methods in Fluids*, 31:79–95, 1999.

[32] T. W. Baumgarte and S. L. Shapiro. General Relativistic Magnetohydrodynamics for the Numerical Construction of Dynamical Spacetimes. *Astrophys. Journal*, 585:921–929, 2003.

[33] Kris Beckwith and James M. Stone. a Second-Order Godunov Method for Multi-Dimensional Relativistic Magnetohydrodynamics. *The Astrophysical Journal Supplement Series*, 193(1):6, 2011. ISSN 0067-0049.

[34] M. C. Begelman, R. D. Blandford, and M. J. Rees. Theory of extragalactic radio sources. *Reviews of Modern Physics*, 56:255–351, 1984.

[35] M. Ben-Artzi and J. Falcovitz. A second-order godunov-type scheme for compressible fluid dynamics. *Journal of Computational Physics*, 55:1–32, 1984.

[36] M. J. Berger and P. Colella. Local adaptive mesh refinement for shock hydrodynamics. *Journal of Computational Physics*, 82:64–84, 1989.

[37] M. J. Berger and J. Oliger. Adaptive Mesh Refinement for Hyperbolic Partial Differential Equations. *Journal of Computational Physics*, 53:484, 1984.

[38] D. Biskamp. Magnetic reconnection via current sheets. *Physics of Fluids*, 29: 1520–1531, 1986.

[39] D. Biskamp. *Magnetohydrodynamic Turbulence*. Cambridge University press, 2008.

[40] J. P. Boris. Relativistic plasma simulation-optimization of a hybrid code. *Proceeding of Fourth Conference on Numerical Simulations of Plasmas*, November 1970.

[41] W. Boscheri, M. Dumbser, and M. Righetti. A semi-implicit scheme for 3d free surface flows with high order velocity reconstruction on unstructured Voronoi meshes. *International Journal for Numerical Methods in Fluids*, 72:607–631, 2013.

[42] A. Bourgeade, P. LeFloch, and P.A. Raviart. An asymptotic expansion for the solution of the generalized riemann problem. Part II: application to the gas dynamics equations. *Annales de l'institut Henri Poincaré (C) Analyse non linéaire*, 6:437–480, 1989.

[43] M. E. Brachet, D. I. Meiron, S. A. Orszag, B. G. Nickel, R. H. Morf, and U. Frisch. Small-scale structure of the Taylor-Green vortex. *Journal of Fluid Mechanics*, 130:411–452, 1983. ISSN 1469-7645.

[44] J. Brackbill. Fluid modeling of magnetized plasmas. *Space Science Reviews*, 42(1):153–167, 1985.

[45] J. U. Brackbill and D. C. Barnes. The effect of nonzero $\nabla \cdot B = 0$ on the numerical solution of the magnetohydrodynamic equations. *Journal of Computational Physics*, 35(3):426–430, 1980.

[46] D. L. Brown and M. L. Minion. Performance of under-resolved two-dimensional incompressible flow simulations. *Journal of Computational Physics*, 122(1):165–183, 1995. ISSN 0021-9991.

[47] L. Brugnano and V. Casulli. Iterative solution of piecewise linear systems. *SIAM Journal on Scientific Computing*, 30:463–472, 2008.

[48] L. Brugnano and V. Casulli. Iterative solution of piecewise linear systems and applications to flows in porous media. *SIAM Journal on Scientific Computing*, 31:1858–1873, 2009.

[49] N. Bucciantini and L. Del Zanna. A fully covariant mean-field dynamo closure for numerical 3 + 1 resistive GRMHD. *Mon. Not. R. Astron. Soc.*, 428: 71–85, 2013.

[50] A. Burbeau, P. Sagaut, and C.H. Bruneau. A problem-independent limiter for high-order Runge-Kutta discontinuous Galerkin methods. *J. Comput. Phys.*, 169(1):111–150, 2001.

[51] E. Casoni, J. Peraire, and A. Huerta. One-dimensional shock-capturing for high-order discontinuous Galerkin methods. *International Journal for Numerical Methods in Fluids*, 71(6):737–755, 2013.

[52] C. C. Castro and E. F. Toro. Solvers for the high-order riemann problem for hyperbolic balance laws. *Journal of Computational Physics*, 227:2481–2513, 2008.

[53] V. Casulli. Semi-implicit finite difference methods for the two-dimensional shallow water equations. *J. Comp. Phys.*, 86:56–74, 1990.

[54] V. Casulli. A semi-implicit finite difference method for non-hydrostatic, free-surface flows. *Int. J. Numeric. Meth. Fluids*, 30:425–440, 1999.

[55] V. Casulli. A high-resolution wetting and drying algorithm for free-surface hydrodynamics. *International Journal for Numerical Methods in Fluids*, 60:391–408, 2009.

[56] V. Casulli. A semi–implicit numerical method for the free–surface Navier–Stokes equations. *International Journal for Numerical Methods in Fluids*, 74: 605–622, 2014.

[57] V. Casulli and E. Cattani. Stability, accuracy and efficiency of a semi implicit method for three-dimensional shallow water flow. *Comp. Math. Appl.*, 27: 99–112, 1994.

[58] V. Casulli and R. T. Cheng. Semi-implicit finite difference methods for three-dimensional shallow water flow. *Int. J. Numeric. Meth. Fluids*, 15:629–648, 1992.

[59] V. Casulli and D. Greenspan. Pressure method for the numerical solution of transient, compressible fluid flows. *International Journal for Numerical Methods in Fluids*, 4(11):1001–1012, 1984.

[60] V. Casulli and G. S. Stelling. Semi-implicit subgrid modelling of three-dimensional free-surface flows. *International Journal for Numerical Methods in Fluids*, 67:441–449, 2011.

[61] V. Casulli and R. A. Walters. An unstructured grid, three-dimensional model based on the shallow water equations. *Int. J. Numeric. Meth. Fluids*, 32:331–348, 2000.

[62] V. Casulli and P. Zanolli. Semi-implicit numerical modeling of nonhydrostatic free-surface flows for environmental problems. *Math. Comp. Model.*, 36:1131–1149, 2002.

[63] V. Casulli and P. Zanolli. Iterative solutions of mildly nonlinear systems. *J. Comp. Appl. Math.*, 236:3937–3947, 2012.

[64] V. Casulli, M. Dumbser, and E.F. Toro. Semi-implicit numerical modeling of axially symmetric flows in compliant arterial systems. *Int. J. Numeric. Meth. Biomed. Engng.*, 28:257–272, 2012.

[65] J. Cesenek, M. Feistauer, J. Horacek, V. Kucera, and J. Prokopova. Simulation of compressible viscous flow in time–dependent domains. *Applied Mathematics and Computation*, 219:7139–7150, 2013.

[66] F.F. Chen. *Introduction to Plasma Physics and Controlled Fusion*. Number v. 1 in Introduction to Plasma Physics and Controlled Fusion. Springer, 1984.

[67] M. Cheng, J. Lou, and T. T. Lim. Leapfrogging of multiple coaxial viscous vortex rings. *Physics of Fluids*, 27(3):031702, 2015.

[68] S.W. Cheung, E. Chung, H.H. Kim, and Y. Qian. Staggered discontinuous Galerkin methods for the incompressible Navier-Stokes equations. *Journal of Computational Physics*, 302:251–266, 2015.

[69] S. Childress. New solutions of the kinematic dynamo problem. *Journal of Mathematical Physics*, 11:3063–3076, 1970.

[70] E.T. Chung and C.S. Lee. A staggered discontinuous Galerkin method for the convection–diffusion equation. *Journal of Numerical Mathematics*, 20(1): 1–32, 2012.

[71] S. Clain, S. Diot, and R. Loubère. A high-order finite volume method for systems of conservation laws-multi-dimensional optimal order detection (MOOD). *Journal of Computational Physics*, 230(10):4028 – 4050, 2011. ISSN 0021-9991.

[72] B. Cockburn and C. W. Shu. TVB Runge-Kutta local projection discontinuous Galerkin finite element method for conservation laws II: general framework. *Mathematics of Computation*, 52:411–435, 1989.

[73] B. Cockburn and C. W. Shu. The Runge-Kutta local projection P1-Discontinuous Galerkin finite element method for scalar conservation laws. *Mathematical Modelling and Numerical Analysis*, 25:337–361, 1991.

[74] B. Cockburn and C. W. Shu. The Runge-Kutta discontinuous Galerkin method for conservation laws V: multidimensional systems. *Journal of Computational Physics*, 141:199–224, 1998.

[75] B. Cockburn and C.W. Shu. The local discontinuous Galerkin method for time-dependent convection-diffusion systems. *SIAM Journal on Numerical Analysis*, 35(6):2440–2463, 1998.

[76] B. Cockburn, S. Y. Lin, and C.W. Shu. TVB Runge-Kutta local projection discontinuous Galerkin finite element method for conservation laws III: one dimensional systems. *Journal of Computational Physics*, 84:90–113, 1989.

[77] B. Cockburn, S. Hou, and C. W. Shu. The Runge-Kutta local projection discontinuous Galerkin finite element method for conservation laws IV: the multidimensional case. *Mathematics of Computation*, 54:545–581, 1990.

[78] T. Colonius, S.K. Lele, and P. Moin. Sound generation in a mixing layer. *Journal of Fluid Mechanics*, 330:375–409, 1997.

[79] R. Courant and D. Hilbert. *Methods of mathematical physics, Volume 2: Partial differential equations.* Wiley classics library. Wiley - Interscience Publishers, 1989.

[80] A. Crivellini, V. D'Alessandro, and F. Bassi. High-order discontinuous Galerkin solutions of three-dimensional incompressible RANS equations. *Computers & Fluids*, 81:122–133, 2013.

[81] R. B. Dahlburg and J. M. Picone. Evolution of the orszag-tang vortex system in a compressible medium. I. initial average subsonic flow. *Phys. Fluids B*, 1: 2153–2171, 1989.

[82] A. Dedner, F. Kemm, D. Kröner, C.-D. Munz, T. Schnitzer, and M. Wesenberg. Hyperbolic divergence cleaning for the MHD equations. *Journal of Computational Physics*, 175:645–673, 2002.

[83] L. Del Zanna, N. Bucciantini, and P. Londrillo. An efficient shock-capturing central-type scheme for multidimensional relativistic flows. II. Magnetohydrodynamics. *Astron. Astrophys.*, 400:397–413, 2003.

[84] L. Del Zanna, O. Zanotti, N. Bucciantini, and P. Londrillo. ECHO: a Eulerian conservative high-order scheme for general relativistic magnetohydrodynamics and magnetodynamics. *Astron. Astrophys.*, 473:11–30, 2007.

[85] K. Dionysopoulou, D. Alic, C. Palenzuela, L. Rezzolla, and B. Giacomazzo. General-Relativistic Resistive Magnetohydrodynamics in three dimensions: formulation and tests. *Phys. Rev. D*, 88:044020, 2013.

[86] S. Diot, S. Clain, and R. Loubère. Improved detection criteria for the multi-dimensional optimal order detection (MOOD) on unstructured meshes with very high-order polynomials. *Computers & Fluids*, 64:43 – 63, 2012. ISSN 0045-7930.

[87] S. Diot, R. Loubère, and S. Clain. The MOOD method in the three-dimensional case: Very-high-order finite volume method for hyperbolic systems. *International Journal of Numerical Methods in Fluids*, 73:362–392, 2013.

[88] D.Kuzmin. Hierarchical slope limiting in explicit and implicit discontinuous Galerkin methods. *Journal of Computational Physics*, 257, Part B(0):1140 – 1162, 2014. ISSN 0021-9991. Physics-compatible numerical methods.

[89] V. Dolejsi. Semi-implicit interior penalty discontinuous Galerkin method for viscous compressible flows. *Communications in Computational Physics*, 4(2): 231–274, 2008.

[90] V. Dolejsi and M. Feistauer. A semi-implicit discontinuous Galerkin finite element method for the numerical solution of inviscid compressible flow. *Journal of Computational Physics*, 198(2):727 – 746, 2004.

[91] V. Dolejsi, M. Feistauer, and C. Schwab. On some aspects of the discontinuous Galerkin finite element method for conservation laws. *Mathematics and Computers in Simulation*, 61(3-6):333–346, 2003.

[92] V. Dolejsi, M. Feistauer, and J. Hozman. Analysis of semi-implicit DGFEM for nonlinear convection-diffusion problems on nonconforming meshes. *Computer Methods in Applied Mechanics and Engineering*, 196(29-30):2813 – 2827, 2007.

[93] R. Donat, M. C. Martí, A. Martínez-Gavara, and Mulet. P. Well-balanced adaptive mesh refinement for shallow water flows. *Journal of Computational Physics*, 257, Part A(0):937 – 953, 2014. ISSN 0021-9991.

[94] Matthew D. Duez, Yuk Tung Liu, Stuart L. Shapiro, and Branson C. Stephens. Relativistic magnetohydrodynamics in dynamical spacetimes: Numerical methods and tests. *Phys. Rev. D*, 72:024028, 2005. astro-ph/0503420.

[95] M. Dumbser. Arbitrary high order PNPM schemes on unstructured meshes for the compressible Navier–Stokes equations. *Computers & Fluids*, 39:60–76, 2010.

[96] M. Dumbser and D.S. Balsara. High-order unstructured one-step pnpm schemes for the viscous and resistive mhd equations. *CMES*, 52(2):301–332, 2009.

[97] M. Dumbser and V. Casulli. A staggered semi-implicit spectral discontinuous Galerkin scheme for the shallow water equations. *Applied Mathematics and Computation*, 219(15):8057 – 8077, 2013.

[98] M. Dumbser and V. Casulli. A conservative, weakly nonlinear semi-implicit finite volume scheme for the compressible Navier–Stokes equations with general equation of state. *Applied Mathematics and Computation*, 272, Part 2: 479 – 497, 2016.

[99] M. Dumbser and C.D. Munz. Building blocks for arbitrary high order discontinuous Galerkin schemes. *Journal of Scientific Computing*, 27:215–230, 2006.

[100] M. Dumbser and E.F. Toro. On universal Osher–type schemes for general nonlinear hyperbolic conservation laws. *Communications in Computational Physics*, 10:635–671, 2011.

[101] M. Dumbser and O. Zanotti. Very high order PNPM schemes on unstructured meshes for the resistive relativistic MHD equations. *Journal of Computational Physics*, 228:6991–7006, 2009.

[102] M. Dumbser, F. Fambri, I. Furci, M. Mazza, M. Tavelli, and S. Serra-Capizzano. Staggered discontinuous Galerkin methods for the incompressible Navier-Stokes equations: spectral analysis and computational results. *submitted to*. ISSN arXiv:1612.04529.

[103] M. Dumbser, M. Kaeser, V. A. Titarev, and E. F. Toro. Quadrature-free non-oscillatory finite volume schemes on unstructured meshes for nonlinear hyperbolic systems. *Journal of Computational Physics*, 226:204–243, 2007.

[104] M. Dumbser, M. Käser, and E. F. Toro. An arbitrary high order discontinuous Galerkin method for elastic waves on unstructured meshes V: Local time stepping and p-adaptivity. *Geophysical Journal International*, 171:695–717, 2007.

[105] M. Dumbser, D. S. Balsara, E. F. Toro, and C.-D. Munz. A unified framework for the construction of one-step finite volume and discontinuous Galerkin schemes on unstructured meshes. *Journal of Computational Physics*, 227:8209–8253, 2008.

[106] M. Dumbser, C. Enaux, and E.F. Toro. Finite volume schemes of very high order of accuracy for stiff hyperbolic balance laws. *Journal of Computational Physics*, 227:3971–4001, 2008.

[107] M. Dumbser, O. Zanotti, A. Hidalgo, and D.S. Balsara. ADER-WENO Finite Volume Schemes with Space-Time Adaptive Mesh Refinement. *Journal of Computational Physics*, 248:257–286, 2013.

[108] M. Dumbser, A. Hidalgo, and O. Zanotti. High Order Space-Time Adaptive ADER-WENO Finite Volume Schemes for Non-Conservative Hyperbolic Systems. *Computer Methods in Applied Mechanics and Engineering*, 268: 359–387, 2014.

[109] M. Dumbser, O. Zanotti, R. Loubère, and S. Diot. A posteriori subcell limiting of the discontinuous Galerkin finite element method for hyperbolic conservation laws. *Journal of Computational Physics*, 278:47–75, 2014.

[110] M. Dumbser, U. Iben, and M. Ioriatti. An efficient semi-implicit finite volume method for axially symmetric compressible flows in compliant tubes. *Applied Numerical Mathematics*, 89:24 – 44, 2015. ISSN 0168-9274.

[111] M. Dumbser, I. Peshkov, and E. Romenski. High order ADER schemes for a unified first order hyperbolic formulation of continuum mechanics: Viscous heat-conducting fluids and elastic solids. *Journal of Computational Physics*, 314:824–862, 2016.

[112] E. Erturk. Numerical solutions of 2-d steady incompressible flow over a backward-facing step, part i: High reynolds number solutions. *Computers & Fluids*, 37(6):633 – 655, 2008.

[113] Zachariah B. Etienne, Yuk Tung Liu, and Stuart L. Shapiro. Relativistic magnetohydrodynamics in dynamical spacetimes: A new AMR implementation. *Phys. Rev. D*, 82:084031, 2010.

[114] F. Fambri and M. Dumbser. Semi-implicit discontinuous Galerkin methods for the incompressible Navier-Stokes equations on adaptive staggered Cartesian grids. *to be submitted*.

[115] F. Fambri and M. Dumbser. Spectral semi-implicit and space-time discontinuous Galerkin methods for the incompressible Navier-Stokes equations on staggered Cartesian grids. *Applied Numerical Mathematics*, 110:41–74, 2016.

[116] F. Fambri, M. Dumbser, and O. Zanotti. Space-time adaptive ADER-DG schemes for dissipative flows: compressible Navier-Stokes and resistive MHD equations. *submitted to*.

[117] F. Fambri, M. Dumbser, and V. Casulli. An efficient semi-implicit method for three-dimensional non-hydrostatic flows in compliant arterial vessels. *International Journal for Numerical Methods in Biomedical Engineering*, 30(11):1170–1198, 2014. ISSN 2040-7947.

[118] A. Fasano and S. Marmi. *Meccanica analitica*. Programma di mat. fisica elettronica. Bollati Boringhieri, 2nd edition, 2002.

[119] S. Fechter and C.-D. Munz. A discontinuous Galerkin-based sharp-interface method to simulate three-dimensional compressible two-phase flow. *International Journal for Numerical Methods in Fluids*, pages n/a–n/a, 2015. ISSN 1097-0363.

[120] M. Feistauer, V. Dolejsi, and V. Kucera. On the discontinuous Galerkin method for the simulation of compressible flow with wide range of mach numbers. *Computing and Visualization in Science*, 10(1):17–27, 2007.

[121] M. Feistauer, V. Kucera, and J. Prokopová. Discontinuous Galerkin solution of compressible flow in time–dependent domains. *Mathematics and Computers in Simulation*, 80(8):1612–1623, 2010.

[122] P. Le Floch and P.A. Raviart. An asymptotic expansion for the solution of the generalized riemann problem. Part I: General theory. *Annales de l'institut Henri Poincaré (C) Analyse non linéaire*, 5:179–207, 1988.

[123] D. Garrison and P. Nguyen. Characterization of Relativistic MHD Turbulence. *ArXiv e-prints*, 2015.

[124] G. Gassner, F. Lörcher, and C.D. Munz. A contribution to the construction of diffusion fluxes for finite volume and discontinuous Galerkin schemes. *Journal of Computational Physics*, 224:1049–1063, 2007.

[125] G. Gassner, F. Lörcher, and C. D. Munz. A discontinuous Galerkin scheme based on a space-time expansion II. viscous flow equations in multi dimensions. *Journal of Scientific Computing*, 34:260–286, 2008.

[126] Emmanuil H. Georgoulis, Edward Hall, and Paul Houston. Discontinuous galerkin methods on hp-anisotropic meshes ii: a posteriori error analysis and adaptivity. *Applied Numerical Mathematics*, 59(9):2179 – 2194, 2009.

[127] U. Ghia, K.N. Ghia, and C.T. Shin. High-Re solutions for incompressible flow using the Navier-Stokes equations and a multigrid method. *Journal of Computational Physics*, 48(3):387 – 411, 1982. ISSN 0021-9991.

[128] D. Ghosh and J. D. Baeder. High-order accurate incompressible Navier-Stokes algorithm for vortex-ring interactions with solid wall. *AIAA Journal*, 50(2):2408–2433, 2012.

[129] Bruno Giacomazzo and Luciano Rezzolla. The Exact Solution of the Riemann Problem in Relativistic MHD. *Journal of Fluid Mechanics*, 562:223–259, 2006.

[130] Bruno Giacomazzo and Luciano Rezzolla. WhiskyMHD: a new numerical code for general relativistic magnetohydrodynamics. *Classical Quantum Gravity*, 24:S235, 2007.

[131] F. X. Giraldo and M. Restelli. High-order semi-implicit time-integrators for a triangular discontinuous Galerkin oceanic shallow water model. *International Journal for Numerical Methods in Fluids*, 63(9):1077–1102, 2010. ISSN 1097-0363.

[132] S. K. Godunov and V. S. Ryabenkii. *Difference schemes: an introduction to the underlying theory*. Elsevier, 1987.

[133] S.K. Godunov. Finite difference methods for the computation of discontinuous solutions of the equations of fluid dynamics. *Mathematics of the USSR - Sbornik*, 47:271–306, 1959.

[134] S.K. Godunov. An interesting class of quasilinear systems. *Dokl. Akad. Nauk SSSR*, 139(3):521–523, 1961.

[135] S.K. Godunov. Symmetric form of the magnetohydrodynamic equation. *Numerical Methods for Mechanics of Continuum Medium*, 3(1):26–34, 1972.

[136] S.K. Godunov and E.I. Romenski. *Elements of continuum mechanics and conservation laws*. Kluwer Academic/Plenum Publishers, 2003.

[137] J. P. Goedbloed and S. Poedts. Principles of magnetohydrodynamics: with applications to laboratory and astrophysical plasmas, 2004.

[138] C. R. Goetz and A. Iske. Approximate solutions of generalized Riemann problems for nonlinear systems of hyperbolic conservation laws. *Math. Comp.*, 85:35–62, 2016.

[139] S. Gottlieb and C.W. Shu. Total variation diminishing Runge-Kutta schemes. *Mathematics of Computation*, 67:73–85, 1998.

[140] U. Grenander and G. Szegö. *Toeplitz Forms and Their Applications*, volume 321. Second Edition, Chelsea, New York, 1984.

[141] S. Hahn and G. Iaccarino. Towards adaptive vorticity confinement. *47th AIAA Aerospace Sciences Meeting*, Orlando(FL):AIAA Paper 2009–1613, Jan. 2009.

[142] A. Harten, B. Engquist, S. Osher, and S. Chakravarthy. Uniformly high order essentially non-oscillatory schemes, III. *Journal of Computational Physics*, 71: 231–303, 1987.

[143] R. Hartmann and P. Houston. Symmetric interior penalty DG methods for the compressible Navier–Stokes equations I: Method formulation. *Int. J. Num. Anal. Model.*, 3:1–20, 2006.

[144] R. Hartmann and P. Houston. An optimal order interior penalty discontinuous Galerkin discretization of the compressible Navier–Stokes equations. *Journal of Computational Physics*, 227:9670–9685, 2008.

[145] A. Hidalgo and M. Dumbser. ADER schemes for nonlinear systems of stiff advection-diffusion-reaction equations. *Journal of Scientific Computing*, 48: 173–189, 2011.

[146] H.Luo, J.D.Baum, and R.Löhner. A hermite weno-based limiter for discontinuous Galerkin method on unstructured grids. *J. Comput. Phys.*, 225(1): 686–713, 2007. ISSN 0021-9991.

[147] V. Honkkila and P. Janhunen. HLLC solver for ideal relativistic MHD. *Journal of Computational Physics*, 223:643–656, 2007.

[148] P. Houston and E. SÃŒli. hp-adaptive discontinuous Galerkin finite element methods for first-order hyperbolic problems. *SIAM Journal on Scientific Computing*, 23(4):1226–1252, 2002.

[149] P. Houston, C. Schwab, and E. SÃŒli. Stabilized hp-finite element methods for first-order hyperbolic problems. *SIAM Journal on Numerical Analysis*, 37 (5):1618–1643, 2000.

[150] P. Houston, C. Schwab, and E. SÃºli. Discontinuous hp-finite element methods for advection-diffusion-reaction problems *. *SIAM Journal on Numerical Analysis*, 39(6):2133–2163, 2002.

[151] A. Huerta, E. Casoni, and J. Peraire. A simple shock-capturing technique for high-order discontinuous Galerkin methods. *International Journal for Numerical Methods in Fluids*, 69(10):1614–1632, 2012.

[152] Lucian Ivan and Clinton P.T. Groth. High-order central eno finite-volume scheme with adaptive mesh refinement for the advection-diffusion equation. *Computational Fluid Dynamics 2008*, pages 443 – 449, 2009.

[153] Lucian Ivan and Clinton P.T. Groth. High-order solution-adaptive central essentially non-oscillatory (ceno) method for viscous flows. *Journal of Computational Physics*, 257, Part A(0):830 – 862, 2014. ISSN 0021-9991.

[154] J. D. Jackson. *Classical Electrodynamics*. Wiley, New York, 3rd edition, 1999. ISBN 0-471-30932-X.

[155] B. M. Javorskij and A. A. Detlaf. *Manuale di fisica*. Edizioni MIR, Mosca, 2nd edition, 1977. (Spravo čnik po fizike).

[156] G. Jiang and C.W. Shu. On a cell entropy inequality for discontinuous Galerkin methods. *Mathematics of Computation*, 62:531–538, 1994.

[157] G.-S. Jiang and C.W. Shu. Efficient implementation of weighted ENO schemes. *Journal of Computational Physics*, 126:202–228, 1996.

[158] G.S. Jiang and C.C. Wu. A high-order WENO finite difference scheme for the equations of ideal magnetohydrodynamics. *Journal of Computational Physics*, 150:561–594, 1999.

[159] J.Qiu and C-W.Shu. Hermite weno schemes and their application as limiters for Runge-Kutta discontinuous Galerkin method: One-dimensional case. *J. Comput. Phys.*, 193(1):115–135, 2004. ISSN 0021-9991.

[160] J.Zhu, J. Qiu, C.-W.Shu, and M.Dumbser. Runge-Kutta discontinuous Galerkin method using weno limiters ii: Unstructured meshes. *J. Comput. Phys.*, 227(9):4330–4353, 2008. ISSN 0021-9991.

[161] C.W. Shu J.Zhu, X.Zhong and J. Qiu. Runge-Kutta discontinuous Galerkin method using a new type of weno limiters on unstructured meshes. *J. Comp. Phys.*, 248:200–220, 2013.

[162] G. E. Karniadakis, M. Israeli, and S. A. Orszag. High-order splitting methods for the incompressible Navier-Stokes equations. *Journal of Computational Physics*, 97(2):414 – 443, 1991. ISSN 0021-9991.

[163] R. Keppens, Z. Meliani, A. J. van Marle, P. Delmont, A. Vlasis, and B. van der Holst. Parallel, grid-adaptive approaches for relativistic hydro and magnetohydrodynamics. *Journal of Computational Physics*, 231:718–744, 2012.

[164] A.M Khokhlov. Fully threaded tree algorithms for adaptive refinement fluid dynamics simulations. *Journal of Computational Physics*, 143(2):519 – 543, 1998.

[165] S. Kida and Takaoka. Vortex reconnection. *Annu. Rev. Fluid Mech.*, 26:169–189, 1994.

[166] S. Kida, M. Takaoka, and F. Hussain. Collision of two vortex rings. *Journal of Fluid Mechanics*, 230:583–646, 1991.

[167] J. Kim and D. S. Balsara. A stable HLLC Riemann solver for relativistic magnetohydrodynamics. *Journal of Computational Physics*, 270:634–639, 2014.

[168] J. Kim and P. Moin. Application of a fractional-step method to incompressible Navier–Stokes equations. *Journal of Computational Physics*, 59(2):308 – 323, 1985. ISSN 0021-9991.

[169] C. Klaij, J.J.W. Van der Vegt, and H. Van der Ven. Space-time discontinuous Galerkin method for the compressible navier-stokes equations. *Journal of Computational Physics*, 217:589–611, 2006.

[170] S. Klainermann and A. Majda. Singular limits of quasilinear hyperbolic systems with large parameters and the incompressible limit of compressible fluid. *Comm. Pure Appl. Math.*, XXXIV:481–524, 1981.

[171] B. Klein, F. Kummer, and M. Oberlack. A SIMPLE based discontinuous Galerkin solver for steady incompressible flows. *Journal of Computational Physics*, 237:235–250, 2013.

[172] S. S. Komissarov. On the properties of Alfvén waves in relativistic magnetohydrodynamics. *Physics Letters A*, 232:435–442, 1997.

[173] S. S. Komissarov. A Godunov-type scheme for relativistic magnetohydrodynamics. *Mon. Not. R. Astron. Soc.*, 303:343–366, 1999.

[174] S. S. Komissarov. Multidimensional numerical scheme for resistive relativistic magnetohydrodynamics. *Mon. Not. R. Astron. Soc.*, 382:995–1004, 2007.

[175] M. A. Kopera and F. X. Giraldo. Analysis of adaptive mesh refinement for {IMEX} discontinuous Galerkin solutions of the compressible Euler equations with application to atmospheric simulations. *Journal of Computational Physics*, 275:92–117, 2014.

[176] C. Kouveliotou, C. A. Meegan, G. J. Fishman, N. P. Bhat, M. S. Briggs, T. M. Koshut, W. S. Paciesas, and G. N. Pendleton. Identification of two classes of gamma-ray bursts. *Astrophys. J.*, 413:L101–L104, 1993.

[177] H. C. Ku, R. S. Hirsh, and T. D. Taylor. A pseudospectral method for solution of the three-dimensional incompressible Navier-Stokes equations. *Journal of Computational Physics*, 70(2):439 – 462, 1987. ISSN 0021-9991.

[178] A. Kurganov and E. Tadmor. Solution of two-dimensional Riemann problems for gas dynamics without Riemann problem solvers. *Numer. Methods Partial Differential Equations*, 18:584–608, 2002.

[179] U. H. Kurzweg. Enhanced heat conduction in oscillating viscous flows within parallel-plate channels. *Journal of Fluid Mechanics*, 156:291–300, 1985. ISSN 1469-7645.

[180] L. D. Landau, L. P. Pitaevskii, and E.M. Lifshitz. *Electrodynamics of Continuous Media, Course of Theoretical Physics, Volume 8*. Pergamon, Amsterdam, 2nd edition, 1984.

[181] L. D. Landau, E. M. Lifshitz, J. B. Sykes, and Bell. *Fluid Mechanics, Course of Theoretical Physics, Volume 6*. Elsevier Butterworth-Heinemann, Oxford, 2004.

[182] S. Landi, L. Del Zanna, E. Papini, F. Pucci, and M. Velli. Resistive magnetohydrodynamics simulations of the ideal tearing mode. *Astrophysical Journal*, 806:131, 2015.

[183] A.T. Layton. On the choice of correctors for semi-implicit Picard deferred correction methods. *Applied Numerical Mathematics*, 58(6):845–858, 2008.

[184] T. Lee and D. Mateescu. Experimental and numerical investigation of 2-d backward-facing step flow. *Journal of Fluids and Structures*, 12(6):703 – 716, 1998. ISSN 0889-9746.

[185] T. Leicht and R. Hartmann. Anisotropic mesh refinement for discontinuous galerkin methods in two-dimensional aerodynamic flow simulations. *International Journal for Numerical Methods in Fluids*, 56(11):2111–2138, 2008.

[186] T. Leismann, L. Antón, M. A. Aloy, E. Müller, J. M. Martí, J. A. Miralles, and J. M. Ibáñez. Relativistic MHD simulations of extragalactic jets. *Astronomy and Astrophyiscs*, 436:503–526, 2005.

[187] R. J. Leveque. *Numerical Methods for Conservation Laws*. Birkhauser Verlag, Basel, 1992.

[188] D. Levy, G. Puppo, and G. Russo. Central weno schemes for hyperbolic systems of conservation laws. *ESAIM: Mathematical Modelling and Numerical Analysis*, 33(3):547–571, 1999.

[189] C. Liu, C.W. Shu, E. Tadmor, and M. Zhang. L2 stability analysis of the central discontinuous Galerkin method and a comparison between the central and regular discontinuous Galerkin methods. *ESAIM: Mathematical Modelling and Numerical Analysis*, 42(04):593–607, 2008.

[190] Y. Liu, C.W. Shu, E. Tadmor, and M. Zhang. Central discontinuous Galerkin methods on overlapping cells with a nonoscillatory hierarchical reconstruction. *SIAM Journal on Numerical Analysis*, 45(6):2442–2467, 2007.

[191] L.Krivodonova. Limiters for high-order discontinuous Galerkin methods. *Journal of Computational Physics*, 226:879–896, 2007.

[192] P. Londrillo and L. Del Zanna. High-Order Upwind Schemes for Multidimensional Magnetohydrodynamics. *Astrophysical Journal*, 530:508–524, 2000.

[193] F. Lörcher, G. Gassner, and C. D. Munz. A discontinuous Galerkin scheme based on a space-time expansion. I. inviscid compressible flow in one space dimension. *Journal of Scientific Computing*, 32:175–199, 2007.

[194] R. Loubère, M. Dumbser, and S. Diot. A new family of high order unstructured mood and ader finite volume schemes for multidimensional systems of hyperbolic conservation laws. *Communication in Computational Physics*, 16: 718–763, 2014.

[195] C. Loudon and A. Tordesillas. The use of the dimensionless womersley number to characterize the unsteady nature of internal flow. *Journal of Theoretical Biology*, 191(1):63 – 78, 1998. ISSN 0022-5193.

[196] N. F. Loureiro, A. A. Schekochihin, and S. C. Cowley. Instability of current sheets and formation of plasmoid chains. *Physics of Plasmas*, 14(10):100703, 2007.

[197] H. Lu and Q. Sun. A straightforward hp-adaptivity strategy for shock-capturing with high-order discontinuous galerkin methods. *Advances in Applied Mathematics and Mechanics*, 6(1):135–144, 2014.

[198] H. Luo, J.D. Baum, and R. Löhner. A discontinuous Galerkin method based on a Taylor basis for the compressible flows on arbitrary grids. *Journal of Computational Physics*, 227:8875–8893, 2008.

[199] Philip S. Marcus. Simulation of taylor-couette flow. part 1. numerical methods and comparison with experiment. *Journal of Fluid Mechanics*, 146:45–64, 1984. ISSN 1469-7645.

[200] M. Marder. A method for incorporating Gauss' law into electromagnetic PIC codes. *Journal of Computational Physics*, 68(1):48–55, 1987. ISSN 0021-9991.

[201] J. M. Martí and E. Müller. Numerical hydrodynamics in special relativity. *Living Rev. Relativ.*, 6:7, 2003.

[202] A. Meister and S. Ortleb. A positivity preserving and well-balanced DG scheme using finite volume subcells in almost dry regions. *Applied Mathematics and Computation*, 272:259–273, 2016. in press.

[203] F.C. Michel. *Theory of Neutron Star Magnetospheres*. Theoretical Astrophysics. University of Chicago Press, 1991.

[204] A. Mignone and G. Bodo. An HLLC Riemann solver for relativistic flows - II. Magnetohydrodynamics. *Mon. Not. R. Astron. Soc.*, 368:1040–1054, 2006.

[205] A. Mignone and J. C. McKinney. Equation of state in relativistic magnetohydrodynamics: variable versus constant adiabatic index. *Mon. Not. R. Astron. Soc.*, 378:1118–1130, 2007.

[206] A. Mignone, M. Ugliano, and G. Bodo. A five-wave Harten-Lax-van Leer Riemann solver for relativistic magnetohydrodynamics. *Monthly Notices of the Royal Astronomical Society*, 393(4):1141–1156, 2009. ISSN 00358711.

[207] A. Mignone, C. Zanni, P. Tzeferacos, B. van Straalen, P. Colella, and G. Bodo. The PLUTO Code for Adaptive Mesh Computations in Astrophysical Fluid Dynamics. *Astrophys. J. Suppl. Ser.*, 198:7, 2012.

[208] M. L. Minion. Semi-implicit spectral deferred correction methods for ordinary differential equations. *Commun. Math. Sci.*, 1(3):471–500, 2003.

[209] M. L. Minion. Higher-order semi-implicit projection methods. *in M. Hafez, editor*, Numerical Simulations of Incompressible Flows: Proceedings of a Conference Held at Half Moon Bay, CA (June 18-20, 2001), January 2003.

[210] M. L. Minion and Brown D. L. Performance of under-resolved two-dimensional incompressible flow simulations, II. *Journal of Computational Physics*, 138(2):734–765, 1997. ISSN 0021-9991.

[211] G. Montecinos, C.E. Castro, M. Dumbser, and E.F. Toro. Comparison of solvers for the generalized riemann problem for hyperbolic systems with source terms. *Journal of Computational Physics*, 231(19):6472–6494, 2012.

[212] R. H. Morf, S. A. Orszag, and U. Frisch. Spontaneous singularity in three-dimensional inviscid, incompressible flow. *Phys. Rev. Lett.*, 44:572–575, 1980.

[213] A.A. Mouza, M.N. Pantzali, S.V. Paras, and J. Tihon. Experimental and numerical study of backward-facing step flow. *5th National Chemical Engineering Conference, Thessaloniki, Greece*, 2005.

[214] C.-D. Munz, R. Schneider, E. Sonnendrücker, and U. Voß. Maxwell's equations when the charge conservation is not satisfied. *Comptes Rendus de l'Académie des Sciences - Series I - Mathematics*, 328(5):431–436, 1999. ISSN 0764-4442.

[215] C.-D. Munz, P. Omnes, R. Schneider, E. Sonnendrücker, and U. Voß. Divergence correction techniques for maxwell solvers based on a hyperbolic model. *Journal of Computational Physics*, 161(2):484–511, 2000.

[216] D. Neilsen, E. W. Hirschmann, and R. S. Millward. Relativistic MHD and excision: formulation and initial tests. *Classical and Quantum Gravity*, 23:505, 2006.

[217] S. C. Noble, C. F. Gammie, J. C. McKinney, and L. Del Zanna. Primitive Variable Solvers for Conservative General Relativistic Magnetohydrodynamics. *Astrop. J.*, 641:626–637, 2006.

[218] S. A. Orszag and C. M. Tang. Small-scale structure of two-dimensional magnetohydrodynamic turbulence. *Journal of Fluid Mechanics*, 90:129, 1979.

[219] C. Palenzuela, L. Lehner, O. Reula, and L. Rezzolla. Beyond ideal MHD: towards a more realistic modelling of relativistic astrophysical plasmas. *Mon. Not. R. Astron. Soc.*, 394:1727–1740, 2009.

[220] L. Pareschi and G. Russo. Implicit-explicit runge-kutta schemes and applications to hyperbolic systems with relaxation. *Journal of Scientific Computing*, 25:129–155, 2005.

[221] P.-O. Persson and J. Peraire. Sub-cell shock capturing for discontinuous Galerkin methods. *AIAA Paper 2006-112*, 2006.

[222] I. Peshkov and E. Romenski. A hyperbolic model for viscous Newtonian flows. *Continuum Mechanics and Thermodynamics*, 28:85–104, 2016.

[223] J. M. Picone and R. B. Dahlburg. Evolution of the orszag-tang vortex system in a compressible medium. II. supersonic flow. *Phys. Fluids B*, 3:29–44, 1991.

[224] K. G. Powell. *An approximate Riemann solver for magnetohydrodynamics (That Works in More Than One Dimension)*. Institute for Computer Applications in Science and Engineering (ICASE), 1994.

[225] K. G. Powell, P. L. Roe, T. J. Linde, T. I. Gombosi, and D. L. De Zeeuw. A solution-adaptive upwind scheme for ideal magnetohydrodynamics. *Journal of Computational Physics*, 154(2):284–309, 1999.

[226] L. Prandtl. Über Flüssigkeitsbewegung bei sehr kleiner Reibung. *Verhandlg. III. Intern. Math. Kongr. Heidelberg*, pages 484–491, 1904.

[227] J. Qiu and C.W. Shu. Runge-Kutta discontinuous Galerkin method using WENO limiters. *SIAM Journal on Scientific Computing*, 26:907–929, 2005.

[228] J. Qiu and C.W. Shu. Hermite WENO schemes and their application as limiters for Runge-Kutta discontinuous Galerkin method II: two dimensional case. *Computers & Fluids*, 34:642–663, 2005.

[229] J. Qiu, M. Dumbser, and C.W. Shu. The discontinuous Galerkin method with Lax-Wendroff type time discretizations. *Computer Methods in Applied Mechanics and Engineering*, 194:4528–4543, 2005.

[230] D. Radice and L. Rezzolla. Discontinuous Galerkin methods for general-relativistic hydrodynamics: Formulation and application to spherically symmetric spacetimes. *Phys. Rev. D*, 84(2):024010, 2011.

[231] D. Radice and L. Rezzolla. THC: a new high-order finite-difference high-resolution shock-capturing code for special-relativistic hydrodynamics. *Astron. Astrophys.*, 547:A26, 2012.

[232] H. P. Rani, Tony W. H. Sheu, and Eric S. F. Tsai. Eddy structures in a transitional backward-facing step flow. *Journal of Fluid Mechanics*, 588:43–58, 2007. ISSN 1469-7645.

[233] A. Rault, G. Chiavassa, and R. Donat. Shock-vortex interactions at high mach numbers. *Journal of Scientific Computing*, 19:347–371, 2003.

[234] R.Biswas, K. D. Devine, and J. E. Flaherty. Parallel, adaptive finite element methods for conservation laws. *APPL. NUMER. MATH*, 14:255–283, 1994.

[235] W.H. Reed and T.R. Hill. Triangular mesh methods for neutron transport equation. Technical Report LA-UR-73-479, Los Alamos Scientific Laboratory, 1973.

[236] L. Rezzolla and O. Zanotti. *Relativistic Hydrodynamics*. Oxford University Press, Oxford UK, 2013.

[237] R.Hartmann and P.Houston. Adaptive discontinuous Galerkin finite element methods for the compressible Euler equations. *J. Comp. Phys.*, 183(2):508–532, 2002.

[238] S. Rhebergen, B. Cockburn, and Jaap J.W. van der Vegt. A space-time discontinuous Galerkin method for the incompressible Navier-Stokes equations. *Journal of Computational Physics*, 233:339–358, 2013.

[239] W. Ritz. Über eine neue methode zur lösung gewisser variationsprobleme der mathematischen physik. *Journal fur die Reine und Angewandte Mathematik*, 1909(135):1–61, 1909.

[240] E.I. Romenski. Hyperbolic systems of thermodynamically compatible conservation laws in continuum mechanics. *Mathematical and computer modelling*, 28(10):115–130, 1998.

[241] V. V. Rusanov. Calculation of Interaction of Non–Steady Shock Waves with Obstacles. *J. Comput. Math. Phys. USSR*, 1:267–279, 1961.

[242] Y. Saad and M. H. Schultz. GMRES: A generalized minimum residual algorithm for solving nonsymmetric linear systems. *SIAM J. Sci. Stat. Comput.*, 7(3):856–869, 1986.

[243] R. Samtaney, N. F. Loureiro, D. A. Uzdensky, A. A. Schekochihin, and S. C. Cowley. Formation of Plasmoid Chains in Magnetic Reconnection. *Phys. Rev. Lett.*, 103(10):105004, 2009.

[244] H. Schlichting and K. Gersten. *Grenzschichttheorie*. Springer Verlag, 2005.

[245] S. Serra-Capizzano. Asymptotic results on the spectra of block Toeplitz preconditioned matrices. *SIAM journal on matrix analysis and applications*, 20 (1):31–44, 1998.

[246] S Serra-Capizzano. Generalized locally Toeplitz sequences: spectral analysis and applications to discretized partial differential equations. *Linear Algebra Appl.*, 366:371–402, 2003.

[247] C.W. Shu. Essentially non-oscillatory and weighted essentially non-oscillatory schemes for hyperbolic Conservation Laws. *NASA/CR-97-206253 ICASE Report No.97-65*, November 1997.

[248] M. Sonntag and C.D. Munz. Shock capturing for discontinuous Galerkin methods using finite volume subcells. In J. Fuhrmann, M. Ohlberger, and C. Rohde, editors, *Finite Volumes for Complex Applications VII*, pages 945–953. Springer, 2014.

[249] S. K. Stanaway, B. Cantwell, P. R. Spalart, and Ames Research Center. *A numerical study of viscous vortex rings using a spectral method [microform]*. National Aeronautics and Space Administration, Ames Research Center, 1988.

[250] M. Takamoto and T. Inoue. A New Numerical Scheme for Resistive Relativistic Magnetohydrodynamics Using Method of Characteristics. *Astrophys. J.*, 735:113, 2011.

[251] A. H. Taub. Relativistic Rankine-Hugoniot Equations. *Phys. Rev.*, 74:328–334, 1948.

[252] M. Tavelli and M. Dumbser. A high order semi-implicit discontinuous Galerkin method for the two dimensional shallow water equations on staggered unstructured meshes. *Applied Mathematics and Computation*, 234:623 – 644, 2014. ISSN 0096-3003.

[253] M. Tavelli and M. Dumbser. A staggered semi-implicit discontinuous Galerkin method for the two dimensional incompressible Navier-Stokes equations. *Applied Mathematics and Computation*, 248:70 – 92, 2014.

[254] M. Tavelli and M. Dumbser. A staggered space-time discontinuous Galerkin method for the incompressible Navier-Stokes equations on two-dimensional triangular meshes. *Computers & Fluids*, 119:235 – 249, 2015.

[255] M. Tavelli and M. Dumbser. A staggered space-time discontinuous Galerkin method for the three-dimensional incompressible Navier-Stokes equations on unstructured tetrahedral meshes. *Journal of Computational Physics*, 319: 294 – 323, 2016.

[256] V.A. Titarev and E.F. Toro. ADER: Arbitrary high order Godunov approach. *Journal of Scientific Computing*, 17(1-4):609–618, 2002.

[257] V.A. Titarev and E.F. Toro. Finite-volume weno schemes for three-dimensional conservation laws. *Journal of Computational Physics*, 201:238–260, 2004.

[258] V.A. Titarev and E.F. Toro. ADER schemes for three-dimensional nonlinear hyperbolic systems. *Journal of Computational Physics*, 204:715–736, 2005.

[259] E. F. Toro. *Riemann Solvers and Numerical Methods for Fluid Dynamics, Third Edition*. Springer-Verlag, 2009.

[260] E. F. Toro and V. A. Titarev. Solution of the generalized riemann problem for advection-reaction equations. *Proc. Roy. Soc. London*, 458(2018):271–281, 2002.

[261] E. F. Toro and V. A. Titarev. Derivative Riemann solvers for systems of conservation laws and ADER methods. *Journal of Computational Physics*, 212 (1):150–165, 2006.

[262] E.F. Toro. *Riemann Solvers and Numerical Methods for Fluid Dynamics*. Springer, second edition, 1999.

[263] E.F. Toro, R.C. Millington, and L.A.M Nejad. Towards very high order Godunov schemes. In E.F. Toro, editor, *Godunov Methods. Theory and Applications*, pages 905–938. Kluwer/Plenum Academic Publishers, 2001.

[264] G. Tóth. The $\nabla \cdot B = 0$ constraint in shock-capturing magnetohydrodynamics codes. *Journal of Computational Physics*, 161(2):605 – 652, 2000. ISSN 0021-9991.

[265] C.-C. Tsai, T.-H. Hou, S. Popinet, and Y. Y. Chao. Wind wave prediction of tropical cyclones by a quadtree-adaptive model. *Coastal Engineering*, pages 108–119, 2013.

[266] G. Tumolo, L. Bonaventura, and M. Restelli. A semi-implicit, semi-lagrangian, p-adaptive discontinuous Galerkin method for the shallow water equations. *Journal of Computational Physics*, 232(1):46 – 67, 2013. ISSN 0021-9991.

[267] N. Tylli, L. Kaiktsis, and B. Ineichen. Sidewall effects in flow over a backward-facing step: Experiments and numerical simulations. *Physics of Fluids*, 14(11):3835–3845, 2002.

[268] J. J. W. van der Vegt and H. van der Ven. Space–time discontinuous Galerkin finite element method with dynamic grid motion for inviscid compressible flows I. general formulation. *Journal of Computational Physics*, 182:546–585, 2002.

[269] H. van der Ven and J. J. W. van der Vegt. Space–time discontinuous Galerkin finite element method with dynamic grid motion for inviscid compressible flows II. efficient flux quadrature. *Comput. Methods Appl. Mech. Engrg.*, 191: 4747–4780, 2002.

[270] Maurice H.P.M. vanPutten. A numerical implementation of {MHD} in divergence form. *Journal of Computational Physics*, 105(2):339 – 353, 1993. ISSN 0021-9991.

[271] J. R. Womersley. Method for the calculation of velocity, rate of flow and viscous drag in arteries when the pressure gradient is known. *The Journal of Physiology*, 127(3):553–563, 1955. ISSN 1469-7793.

[272] P. Woodward and P. Colella. The numerical simulation of two-dimensional fluid flow with strong shocks. *J. Comput. Phys.*, 54:115–173, 1984.

[273] P. Woodward and P. Colella. The numerical simulation of two-dimensional fluid flow with strong shocks. *Journal of Computational Physics*, 54:115–173, 1984.

[274] J. Yan and C.W. Shu. A local discontinuous Galerkin method for KdV type equations. *SIAM Journal on Numerical Analysis*, 40(2):769–791, 2002.

[275] M. Yang and Z. Wang. A Parameter-Free Generalized Moment Limiter for High-Order Methods on Unstructured Grids. *Advances in Applied Mathematics and Mechanics*, 2009.

[276] Y. Yu, D. Wu, and Y. Xu. Three dimensional discontinuous galerkin methods for euler equations on adaptive conforming meshes. *Computer Physics Communications*, 182(9):1771 – 1775, 2011.

[277] T. A. Zang and M. Y. Hussaini. On spectral multigrid methods for the time-dependent Navier–Stokes equations. *Applied Mathematics and Computation*, 19(1-4):359 – 372, 1986. ISSN 0096-3003.

[278] O. Zanotti and M. Dumbser. Numerical simulations of high Lundquist number relativistic magnetic reconnection. *Mon. Not. R. Astron. Soc.*, 418:1004–1011, 2011.

[279] O. Zanotti and M. Dumbser. A high order special relativistic hydrodynamic and magnetohydrodynamic code with space-time adaptive mesh refinement. *Computer Physics Communications*, 188:110–127, 2015.

[280] O. Zanotti, F. Fambri, and M. Dumbser. Solving the relativistic magnetohydrodynamics equations with ADER discontinuous Galerkin methods, a posteriori subcell limiting and adaptive mesh refinement. *Mon. Not. R. Astron. Soc.*, 452:3010–3029, 2015.

[281] O. Zanotti, F. Fambri, M. Dumbser, and A. Hidalgo. Space-time adaptive ADER discontinuous Galerkin finite element schemes with a posteriori subcell finite volume limiting. *Computers & Fluids*, 118:204 – 224, 2015. ISSN 0045-7930.

[282] S. Zenitani, M. Hesse, and A. Klimas. Two-Fluid Magnetohydrodynamic Simulations of Relativistic Magnetic Reconnection. *Astrophys. J.*, 696:1385–1401, 2009.

[283] S. Zenitani, M. Hesse, and A. Klimas. Resistive Magnetohydrodynamic Simulations of Relativistic Magnetic Reconnection. *Astrophysical Journal Lett.*, 716:L214–L218, 2010.

[284] W. Zhang, A. MacFadyen, and P. Wang. Three-Dimensional Relativistic Magnetohydrodynamic Simulations of the Kelvin-Helmholtz Instability: Magnetic Field Amplification by a Turbulent Dynamo. *Astrophys. J.*, 692:L40–L44, 2009.

[285] Jonathan Zrake and Andrew I. MacFadyen. Numerical simulations of driven relativistic magnetohydrodynamic turbulence. *Astrophys. J.*, 744(1):32, 2012. ISSN 0004-637X.

[286] G Zumbusch. Finite element, discontinuous Galerkin, and finite difference evolution schemes in spacetime. *Classical Quantum Gravity*, 26(17):175011, 2009.

LIST OF FIGURES

LIST OF TABLES